International Journal of Antennas and Propagation

Wideband, Multiband, Tunable, and Smart Antenna Systems for Mobile and UWB Wireless Applications

Guest Editors: Renato Cicchetti, Antonio Faraone, Diego Caratelli, and Massimiliano Simeoni

Wideband, Multiband, Tunable, and Smart Antenna Systems for Mobile and UWB Wireless Applications

International Journal of Antennas and Propagation

Wideband, Multiband, Tunable, and Smart Antenna Systems for Mobile and UWB Wireless Applications

Guest Editors: Renato Cicchetti, Antonio Faraone, Diego Caratelli, and Massimiliano Simeoni

Editorial Board

Contents

Hindawi Publishing Corporation
International Journal of Antennas and Propagation
Volume 2013, Article ID 254807, 3 pages
http://dx.doi.org/10.1155/2013/254807

Editorial

Wideband, Multiband, Tunable, and Smart Antenna Systems for Mobile and UWB Wireless Applications

Renato Cicchetti,[1] Antonio Faraone,[2] Diego Caratelli,[3] and Massimiliano Simeoni[4]

[1] *Department of Information, Electronic and Telecommunication Engineering, University of Rome "La Sapienza", Rome, Italy*
[2] *Chief Technical Office, Motorola Solutions Inc., Fort Lauderdale, FL 33322, USA*
[3] *Microwave Technology and Systems for Radar, Delft University of Technology, The Netherlands*
[4] *European Space Agency, ESTEC-Keplerlaan, ZH Noordwijk, The Netherlands*

Correspondence should be addressed to Renato Cicchetti; cicchetti@die.uniroma1.it

Received 6 August 2013; Accepted 6 August 2013

1. Introduction

With the advent of high data rate 3G and 4G wireless communication systems and the app-based use paradigm, wireless connectivity through multiple air interfaces has become a common requirement in the RF architecture of new generation mobile communication devices. The modern wireless handset easily incorporates three or more antennas to enable cellular, Wi-Fi, and GPS connectivity, frequently over multiple bands. Multiple antenna systems are frequently designed to implement diversity or spatial multiplexing schemes, as in the case of WCDMA and LTE, to increase the resiliency and capacity of wireless links, and even to operate multiple voice/data links simultaneously. Concurrently, ultra-wideband (UWB) systems used in short range communications, remote sensing, and through-the-wall radar imaging have introduced a new paradigm in antenna design where the mitigation of pulse distortion is of the essence, thus requiring a shift in antenna design approach and the introduction of novel radiating systems.

This special issue is intended to reflect current R&D trends and novel approaches in the analysis and synthesis of antenna systems for the new generation of mobile communication devices, such as smartphones, tablets, and laptop computers as well as for UWB communication systems and radars. A particular emphasis has been paid to the analysis and design of broadband, multiband, and reconfigurable antennas for wireless and UWB applications, as well as to the identification of integration techniques with the host platform. Important efforts have been devoted to the characterization of the radio channel for MIMO systems.

The special issue is composed of 18 contributions that can be divided into the following 8 clusters.

2. Contributions to Reconfigurable and Multiband Antenna Technology

In "*Recent developments in reconfigurable and multiband antenna technology*" by N. Haider et al., the authors present a comparative analysis of various reconfigurable and multiband antenna concepts. In particular, three basic approaches, tunable/switchable antenna integration with radiofrequency switching devices, wideband or multiband antenna integration with tunable filters, and array architectures with the same aperture utilized for different operational modes, have been analyzed in detail showing inherent benefits and challenges.

In "*A reconfigurable triple-Notch-Band antenna integrated with defected microstrip structure band-stop filter for ultra-wideband cognitive radio applications*" by Y. Li et al., the authors describe a reconfigurable UWB monopole antenna for cognitive radio applications. Three narrow band-notched frequencies are obtained using a defected microstrip structure (DMS), a stop band filter (BSF) embedded in the microstrip feed line, and an inverted π-shaped slot etched in the rectangular radiant patch, respectively. Reconfigurable

characteristics of the proposed cognitive radio antenna are achieved by means of four ideal switches integrated on the DMS-BSF and the inverted π-shaped slot.

In "*Planar ultrawideband antenna with photonically controlled notched bands*" by D. Draskovic et al., the authors describe a planar microstrip-fed UWB printed circular monopole antenna with optically controlled notched bands. The proposed antenna is composed of a circular UWB patch, with an etched T-shaped slot controlled by an integrated optical switch. The slot modifies the frequency response of the antenna suppressing the 3.5–5 GHz band when the switch is in an open state. The optical switch is controlled by a low-power laser diode rendering the antenna remotely controlled by means of an optical fiber.

In "*Compact, frequency reconfigurable, printed monopole antenna*" by R. Gonçalves et al., the authors propose, a compact reconfigurable printed monopole antenna, useful to operate in the UMTS and WLAN bands. To this purpose a chip inductor and PIN diode are employed to modify the electrical length of the monopole making the antenna able to operate in the mentioned frequency bands.

3. Contributions to Broad- and Multibanding Techniques

In "*Analysis and design of a novel compact multiband printed monopole antenna*" by J. Wang and X. He, the authors present a compact T-shaped multiband printed monopole antenna integrating some U-shaped band-notch structures. The proposed antenna operates at 2.25–2.7 GHz, 3.25–3.6 GHz, 4.95–6.2 GHz, and 7-8 GHz, covering the operation bands of Bluetooth, WiMAX, and WLAN and the downlink of the X-band satellite communication systems.

In "*Dual-band integrated antennas for DVB-T receivers*" by A. D'alessandro et al., the authors present an overview on compact Planar Inverted-F Antennas (PIFAs) that are suitable for monitor-equipped devices. High efficiency PIFAs with a percentage bandwidth greater than 59% (470–862 MHz DVB-T band) are shown. Finally, to show the extreme flexibility of the previous two configurations, a novel dual-band L-shape PIFA has been proposed. The L-shape PIFA prototype is obtained by properly cutting and folding a single metal sheet, thus resulting in a relatively low-cost and mechanically robust antenna configuration.

In "*Planar printed shorted monopole antenna with coupled feed for LTE/WWAN mobile handset applications*" by D. Kang and Y. Sung, the authors present a shorted monopole antenna with coupled feed for LTE/WWAN mobile handset applications. The basic resonance of the shorted monopole combines with the resonance caused by the interaction between the coupling strip and the feeding pad to cover the LTE700, GSM850, and GSM900 bands. Both the feeding pad and the coupling strip operate with the shorting strip as a loop antenna. The resonance of the loop antenna and the harmonics of the shorted monopole combine to cover the GSM1800, GSM1900, UMTS, and LTE2300 bands. A stable and omnidirectional radiation pattern with reasonable gain has been observed over the operating bandwidth.

In "*Parasitic-element-loaded UWB antenna with band-stop function for mobile handset wireless USB*" by Y. Lim et al., the authors present an antenna loaded by parasitic elements for the wireless USB of mobile handsets useful for UWB service in which a band-stop function of 5.725–5.825 GHz WLAN band is required. To this end, two kinds of parasitic elements are incorporated into a rectangular radiator to obtain enhanced impedance bandwidth and band-stop function. In this way, bandwidths of 3.15–4.75 GHz and of 7.2–10.2 GHz are achieved, while the frequency band 5.725–5.825 GHz is suppressed.

4. Contributions to Antennas for UWB Applications

In "*A compact UWB antenna with a quarter-wavelength Strip in a Rectangular slot for 5.5 GHz band notch*" by P. Moeikham et al., the authors present a monopole UWB antenna integrating a notch filter to reduce the electromagnetic interferences (EMIs) with WLAN/WiMAX communication systems operating in the frequency band located around 5.5 GHz. Consisting in a rectangular slot including a quarter-wavelength strip integrated on the lower inner edge of the UWB radiating patch, the filter proposed by the authors is capable of reducing the energy emission in the frequency range between 5.1 and 5.75 GHz resulting in lower EMIs with sensible electronic equipment working in this frequency band.

In "*A modified vivaldi antenna for improved angular-dependent fidelity property*" by Z. Zeng et al., the authors present a modified Vivaldi antenna optimized to radiate impulsive signals. To this end, a spatial filter consisting of two suitable dielectric slabs parallel to the antenna substrate is introduced. As a result, the fidelity factor indicating the quality of the radiated field is significantly improved. In fact, the experimental measurements show that the ranges with the fidelity factor better than the value of 0.9 are improved by 95% in H-plane and by 14% in E-plane, respectively, with respect to a conventional Vivaldi antenna.

In "*High gain compact strip and slot UWB sinuous antennas*" by E. Agastra et al., the authors analyze three ground-backed compact strip and slot sinuous antennas. The proposed configuration allows for a single lobe, polarization-versatile, high efficiency, and ultrawideband antenna not needing a cumbersome lossy back cavity typical of conventional single-lobe sinuous antennas.

5. Contributions to Special Materials, and Fabrication Techniques

In "*Innovative radiating systems for train localization in interference conditions*" by C. Vegni et al., the authors, firstly, propose an innovative radiating systems based on the metamaterial technology for global navigation satellite system (GNSS) applications in radio frequency interference conditions. Secondly, fixed radiation pattern antenna (FRPA), and controlled radiation pattern antenna (CRPA) phased array configurations of miniaturized patch antennas are studied.

Finally, the design of the phased array is applied to a GNSS user receiver in a realistic railway environment.

6. Contributions to Wireless Systems for Remote Control of Vital Parameters

In "*A twin spiral planar antenna for UWB medical radars*" by G. A. Zito et al., the authors propose a planar-spiral antenna useful to be employed in an UWB radar system for heart activity monitoring. The proposed antenna presents a reflection coefficient lower than −8 dB over the 3–12 GHz band, while the coupling between the two spiral dipoles is about −20 dB. Numerical simulations indicate that the radiation impedance variation, caused by the thorax vibrations associated with heart activity, is the most likely explanation of the UWB radar operation.

In "*Wireless sensing for the respiratory activity of human beings: measurements and wide-band numerical analysis*" by L. Scalise et al., the authors propose an RF sensing system for the remote control of the respiratory activity. The proposed sensing system is based on the measurement of the phase variation of the reflection coefficient caused by the respiratory activity. The phase signal compared with the thorax displacement measured by a reference instrument shows a high correlation with different subject postures (sitting, standing, and lying), and a reduction of the signal amplitude with the distance −0.11 dB/cm is reported. The proposed system makes it possible to operate at distances up to 2.5 m.

In "*Safety aspects of people exposed to ultra wideband radar fields*" by M. Cavagnaro et al., the authors analyze the safety aspects of people exposed to a field emitted by UWB radar for breath activity monitoring, operating both in the spatial environment and on ground. The basic restrictions and reference levels reported in the ICNIRP safety guideline are considered, and the compliance of electromagnetic fields radiated by a UWB radar with these limits has been evaluated. The authors show that if the field emitted by the UWB radar is compliant with spatial and/or ground emission masks, then both reference levels and basic restrictions are largely satisfied.

7. Contributions to Numerical and Analytical Techniques for Antenna Modeling and Design

In "*Structure-based evolutionary programming design of broadband wire antennas*" by G. A. Casula et al., the authors present a designed technique for wideband wire antennas. The technique, based on the structure-based evolutionary programming, is used to design a broadband antenna, operating in the 3–16 GHz frequency band, with an end-fire radiation pattern, high gain, good impedance matching, and robustness with respect to realization tolerances.

8. Contributions to Passive Devices per UWB Applications

In "*Optimized ultrawideband and uniplanar minkowski fractal branch line coupler*" by M. Jahanbakht and M. T. Aghmyoni, the authors present a directional coupler, based on a non-Euclidean Minkowski fractal geometry able to operate with excellent isolation and low insertion losses over the UWB frequency range. The proposed device presents good integration features that make it suitable to be employed as a power divider in electronic circuitry or in the array of broadband or UWB antennas.

9. Contributions to MIMO Antenna Systems and Channel Modeling

In "*Sparse channel estimation for MIMO-OFDM two-way relay network with compressed sensing*" by A. Zhang et al., the authors propose a sparse channel estimation scheme at end users under the relay channel to enable us to exploit sparsity. First, they formulate the sparse channel estimation problem as a compressed sensing problem by using the sparse decomposition theory. Second, the CIR is reconstructed by CoSaMP and OMP algorithms. The numerical results confirm the superiority of the proposed methods over the traditional linear channel estimation methods.

Acknowledgments

The editors would like to express their gratitude to the authors and the anonymous reviewers for their contributions to this special issue.

Renato Cicchetti
Antonio Faraone
Diego Caratelli
Massimiliano Simeoni

Hindawi Publishing Corporation
International Journal of Antennas and Propagation
Volume 2013, Article ID 623950, 13 pages
http://dx.doi.org/10.1155/2013/623950

Research Article

Innovative Radiating Systems for Train Localization in Interference Conditions

C. Vegni,[1] M. Tosti,[2] and A. M. Vegni[3]

[1] *Thales Alenia Space Italia, Navigation & Integrated Communication Directorate, Via Saccomuro 24, 00131 Rome, Italy*
[2] *NEXT, Ingegneria dei Sistemi, Via Andrea Noale 345/b, 00155 Rome, Italy*
[3] *University Roma Tre, Department of Engineering, Via Vito Volterra 62, 00146 Rome, Italy*

Correspondence should be addressed to C. Vegni; claudio.vegni@thalesaleniaspace.com

Received 5 December 2012; Revised 21 February 2013; Accepted 3 June 2013

Academic Editor: Renato Cicchetti

The design of innovative radiating systems based on the metamaterial technology for GNSS (Global Navigation Satellite System) applications in radio frequency (RF) interference conditions is proposed. To this aim, firstly two typical adaptive array techniques (i.e., *nulling* and *beam-forming*) are discussed and tradeed off. Secondly, FRPA (Fixed Radiation Pattern Antenna) and CRPA (Controlled Radiation Pattern Antenna) phased array configurations of miniaturized patch antennas are studied by means of electromagnetic commercial tools and phased array optimization algorithms. This process leads to the identification of a phased array design. Benefits and drawbacks for GNSS applications are highlighted. Finally, the design of the phased array is applied to a GNSS user receiver in a navigation realistic environment. Simulation results are obtained in a realistic scenario for railway applications, comprising of a GNSS satellite constellation, a GNSS user receiver (i.e., on-board train equipment) running along a track in Western Australia, and a constellation of interfering satellites. Navigation service performances (i.e., user location accuracy and service availability) are computed taking into account the adaptive array radiation pattern in two different modes (i.e., FRPA or CRPA) and band-limited white noise interference.

1. Introduction

Concern about GPS (Global Positioning System) vulnerability has received a great deal of attention recently [1, 2]. GNSS receivers are highly susceptible to interference caused by jamming and spoofing. Historically, signal jamming and the design have been primarily considered as a military problem. Now, signal interference threatens all the GNSS receivers, military and civilian.

GPS signal typical level on Earth surface is around −163 dB W, that is, below the noise floor of the receiver (i.e., $N = K \cdot T_{\mathrm{SYS}} \cdot B$, e.g., −228.6 + 27 + 63 dB-Hz = −138 dB for 20 MHz bandwidth L band signal).

The reason why GPS signals can survive to degradation effects like interference is due to the spread-spectrum nature of the transmission, allowing receivers to correlate the satellite signal out from below the background noise [2, 3]. However, each receiver exhibits a limitation to the amount of non-GNSS interference it can cope with, whilst still acquiring or tracking the desired signals. In other words, each receiver has a maximum Jammer-to-Signal ratio (i.e., J/S) that is able to tolerate.

Recent studies [1, 2] demonstrated that a 10 mW jammer at a distance less than 10 km can seriously disturb the acquisition process of a GPS receiver. Jamming is not the only form of GNSS interference; spoofing is a more recent one. Spoofing (i.e., data level interference) can be considered as a more dangerous form of interference than jamming, because it is not obvious that the GNSS receiver is being spoofed, while jamming constitutes a denial of service and it is easily detectable.

In this paper a band-limited white noise interference is considered. When the interference has flat spectrum centred in f frequency and extending in the range $(f_i - \beta_i/2) \leq f \leq (f_i + \beta_i/2)$, its spectrum is expressed as follows [2]:

$$S_i(f) = \begin{cases} \dfrac{1}{\beta_i}, & \left(f_i - \dfrac{\beta_i}{2}\right) \leq f \leq \left(f_i + \dfrac{\beta_i}{2}\right), \\ 0, & \text{elsewhere.} \end{cases} \tag{1}$$

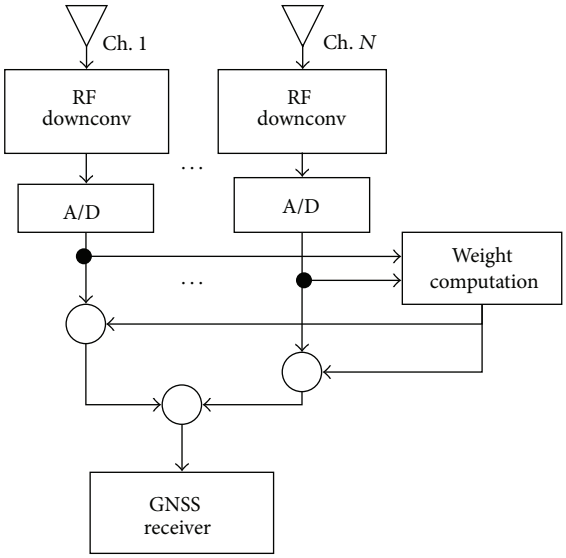

Figure 1: *Single-output nulling* antenna block diagram.

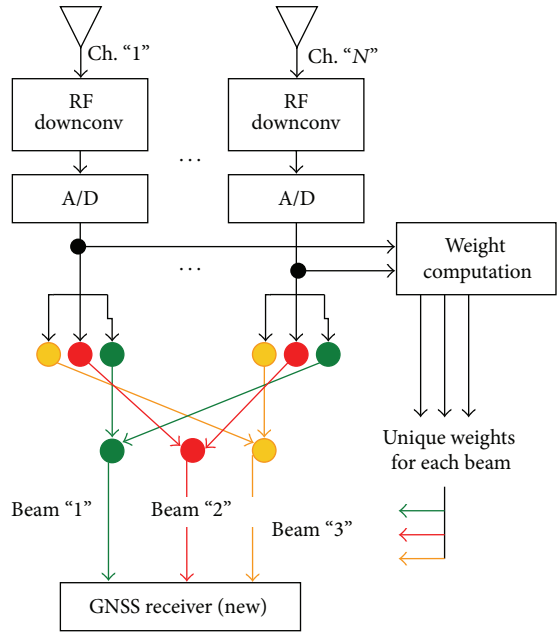

Figure 2: *Multiple-output beam-steering* antenna block diagram.

RF interference and multipath effects can be mitigated or eliminated by an appropriate GNSS antenna and receiver design [1]. In particular, we focus on antenna solutions as adaptive arrays. They are considered the single most powerful antijamming tool in the GNSS systems engineer's toolkit. They provide jamming rejection from 15 to 90 dB depending on the specific architecture used. Their main drawback is that they require an array of antenna elements, each spaced about ten centimetres (*center-to-center*) in S band, and thus their physical envelope cannot meet the antenna room constraints.

Therefore, the paper will be organized according to three following steps.

(1) Adaptive array typology trade-off: two typical techniques (i) *nulling* and (ii) *beam-forming* are discussed and compared in Section 2.

(2) Adaptive array antenna design: in Section 3 the RF design of a phased array antenna is presented in terms of array geometric layout and single radiator element in metamaterial technology.

(3) GNSS study case: a realistic navigation case is investigated in Section 4. Specifically, the train localization problem by GPS satellites is studied in conditions of RF interfering satellites.

FRPA and CRPA solutions are considered, and for each one GPS service performances (i.e., train accuracy and service availability) are computed. In other words, the RF design is validated in terms of GNSS system performances in a realistic scenario. Conclusions are finally drawn.

2. Adaptive Array Typology Trade-Off

Two types of adaptive array antenna are used with GNSS receivers, that is, (i) *single-output nulling* (Figure 1) antennas, and (ii) *multiple-output beam-steering* (Figure 2) antennas [4].

Most of deployed systems are single-output adaptive *nulling* antennas that operate as an antijamming appliqué. In this way the GNSS receiver does not need to know what type of antenna is connected to, that is, FRPA or CRPA.

Some development systems [6] tend to emphasize *multiple-output beam-steering* antennas because of their better performance. However, in order to handle the *multiple-output* channels, a new receiver is required too. The trend is to integrate the array processing with the GNSS receiver in a single unit.

On the other side, a *single-output nulling* antenna uses a common set of weights for all GNSS signals. The objective is to minimize the output power subject to the constraint that one element is turned on. Remaining channels have their output phase and amplitude dynamically adjusted, so as to cancel out jammers in the summation process. The result consists in very sharp spatial nulls in the directions of the jammers but, because the GNSS signal direction of arrival is not taken into account, a significant possibility arises for low gain in some signal directions.

However, in GNSS applications, the antenna has to receive navigation signal from as many satellites as possible.

On the other side, GNSS antenna is requested to reject as many interfering satellites as possible along single or multiple directions.

In principle, an N-element array can independently steer $N-1$ spatial nulls in the direction of jammers. Moreover, in the *multiple-output beam-forming* array configuration, a unique set of weights is generated and optimized for each signal. The weight information process takes into account the desired signal direction of arrival, and, in absence of jamming, it will phase the input channels so they coherently add together to create a beam in the direction of the satellite.

Table 1: Adaptive antenna *nulling* versus *beam-forming* techniques.

N-elements antenna feature	*Nulling*	*Beam-forming*
Robustness to interference	Low (low gain along not IF directions)	Medium (adequate gain roll-off shown)
Maximum number of spatial nulls	$N-1$	$N-1$
Null depth	<-20 dB	<-20 dB
Directional beam capability	No	Yes
Impact on accuracy measurement	Not compatible with high precision applications	More than 100° on carrier phase meas.; 1 meter on code phase meas.

In addition, to enable an adaptive antenna array to steer minimal antenna gain towards jammers, *beam-forming* simultaneously ensures that the antenna steers maximum gain towards GNSS satellites.

In other words, instead of minimizing the interference-to-noise ratio (INR), the aim is to maximize the signal-to-interference-plus-noise ratio (SINR).

Like the *nuller*, the *beam-former* can independently steer $N-1$ spatial nulls.

Both the *nuller* and the *beam-former* perform much better (i.e., >20 dB) against narrow-band jammers.

The advantages of *nulling* and *beam-forming* antennas can be reported as follows.

(i) *Nulling* solution appears less complex than *beam-former* one.

(ii) *Nullers* synthetize sympathetic nulls in directions other than those of jammers. Sometimes, this happens in the direction of a desired signal and the signal is lost. It corresponds to a decrease of the number of visible satellites and consequently to a degradation of GNSS performance parameters (e.g., accuracy, continuity).

(iii) *Beam-formers* provide a broad-beam in the direction of the desired signal and lower gain in other directions. Multipath arriving from low gain directions is more strongly attenuated and has less ability to corrupt code and carrier phase observables.

(iv) *Nullers* do not provide this performance gain as they do not seek to generate directional beam.

In general, adaptive arrays improve signal-to-noise ratio in presence of jamming and thus permit signal tracking in environments that otherwise would lack code and carrier phase observables (lack of pseudorange measurement). However, this benefit is not without cost: adaptive arrays can bias code and carrier phase observables. The array antenna is a spatial filter, and its distortion effects are also direction dependent. The distortion is unique for each desired signal and does not necessarily *common-mode out* in subsequent processing.

In absence of jamming, the biases are fairly benign, while in jamming conditions the biases can become large and sustained.

Beam-formers can show 100-degree carrier phase biases and upwards of 1-meter code phase biases.

Nullers do even worse. For high precision systems, these errors can be a significant component of the overall error budget. Table 1 summarizes the previous considerations.

In this paper, the synthesis algorithm MVDR (Minimum Variance Distortionless Response) is applied [4, 6]. It falls into the category of *beam-forming* adaptive array. This algorithm allows the synthesis of up to $N-1$ nulls and the pointing of the main beam along one single direction. The considered direction is the broad-side one ($\theta = 90^\circ$ with respect to horizon).

In case interfering direction is close to or coincides with the broad-side one, the algorithm shall show convergence problems.

However, this satellite geometric configuration is highly unlikely. In that case the antenna beam shall point to a direction computed as the mean value among all the interfering directions.

3. Adaptive Array Antenna Design

In this section, firstly, we show the basic concepts to be followed to design a GNSS antenna. Secondly, the phased array element innovative design is illustrated by VSWR, axial ratio (AR), and radiation pattern curves. Finally, the adaptive *beam-forming* phased array design is shown, in terms of array layout and radiation patterns.

3.1. GNSS Antenna Guidelines. The guidelines consider four typical specific antenna parameters, that is, (i) pattern, (ii) roll-off, (iii) polarization purity, and (iv) phase centre.

(i) Antenna pattern: the GNSS antenna has to receive all the navigation signals transmitted by the GNSS satellites in visibility. Ideally, it should show an omnidirectional radiation pattern. The GPS receiver operates best with only a small difference in power among the signals from the various satellites, and, ideally, the antenna covers the entire hemisphere with no variation in gain. This has to do with potential cross-correlation problems in the receiver and the fact that excessive gain roll-off may cause signals from satellites at low elevations to drop well below the noise floor of the receiver. On the other hand, optimization for multipath rejection and antenna noise temperature require some gain roll-off.

(ii) Antenna roll-off: antenna should show perfect hemispherical radiation pattern. However, such an antenna cannot be practically built, and real-world GNSS antennas experience a gain roll-off of 10 to 20 dB from broad-side to the horizon.

Table 2: GNSS antenna design guidelines.

Antenna parameter	Guidelines for GNSS applications
Radiation pattern	Hemispherical
Roll-off	11–13 dB (from broad-side to 10° elevation direction)
Polarization purity	(i) 1 dB at broad-side (ii) <6 dB at 10° elevation
Phase centre	(i) Stable versus frequency (ii) Stable versus Az, El angles

(iii) Antenna polarization purity: a right hand circular polarization (RHCP) antenna will pick up some left hand circular polarization (LHCP) energy. For high-end (geodetic/choke ring) GNSS antennas, the typical AR in broad-side should be around 1 dB. AR increases toward the lower elevations (less than 3 to 6 dB at 10° elevation for a high-performance antenna). Maintaining a good AR (i.e., 1-2 dB) over the entire hemisphere and at all the frequencies is a challenge for the antenna RF designer. Good polarization purity represents a valid rejection to multipath/interference effect. In fact, reflected signals are LHCP (single reflection). Consequently, multipath signals from reflections against vertical objects such as buildings can be deeply attenuated or even suppressed.

(iv) Antenna phase centre: in GNSS applications, the user position is relative to the phase centre of the GNSS receiving antenna. The phase centre is the point in space from which all the rays appear to emanate (or converge on) the antenna. Put in another way, it is the point where the fields from all the incident rays appear to add up in phase. Determining the phase centre is important in GNSS systems, particularly when millimetre positioning resolution is desired. Ideally, the phase centre is a single point in space for all directions at all frequencies. A real-world antenna often will possess multiple phase centre points or a phase centre that appears "*smeared out*" as frequency and viewing angle vary. For well-designed high-end (geodetic/choke ring) GNSS antennas, phase centre variations in azimuth are small and in the order of a couple of millimetres. The vertical phase offsets are typically 10 mm or less.

The above-discussed guidelines can be summarized in Table 2.

3.2. Element Design. The single radiator configuration is shown in the top view (Figure 3), in the cross-view (Figure 4), and in 3D view (Figure 5). This is a dual probe miniaturized monolayer patch in L1 band, at 1.55 GHz central frequency. The circular polarization is obtained by two inputs (probes). Each probe is electromagnetically coupled to the radiating patch by a parasitic disk. Moreover, four mushrooms (depicted in yellow in Figure 3) are introduced to reduce the envelope of the squared ring. In particular, mushrooms are folded (dotted lines) in order to improve capacitive effects.

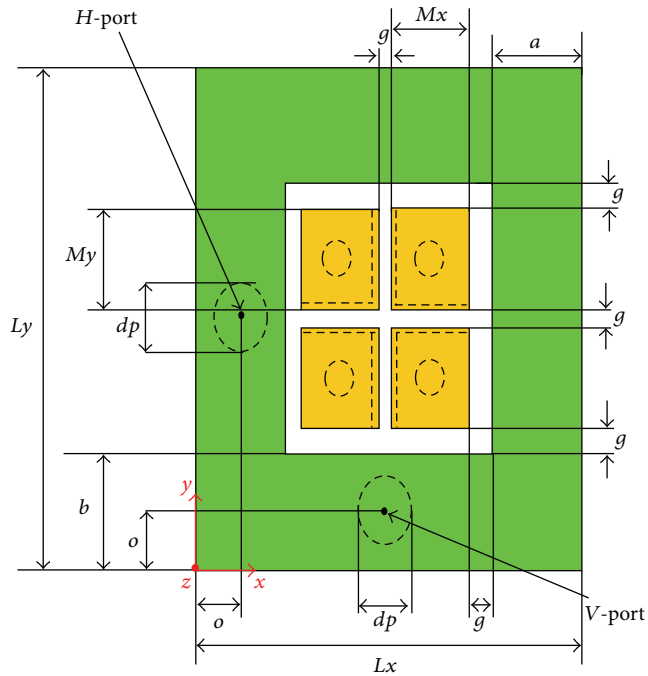

Figure 3: Single element—top view.

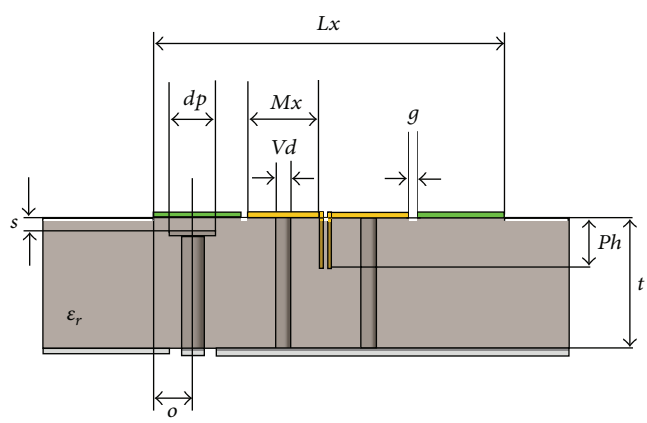

Figure 4: Single element—cross view (V-port not shown).

Balanced feeds tend to have superior scanning performance as the higher order modes are naturally suppressed by the symmetrical feeding arrangement. Moreover, polarization purity is improved using two inputs instead of a single port. A dual-probe interconnect is chosen as a result of these performance advantages.

The miniaturized monolayer patch can be easily obtained by using the metamaterial technology. It is well known that this technology allows several advantages in the realization of antennas, namely, the printed ones. One of these advantages (miniaturization) is obtained by using "*metamaterial-based*" antennas or "*metamaterial-inspired*" ones.

The difference among "*metamaterial-based*" antennas and "*metamaterial-inspired*" ones stands either using unconventional dielectric slabs (for "*metamaterial-based*"

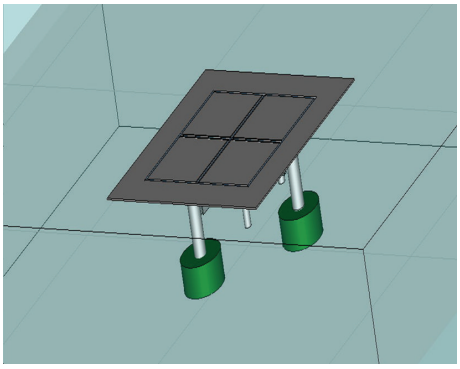

Figure 5: Single element 3D view.

antennas) or parasitic elements/cuts nearby/inside the radiating patch (for "*metamaterial-inspired*" antennas) [7–12].

This means that major dimension of metamaterial antenna elements used in array configuration is smaller than usual ones (from $\lambda_g/2$ to $\lambda_g/20$ or more, corresponding to an area reduction of 90% or more). Consequently, the dimensions of the whole antenna (e.g., the array) can be drastically reduced [13, 14].

The patch ground-plane separation is about 5 mm, and the underlying substrate permittivity is 2.2. The envelope area is 3.38 cm^2 (i.e., 1.84 × 1.84 cm ≈ 3.38). It is noted that, at the same working frequency (1.55 GHz) in case of standard monolayer (i.e., $\varepsilon_r = 2.2$) patch (typical $\lambda_g/2$), the single element envelope would be 6.41 × 6.41 = 41.08 cm^2. Metamaterial radiator technology area is the 3.38/41.08 = 8.22% of a standard monolayer patch.

A Cartesian reference system adopted to define the field quantities is introduced in Figure 3. Its origin is coincident to the left-side angle of the squared ring as shown in the figure.

Table 3 reports the single element physical parameters (distances expressed in mm).

Finally, the −15 dB return loss (Figure 6) bandwidth is 25.2 MHz (1.6%).

On the other side, the reduction of the antenna aperture generally corresponds to a decrease of the single element antenna gain. This effect has been taken into account in the design of the phased array antenna. The radiation pattern is shown in Figure 7, where it can be noted the peak gain around 5.7 dBi.

The axial ratio value is about 2 dB and shows a flat trend (Figure 8). It is in line with the guidelines described in the previous paragraph which are low AR values for low elevation angles.

3.3. Array Layout Optimization. The antenna aperture is a design driver. The layout definition process is addressed considering the following aspects.

(i) The envelope diameter shall be compatible to train roof accommodation, that is, 80 cm (*goal*) and 30 cm (*nice-to-have*).

(ii) The guidelines are those described in Section 3.1.

Table 3: Single element physical parameters.

Parameter	Value	Note
ε_r	2.2	Dielectric constant
t	4	Substrate thickness
a	2.8	Patch arm width
b	2.8	Patch arm length
M_x	6.1	Mushroom width
M_y	6.1	Mushroom length
mt	0.1	Mushroom thickness
dp	1.8	Probe plate diameter
s	0.15	Gap probe-patch
Vd	0.7	Via diameter
Ph	2	Parallel plates capacitors height
dh	3.85	Parasitic element height ($t - s$)
g	0.2	Gap between metals
o	1.9	Feed offset
L_x	18.4	Square ring x-size
L_y	18.4	Square ring y-size
H-port x	1.9	Feed offset
H-port y	9.2	$L_y/2$
V-port x	9.2	$L_x/2$
V-port y	1.9	Feed offset

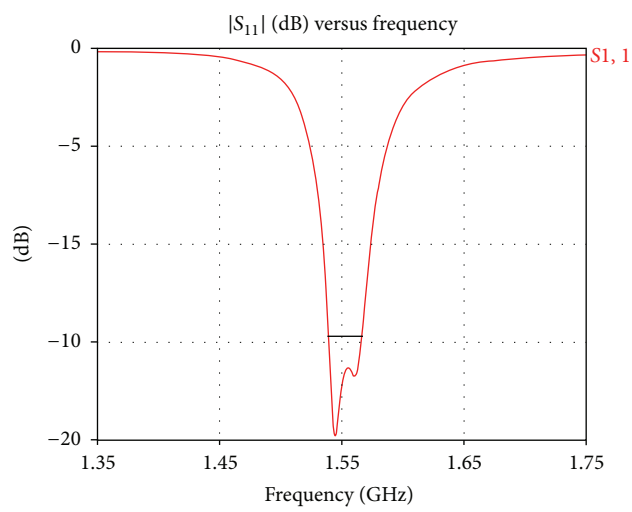

Figure 6: Single element return loss versus frequency.

Two layouts have been identified, that is, (i) the 13 elements, and (ii) the 7 elements configuration, as depicted in Figures 9 and 10, respectively. The first configuration is compliant to the 80 cm envelope constraint, while the second one to the *nice-to-have* constraint (i.e., 30 cm). The geometry proposed in the 7 elements configuration has been already studied in the frame of GNSS studies [15]. Both layouts show physical symmetry along three symmetry axes, as depicted in Figures 9 and 10. As a consequence, a symmetrical pattern shall derive. It will optimize the GNSS satellites visibility.

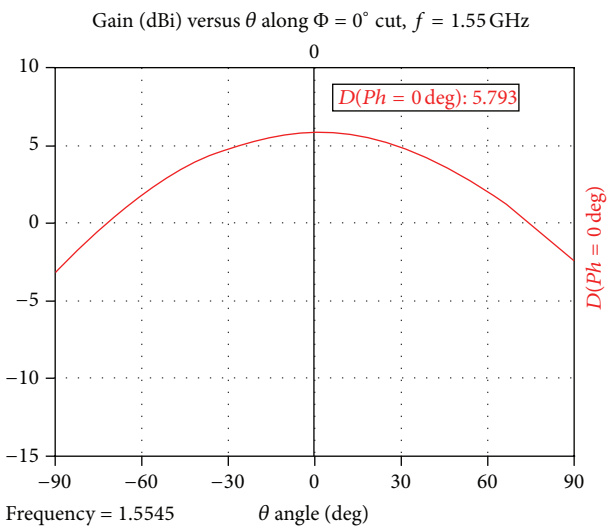

FIGURE 7: Single element gain versus elevation angle.

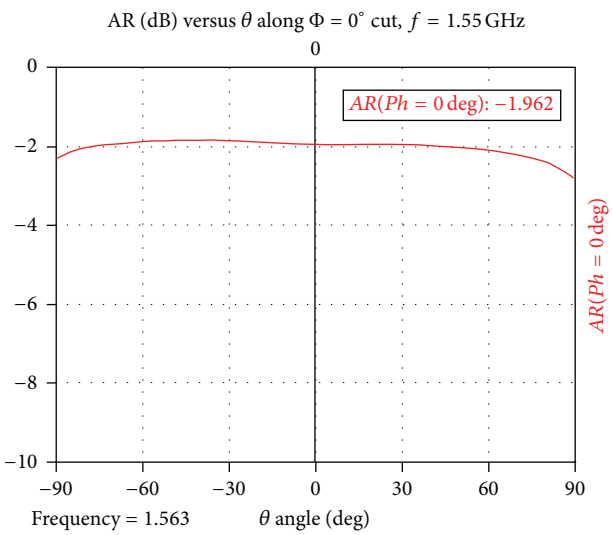

FIGURE 8: Single element axial ratio versus elevation angle.

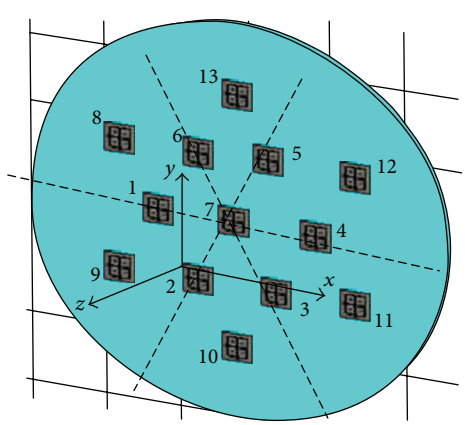

FIGURE 9: 13 elements array configuration—3D view.

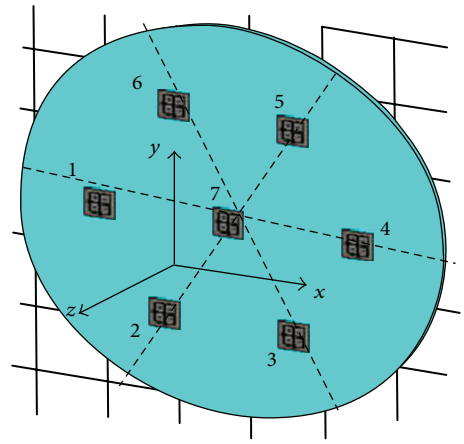

FIGURE 10: 7 elements array configuration—3D view.

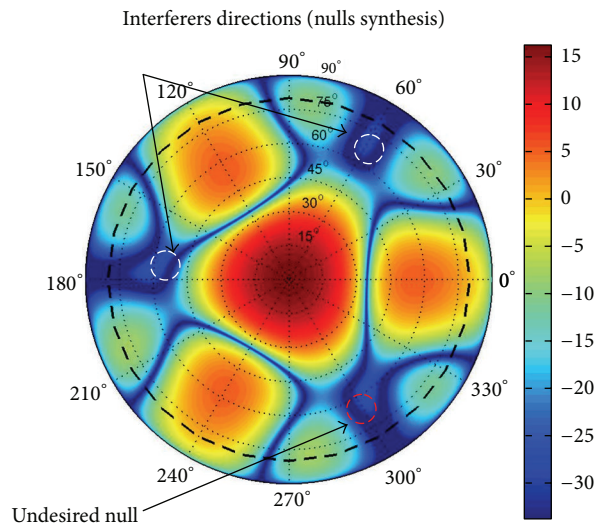

FIGURE 11: 7 elements array adaptive beam-forming antenna pattern—two nulls synthesis.

In both layouts the radiating elements are 0.73 λ_g spaced. This value derives from a trade-off between accommodation issues ($d/\lambda_g > 0.5$) and grating lobes effect ($d/\lambda_g < 1$).

Assuming 0.73 λ_g, for the 7 elements configuration and radiator in metamaterial technology, the antenna diameter is 20.57 cm. The total envelope is obtained by adding the 25% of antenna diameter value. The value is compliant to the accommodation constraint (<30 cm).

It is noted that considering standard antenna technology the overall envelope of the antenna would have exceeded the above-mentioned constraint.

The excitation coefficients for elements of the configurations at 13 and at 7 elements have been optimized by MVDR algorithm in order to synthesize nulls (up to 6) keeping the main lobe pointing $\theta = 0^\circ$ (zenith direction).

Figure 11 shows an example of synthesis of two nulls for 7 elements antenna, along $\theta_1 = 60^\circ$, $\Phi_1 = 60^\circ$ and $\theta_2 = 70^\circ$, $\Phi_2 = 180^\circ$ directions. They are marked in white. On the other side, main *beam-steering* direction is set to

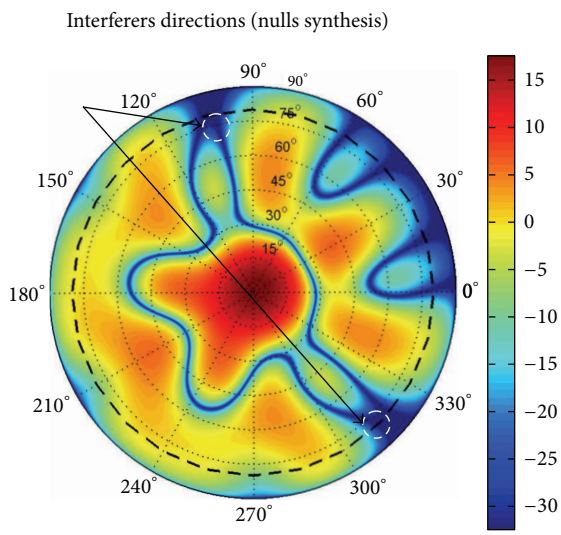

Figure 12: 13 elements array adaptive beam-forming antenna pattern—two nulls synthesis.

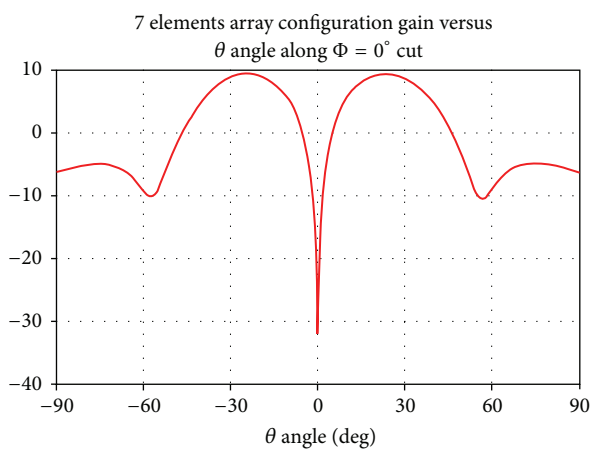

Figure 13: 7 elements array: adaptive beam-forming antenna pattern—single null synthesis.

Table 4: Excitation synthesized coefficients of pattern shown in Figure 13.

Element Id.	Amplitude [dB]	Phase [deg]
1	0	0
2	0	+60
3	0	+120
4	0	+180
5	0	+240
6	0	+300
7	−30	0

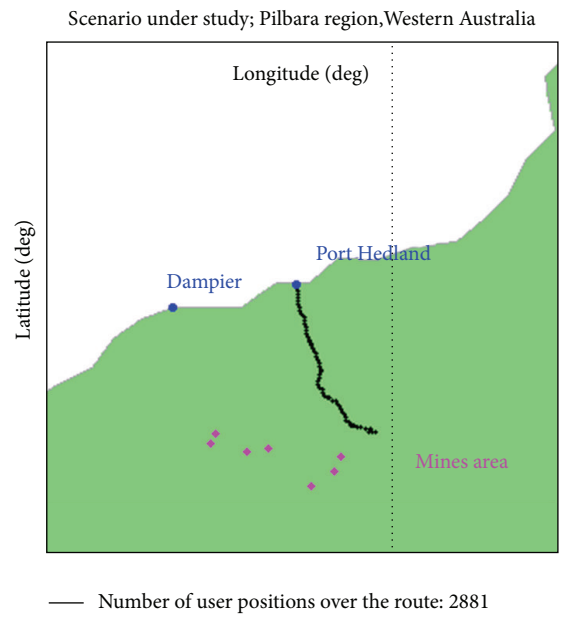

Figure 14: GNSS scenario under study—train path trajectory.

Table 5: 7 elements array: cases considered in the navigation realistic scenario.

Case	Meaning
FRPA cosine-like	The radiation pattern of the user antenna is a fixed beam approximated by a *cosine*^{p} function (p: integer). No interfering satellite is considered in the analysis.
FRPA simulated	The radiation pattern of the user antenna is a fixed beam (Figure 15) designed and simulated by electromagnetic commercial tool (i.e., "CST studio suite"). No interfering satellite is considered in the analysis.
FRPA cosine-like with IF	The radiation pattern of the user antenna is a fixed beam approximated by a *cosine*^{p} function (p: integer). Interfering satellite is considered in the analysis.
FRPA simulated with IF	The radiation pattern of the user antenna is a fixed beam (Figure 15) designed and simulated by electromagnetic commercial tool. Interfering satellite is considered in the analysis.
CRPA	The radiation pattern of the user antenna is synthesised by MVDR algorithm (*beam-forming*) implemented by "MatLab" software tool. In other words, the antenna dynamically synthesizes null/s along direction of interferer/s. Interfering satellite is considered in the analysis.

$\theta_0 = 0^\circ$ (zenith direction, $\Phi_0 = 0^\circ$). (Note that θ angle defined in antenna reference system (par. 3) and θ elevation angle defined in GNSS user reference system (par. 4) are 90° offsets: zenith direction is $\theta = 0^\circ$ at par. 3, it is $\theta = 90^\circ$ at par. 4.) It is noted that antenna diagram shows nulls also in noninterfering directions (e.g., at $\theta_1 = 70^\circ$, $\Phi_1 = 300^\circ$, marked in red). This can limit the visibility of GNSS (useful) satellites. The decrease of the number of tracked satellites can

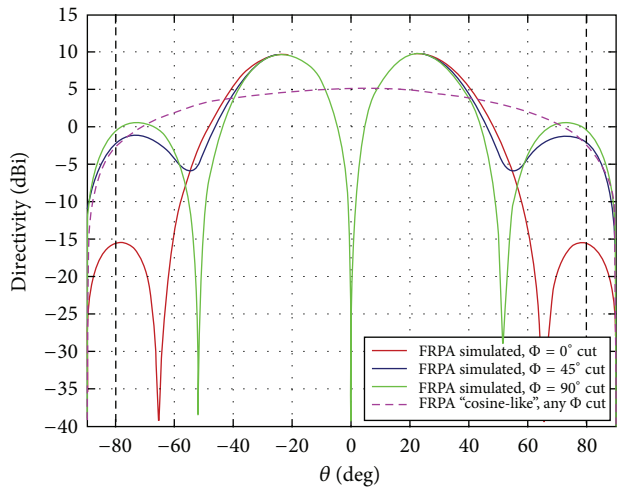

Figure 15: Ground planar array antenna. FRPA simulated and "cosine-like" pattern.

Table 6: UERE figure for GPS L1 receiver.

It.	Error source	Value (rms-m)
1	Satellite clock synchronization	0[1]
2	Satellite perturbations	0[2]
3	Ephemeris prediction error	0[1]
4	Ionosphere delay	4.87[3]
5	Troposphere delay	0.1[4]
6	Multipath	0.2[5]
7	Receiver noise and resolution thermal noise	0.20[6]
8	**UERE**	**4.87**

[1]GNSS receiver augmented by SBAS satellites (e.g., QZSS for Australia) from direct signal in space (SIS).
[2]GNSS receiver augmented by SBAS satellites.
[3]Single frequency GNSS receiver, no corrections applied.
[4]Value obtained by "Ifadis" model [5].
[5]Assuming signal-to-multipath ratio: 27.5 dB, path delay: 26 m, E-L narrow spacing: 0.1 chip, signal bandwidth = 24 MHz.
[6]Assuming noncoherent discriminator DLL with early-late spacing: 0.1; C/No: 40 dB-Hz; code loop noise bandwidth: 0.1 Hz integration time: 20 msec; chip length of code: 293.2551 m.

lead to a reduction of the service accuracy/time availability. This impact shall be evaluated in the next paragraph in the frame of the study of the navigation realistic scenario.

The 13 elements configuration design does not meet the 30 cm constraint. It is considered as a back-up design. However, as a title of example, Figure 12 shows a radiation pattern for a 13 elements array configuration in case of two nulls synthesis.

Phased array electromagnetic analysis has been addressed by electromagnetic commercial tool (i.e., CST Studio Suite) in order to take into account RF mutual coupling effects: in Figure 13, another example of radiation pattern optimization is provided. It represents a null synthesis along broad-side (zenith) direction. The diagram appears balanced, symmetrical with respect to zenith direction. The antenna

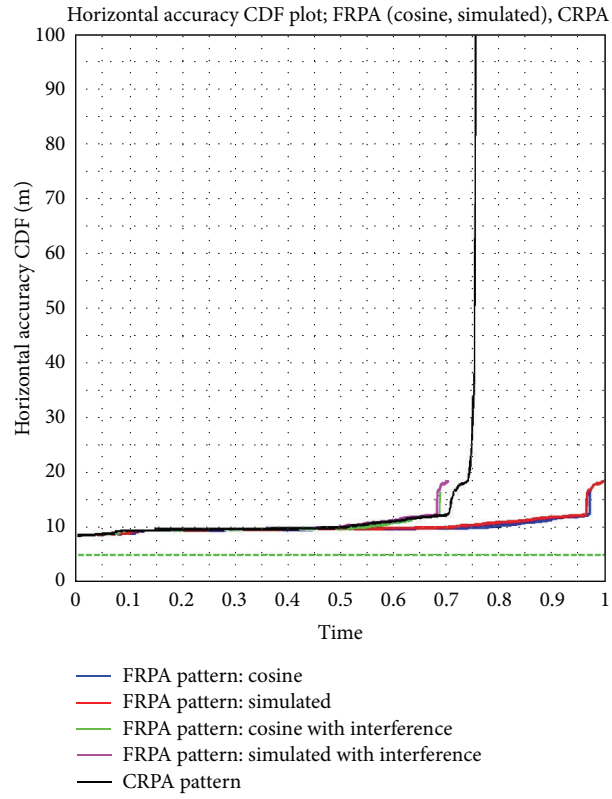

Figure 16: Horizontal accuracy CDF curve −24/24 GPS constellation and 1 RF interfering satellite.

RF design allows the rejection to the interference signal (supposed along zenith direction in this case) and, on the other side, the maximization of the gain in order to receive the maximum number of GNSS useful signals with a signal-to-noise ratio adequate to ensure the tracking of the GNSS receiver [16].

It is important to note that the symmetry of the radiation pattern and the depth of the null (about −30 dB in Figures 11 and 13) demonstrate that degradation effects like RF coupling among elements and *beam-forming* network effects (i.e., excitation coefficients truncation) are well taken into account in the antenna RF design.

In the current paper, focus is given to the innovative radiating part of the antenna. Contribution of the antenna feeding network (i.e., typical values of excitation coefficients stability over frequency/temperature, truncation of excitation coefficients) is taken into account in the design.

The excitation synthesized coefficients are shown in the following Table 4 (see also Figure 10).

Finally, it is worth to note that antenna centre of phase has not been considered due to negligible contribution to accuracy error (order of millimetres).

4. GNSS Study Case

In the current paragraph, the design of the phased array shown in the previous part is applied to a GNSS user receiver

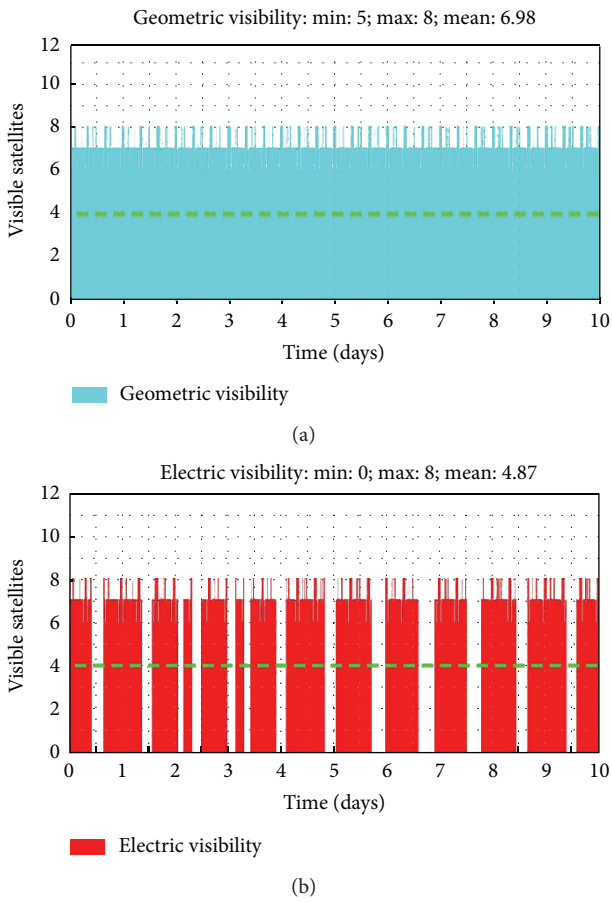

Figure 17: Number of visible satellites −24/24 GPS constellation and 1 RF interfering satellite.

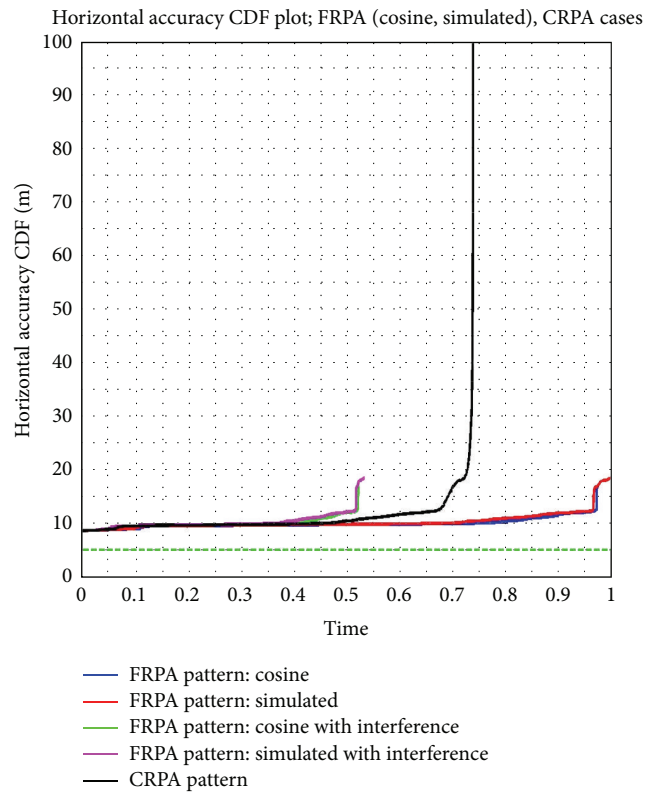

Figure 18: Horizontal accuracy CDF curve −24/24 GPS constellation and 2 RF interfering satellites.

antenna in a navigation realistic environment consisting of

(i) GNSS satellite constellation (e.g., GPS, Galileo, GLONASS, and Compass);

(ii) SBAS satellite constellation (e.g., QZSS for Japan and Australia, EGNOS for Europe, and WAAS for U.S.);

(iii) GNSS user receiver antenna accommodated on the train roof. The train is travelling along a more than 200 km long route from a mines area to "Port Headland" (and back) in Western Australia region, rural rail environment at an average speed of 80 km/h (Figure 14);

(iv) Satellite constellation of interfering satellites (from 1 to 6, randomly selected) transmitting 20 dBW over the GPS EIRP nominal value on L1 bandwidth;

(v) Train running in adverse conditions (totally disconnected scenario, no ground infrastructures).

In particular, the GNSS antenna (7 elements array discussed at par. 3.1, 3.2) is supposed to work in FRPA or CRPA modes. Consequently, five cases are taken into account (Table 5).

Figure 15 shows the FRPA simulated pattern (three Φ cuts) and the FRPA "cosine-like" pattern (pink dotted line).

The assumptions followed in the realistic scenario simulation are the following.

(i) The observation period is 10 days, 5 minutes sampling: the train is running from mines area point to "Port Headland" and back; the total number of points described by the trajectory is 2881;

(ii) the accuracy value is computed with 95% confidence level;

(iii) GPS signal on-ground power level as defined in [16];

(iv) the attenuation by atmospheric gases is computed by *ITU-R P.676-2* model [17];

(v) the rainfall attenuation is modelled as described in [17];

(vi) masked areas as those pertaining to a tunnel and bridges are neglected;

(vii) no GNSS satellite failure (i.e., on-board clocks) is assumed;

(viii) GNSS receiver mask angle >10° with respect to horizon (as shown in Figure 15);

(ix) GPS receiver acquisition threshold: 30 dB-Hz (typical value);

(x) GNSS user receiver antenna given by a 7 elements phased array working in FRPA mode (cosine-like pattern or simulated in Figure 15) or CRPA mode;

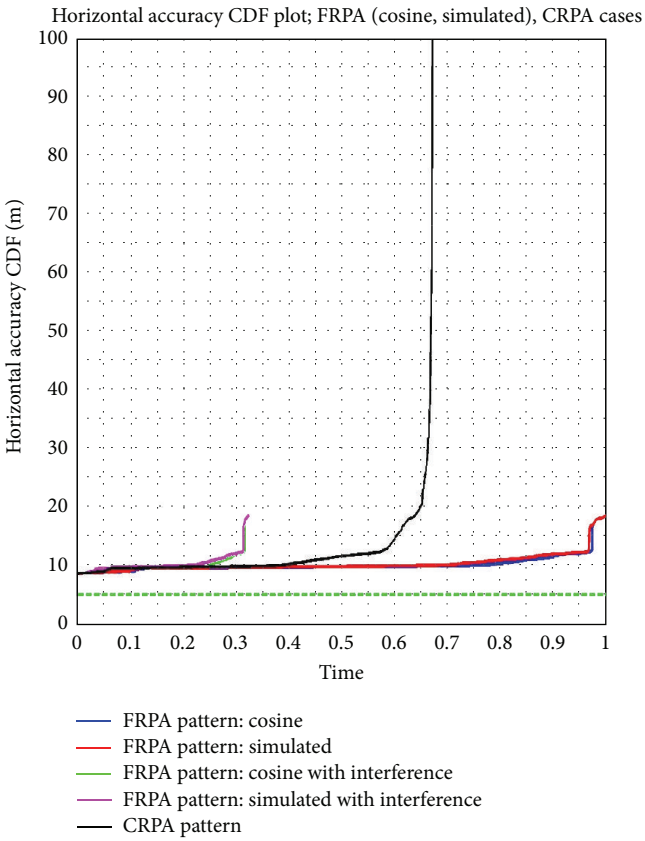

Figure 19: Horizontal accuracy CDF curve −24/24 GPS constellation and 3 RF interfering satellites.

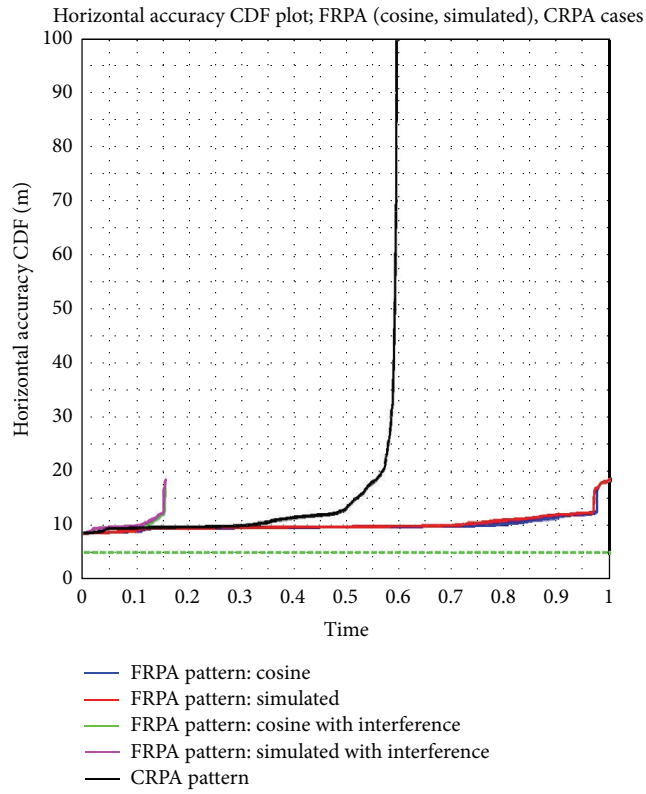

Figure 20: Horizontal accuracy CDF curve −24/24 GPS constellation and 4 RF interfering satellites.

(xi) user equivalent ranging error (UERE) figure is considered common to each GPS satellite. The value is equal to 4.87 meters (at 1σ) computed at $\theta = 15^{\circ}$ (conservative approach). Source error typical standard deviations in L1 band only are reported in Table 6.

The UERE budget driver is the ionosphere residual error.

For each case of the described navigation scenario, user location 2D accuracy versus time and service availability figures are computed, and the results are compared in order to have evidence of the impact of user antenna pattern on the GNSS service performance.

In particular, a constellation of 24/24 GPS satellites disposed over 6 orbital planes (4 satellites per plane) is studied. RF interferers are gradually introduced (from 1 to 6) in the scenario. Figures 16–24 show the horizontal accuracy cumulative distribution function (CDF) for the cases described in Table 5.

In Figure 16, in absence of interference, the horizontal accuracy at a time availability of 95% is about 12 meters both for FRPA cosine and simulated pattern antenna. In interference conditions, the GPS receiver *"sees"* a useful link with the GPS satellite, whose C/N_0 is between 35 and 50 dB-Hz (according to user elevation angle) and noise contribution I_0 due to RF interference.

Consequently, total GPS satellite $C/(N_0 + I_0)$ figure is degraded; the signal-to-noise ratio starts to decrease as soon as the interfering satellite is in visibility of the GPS user receiver. If the GPS satellite signal-to-noise ratio is less than the receiver acquisition threshold, satellite signal cannot be acquired and satellite cannot be tracked by the receiver, so the number of useful (necessary to compute user position) satellites starts to decrease.

This concept is illustrated in Figure 17. It represents the number of GNSS satellites geometrically visible (in light blue), electrically visible (in red) to the train along its route (versus observation time). In absence of interference, satellites that are visible geometrically are also electrically (even with a 0 dBi gain antenna) visible. In case of interference, as mentioned before, the useful signal power shall be below the noise (thermal and interference nature) more than 30 dB-Hz leading to the loss of satellite track. In addition, the DOC_4 figure (Depth of Coverage 4: time percentage to have at least four satellites in visibility to the GPS receiver) shall pass from 100% to 70.53% as shown in Figure 16. (Note that 4 is the minimum number of GNSS satellite to compute the user 3D location.) The threshold of 4 satellites (minimum number to compute GNSS user position) is highlighted in Figure 17 by dotted green line.

Consequently, the user accuracy is computed by a reduced number of satellites. It is degraded (about 18 meters) with a reduced availability (about 70%) both for cosine and simulated FRPA antennas. Adopting the CRPA solution,

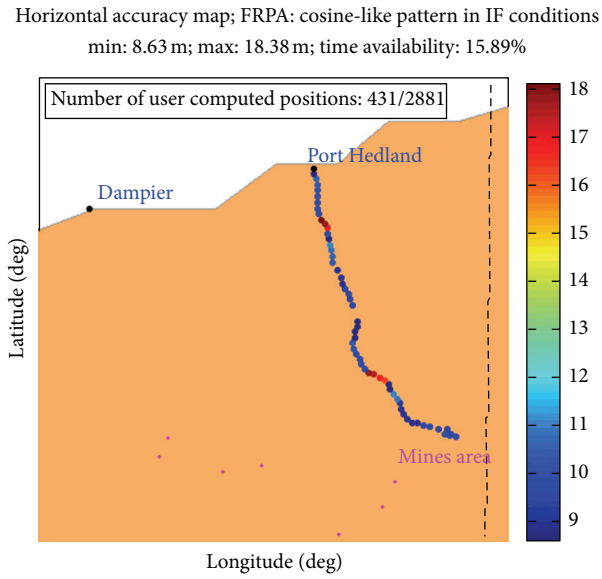

Figure 21: Horizontal accuracy mapping −24/24 GPS constellation and 4 RF interfering satellites.

a null is synthesized along interfering direction and the antenna main beam points the broad-side direction. It mitigates the effects of the interference; however, the synthesized radiation pattern can show undesired nulls that can limit the GPS satellite visibility (Figure 11). Consequently, the service can be provided with a maximum 2D accuracy of 30 meters with a time availability of about 75%.

In Figure 18 two interfering satellites are considered. The 2D accuracy figure is reduced to 18 m with 52% time availability both for FRPA cosine and FRPA simulated. CRPA antenna solution mitigates the interference effect (30 meters accuracy with about 74% time availability). This value is very similar to the one obtained for one single interfering satellite case. It is noted that CRPA provides robustness to interference without affecting the GPS satellite visibility.

For the 3 interfering satellites option (Figure 19), the horizontal accuracy of the train is degraded to 18 meters at 52% of the time for FRPA patterns. Adopting CRPA solution it is 30 meters at 68% of the time (10 days).

On each curve, a reference value of 5 meters has been considered (green dotted line). An horizontal accuracy of 5 meters represents a typical value for train applications (this is why user antenna phase centre error contribution is not taken into account). This value can be even lower when additional capabilities, like parallel track discrimination is required [18].

The multiconstellation capabilities relying on GPS, GLONASS, and in perspective Galileo and Compass offer a higher degree of flexibility to reach better performance.

For the 4 interfering satellites option (Figures 20 and 21), the horizontal accuracy is degraded to 18 meters at about 15% of the observation time for FRPA patterns. Adopting CRPA solution it is 30 meters at 55% of the time.

More specifically, it means that, in conditions of interference, the train position can be computed by the GPS receiver in 15% of the total time (in other words, for the 15% of the

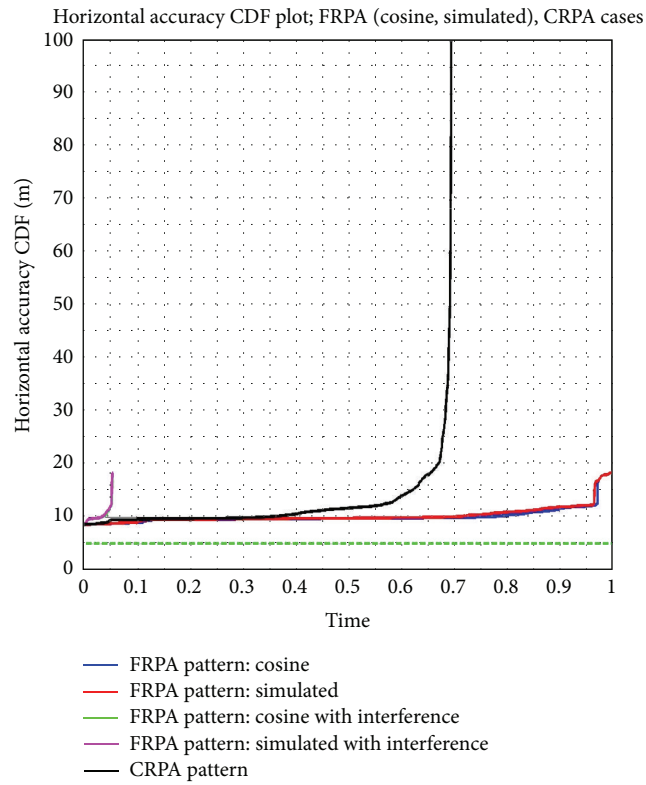

Figure 22: Horizontal accuracy CDF curve −24/24 GPS constellation and 5 RF interfering satellites.

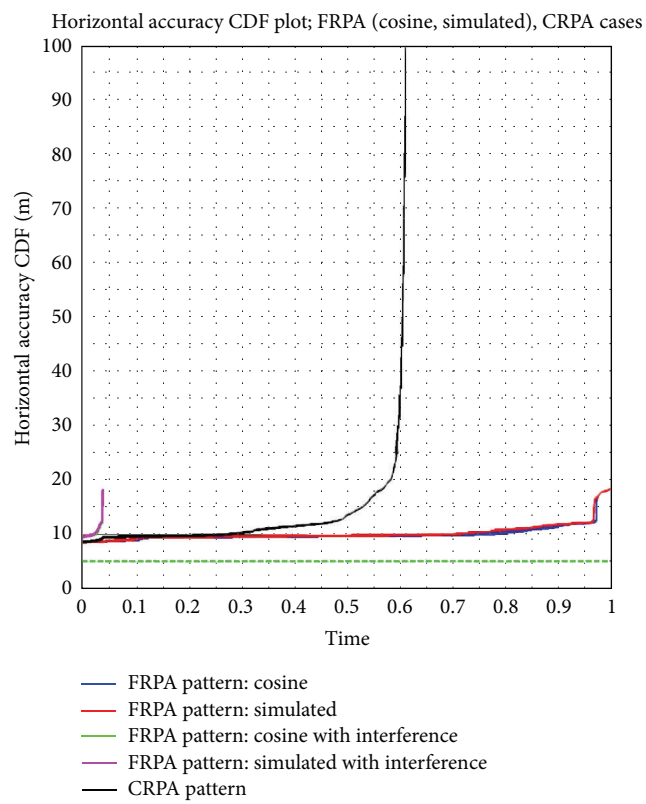

Figure 23: Horizontal accuracy CDF curve −24/24 GPS constellation and 6 RF interfering satellites.

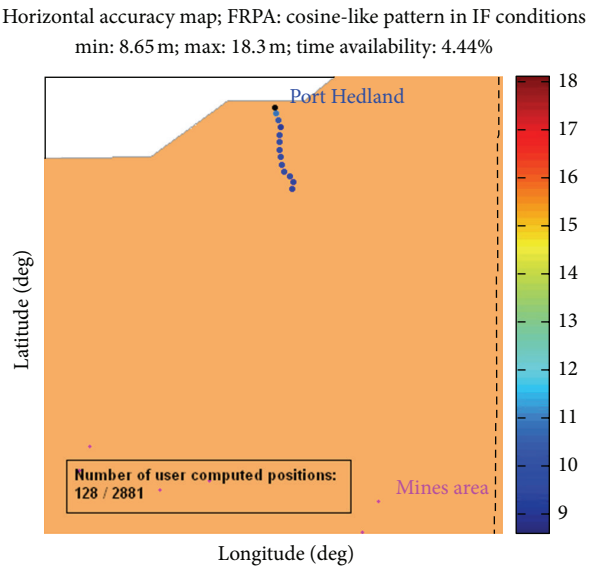

Figure 24: Horizontal accuracy mapping ("zoomed" view) −24/24 GPS constellation and 6 RF interfering satellites.

points of the train route shown at Figure 14) with a minimum 2D accuracy of 8.63 m and a maximum 2D accuracy of 18.38 m (Figure 21).

For the 5 interfering satellites option (Figure 22), the horizontal accuracy is degraded to 18 meters at 5% of the time for FRPA patterns. Adopting CRPA solution it is 30 meters at 68% of the time (10 days).

For the 6 interfering satellites option (Figures 23 and 24), the horizontal accuracy is degraded to 18 meters at 5% of the time for FRPA patterns. It is noted that CRPA antenna solution strongly mitigates the interference effects. In other words, the train position can be located along the route with a 2D maximum accuracy of 30 meters at 60% of the time (10 days).

By adopting an FRPA antenna, the 2D position of the train is known with an accuracy of 18.3 meters (Figure 23) at about the 5% of the train route (Figure 14). Comparing Figures 24 and 13, it is noted that the points (user positions computed by the receiver—128) do not encompass the whole rail path (2881 points). It is due to the lack of GPS visible satellites (caused by RF interference) to the receiver. If the number of GPS satellites visible is less than 4, the receiver cannot compute the user position; consequently, the marker is, respectively, blank in Figures 21 and 24.

5. Conclusions

In this paper an innovative radiating system for train localization in interference conditions is presented. This system consists of a *beam-forming* adaptive antenna, a phased array of miniaturized (metamaterial technology) patch radiators. The design of the *beam-forming* antenna is presented (working in FRPA or CRPA mode).

Phased array antenna is embedded into a navigation realistic scenario in interference conditions, and the problem of localization-by-GNSS-satellite of a train travelling along a route in Australia is approached.

Service performance figures (i.e., accuracy, time availability) are evaluated, and emphasis is given to the capability of the GNSS-designed array to mitigate RF interference effects (reduction of service availability, increase of location accuracy).

References

[1] M. Jones, "Protecting GNSS receivers from interference and jamming," *Inside GNSS*, pp. 40–49, March-April 2011.

[2] E. D. Kaplan and C. J. Hegarty, *Understanding GPS: Principles and Applications*, Artech House, 2006.

[3] A. Joseph, "Measuring GNSS signal strength," *Inside GNSS*, pp. 20–25, November-December 2010.

[4] H. L. Van Trees, *Optimum Array Processing, Part IV of Detection, Estimation, and Modulation Theory*, John Wiley & Sons, 2002.

[5] S. Katsougiannopoulos, C. Pikridas, D. Rossikopoulos et al., "Tropospheric refraction estimation using various models, radiosonde measurements and permanent GPS data," in *Shaping the Change, XXIII FIG Congress*, Munich, Germany, October 2006.

[6] R. T. Campton Jr., *Adaptive Antennas: Concepts and Performance*, Prentice-Hall, 1988.

[7] F. Capolino, Ed., *Metamaterials Handbook*, CRC Press, 2009.

[8] C. Vegni and F. Bilotti, "Parametric analysis of slot-loaded trapezoidal patch antennas," *IEEE Transactions on Antennas and Propagation*, vol. 50, no. 9, pp. 1291–1298, 2002.

[9] S. Contu, C. Vegni, F. Bilotti, and L. Vegni, "Slotted patch antennas for space applications," in *Proceedings of the USNC/URSI National Radio Science Meeting*, p. 695, Columbus, Ohio, USA, June 2003.

[10] F. Bilotti and C. Vegni, "Design of metamaterial based patch antennas with reduced back-radiation for radio navigation systems," in *Proceedings of the 1st International Congress on Advanced Electromagnetic Materials in Microwaves and Optics (Metamaterials '07)*, pp. 493–494, 2007, Rome, Italy, October 2007.

[11] F. Bilotti and C. Vegni, "Employment of artificial magnetic metamaterials to effectively reduce the back-lobe of patch antennas," *Electromagnetics*, vol. 28, no. 7, pp. 513–522, 2008.

[12] F. Bilotti and C. Vegni, "Design of high-performing microstrip receiving GPS antennas with multiple feeds," *IEEE Antennas and Wireless Propagation Letters*, vol. 9, pp. 248–251, 2010.

[13] G. Bertin, B. Piovano, R. Vallauri, F. Bilotti, and L. Vegni, "Metamaterial-inspired antennas for telecommunication applications," in *Proceedings of the 6th European Conference on Antennas and Propagation (EuCAP '12)*, pp. 2739–2740, Prague, Czech Republik, March 2012.

[14] G. Bertin, F. Bilotti, B. Piovano, R. Vallauri, and L. Vegni, "Switched beam antenna employing metamaterial-inspired radiators," *IEEE Transactions on Antennas and Propagation*, vol. 60, no. 8, pp. 3583–3593, 2012.

[15] C. Vegni and F. Bilotti, "Spaceborne orbito payload study and L2c antenna design for precise geosynchronous orbit/time determination," in *Proceedings of the European Navigation Conference—Global Navigation Satellite Systems (ENC-GNSS '09)*, Napoli, Italy, May 2009.

[16] Global Positioning System Wing (GPS)-Systems Engineering & Integration Interface Specification IS-GPS-200, Revision E. IS-GPS-200E, June 2010.

[17] G. Maral and M. Bousquet, *Satellite Communication Systems*, Wiley, 5th edition, 2009.

[18] A. Neri, A. Filip, F. Rispoli, and A. M. Vegni, "An analytical evaluation for hazardous failure rate in a satellite-based train positioning system with reference to the ERTMS train control systems," in *Proceedings of the 25th International Technical Meeting of the Satellite Division of the Institute of Navigation (ION GNSS '12)*, p. 2770, Nashville, Tenn, USA, September 2012.

Hindawi Publishing Corporation
International Journal of Antennas and Propagation
Volume 2013, Article ID 694819, 8 pages
http://dx.doi.org/10.1155/2013/694819

Application Article

Analysis and Design of a Novel Compact Multiband Printed Monopole Antenna

Junjun Wang and Xudong He

EMC Lab, School of Electronic and Information Engineering, Beihang University, Beijing 100191, China

Correspondence should be addressed to Junjun Wang; wangjunjun@buaa.edu.cn

Received 7 December 2012; Revised 2 May 2013; Accepted 29 May 2013

Academic Editor: Renato Cicchetti

A compact multiband printed monopole antenna is presented. The proposed antenna, composed of a modified broadband T-shaped monopole antenna integrating some band-notch structures in the metallic patch, is excited by means of a microstrip line. To calculate the bandwidth starting frequency (BSF) of the T-shaped broadband antenna, an improved formula is proposed and discussed. The multiband operation is achieved by etching three inverted U-shaped slots on the radiant patch. By changing the length of the notch slots, operation bands of the multiband antenna can be adjusted conveniently. The antenna is simulated in Ansoft HFSS and then fabricated and measured. The measurement results show that the proposed antenna operates at 2.25–2.7 GHz, 3.25–3.6 Hz, 4.95–6.2 GHz, and 7-8 GHz, covering the operation bands of Bluetooth, WiMAX, WLAN, and downlink of X-band satellite communication system and thus making it a proper candidate for the multiband devices.

1. Introduction

With the rapid development of the communication technology, there is a great demand for antennas suitable to operate with dual- or multibands characteristics in wireless communication devices, such as mobile phones and laptops. Printed antennas have been paid great attention in recent years because of their compact size, low profile, light weight, and low cost. A great quantities of printed antennas for dual- or multibands operations have been reported in the literature [1–12]. In [1–7], the authors have presented several kinds of printed monopole or dipole antennas for dual-band operation. In [8–12], slot antennas have been utilized. Antennas mentioned above achieve dual- or multibands operation; however, they usually have complicated structures or narrow bandwidth, and their operation bands cannot be adjusted easily either.

Recently, a lot of wideband antennas have been proposed because of the wide operation band and high date rate [13–15]. To avoid the interference between UWB (ultrawideband) antennas and narrow bandwidth communication systems, antenna designers have proposed several UWB antennas with band-notch characteristics [16–19]. The above-mentioned design solutions provide us a different way to achieve the multiband operation.

In this paper, we present a novel compact multiband monopole antenna based on the broadband antenna theory and employing band-notch technique. A T-shaped monopole antenna is designed to achieve a broad impedance bandwidth. Using the techniques suitable to widening of the operative frequency band, three inverted U-shaped slots are etched on the metallic patch to reject the undesired bands; in this way the multiband operation is achieved. The operation bands of the proposed antenna can be adjusted conveniently by changing the length of each band-notch slot.

The organization of the paper is as follows. In Section 2, the configuration of the proposed antenna is introduced. An improved formula for computing the bandwidth starting frequency (BSF) with higher accuracy is proposed and discussed. Then the broadband characteristic of the T-shaped monopole antenna is analyzed. Finally, the frequency behaviour of the band-notch structures consisting of three inverted U-shaped slots etched on the metallic patch is investigated. Results of the proposed antenna (return loss, normalized radiation pattern, and peak gain) are presented and discussed in Section 3, while some conclusions are drawn in Section 4.

Table 1: Optimized geometrical parameters of the proposed multiband antenna.

Parameters	W	w_1	w_2	w_f	L	l_1	l_2	l_g	l_{n1}	l_{n2}	l_{n3}	w_{n1}	w_{n2}	w_{n3}	d_1	d_2	d_3	g
Values (mm)	30	11.5	21.5	1.5	40	10	19	5	32	23	16	18	12	6	26.5	20.5	14.5	2

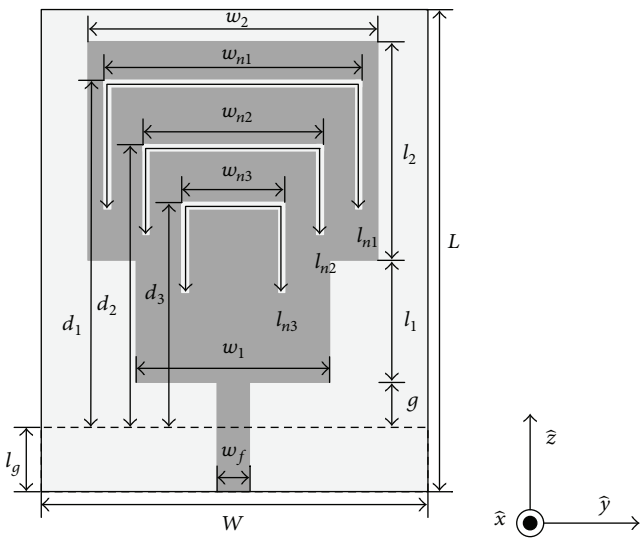

Figure 1: Geometry of the proposed multiband antenna.

2. Antenna Analysis and Design

Figure 1 shows the geometry of the proposed multiband antenna. The proposed antenna is printed on a low-cost FR4 substrate with relative permittivity of 4.4, dielectric loss tangent of 0.02, and thickness of 1 mm. A T-shaped patch is printed on one side of the substrate and a truncated ground plane on the other. The T-shaped patch is realized by removing two symmetric metal notches at the bottom of a rectangular patch in order to improve significantly the impedance matching of the monopole antenna at high frequency. Three inverted U-shaped slots with different sizes are etched on the T-shaped patch to reject the undesired frequency bands of the proposed multiband antenna. The commercial software Ansoft HFSS has been adopted for the analysis and design of the proposed antenna. The optimized geometrical parameters describing the antenna are reported in Table 1.

An improved formula useful to calculate the BSF in terms of the antenna parameters is proposed and discussed firstly. Then the effects of the antenna parameters are investigated. Finally, the inverted U-shaped band-notch structures are studied.

2.1. Improved Formula for BSF of the Broadband Antenna. For a broadband antenna, the BSF and bandwidth are two important factors to evaluate its frequency performance. An accurate formula to calculate BSF of a broadband antenna is quite necessary for antenna designers to save simulation time and accelerate the design process. In this paper, an improved formula is presented to provide a much more accurate prediction of BSF of the T-shaped monopole.

Kumar and Ray have proposed a formula to calculate the BSF of the planar monopole [19]. Thomas and Sreenivasan improved the formula by considering the effect of the substrate [20]. Equation (1) is the formula proposed by Thomas and Sreenivasan:

$$\mathrm{BSF} = \frac{72}{l + r + g}\ \mathrm{GHz}, \tag{1}$$

where l denotes the length of the monopole (both the planar monopole and the equivalent cylinder monopole), g denotes the gap between the ground plane and the monopole, and r denotes the radius of the equivalent cylinder monopole. The equivalent radius r is expressed as

$$r = \frac{A}{2\pi l\sqrt{\varepsilon_e}}, \tag{2}$$

where A denotes the area of the radiant patch and the area of the side face of the equivalent cylinder monopole, ε_e is the effective dielectric constant of the air-substrate composite dielectric and can be calculated by $\varepsilon_e = (1 + \varepsilon_r)/2$, and ε_r denotes the relative constant of substrate. The parameters l, r, and g appearing in (1) and (2) are expressed in millimeters.

However, (1) is not accurate enough to calculate the BSF of the T-shaped monopole antenna because the parameter g does not take into account the effect of the two bevel cuts on the feeding gap. Therefore, we propose to replace it by an effective parameter g_e defined as follows:

$$g_e = g + l - \frac{A}{w_2}. \tag{3}$$

Here w_2 denotes the width of the higher edge of the radiant patch, and g, l, and A have the same meanings as in (1), while in this paper, $l = l_1 + l_2$ and $A = w_1 l_1 + w_2 l_2$. Then (3) can be rewritten as

$$g_e = g + l_1 - \frac{w_1 l_1}{w_2}. \tag{4}$$

The modified formula to calculate BSF of the T-shaped monopole is

$$\mathrm{BSF} = 72\left(2l_1 + l_2 - (w_1 l_1/w_2) + g + \left((w_1 l_1 + w_2 l_2)/\pi\left(l_1 + l_2\right)\sqrt{2\varepsilon_r + 2}\right)\right)^{-1}(\mathrm{GHz}). \tag{5}$$

After performing some numerical simulations it is found that the values of the BSF calculated by (5) are smaller than

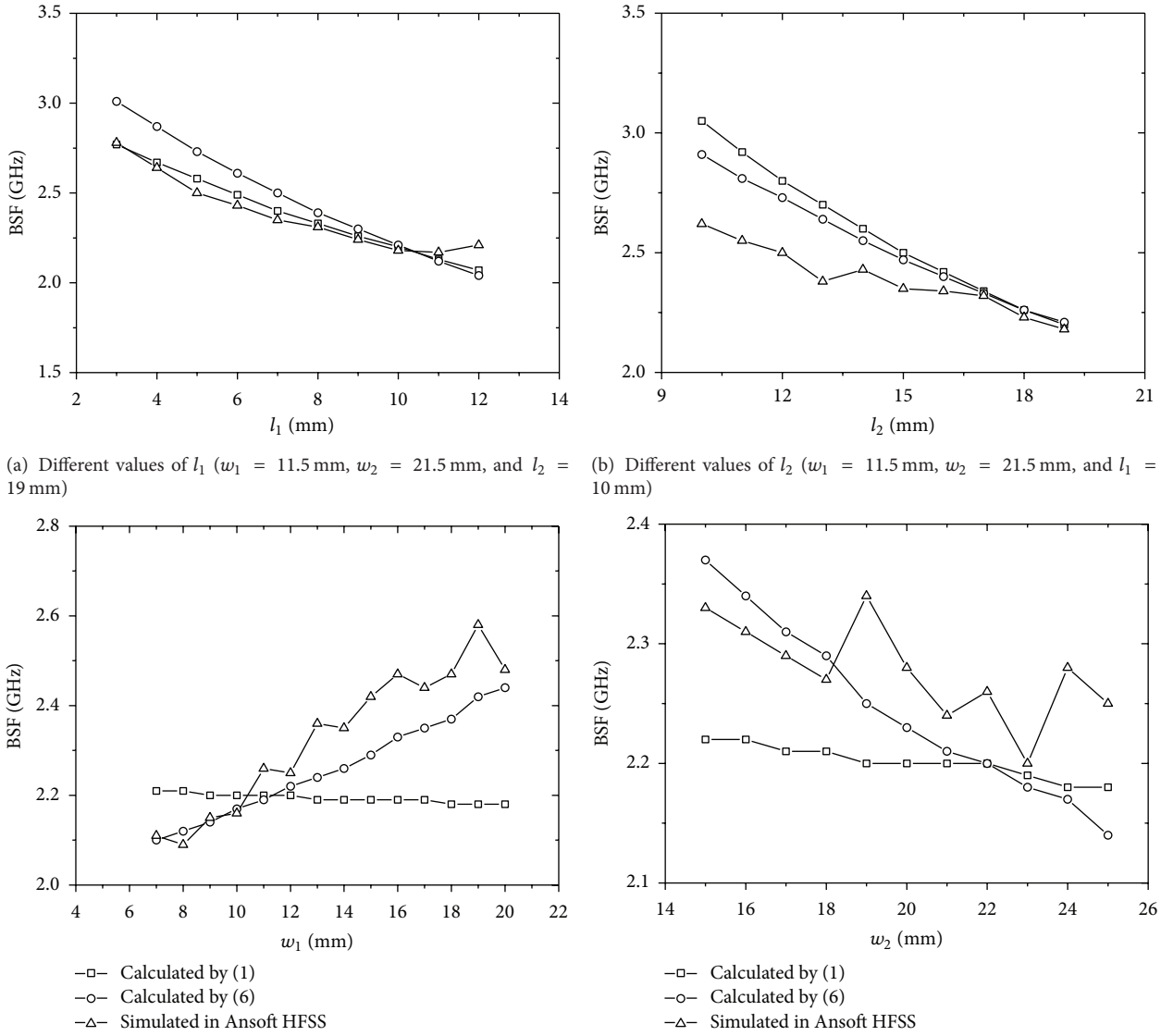

(a) Different values of l_1 (w_1 = 11.5 mm, w_2 = 21.5 mm, and l_2 = 19 mm)

(b) Different values of l_2 (w_1 = 11.5 mm, w_2 = 21.5 mm, and l_1 = 10 mm)

(c) Different values of w_1 (w_2 = 21.5 mm, l_1 = 10 mm, and l_2 = 19 mm)

(d) Different values of w_2 (w_1 = 11.5 mm, l_1 = 10 mm, and l_2 = 19 mm)

Figure 2: Calculated and simulated BSF for different values of the geometrical parameters.

the simulated ones. So a calibration factor F_c with its value of 1.145 is introduced. Then (5) can be modified as

$$\mathrm{BSF} = 72F_c\left(2l_1 + l_2 - (w_1 l_1/w_2) + g + \left((w_1 l_1 + w_2 l_2)/\pi\,(l_1+l_2)\sqrt{2\varepsilon_r+2}\right)\right)^{-1}\ (\mathrm{GHz}). \quad (6)$$

Figure 2 shows the calculated and simulated BSF of the T-shaped monopole with different l_1, l_2, w_1, w_2, respectively, while the other parameters of the broadband antenna stay unchanged. From Figures 2(a) and 2(b) it can be observed that, for l_1, l_2, the values of BSF calculated by (1) and (6) almost have the same accuracy. For w_1, w_2, however, the values of BSF calculated by (6) are obviously much more accurate than those calculated by (1) compared to the simulated ones as shown in Figures 2(c) and 2(d), validating the accuracy of (6). The relative error of the proposed BSF formula comparing with the simulation is calculated; the maximum and mean values are 11.07% and 4.06%, respectively.

2.2. Broadband Antenna Design. In this section, the parameters of the broadband antenna are analyzed and discussed in detail. Figure 3 shows the frequency behavior of the scattering parameter S_{11} for the different dimensions of the T-shaped structure. From Figures 3(a) and 3(b), it can be observed that the two cuts at the lower edge of the radiant patch have a significant effect on the impedance matching at higher frequency. Correspondently, the impedance match at higher frequency is improved. It is also seen in Figures 3(a) and 3(b)

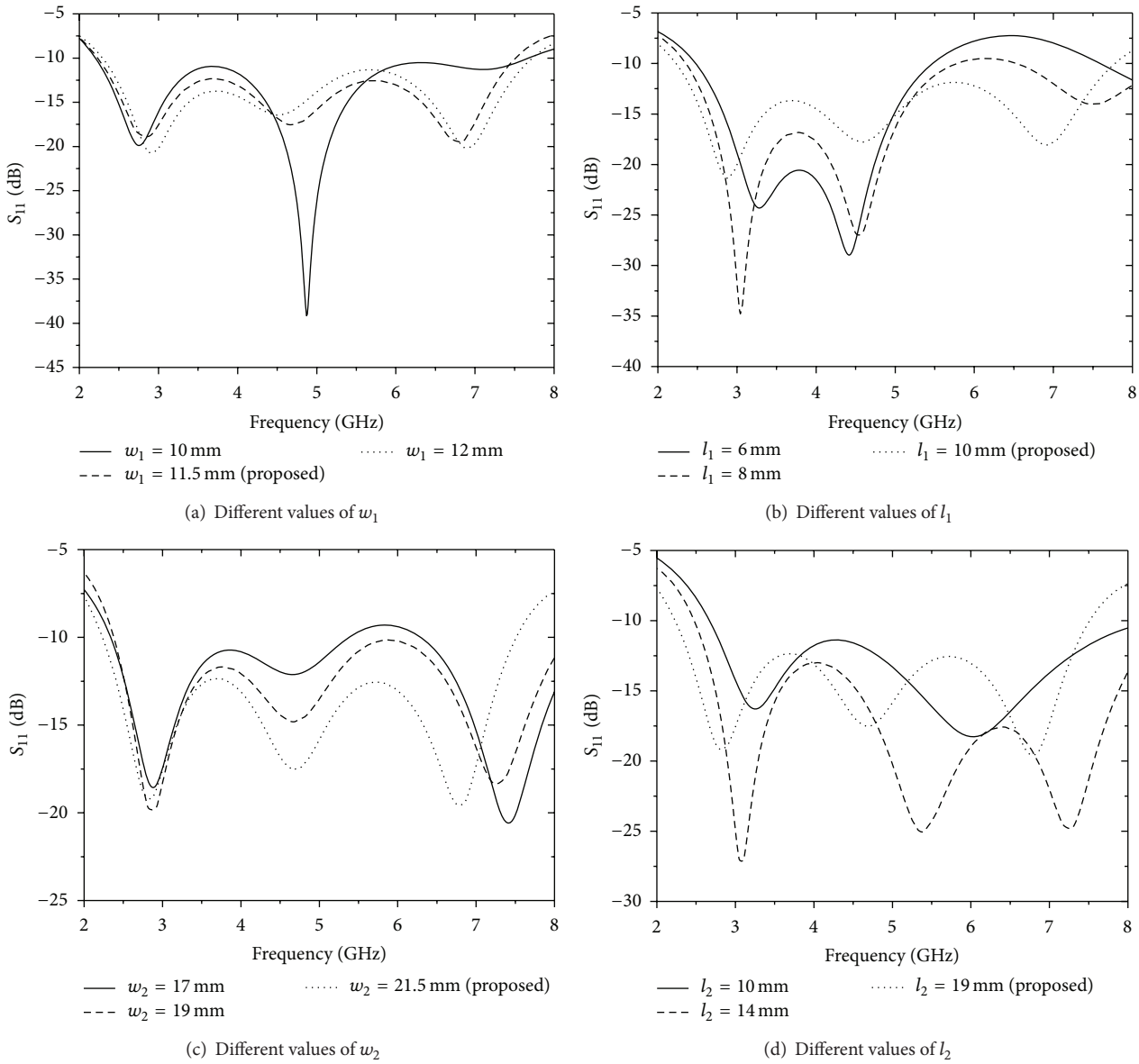

(a) Different values of w_1

(b) Different values of l_1

(c) Different values of w_2

(d) Different values of l_2

Figure 3: Frequency behavior of the scattering parameter S_{11} of the T-shaped antenna for different values of the geometrical parameters.

that the BSF of the broadband antenna decreases when w_1 decreases or l_1 increases. The reason is that the effective gap between the ground plane and the radiant patch increases while the width or length of the cuts increases. Because of the same reason, the BSF decreases when w_2 increases as shown in Figure 3(c) and when l_2 increases as shown in Figure 3(d), and we can see that with the increase of l_2, the BSF of the monopole antenna decreases and the impedance matching at higher frequency degrades. Because longer l_2 provides a longer current path at lower frequency, thus a lower BSF.

2.3. Multiband Antenna Design. Based on the broadband antenna design, three inverted U-shaped slots are etched on the T-shaped radiant patch to reject the undesired frequency bands, thus achieving the multiband operation. The resonant frequency of each inverted U-shaped slot can be approximately calculated by (7) reported in [21]:

$$f_{ni} = \frac{150}{l_{ni}\sqrt{\varepsilon_e}}\ \text{GHz}, \tag{7}$$

where f_{ni} denotes the resonant frequency of the ith band-notch structure and l_{ni} denotes the length, expressed in millimeters, of the ith band-notch structure with $i = 1, 2, 3$. Equation (7) predicts a decrement of the resonant frequency f_{ni} as the parameter l_{ni} is increased.

Figure 4 shows the frequency behavior of the scattering parameter S_{11} for different values of the geometrical parameters l_{n1}, l_{n2}, and l_{n3}. It can be seen that with the increase of the length of the band-notch structures, the resonant frequency decreases and the bandwidth also changes, verifying the behavior predicted by (7). It is also found that the

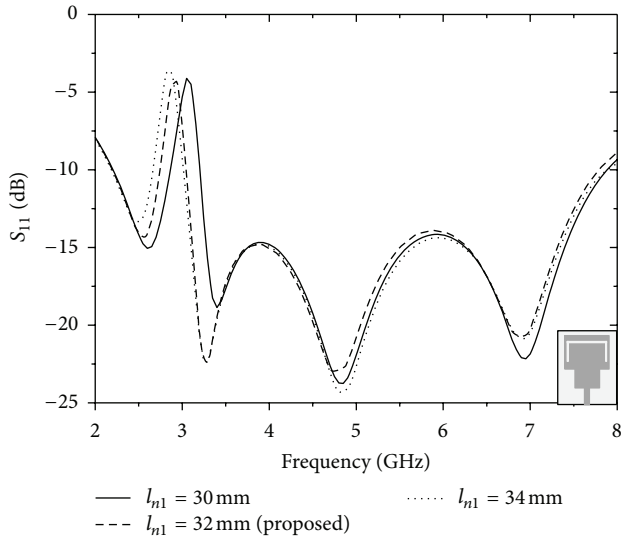

(a) With U-slot1

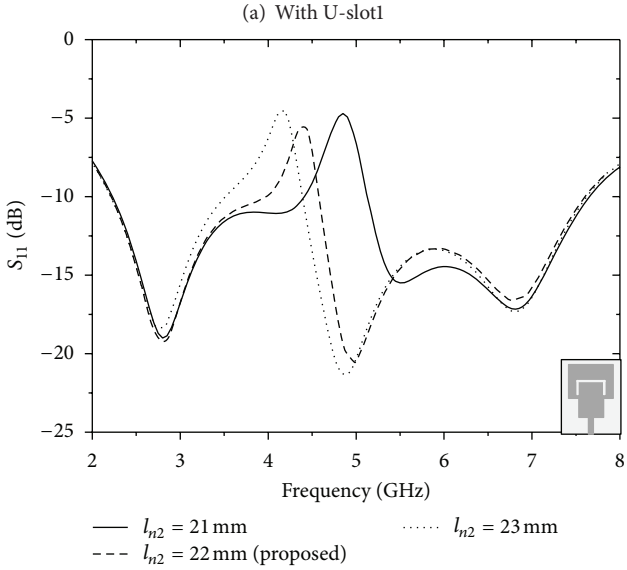

(b) With U-slot2

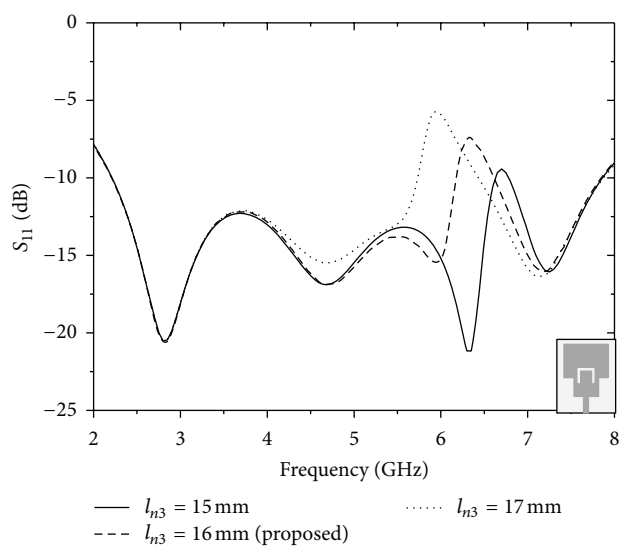

(c) With U-slot3

Figure 4: Frequency behavior of the scattering parameter S_{11} for different values of the geometrical parameters.

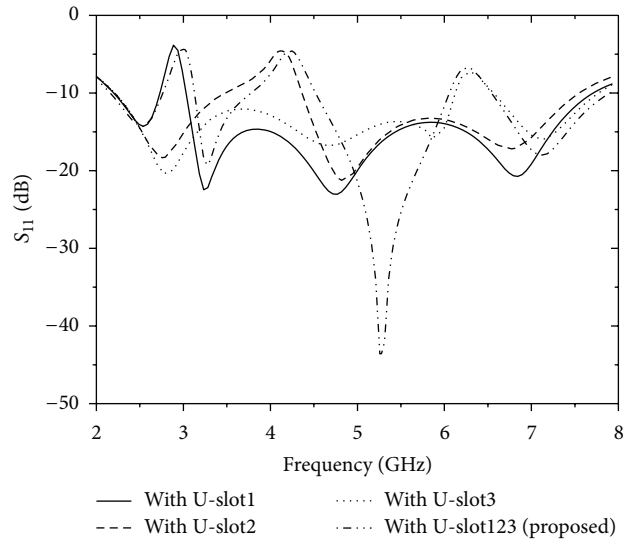

Figure 5: Frequency behavior of the scattering parameter S_{11} for the multiband antenna with one, two, and three U-slots.

width w_{ni} and the position d_{ni} of the inverted U-slots also have effects on the frequency performance of the band-notch structures, with $i = 1, 2, 3$.

Figure 5 shows the frequency behavior of the scattering parameter S_{11} of the broadband antenna with only one inverted U-shaped slot and with all the three slots (the proposed multiband antenna). It can be seen that each band-notch structure can work independently and has little effect on the frequency performance of the other band-notch structures.

The maps of the surface current distributions, excited on the monopole antenna at each one of the operative frequency bands, are shown in Figure 6.

3. Results and Discussion

The proposed antenna has been fabricated and then measured using Agilent Vector Network Analyzer E5071C. Figure 7 shows the simulated and measured S_{11} of the proposed multiband antenna. It can be seen that reasonable agreement has been achieved between the simulated and measured results. Because of the fabrication tolerances and of the perturbation effect caused by the SMA connector, there are some discrepancies between the two results. The fluctuation of relative permittivity and loss tangent of the FR4 substrate at high frequency also contributes to the disagreement.

The radiated electric field has a linear polarization for the proposed antenna. Figure 8 shows the computed radiation patterns of the proposed antenna at the working frequency of 2.4, 3.5, 5.5, and 7.5 GHz. It can be seen that the proposed antenna, similar to the typical monopole antennas, has nearly omnidirectional radiation pattern on H-plane except at 7.5 GHz. The degradation at 7.5 GHz can be explained as the following: with the increasing frequency the electrical length of the antenna is more than the half wavelength; then the surface current distributed on the radiant patch will be destructive, thus degradation of the radiation pattern at this frequency is observed.

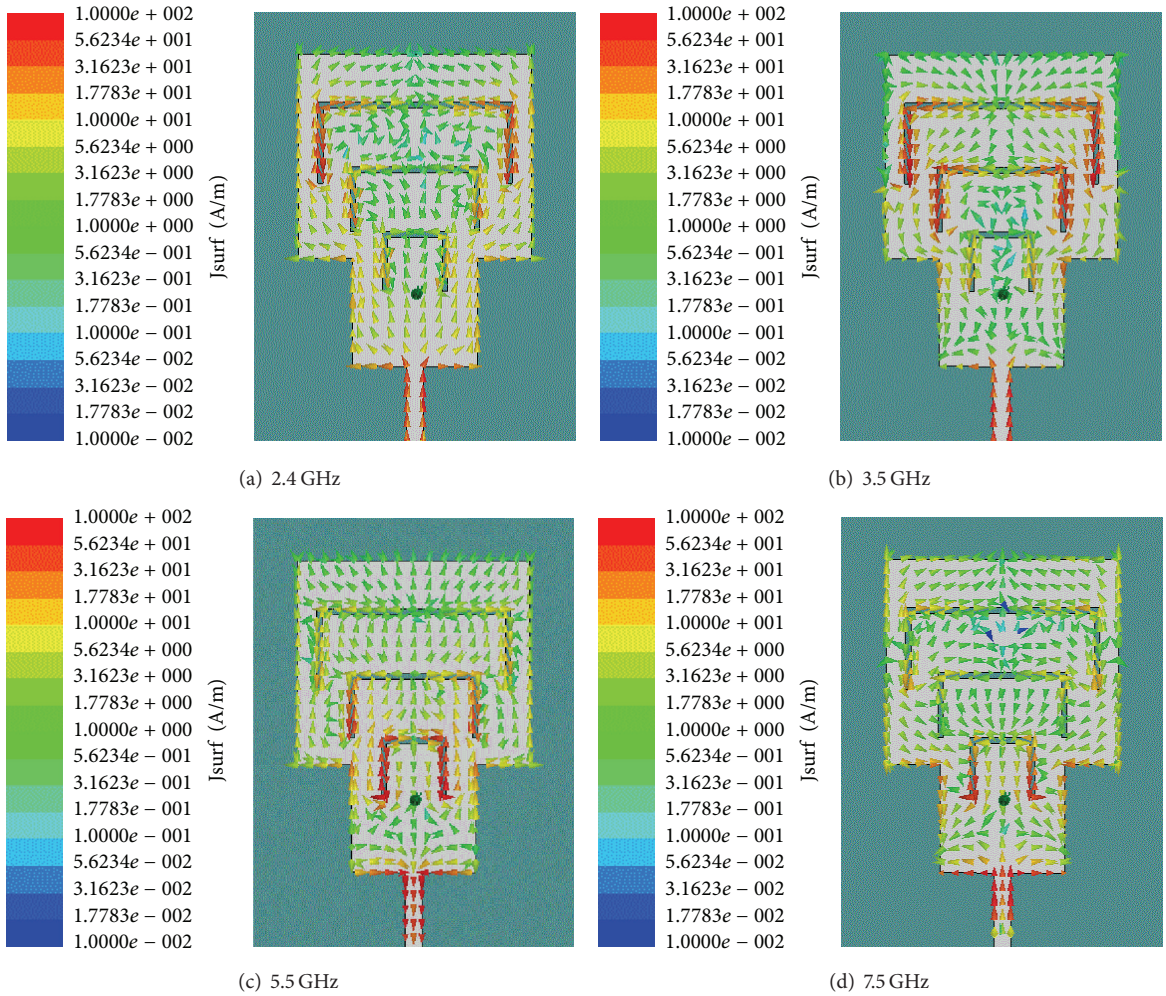

(a) 2.4 GHz (b) 3.5 GHz

(c) 5.5 GHz (d) 7.5 GHz

Figure 6: Maps of the surface current distributions at the frequency of (a) 2.4 GHz, (b) 3.5 GHz, (c) 5.5 GHz, and (d) 7.5 GHz.

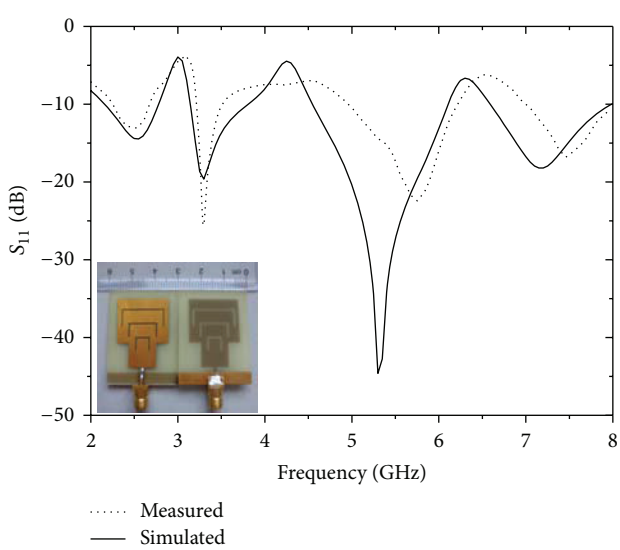

Figure 7: Frequency behavior of the simulated and measured S_{11} parameter of the proposed multiband antenna.

Figure 9 shows the simulated peak gain of the multiband antenna at the proposed frequency band. From the figure it appears that the peak gain increases as the frequency increases. The deviation between the maximum and minimum peak gain in each operation band is less than 1.5 dBi.

4. Conclusion

A multiband antenna based on a broadband antenna and the band-notch structures has been presented. A compact T-shaped monopole antenna with three inverted U-shaped slots has been adopted to achieve a multiband frequency behavior. After simulation and optimization in Ansoft HFSS, the proposed antenna is fabricated and measured. The measured results have shown that the frequency range of the proposed antenna can cover the operation bands of Bluetooth (2.4–2.484 GHz), WiMax (3.3–3.69 GHz), WLAN (5.15–5.875 GHz), and downlink of X-band satellite communication system (7.25–7.75 GHz). An improved formula useful to calculate the BSF of a general the T-shaped monopole

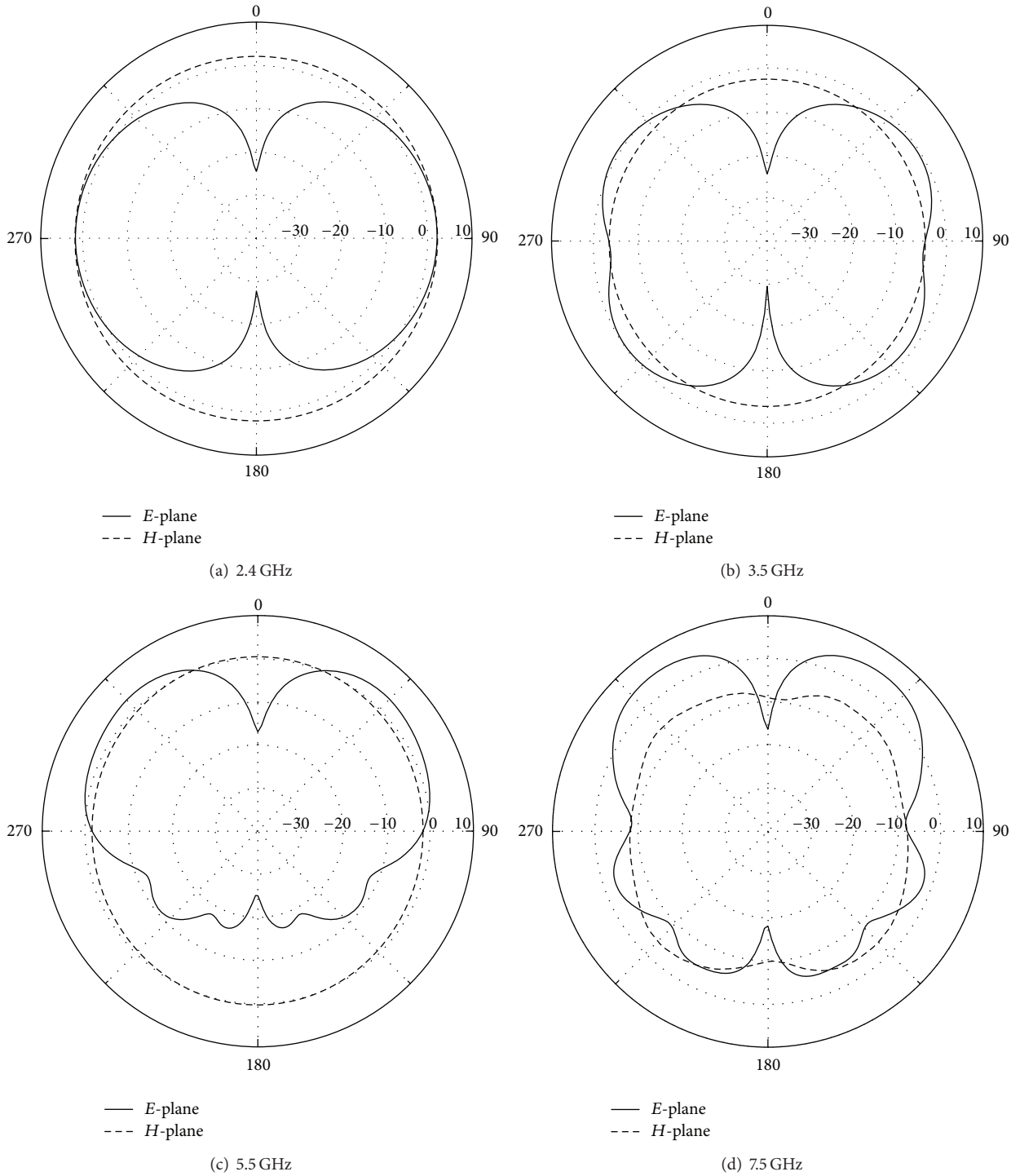

Figure 8: Simulated gain patterns in the E-plane (phi = 90 degree) and H-plane for the proposed antenna at the frequency of (a) 2.4 GHz, (b) 3.5 GHz, (c) 5.5 GHz, and (d) 7.5 GHz.

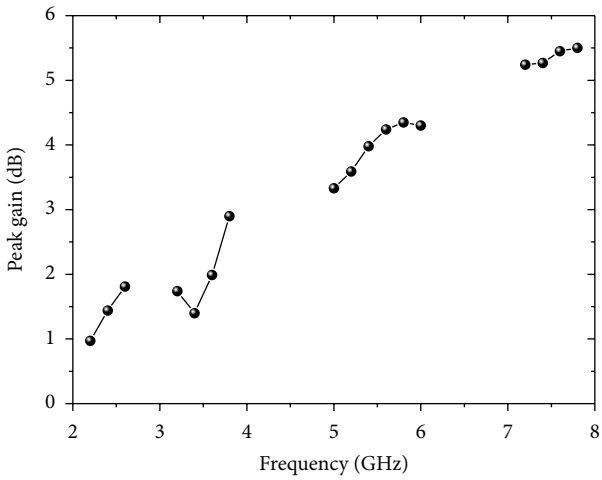

Figure 9: Peak gain for the proposed antenna.

antenna has been proposed and discussed. Comparison between the simulated and calculated BSF with different parameters of the T-shaped monopole has shown the good accuracy of the modified formula presented in this work.

Conflict of Interests

The authors declare that they have no conflict of interests with software Ansoft HFSS, in this paper.

References

[1] A. Mehdipour, A. R. Sebak, C. W. Trueman, and T. A. Denidni, "Compact multiband planar antenna for 2.4/3.5/5.2/5.8-GHz wireless applications," *IEEE Antennas and Wireless Propagation Letters*, vol. 11, pp. 144–147, 2012.

[2] F. Mirzamohammadi, J. Nourinia, and C. Ghobadi, "A novel dual-wideband monopole-like microstrip antenna with controllable frequency response," *IEEE Antennas and Wireless Propagation Letters*, vol. 11, pp. 289–292, 2012.

[3] M. J. Kim, C. S. Cho, and J. Kim, "A dual band printed dipole antenna with spiral structure for WLAN application," *IEEE Microwave and Wireless Components Letters*, vol. 15, no. 12, pp. 910–912, 2005.

[4] O. Tze-Meng, T. K. Geok, and A. W. Reza, "A dual-band omnidirectional microstrip antenna," *Progress in Electromagnetics Research*, vol. 106, pp. 363–376, 2010.

[5] K. G. Thomas and M. Sreenivasan, "Compact CPW-fed dual-band antenna," *Electronics Letters*, vol. 46, no. 1, pp. 13–14, 2010.

[6] N. Zhang, P. Li, B. Liu, X. W. Shi, and Y. J. Wang, "Dual-band and low cross-polarisation printed dipole antenna with L-slot and tapered structure for WLAN applications," *Electronics Letters*, vol. 47, no. 6, pp. 360–361, 2011.

[7] Y. L. Kuo and K. L. Wong, "Printed Double-T Monopole Antenna for 2.4/5.2 Ghz dual-band WLAN operations," *IEEE Transactions on Antennas and Propagation*, vol. 51, no. 9, pp. 2187–2192, 2003.

[8] W. C. Liu, C. M. Wu, and N. C. Chu, "A compact CPW-Fed slotted patch antenna for dual-band operation," *IEEE Antennas and Wireless Propagation Letters*, vol. 9, pp. 110–113, 2010.

[9] M. N. Mahmoud and R. Baktur, "A dual band microstrip-fed slot antenna," *IEEE Transactions on Antennas and Propagation*, vol. 59, no. 5, pp. 1720–1724, 2011.

[10] A. A. Gheethan and D. E. Anagnostou, "Broadband and dual-band coplanar folded-slot antennas (CFSAs)," *IEEE Antennas and Propagation Magazine*, vol. 53, no. 1, pp. 80–89, 2011.

[11] C. Hsieh, T. Chiu, and C. Lai, "Compact dual-band slot antenna at the corner of the ground plane," *IEEE Transactions on Antennas and Propagation*, vol. 57, no. 10, pp. 3423–3426, 2009.

[12] Y.-C. Lee and J.-S. Sun, "Compact printed slot antennas for wireless dual- and multi-band operations," *Progress in Electromagnetics Research*, vol. 88, pp. 289–305, 2008.

[13] M. R. Ghaderi and F. Mohajeri, "A compact hexagonal wide-slot antenna with microstrip-fed monopole for UWB application," *IEEE Antennas and Wireless Propagation Letters*, vol. 10, pp. 682–685, 2011.

[14] N. Chahat, M. Zhadobov, R. Sauleau, and K. Ito, "A compact UWB antenna for on-body applications," *IEEE Transactions on Antennas and Propagation*, vol. 59, no. 4, pp. 1123–1131, 2011.

[15] G. Cappelletti, D. Caratelli, R. Cicchetti, and M. Simeoni, "A low-profile printed drop-shaped dipole antenna for wide-band wireless applications," *IEEE Transactions on Antennas and Propagation*, vol. 59, no. 10, pp. 3526–3535, 2011.

[16] C. C. Lin, P. Jin, and R. W. Ziolkowski, "Single, dual and tri-band-notched ultrawideband (UWB) antennas using capacitively loaded loop (CLL) resonators," *IEEE Transactions on Antennas and Propagation*, vol. 60, no. 1, pp. 102–109, 2012.

[17] W. T. Li, Y. Q. Hei, W. Feng, and X. W. Shi, "Planar antenna for 3G/Bluetooth/WiMAX and UWB applications with dual band-notched characteristics," *IEEE Antennas and Wireless Propagation Letters*, vol. 11, pp. 61–64, 2012.

[18] A. A. Gheethan and D. E. Anagnostou, "Dual band-reject UWB antenna with sharp rejection of narrow and closely-spaced bands," *IEEE Transactions on Antennas and Propagation*, vol. 60, no. 4, pp. 2071–2076, 2012.

[19] G. Kumar and K. P. Ray, *Broad Band Microstrip Antennas*, Artech House, Boston, Mass, USA, 2003.

[20] K. G. Thomas and M. Sreenivasan, "A simple ultrawideband planar rectangular printed antenna with band dispensation," *IEEE Transactions on Antennas and Propagation*, vol. 58, no. 1, pp. 27–34, 2010.

[21] Q. X. Chu and Y. Y. Yang, "3.5/5.5 GHz dual band-notch ultra-wideband antenna," *Electronics Letters*, vol. 44, no. 3, pp. 172–174, 2008.

Hindawi Publishing Corporation
International Journal of Antennas and Propagation
Volume 2013, Article ID 472645, 13 pages
http://dx.doi.org/10.1155/2013/472645

Research Article

A Reconfigurable Triple-Notch-Band Antenna Integrated with Defected Microstrip Structure Band-Stop Filter for Ultra-Wideband Cognitive Radio Applications

Yingsong Li,[1] Wenxing Li,[1] and Qiubo Ye[2]

[1] *College of Information and Communications Engineering, Harbin Engineering University, Harbin, Heilongjiang 150001, China*
[2] *Communications Research Centre, 3701 Carling Avenue, Ottawa, Canada K2H 8S2*

Correspondence should be addressed to Yingsong Li; liyingsong82@gmail.com

Received 28 November 2012; Revised 23 May 2013; Accepted 27 May 2013

Academic Editor: Antonio Faraone

A printed reconfigurable ultra-wideband (UWB) monopole antenna with triple narrow band-notched characteristics is proposed for cognitive radio applications in this paper. The triple narrow band-notched frequencies are obtained using a defected microstrip structure (DMS) band stop filter (BSF) embedded in the microstrip feed line and an inverted π-shaped slot etched in the rectangular radiation patch, respectively. Reconfigurable characteristics of the proposed cognitive radio antenna (CRA) are achieved by means of four ideal switches integrated on the DMS-BSF and the inverted π-shaped slot. The proposed UWB CRA can work at eight modes by controlling switches ON and OFF. Moreover, impedance bandwidth, design procedures, and radiation patterns are presented for analysis and explanation of this antenna. The designed antenna operates over the frequency band between 3.1 GHz and 14 GHz (bandwidth of 127.5%), with three notched bands from 4.2 GHz to 6.2 GHz (38.5%), 6.6 GHz to 7.0 GHz (6%), and 12.2 GHz to 14 GHz (13.7%). The antenna is successfully simulated, fabricated, and measured. The results show that it has wide impedance bandwidth, multimodes characteristics, stable gain, and omnidirectional radiation patterns.

1. Introduction

Recently, the increasing demands for antennas with multiband and multimode operation in modern wireless communication applications have attracted much attention in academia and industry. In particular, UWB systems covering wide bandwidth ranging from 3.1 GHz to 10.6 GHz have been released by Federal Communications Commission (FCC) in 2002 for indoor wireless communications [1]. Since then, the UWB systems have drawn the attention of researchers worldwide because of their low cost, high data rate, and good resistance for multipath and jamming.

A UWB antenna is one of the most important components in the system, and a lot of UWB antennas have been proposed and investigated [2–4], such as microstrip line feed antennas and coplanar waveguide feed antennas. However, the UWB communication systems cover such a wide bandwidth that overlaps with existing narrow band communications applications, such as wireless local area network (WLAN), C-band, X-band, and worldwide interoperability for microwave access (WiMAX). For the sake of reducing the potential interference between UWB systems and narrow band systems, narrow BSFs are added to the end of antennas or equipment to reject the unexpected signals [5], which will certainly increase the cost of the UWB systems. A number of UWB antennas with one or two notched bands have been achieved by using various technologies [5–15], such as slots, stubs, and resonators. Widely used methods are etching various slots on radiation patches and the ground plane, such as C-shaped slots [6, 15] and pi-shaped slots [7]. One effective method is to insert stubs into designed antennas [8]. The inserted stub will generate a notched band without deteriorating radiation patterns. Another effective method is to integrate filters into a UWB antenna which can resist narrow band interference [9]. However, the antennas reported above just work in UWB mode or UWB mode with notched bands, which cannot meet explosive demand on radio spectrum resulted from

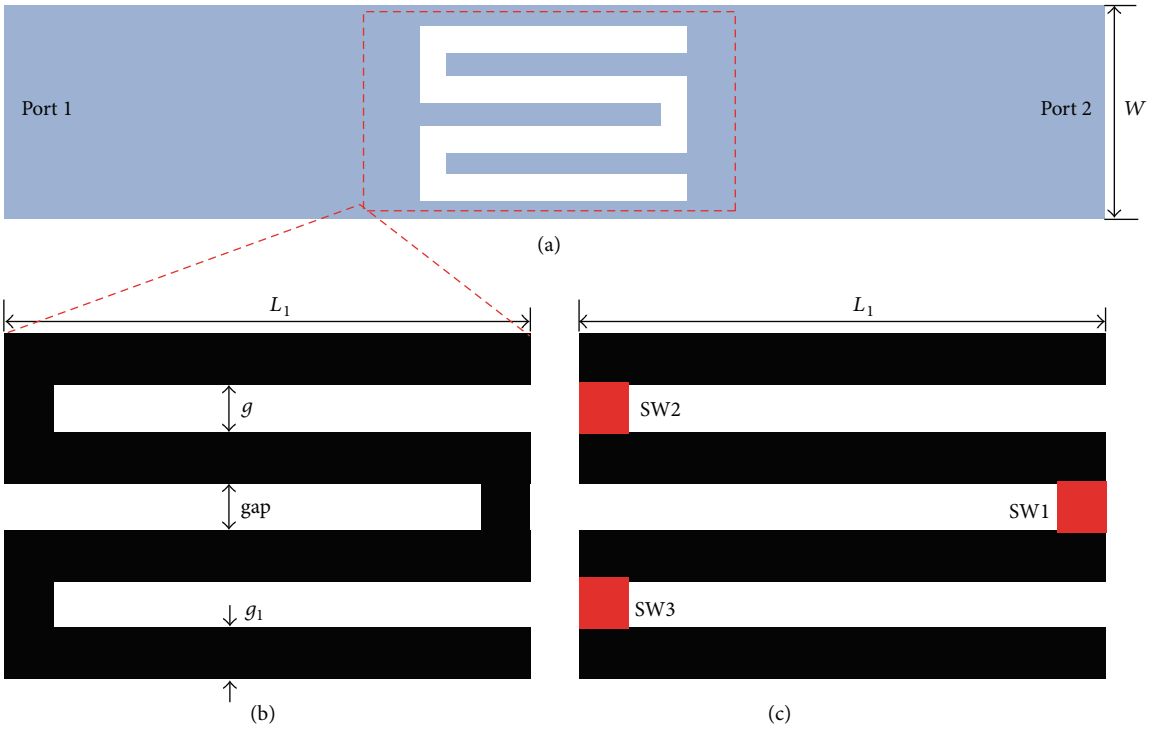

Figure 1: Structure of DMS-BSF.

the low cost systems, various communication protocols, and high data rate wireless communication systems [16, 17]. The current spectrum is scarce. In particular, there are many systems working below 10 GHz, such as WLAN, C-band, radio frequency identification (RFID), and X-band. Antennas are required to change operating modes to meet multimode wireless communication and cognitive radio applications. A more intelligent method is based on dynamic control, where UWB systems will need an algorithm that can detect the presence of interference from narrow band systems and then avoid it upon detection of its presence. One way to perform dynamic control is based on cognitive radio or software defined radio. In order to meet this requirement, several UWB CRAs with complex single- and dual-port structure have been studied and investigated [16–20]. For single UWB CRAs, the previous design cannot be designed flexibly. Most of the proposed single port CRAs are designed with split-ring resonators (SRR) in the radiation patch [19], which will leak electromagnetic wave that deteriorates the radiation patterns.

In this paper, a flexible triple band-notched UWB antenna with reconfigurable characteristics for cognitive radio applications has been studied numerically and experimentally. The triple notched bands are realized using a DMS-BSF embedded in the microstrip feed line and the inverted π-shaped slot etched on the rectangular radiation patch. The reconfigurable characteristics of cognitive radio applications can be controlled by turning switches at ON state or OFF state. The notched bands can be designed by adjusting the dimensions of DMS-BSF and the inverted π-shaped slot. The proposed CRA can work on eighth modes which is suitable for multimode, multiband, and UWB cognitive radio communications.

2. Antenna Design

In this section, the proposed UWB band-notched antenna integrated with DMS-BSF and the inverted π-shaped slot for cognitive radio applications is illustrated in detail. Design procedures are divided into four parts. Firstly, we will introduce the DMS-BSF which will be integrated into the UWB CRA. Secondly, the band-notched UWB antenna integrated with the switchable DMS-BSF will be investigated. Thirdly, the band-notched UWB antenna with the inverted π-shaped slot on the radiation patch will be studied. Finally, we will study the UWB CRA integrated with DMS-BSF and the inverted π-shaped slot. In this study, the ideal switches for reconfigurability are metal bridges. The presence of the metal bridge represents that the switch status is ON; in contrast, the absence of the metal bridge represents that the switch status is OFF [10, 18, 21, 22]. The simulated results are obtained by using Computer Simulation Technology (CST) Microwave Studio based on finite integration technique (FIT).

2.1. Characteristics of the Proposed DMS-BSF. Currently, there has been a growing interest for research on planar filters using defected ground structures (DGS), photonic band gap (PBG), and electromagnetic band gap (EBG) [23]. Both DGS and PBG have been used for designing and improving the performances of various components, such as filters, antennas, and power amplifiers. However, DGSs etched on ground planes have problems such as radiation from ground plane

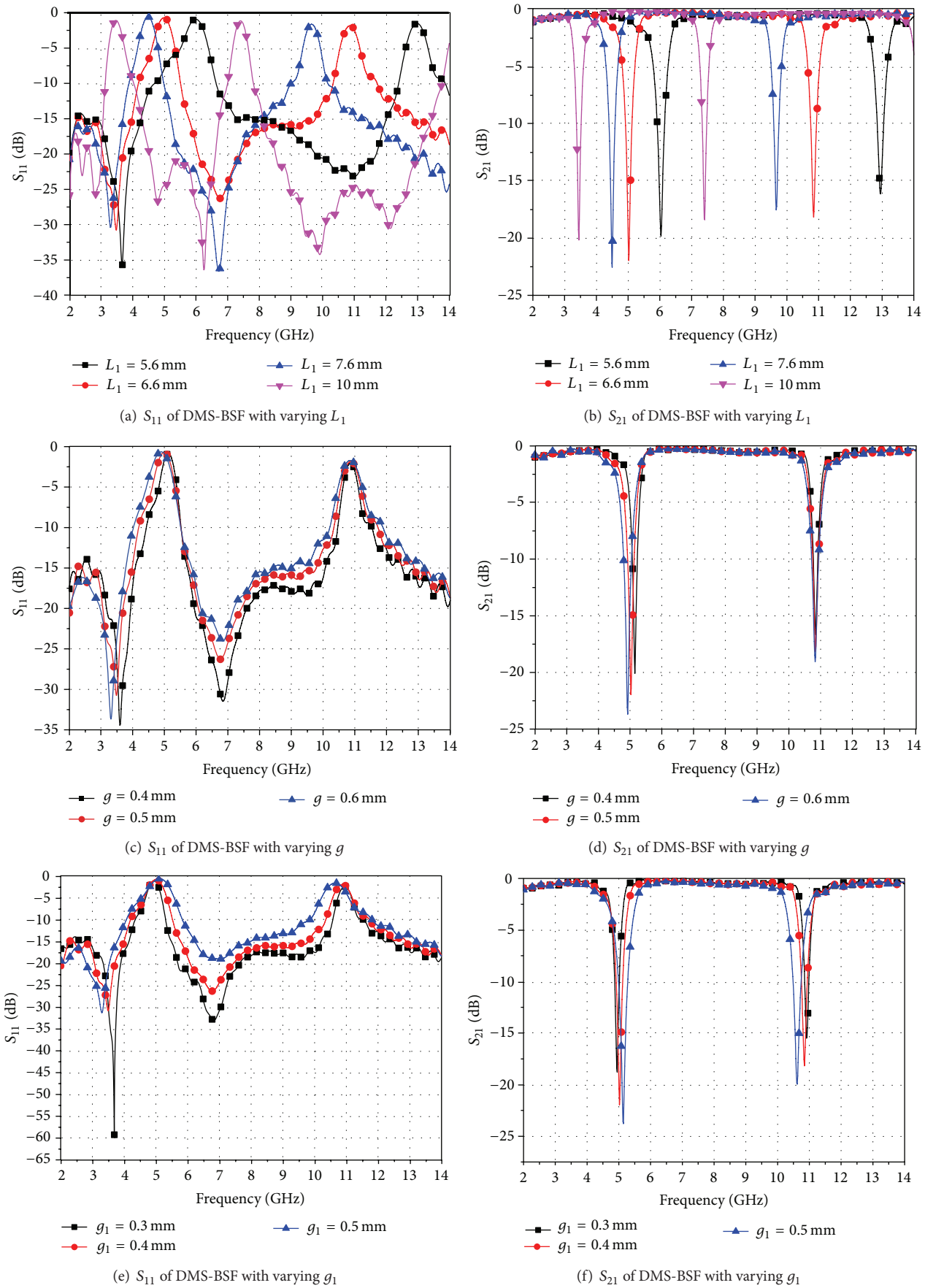

(a) S_{11} of DMS-BSF with varying L_1

(b) S_{21} of DMS-BSF with varying L_1

(c) S_{11} of DMS-BSF with varying g

(d) S_{21} of DMS-BSF with varying g

(e) S_{11} of DMS-BSF with varying g_1

(f) S_{21} of DMS-BSF with varying g_1

Figure 2: Continued.

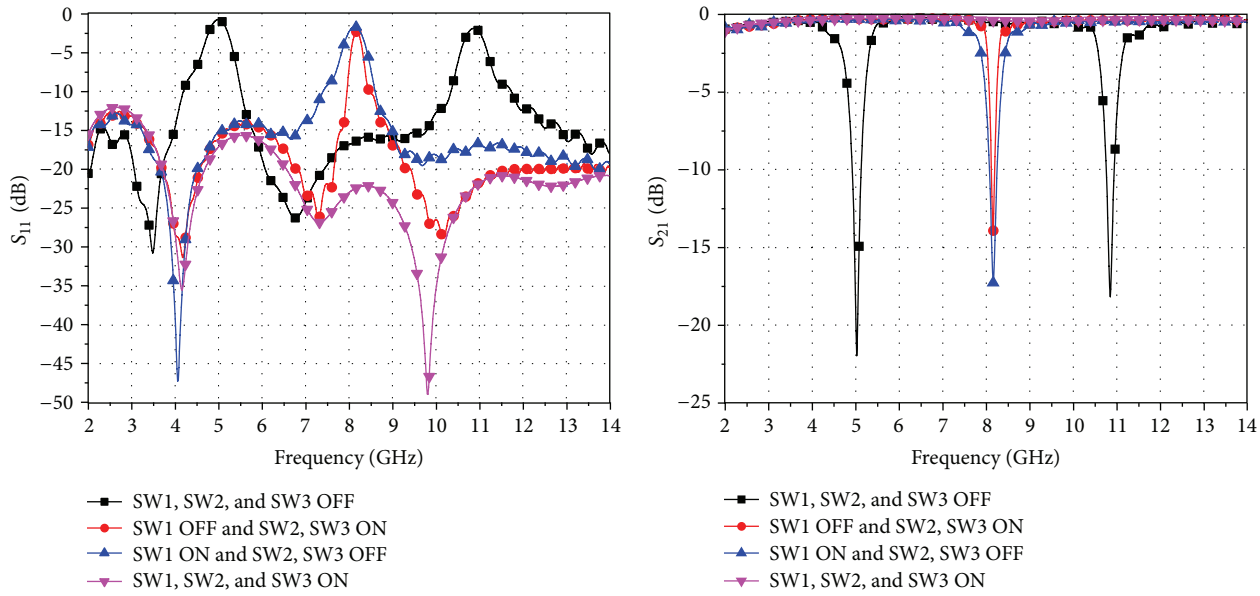

(g) S_{11} of DMS-BSF switchable functions

(h) S_{21} of DMS-BSF switchable functions

Figure 2: S-parameters of DMS-BSF.

which will produce interference to other microwave elements [24]. PBGs and EBGs have many parameters which make them difficult to design. In addition, PBG/EBG parameters also affect the band gap characteristic [23]. On the other hand, the defected microstrip structure (DMS) is of great advantages in design due to its reduced size and the feature of electromagnetic interference (EMI) noise immunity [24–29]. Furthermore, DMS has higher effective inductance compared to DGS [26], PBG, and EBG. Therefore, DMS has been used for designing filters, reducing antenna size, and suppressing the crosstalk of parallel microstrip lines [23, 24, 29]. In this paper, a meander line DMS is employed to design a multimode band-notched UWB antenna. The configuration of DMS-BSF is designed and illustrated in Figure 1, and its performance is investigated using CST.

From Figure 1, we can see that the DMS-BSF consists of a 50 Ω microstrip line with width W and a meander slot with parameters L_1, g, gap, and g_1. Detailed meander slot parameters are shown in Figure 1(b). In order to design a switchable DMS-BSF, three ideal switches are incorporated into the meander slot. The three switches are described as SW1, SW2, and SW3 and shown in Figure 1(c). In general, horizontal slots of the meander slot provide inductance effects, while vertical slots exhibit capacitive characteristics [25]. Thus, the resonant frequency can be adjusted by controlling dimensions of the meander slot. To investigate the characteristics of DMS-BSF, various parameters are analyzed using CST. DMS-BSF is printed on a substrate with a dielectric constant of 2.65, a loss tangent of 0.002, and a thickness of $h = 1.6$ mm, and the dimensions are $L_1 = 6.6$ mm, gap $= g = 0.5$ mm, and $g_1 = 0.4$ mm. In the simulation, one parameter is varied, while others remain fixed. The reflection coefficient (S_{11}) and transmission coefficient (S_{21}) of DMS-BSF are illustrated in Figure 2. Figures 2(a) and 2(b) show effects of varying L_1, and we can see that the DMS-BSF exhibits dual-band band stop characteristics in frequency response. As L_1 increases, the first resonance shifts down slowly to the lower frequencies, while the second resonance moves fast toward lower frequencies. This is because the DMS increases the electric length of the microstrip line and hence changes its current distribution and the effective capacitance and inductance. The increased horizontal length of the meander slot affects the structure inductively [25]. The first resonant frequency has a wide tuning stop band which ranges from 3.5 GHz to 6 GHz, while the second one can adjust from 7.4 GHz to 12.9 GHz. Figures 2(c) and 2(d) demonstrate S_{11} and S_{21} in terms of varying g. By changing g from 0.4 mm to 0.6 mm, the center frequency of the first resonance moves to lower band, while the second resonant frequency keeps constant. The characteristics of S_{11} and S_{21} when varying g_1 are shown in Figures 2(e) and 2(f). With the increase of g_1, the center frequency of the first resonance moves to higher band. On the contrary, the center frequency of the second resonance slightly shifts toward lower frequencies. In addition, the pass band characteristics are also deteriorated with the increase of g_1. The switching characteristics are shown in Figures 2(g) and 2(h). In this simulation, the ideal switches are replaced with three metal strips with length 0.5 mm and width 0.4 mm. It is obvious that DMS-BSF has two stop bands with all switches OFF. The center frequency of the two stop bands can be controlled by adjusting the dimensions of the meander slot. When SW1 is ON and SW2 and SW3 are OFF, the DMS-BSF has only one stop band which is near 8 GHz. For SW1 OFF and SW2 and SW3 ON, the DMS-BSF also has one stop band. However, the stop band characteristics are different for these two situations. The DMS-BSF with SW1 ON and both SW2 and SW3 OFF has wider stop band than the DMS-BSF with SW1 OFF and both SW2 and SW3 ON. When all the

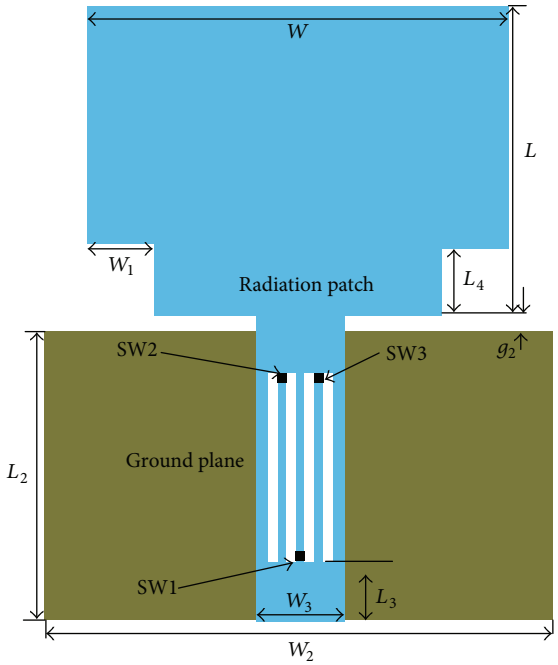

Figure 3: Cognitive radio antenna A.

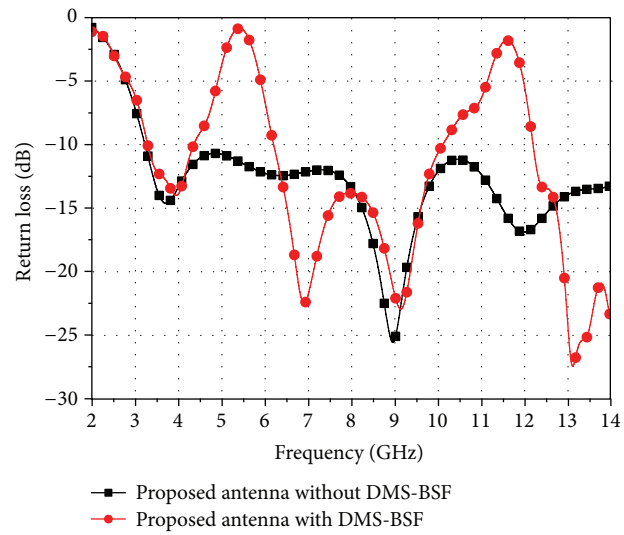

Figure 4: Return loss of CRA_A with all switches OFF with/without DMS-BSF.

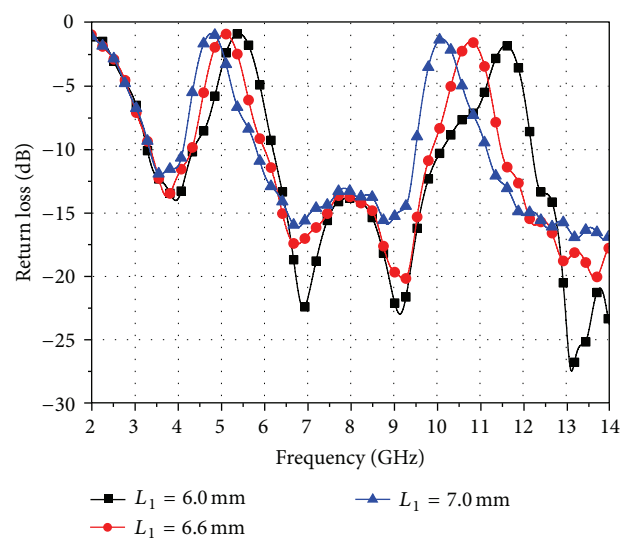

Figure 5: Tunable band-notched characteristics of CRA_A with all switches OFF.

switches are ON, the proposed structure is an all-pass filter which passes all frequency. As can be seen from Figure 2, the meander slot DMS-BSF has dual resonant frequency, while conventional structure has only one resonance [24]. The switchable meander slot DMS-BSF also has tunable functions which can work in all-pass mode, a stop band mode, and dual stop band mode.

2.2. Design of Cognitive Radio Antenna A (CRA_A). A CRA should have reconfigurable characteristics for meeting the cognitive radio requirement. In cognitive radio (CR) communication systems, unlicensed users (secondary users) can access spectrum bands licensed to primary users at spectrum underlay mode or spectrum overlay mode. In the underlay mode, the secondary users are limited under a very low transmission power which is less than −41.3 dBm/MHz for UWB users [1, 19]. This approach can be realized by using impulse radio (IR) based UWB (IR-UWB) technology. For the overlay mode, the secondary users detect the existing narrow band (NB) signals, such as those from WLAN and RFID, and provide immunity to the NB systems. This can be implemented by turning off the corresponding subcarriers in orthogonal frequency division multiplexing (OFDM) UWB (OFDM-UWB), depending on whether any primary users exist or not in a particular band. In other words, the transmission spectrum of UWB radios can be sculpted according to the presence of the primary users in the respective frequency bands in the environment [30]. Therefore, in CR-UWB systems, CRA should cover the entire UWB band from 3.1 GHz to 10.6 GHz with no notch bands for underlay applications and for detecting the licensed primary users and providing immunity to these users using band-notched technologies [19].

Based on the investigation of meander slot DMS-BSF and the requirements for CRAs, a CRA integrated with the meander slot DMS-BSF has been proposed and shown in Figure 3. The configuration of CRA_A is printed on a substrate with a dielectric constant of 2.65, a loss tangent of 0.002, and a thickness of $h = 1.6$ mm. CRA_A consists of a rectangular radiation patch, two square tapers at the bottom of the patch with dimensions L_4 and W_1, a DMS-BSF etched in microstrip feed line, a partial ground plane, and a 50 Ω microstrip line. The radiation patch and the microstrip feed line are printed on top of the substrate, while the ground plane is printed on the bottom of the substrate. The dimensions of the antenna are optimized and listed as follows: $L = 15$ mm, $W = 16$ mm, $W_1 = 2$ mm, $W_2 = 30$ mm, $W_3 = 4.7$ mm, $L_2 = 16.2$ mm, $L_3 = 3.7$ mm, $L_4 = 2.2$ mm, and $g_2 = 0.8$ mm.

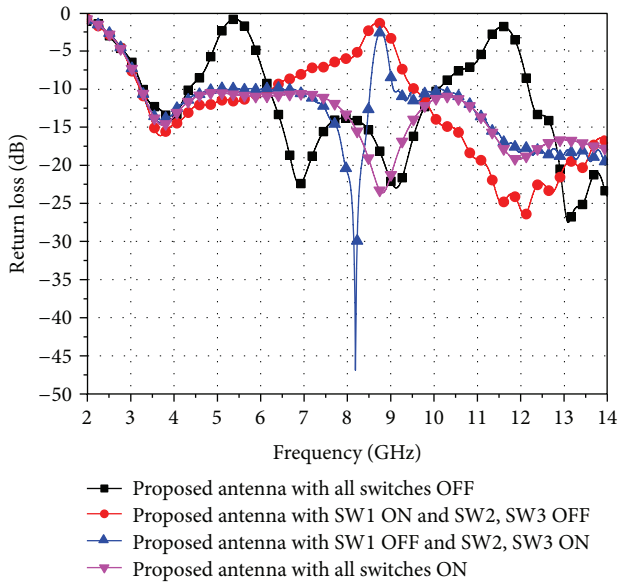

Figure 6: Return loss of switchable characteristics of CRA_A.

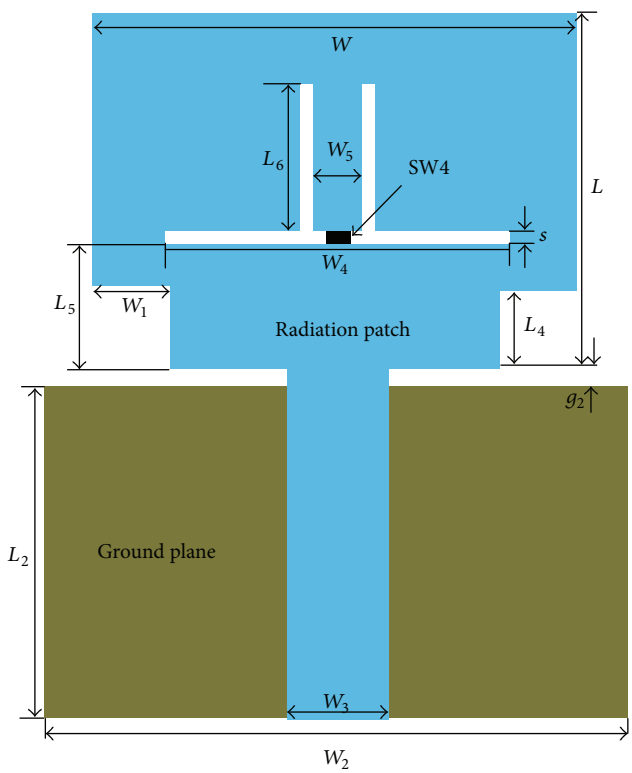

Figure 7: Structure of proposed CRA_B.

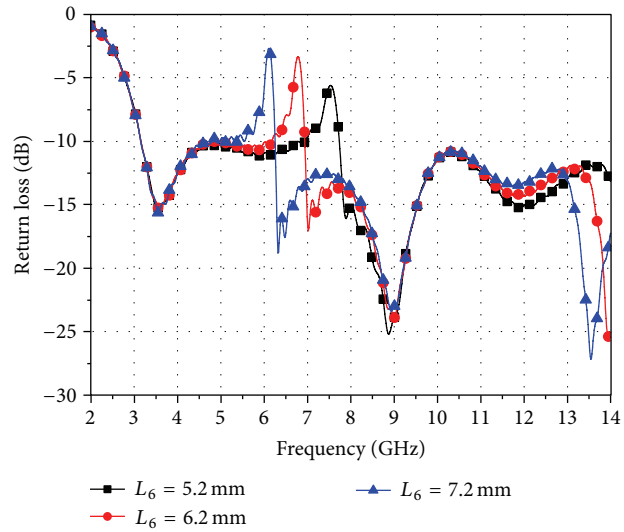

Figure 8: Tunable band-notched characteristics of CRA_B.

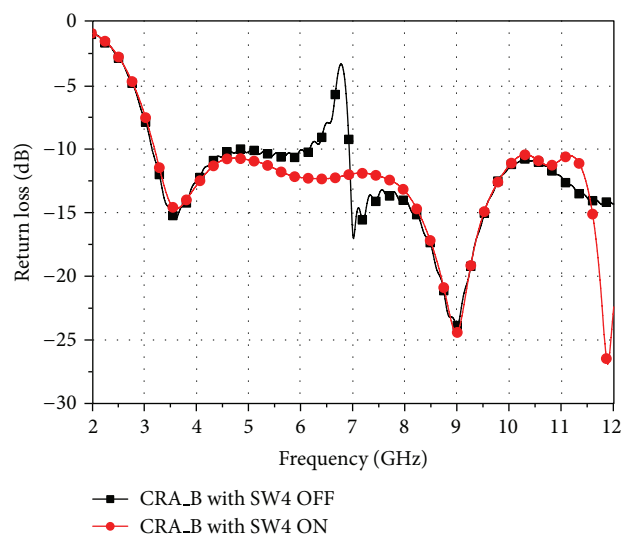

Figure 9: Reconfigurable characteristics of CRA_B.

The dimensions of DMS-BSF of CRA_A are $L_1 = 6.6$ mm, gap $= g = 0.5$ mm, and $g_1 = 0.4$ mm.

In order to investigate the performance of CRA_A, it is evaluated and analyzed using CST. The return losses of CRA_A with and without DMS-BSF are simulated and illustrated in Figure 4. It can be seen that CRA_A without DMS-BSF is a UWB antenna having bandwidth ranging from 3.1 GHz to 14 GHz. CRA_A with DMS-BSF has two stop bands near 5.5 GHz and 11.5 GHz, respectively. The two notched bands are generated by DMS-BSF which changes the distributive inductance and capacitance of the microtrip feed line. This also alters the current path on the microtrip feed line. For comparison, the tuning band-notched characteristics of CRA_A with all switches OFF are analyzed and shown in Figure 5. We can see that both of the notched bands move to lower frequencies by increasing L_1. The lower notched band near 5 GHz shifts slowly, while the higher notched band near 10.5 GHz shifts faster. In addition, the CRA_A works as a tunable band-notched antenna by altering the parameters of DMS-BSF. It is also a UWB antenna with two stop bands which can reduce or avoid EMI between broadband wireless systems and narrow band

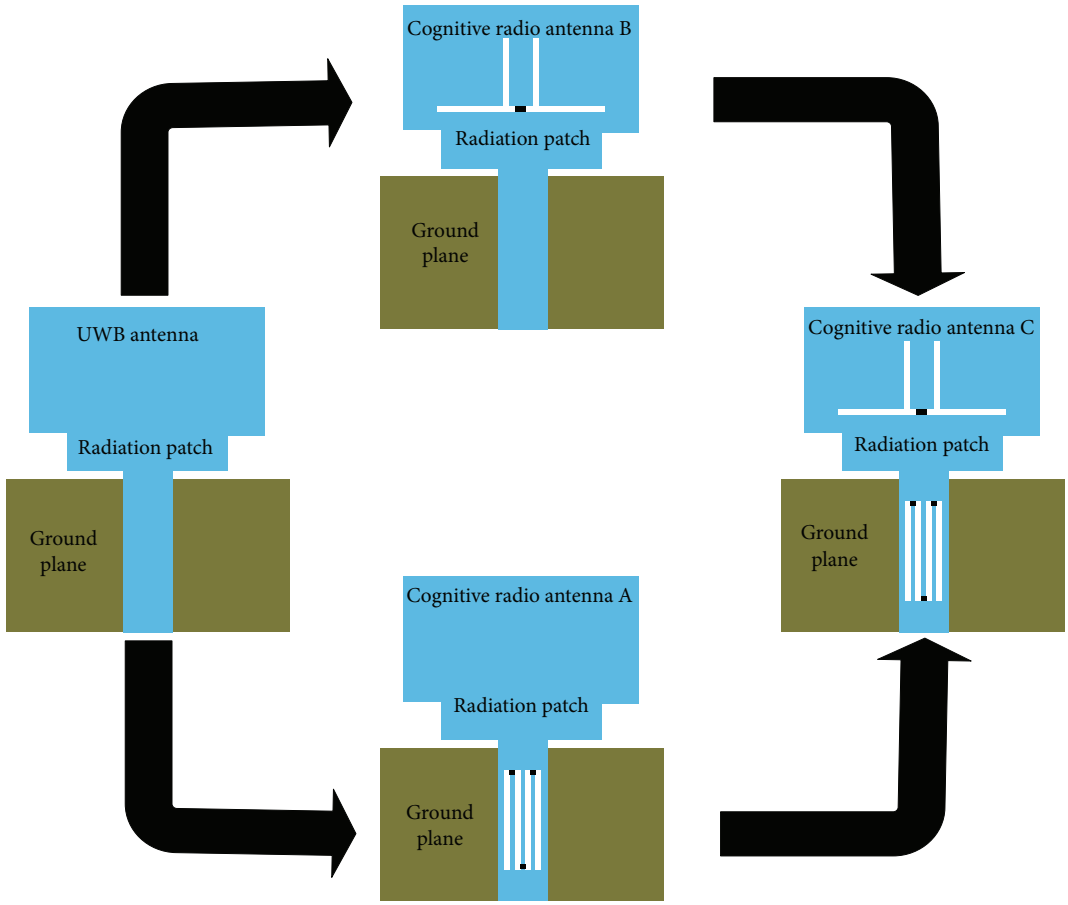

Figure 10: Design procedure of CRA_C.

communication systems. This antenna can also be used for tri-band wireless communication applications.

To meet the requirement of CR communication applications, the switchable characteristics of CRA_A have been studied, and the simulated results are illustrated in Figure 6. We can see that CRA_A has two notched bands near 5.5 GHz and 11.5 GHz with all switches OFF. In order to balance the feed line, SW2 and SW3 turn on or off simultaneously. When SW1 is ON and SW2 and SW3 are OFF, CRA_A has a notch near 8.8 GHz and the bandwidth covers 6.2 GHz to 9.5 GHz. When SW1 is OFF and SW2 and SW3 are ON, CRA_A also has a notch near 8.8 GHz, but the bandwidth is narrower with only about 0.5 GHz. The notched bands help to prevent the potential interference to a primary user or the services operated in these bands. When all the switches are ON, CRA_A is a UWB antenna for underlay CR operation and for channel sensing in overlay CR scenario.

2.3. Design of Cognitive Radio Antenna B (CRA_B). To make the proposed CRA more useful for practical applications, CRA_B is designed by etching an inverted π-shaped slot in the radiation patch. The structure of CRA_B is illustrated in Figure 7. CRA_B is printed on a substrate with a dielectric constant of 2.65, a loss tangent of 0.002, and a thickness of $h = 1.6$ mm. CRA_B consists of a rectangular radiation patch, two square tapers at the bottom of the patch with dimensions L_4 and W_1, an inverted π-shaped slot embedded in the rectangular radiation patch, a partial ground plane, and a 50 Ω microstrip line. The radiation patch and the microstrip feed line are printed on top of the substrate, while the ground plane is printed on the bottom of the substrate. The dimensions of CRA_B are optimized and listed as follows: $L = 15$ mm, $W = 16$ mm, $W_1 = 2$ mm, $W_2 = 30$ mm, $W_3 = 4.7$ mm, $W_4 = 9$ mm, $W_5 = 3.2$ mm, $L_2 = 16.2$ mm, $L_4 = 2.2$ mm, $L_5 = 4.1$ mm, $L_6 = 6.2$ mm, and $g_2 = 0.8$ mm. The width of the inverted π-shaped slot is $s = 0.4$ mm. In the simulation of CRA_B, the switch 4 (SW4) is a metal strip with length of 0.6 mm and width 0.4 mm. This piece of metal strip is approximated as an ideal switch which has been used in the design of most of reconfigurable antennas.

The effects of L_6 of the inverted π-shaped slot with switch 4 OFF are shown in Figure 8. It can be seen that the CRA_B has a notched band near 6.8 GHz which is used for RFID devices. The center frequency of the notched band is tunable by adjusting the dimensions of the inverted π-shaped slot. The notched band moves to lower frequencies with the increase of L_6. In order to reduce the potential interference from RFID systems, the length is set as 6.2 mm. Other parameters that have little effect on the notched band are not analyzed. In order to make the CRA_B reconfigurable,

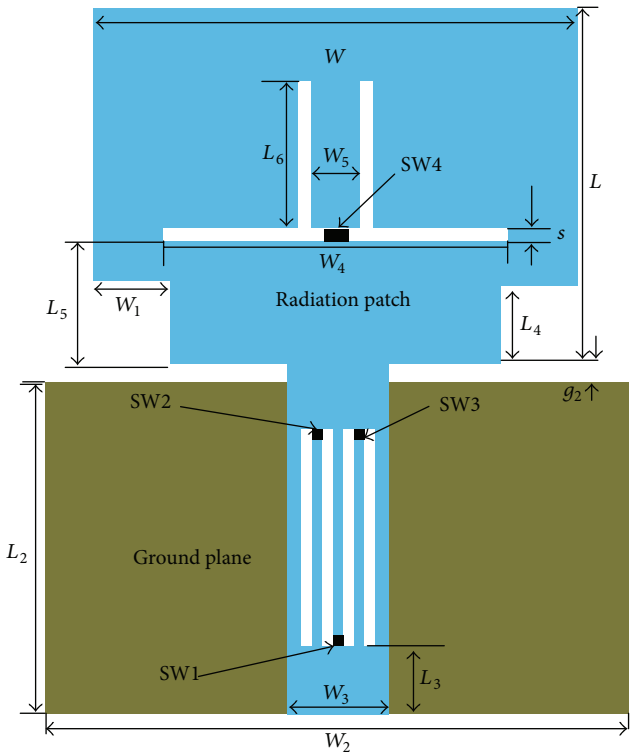

Figure 11: Geometry of CRA_C.

a switch SW4 is used on the inverted π-shaped slot. The dimensions of SW4 are length of 0.6 mm and width of 0.4 mm. The reconfigurable characteristics of CRA_B are investigated and shown in Figure 9. For the case of SW4 OFF, CRA_B has a notched band in the RFID band, and the center frequency can be adjusted by changing the length of L_6. This is due to the fact that changing the length of the inverted π-shaped slot alters the resonant length which corresponds to the resonant frequency. The CRA_B with SW4 OFF can be used in the overlay mode. When the SW4 is ON, the CRA_B is a UWB antenna and can be used in the underlay mode for channel sensing.

2.4. Design of Cognitive Radio Antenna C (CRA_C). Based on the studies of CRA_A and CRA_B, CRA_C integrated with DMS-BSF in CRA_A and the inverted π-shaped slot used in CRA_B has been proposed numerically and experimentally. Design procedures of CRA_C are shown in Figure 10. Firstly, a UWB antenna is designed. Secondly, a DMS-BSF is embedded in the microstrip feed line of the proposed UWB antenna to generate two notched bands for reducing or avoiding potential EMI from WLAN, WiMAX, and X-band, which is CRA_A. Thirdly, an inverted π-shaped slot is etched in the radiation patch of the UWB antenna to produce another notched bands for preventing the potential EMI from RFID systems, which is CRA_B. Finally, DMS-BSF and the inverted π-shaped slot are incorporated into the UWB antenna to form CRA_C which is shown in Figure 11. CRA_C is the combination of CRA_A and CRA_B.

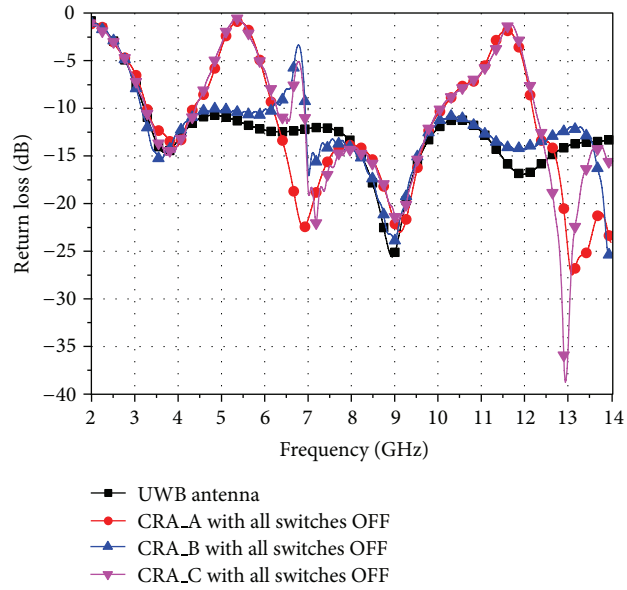

Figure 12: Comparisons of proposed cognitive radio antennas with all switches OFF.

Table 1: Eight switchable cases and corresponding notch bands.

Case	Notch bands (GHz)	SW1	SW2	SW3	SW4
1	5.5, 6.8, 11.5	OFF	OFF	OFF	OFF
2	5.5, 11.5	OFF	OFF	OFF	ON
3	8.7	ON	OFF	OFF	ON
4	8.7	OFF	ON	ON	ON
5	6.8, 8.7	ON	OFF	OFF	OFF
6	6.8, 8.7	OFF	ON	ON	OFF
7	6.8	ON	ON	ON	OFF
8	None (UWB antenna)	ON	ON	ON	ON

The dimensions of CRA_C are optimized and listed as follows: $L = 15$ mm, $W = 16$ mm, $W_1 = 2$ mm, $W_2 = 30$ mm, $W_3 = 4.7$ mm, $W_4 = 9$ mm, $W_5 = 3.2$ mm, $L_2 = 16.2$ mm, $L_3 = 3.7$ mm, $L_4 = 2.2$ mm, $L_5 = 4.1$ mm, $L_6 = 6.2$ mm, $g_2 = 0.8$ mm, and $s = 0.4$ mm. The dimensions of DMS-BSF of CRA_A are $L_1 = 6$ mm, gap $= g = 0.5$ mm, and $g_1 = 0.4$ mm. For comparison, return losses of the UWB antenna, CRA-A, CRA_B, and CRA_C are plotted and shown in Figure 12, where all the switches are OFF. It can be seen that the UWB antenna can work in a wide bandwidth ranging from 3.1 GHz to 14 GHz. The proposed CRA_C has three notched bands which are the combined results of CRA_A and CRA_B. The center frequencies of the three notched bands agree well with CRA_A and CRA_B. In addition, the notched band at 6.8 GHz and the other notched bands can be adjusted by changing the dimensions of the inverted π-shaped slot and DMS-BSF, respectively.

As a CRA, CRA_C should be reconfigurable so that it can work in cognitive radio environment. Therefore, CRA_C is investigated for eight possible operation modes which are listed in Table 1. Return losses of these eight cases are

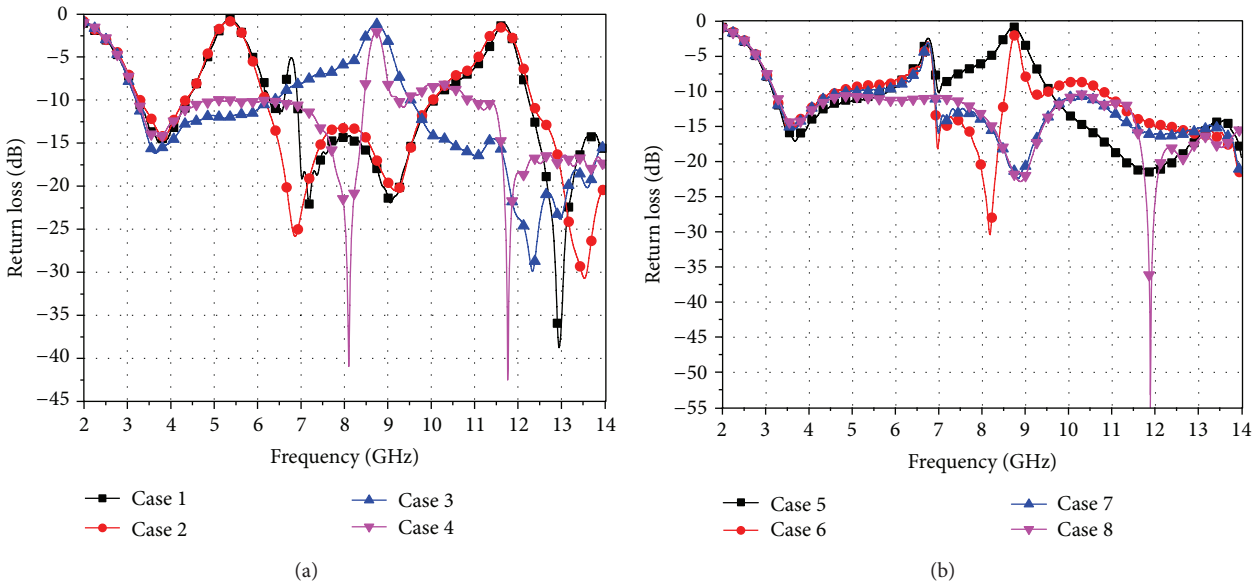

Figure 13: Switchable characteristics of CRA_C with various cases.

demonstrated in Figure 13. For case 1, CRA_C is a UWB antenna with triple notched bands which can prevent the interference from licensed primary users. In case 1, CRA_C can be used as a CRA in overlay mode. CRA_C in case 1 can also be used as a multiband antenna which works at 3.1 GHz–4.2 GHz, 6.2 GHz–6.6 GHz, 7.0 GHz–10 GHz, and 12.2 GHz–14 GHz. When CRA_C works in case 2, case 5, and case 6 modes, it can provide two notched bands. For case 2, the two notched bands are 5.5 GHz for reducing the interference from WLAN, WiMAX, and C-band and 11.5 GHz for preventing the interference from X-band. As for case 5 and case 6, the two notched bands work at 6.8 GHz and 8.7 GHz. In these cases, CRA_C can avoid the interference from RFID and X-band, respectively. Furthermore, case 6 has a narrower notched band than case 5. This has the similar characteristics as DMS-BSF discussed in 2.1. When CRA_C works in case 3, case 4, and case 7, it has a notched band which works at 8.7 GHz, 8.7 GHz, and 6.8 GHz, respectively. However, the bandwidth of the notched band is different. Case 3 has a wider notched band bandwidth than those of case 4 and case 7. The band-notched characteristics of case 3 and case 4 are determined by DMS-BSF, and those of case 7 is mainly determined by the inverted π-shaped slot. In these cases, CRA_C can work in overlay mode. For case 8, CRA_C is a UWB antenna, which can be used in underlay mode.

3. Results and Discussions

To verify the above design and compare with measurement, CRA_C in case 1 and case 8 are fabricated and measured. For comparison, the four ideal switches, switch 1 (SW1), switch 2 (SW2), switch 3 (SW3), and switch 4 (SW4) are also metal bridges which are replaced by a metal strip in fabrication. In simulation and fabrication, the metal bridges with dimensions of 0.5 mm × 0.4 mm are used to approximate SW1, SW2, and SW3. SW4 is replaced with a metal strip with a length 0.6 mm and width 0.4 mm. For reducing the cost of fabrication and measurement, CRA_C with all switches ON and OFF is fabricated and tested to verify the accuracy of CST simulations. CRA_C with all switches ON and OFF is optimized, and the optimal parameters are as follows: L = 15 mm, W = 16 mm, W_1 = 2 mm, W_2 = 30 mm, W_3 = 4.7 mm, W_4 = 9 mm, W_5 = 3.2 mm, L_2 = 16.2 mm, L_3 = 3.7 mm, L_4 = 2.2 mm, L_5 = 4.1 mm, L_6 = 6.2 mm, and g_2 = 0.8 mm. The dimensions of DMS-BSF are again L_1 = 6 mm, g = 0.5 mm, and g_1 = 0.4 mm. The optimized antennas, as shown in Figure 14, are also fabricated and measured using Anritsu 37347D vector network analyzer. Measured and simulated results of return losses are compared in Figure 15.

It can be seen from Figure 15 that CRA_C with all switches ON is a UWB antenna which has a wide bandwidth ranging from 3.1 GHz to 14 GHz. In this case, CRA_C can be used in underlay mode. As for CRA_C with all switches OFF, it is a UWB antenna with triple notched bands which can prevent the interference from C-band, WLAN, WiMAX, RFID, and X-band. In case 1, CRA_C can be used for overlay mode. In addition, CRA_C in case 1 is also a four band antenna which can operate in multiband wireless communication systems. The measured results agree well with the simulated ones, which help to verify the accuracy of the simulation. The discrepancy between simulated and measured curves may be due to the errors of manufactured antennas. Thereby, we can control the switches ON and OFF to allow the proposed antenna to work in underlay and overlay modes for cognitive radio communications. The proposed antennas can also be used for multiband communication systems and multimode wireless communication systems by controlling the switches ON and OFF. Measured radiation patterns at 3.5 GHz, 6.4 GHz, and 9.0 GHz of case 1 and case 8 are shown in Figure 16.

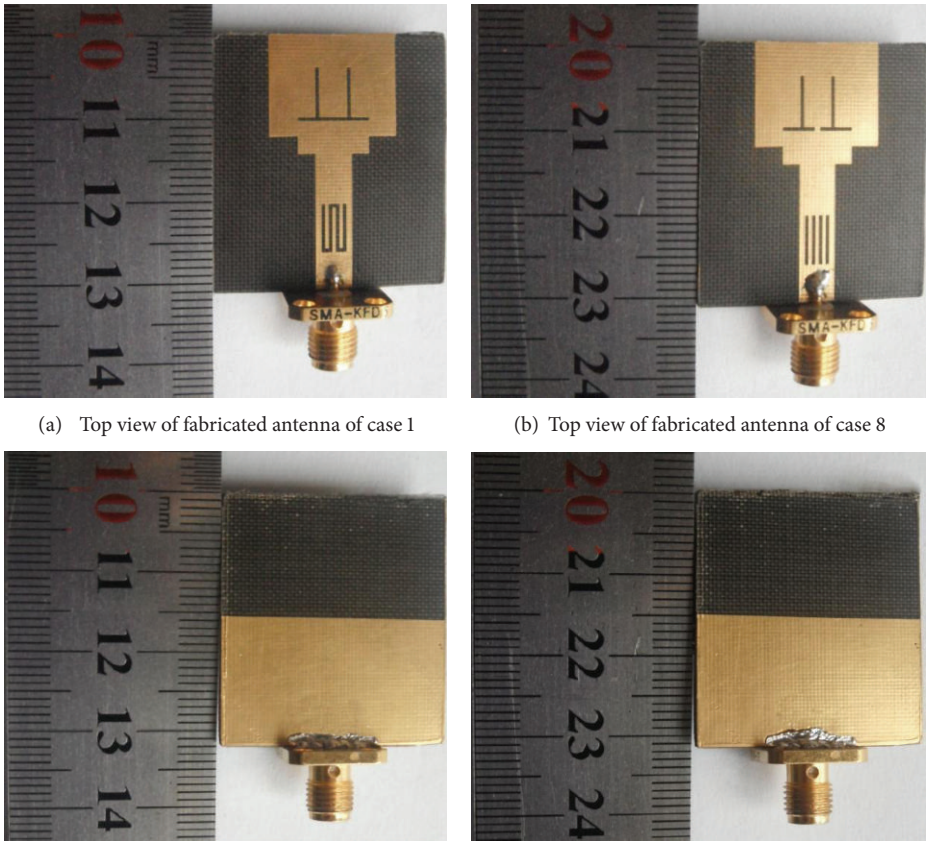

(a) Top view of fabricated antenna of case 1

(b) Top view of fabricated antenna of case 8

(c) Bottom view of fabricated antenna of case 1

(d) Bottom view of fabricated antenna of case 8

Figure 14: The fabricated CRA_C in case 1 and case 8.

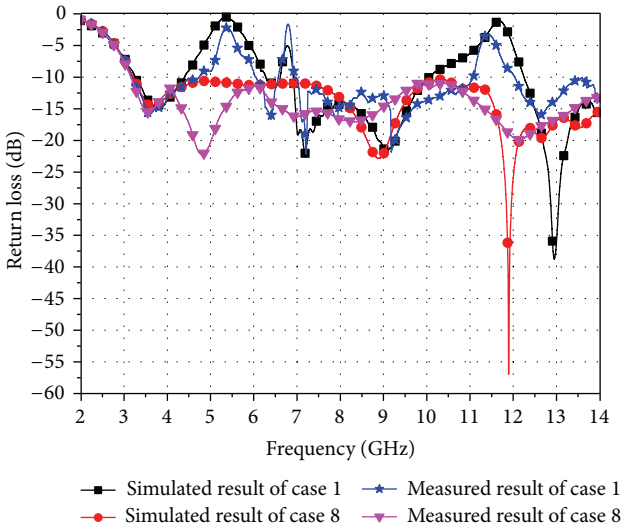

Figure 15: Return losses of fabricated CRA_C in case 1 and case 8.

It is worth noting that the radiation patterns of CRA_C are omnidirectional in the H-plane (xz-plane) and dipole like in the E-plane (yz-plane) when all the switches are turned on or off, respectively. The E-plane radiation patterns of CRA_C with all switches OFF have a little distortion, which is caused by the power leaking of the inverted π-shaped slot. It is found that the measured results of CRA_C using the DMS-BSF, the inverted π-shaped slot, and the ideal switches well satisfy the requirement of UWB cognitive radio communication applications. The peak gains of CRA_C with all switches ON or OFF are obtained by comparing with a double ridged horn antenna in the operation bands. In measuring of the gains of the fabricated antennas, only the key points in the operation bands are measured. As for CRA_C with all switches OFF, addition points are also measured in the notched bands. The measured and simulated peak gains of the fabricated antennas are illustrated in Figure 17. It is found that the stable gains of the fabricated antennas have been obtained with fluctuation less than 2.2 dBi throughout the operation band except the three notched frequencies. As expected, CRA_C with all switches OFF has three sharp gains, which decrease in the vicinity of 5.5 GHz, 6.8 GHz, and 11.5 GHz, namely, the gains drop deeply to −2 dBi, −0.9 dBi, and −0.7 dBi, respectively. However, CRA_C with all switches ON has stable gains over the UWB band. The measured gains are little lower than the simulated ones, which may be caused by the space loss of the environment for measuring the proposed low power antenna.

4. Conclusion

In this paper, a cognitive radio antenna integrated with DMS-BSF and the inverted π-shaped slot has been investigated

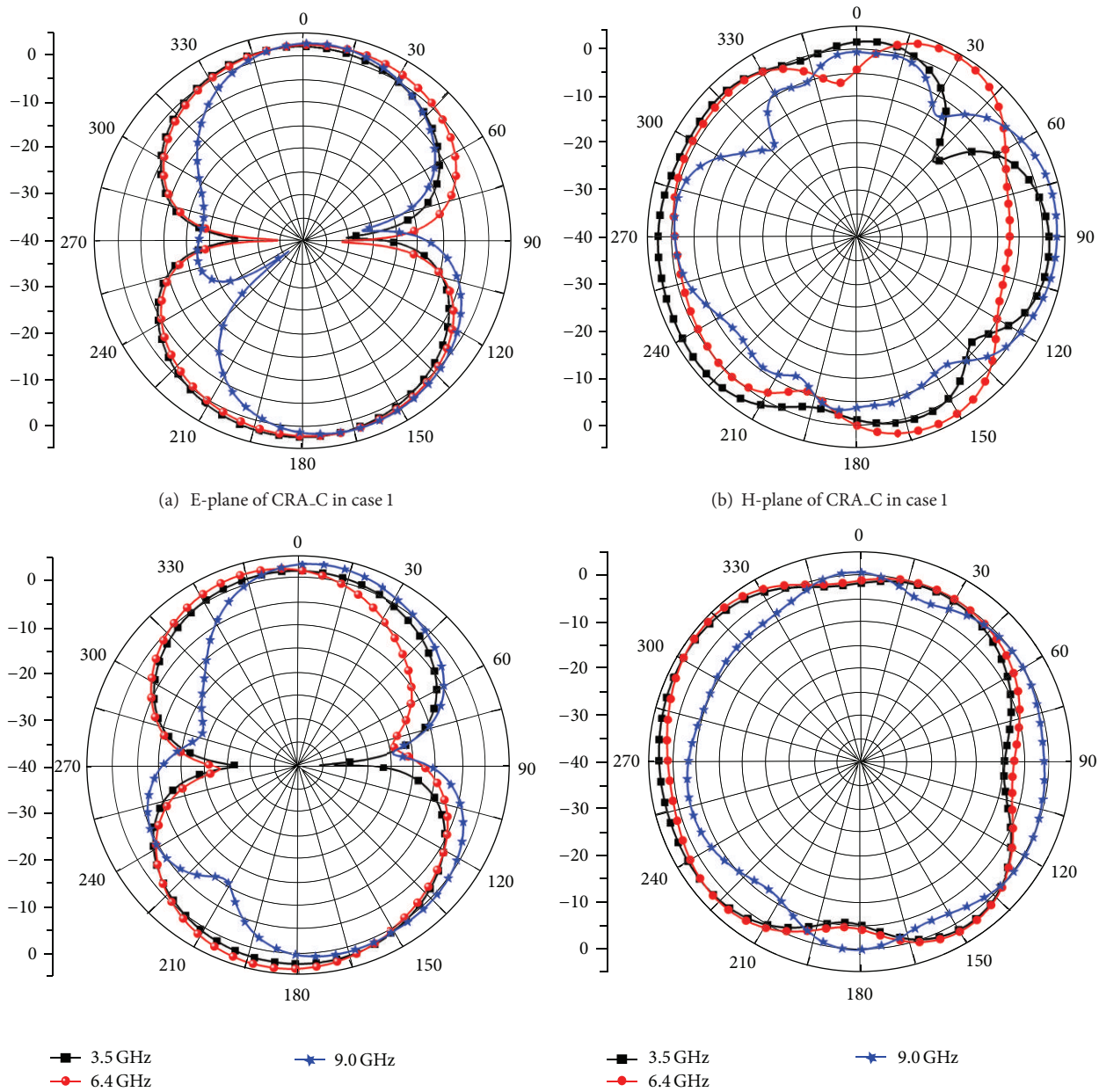

(a) E-plane of CRA_C in case 1

(b) H-plane of CRA_C in case 1

(c) E-plane of CRA_C in case 8

(d) H-plane of CRA_C in case 8

Figure 16: Measured radiation patterns of fabricated CRA_C in case 1 and case 8.

numerically and experimentally. DMS-BSF is analyzed and discussed before CRAs design. The design procedures of proposed CRA_C are illustrated in detail through analyzing CRA_A and CRA_B separately and then combining them together. The reconfigurable functions are obtained using four ideal switches on DMS-BSF and the inverted π-shaped slot. The switchable functions and band-notched characteristics are numerically investigated. By switching ON and OFF status of the four switches, CRA_C can work in eight cases for underlay mode and overlay mode CR applications. CRA_C with all switches ON and OFF is fabricated and measured. However, the ideal switches cannot be adjusted online. In the future, we will investigate the real switches, such as PIN diodes or switch circuit networks. The impedance bandwidth, radiation patterns, and peak gains of the fabricated CRA_Cs are given and discussed. The proposed CRAs can also be used as multiband or multimode antennas. As a result, they can well meet the UWB cognitive radio communication requirement and effectively change the modes to prevent potential interference between secondary users and primary users.

Acknowledgments

This work was supported by a grant from the National Defense "973" Basic Research Development Program of

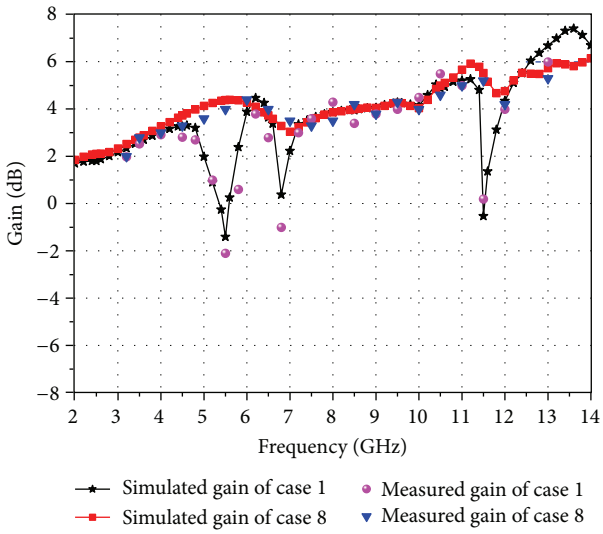

FIGURE 17: Gains of fabricated CRA_C in case 1 and case 8.

China (no. 6131380101). This paper is also supported by the National Nature Science Fund of China (no. 60902014), Nature Science Fund of Heilongjiang (QC2009C66), and the Fundamental Research Funds for the Central Universities (HEUCF1208). The authors are also thankful to Hebei VSTE Science and Technology Co. Ltd. for providing the measurement facility.

References

[1] Federal communications commission, *First report and order, Revision of Part 15 of commission's rule regarding UWB transmission system FCC 02-48*, Washington, DC, USA, 2002.

[2] A. Alipour and H. R. Hassani, "A novel omni-directional UWB monopole antenna," *IEEE Transactions on Antennas and Propagation*, vol. 56, no. 12, pp. 3854–3857, 2008.

[3] M. Kazerooni, A. Cheldavi, and M. Kamarei, "Analysis, modeling, and design of cascaded defected microstrip structure for planar circuits," *International Journal of RF and Microwave Computer-Aided Engineering*, vol. 20, no. 2, pp. 170–181, 2010.

[4] A. M. Abbosh, "Design of a CPW-Fed band-notched UWB antenna using a feeder-embedded slotline resonator," *International Journal of Antennas and Propagation*, vol. 2008, Article ID 564317, 5 pages, 2008.

[5] Y.-S. Li, X.-D. Yang, Q. Yang, and C.-Y. Liu, "Compact coplanar waveguide fed ultra wideband antenna with a notch band characteristic," *International Journal of Electronics and Communications*, vol. 65, no. 11, pp. 961–966, 2011.

[6] Q.-X. Chu and T.-G. Huang, "Compact UWB antenna with sharp band-notched characteristics for lower WLAN band," *Electronics Letters*, vol. 47, no. 15, pp. 838–839, 2011.

[7] M. Moosazadeh, A. M. Abbosh, and Z. Esmati, "Design of compact planar ultrawideband antenna with dual-notched bands using slotted square patch and pi-shaped conductor-backed plane," *IET Microwaves, Antennas and Propagation*, vol. 6, no. 3, pp. 290–294, 2012.

[8] Y. Li, X. Yang, C. Liu, and T. Jiang, "Miniaturization cantor set fractal ultrawideband antenna with a notch band characteristic," *Microwave and Optical Technology Letters*, vol. 54, no. 5, pp. 1227–1230, 2012.

[9] A. Djaiz, M. Nedil, M. A. Habib, and T. A. Denidni, "Design of a new UWB-integrated antenna filter with a rejected WLAN band at 5.8 GHz," *Microwave and Optical Technology Letters*, vol. 53, no. 6, pp. 1298–1302, 2011.

[10] Y. Li, W. Li, and Q. Ye, "Compact reconfigurable UWB antenna integrated with SIRs and switches for multi-mode wireless communications," *IEICE Electronics Express*, vol. 9, no. 7, pp. 629–635, 2012.

[11] R. Eshtiaghi, J. Nourinia, and C. Ghobadi, "Electromagnetically coupled band-notched elliptical monopole antenna for UWB applications," *IEEE Transactions on Antennas and Propagation*, vol. 58, no. 4, pp. 1397–1402, 2010.

[12] A. Nouri and G. R. Dadashzadeh, "A compact UWB band-notched printed monopole antenna with defected ground structure," *IEEE Antennas and Wireless Propagation Letters*, vol. 10, pp. 1178–1181, 2011.

[13] K. S. Ryu and A. A. Kishk, "UWB antenna with single or dual band-notches for lower WLAN band and upper WLAN band," *IEEE Transactions on Antennas and Propagation*, vol. 57, no. 12, pp. 3942–3950, 2009.

[14] R. Zaker, C. Ghobadi, and J. Nourinia, "Novel modified UWB planar monopole antenna with variable frequency band-notch function," *IEEE Antennas and Wireless Propagation Letters*, vol. 7, pp. 112–114, 2008.

[15] J. Xu, D. Y. Shen, G. T. Wang, X. H. Zhang, X. P. Zhang, and K. Wu, "A small UWB antenna with dual band-notched characteristics," *International Journal of Antennas and Propagation*, vol. 2012, Article ID 656858, 7 pages, 2012.

[16] Y. Tawk and C. G. Christodoulou, "A new reconfigurable antenna design for cognitive radio," *IEEE Antennas and Wireless Propagation Letters*, vol. 8, pp. 1378–1381, 2009.

[17] Y. Tawk, J. Costantine, K. Avery, and C. G. Christodoulou, "Implementation of a cognitive radio front-end using rotatable controlled reconfigurable antennas," *IEEE Transactions on Antennas and Propagation*, vol. 59, no. 5, pp. 1773–1778, 2011.

[18] Y. Li, W. Li, and R. Mittra, "A cognitive radio antenna integrated with narrow/ultra-wideband antenna and switches," *IEICE Electronics Express*, vol. 9, no. 15, pp. 1273–1283, 2012.

[19] M. Al-Husseini, A. Ramadan, A. El-Hajj, K. Y. Kabalan, Y. Tawk, and C. G. Christodoulou, "Design based on complementary split-ring resonators of an antenna with controllable band notches for UWB cognitive radio applications," in *Proceedings of the IEEE International Symposium on Antennas and Propagation and USNC/URSI National Radio Science Meeting (APSURSI '11)*, pp. 1120–1122, July 2011.

[20] T. Aboufoul, A. Alomainy, and C. Parini, "Reconfigured and notched tapered slot UWB antenna for cognitive radio applications," *International Journal of Antennas and Propagation*, vol. 2012, Article ID 160219, 8 pages, 2012.

[21] B. Li, J. Hong, and B. Z. Wang, "Switched band-notched UWB/dual-band WLAN slot antenna with inverted S-shapedd slots," *IEEE Antennas and Wireless Propagation Letters*, vol. 11, pp. 572–575, 2012.

[22] M. R. Hamid, P. S. Hall, P. Gardner, and F. Ghanem, "Switched WLAN-wideband tapered slot antenna," *Electronics Letters*, vol. 46, no. 1, pp. 23–24, 2010.

[23] M. Kazerooni, M. A. Salari, and A. Cheldavi, "A novel method for crosstalk reduction in coupled pair microstrip lines," *International Journal of RF and Microwave Computer-Aided Engineering*, vol. 22, no. 2, pp. 167–174, 2012.

[24] S. Zhang, J.-K. Xiao, Z.-H. Wang, and Y. Li, "Novel low pass filters using a defected microstrip structure," *Microwave Journal*, vol. 49, no. 9, pp. 118–128, 2006.

[25] J.-K. Xiao, W.-J. Zhu, and J. S. Fu, "New bandstop filter using simple defected microstrip structure," *Microwave Journal*, vol. 54, no. 9, pp. 134–144, 2011.

[26] M. Kazerooni and O. Abbas, "High isolation dual-frequency patch antenna integrated with cascade defected microstrip structure," *International Journal of RF and Microwave Computer-Aided Engineering*, vol. 21, no. 5, pp. 578–583, 2011.

[27] M. Naser-Moghadasi, M. Alamolhoda, and B. Rahmati, "Spurious-response suppression in microstrip Parallel-Coupled bandpass filters by using Defected Microstrip Structures," *IEICE Electronics Express*, vol. 8, no. 2, pp. 70–75, 2011.

[28] G. Chaudhary, P. Kim, Y. Jeong, J. Lim, and J. Lee, "Analysis and circuit modeling method for defected microstrip structure in planar transmission lines," in *Proceedings of the Asia-Pacific Microwave Conference (APMC '11)*, pp. 999–1002, December 2011.

[29] D. La, Y. Lu, and S. Sun, "Novel bandstop filter using dual-U shape defected microstrip structure," in *Proceedings of the International Symposium on Signals, Systems and Electronics (ISSSE '10)*, pp. 400–402, September 2010.

[30] B. Lembrikov, *Novel Applications of the UWB Technologies*, ch 11, Intech, 2011.

Hindawi Publishing Corporation
International Journal of Antennas and Propagation
Volume 2013, Article ID 270845, 7 pages
http://dx.doi.org/10.1155/2013/270845

Research Article

A Modified Vivaldi Antenna for Improved Angular-Dependent Fidelity Property

Zhi Zeng,[1] Ke Xu,[2] Zhaohui Song,[3] and Qinyu Zhang[1]

[1] *Shenzhen Graduate School, Harbin Institute of Technology, Shenzhen 518055, China*
[2] *Graduate School, Harbin Institute of Technology, Harbin 150001, China*
[3] *Harbin Institute of Technology, Harbin 150001, China*

Correspondence should be addressed to Qinyu Zhang; zqy@hit.edu.cn

Received 23 December 2012; Revised 10 April 2013; Accepted 4 May 2013

Academic Editor: Renato Cicchetti

The analysis, design, and realization of a modified Vivaldi antenna optimized for time domain fidelity factor in the half-space located in the direction of the antenna main beam are presented. The proposed antenna shows improved angular-dependent fidelity property, with respect to the signal transmitted in the main beam direction. A substantial increase in the fidelity factor is achieved by utilizing spatial filter effect introduced by adding two dielectric slabs parallel to the antenna substrate. By choosing optimal dimensions and location of the slabs, the signal waveforms in the mentioned half-space are equalized so as to improve the quality of the radiated signal waveform in the main beam direction. As a result, the fidelity property in the half-space is improved greatly. The simulated and measured fidelity factor in the angular operational region is studied and compared with experimental measurements. The ranges with the fidelity factor better than the value of 0.9 are improved by 95% in H-plane and by 14% in E-plane, respectively.

1. Introduction

Since Federal Communication Commission (FCC) of USA opened up the frequency range 3.1–10.6 GHz for ultrawideband (UWB) communication in 2002, UWB has attracted a lot of attention in the wireless communications field from both academia and industries [1]. UWB system has many advantages, such as high data rate, high spatial resolution, low-cost transceiver, low transmit power, and low interference, which are quite suited to short-range high-rate communication, real-time localization, and see-through-the-wall and ground penetrating radar [2, 3]. There have been lots of investigations about these UWB applications; some of them have already been commercially used.

UWB antenna is one of the key parts in UWB system. A well-designed UWB antenna should have a wide bandwidth, a stable gain pattern that ensures a flat magnitude of the transfer function, and a linear phase response, characteristics useful to minimize the distortion of the transmitted/received pulses [4]. In [5], a nondirective UWB printed antenna for wireless applications, characterized by a low group delay, excellent integration capability with the active/passive components forming the receiver/transmitter front end, and good radiative performances when arranged in arrays, has been presented. In [6], an UWB antenna that rejects extremely sharply the two narrow and closely spaced US WLAN 802.11a bands is presented, while in [7], a compact, low dispersive UWB antenna with sectorial radiation pattern and high front to back ratio has been proposed.

Vivaldi antenna is a kind of tapered slot UWB antenna. The first tapered slot antenna was presented by Lewis et al. in 1974 [8] and named Vivaldi antenna by Gibson in 1979 [9]. Vivaldi antennas are widely used in UWB system for its wide bandwidth, high directivity, low cross-polarization, and easy fabrication. During the past decades, many investigators studied Vivaldi antennas. The miniaturization and the bandwidth performances are key requirements in the design of modern wideband antennas. In this context, Hood presented a compact Vivaldi antenna fabricated with a 39.4×34.6 mm substrate, which operates in the frequency band 3.3–10.6 GHz [10]. In [11], a slot loaded Vivaldi antenna with bandwidth over 25 : 1 is presented. In addition, the pulse

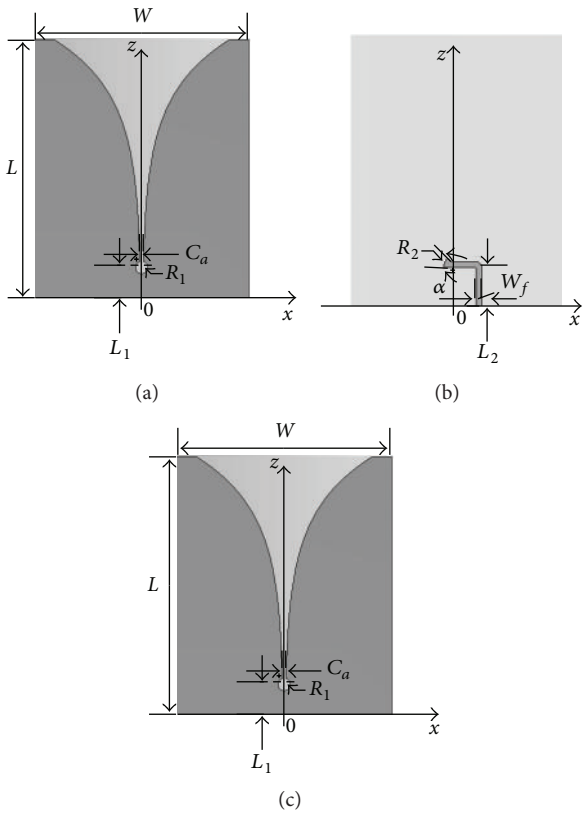

Figure 1: Geometry of the original Vivaldi antenna: (a) top view, (b) central layer (feed), and (c) bottom view.

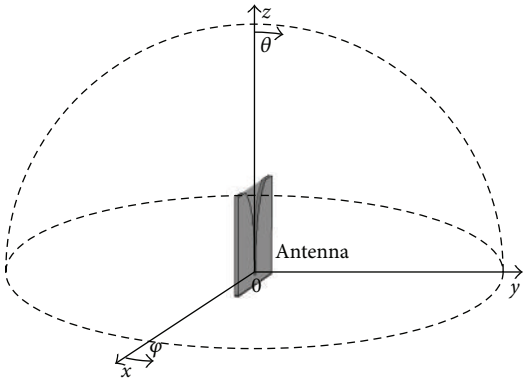

Figure 2: Vivaldi antenna (the reference frame is indicated in the figure).

radiation characteristics are quite important for antennas used in the impulse UWB system. In [12], the authors studied the transient distortion, reflection coefficient, and cross-polarization level of Vivaldi antenna. Vivaldi antenna is quite fitting for UWB antenna array due to its wide bandwidth, high directivity, low cross-polarization, and low profile. In the past decades, especially after the computer is getting powerful enough to analyze antenna arrays, many investigations were carried out to improve the performance of Vivaldi antenna arrays. As of this time, no competing array technology can match the wide bandwidth and wide scanning

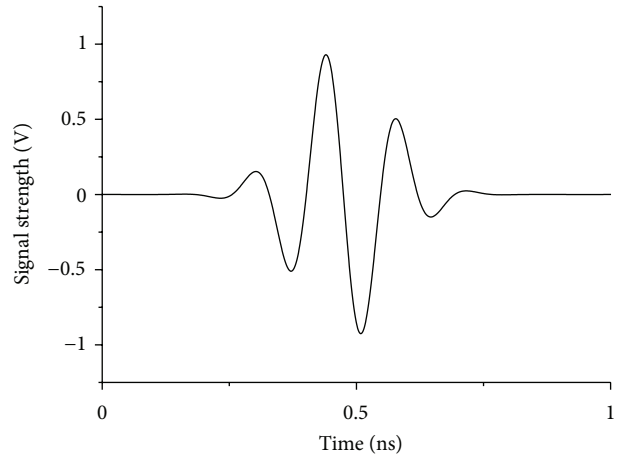

Figure 3: Excitation signal.

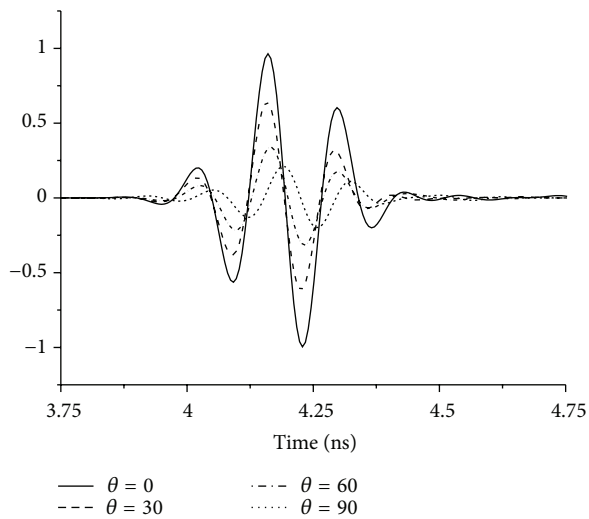

Figure 4: Normalized radiation signal waveform in E-plane ($\varphi = 0^\circ$).

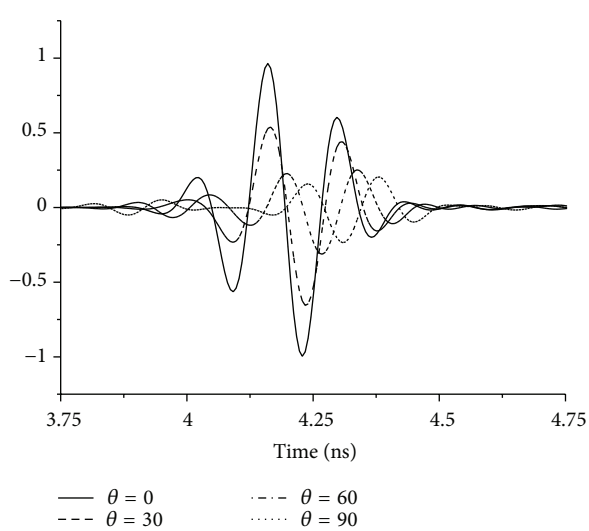

Figure 5: Normalized radiation signal waveform in H-plane ($\varphi = 90^\circ$).

impedance performance of Vivaldi antenna arrays, which are widely used in modern electronic warfare system and radar system [13, 14].

It is quite important for an antenna array element to keep good performance in a wide spatial region while the main beam is scanning. In practice, all the antennas radiate different signals in different spatial directions. So it is quite important to study the correlation between the signal radiated and spatial directions, both in frequency and in time domains. In [15], the angular distortion of the signal radiated with respect to that emitted in the main beam direction of UWB antennas has been investigated. The correlation properties of the pulse signals are determined by the so-called fidelity factor. It can be quantified through the analysis of the correlation between the signal in an arbitrary angular direction and the signal in the main beam direction. Usually, a fidelity factor which is greater than the value of 0.9 could be considered to be acceptable. In [16], Quintero et al. introduced system fidelity factor (SFF) to compare UWB antennas. In [3], the half-spherical fidelity factor pattern measurement results of Bowtie and Vivaldi antenna are presented. The fidelity factor pattern describes how does the signal vary in the different angular directions with respect to the signal in the main beam direction. In [17], Pancera and Wiesbeck introduced an optimization method based on the fidelity factor criterion to improve the radiation properties of Bowtie antennas for medical applications.

In this paper, a method to improve the fidelity factor of Vivaldi antenna in spatial range is presented. The original Vivaldi antenna operates in the frequency band 3.1–10.6 GHz. The modified antenna has two dielectric slabs that are parallel to the antenna substrate. These dielectric slabs are located at a distance d from the upper and bottom faces of the antenna. The dielectric slabs act as a spatial filter to reform the signal waveform. Using the GA algorithm, the parameters of the dielectric slabs have been optimized producing an increment of the fidelity factor in a larger angular range. The simulations of both original antenna and improved antenna are performed using the commercial electromagnetic simulation software CST MWS. The available ranges with the fidelity factor greater than the value of 0.9 in H-plane and in E-plane are improved by 95% and 14%, respectively. The prototypes of both original antenna and improved antenna were fabricated and measured. The numerical results concerning the antenna parameters are found to be in good agreement with the experimental measurements.

2. Improvement of the Vivaldi Antenna Fidelity Factor

2.1. Original Vivaldi Antenna. Vivaldi antenna is one kind of classic end-fired directive travelling wave antennas, which has a tapered slot characterized by a bell-shaped exponential on it. The slot curve on the substrate board becomes wider gradually from the narrow end to the wide end, and it radiates the electromagnetic waves using the corresponding part of the slot as constant electric size at the relevant frequency. So theoretically, Vivaldi antenna has an infinite wide frequency band [5]. In practice, Vivaldi antenna has a band width better than 10 : 1 and has the features of low cross-polarization and highly directive radiation patterns over the whole frequency band. In this paper, a Vivaldi antenna operating in the frequency band 3.1–10.6 GHz is investigated. The antenna is fabricated on a two-layer substrate with dielectric constant of 3.5, size of 85 mm∗70 mm, and each layer thickness of 0.8 mm. The geometry of the original Vivaldi antenna is shown in Figure 1, with the xz-plane and yz-plane referred to as the E-plane and H-plane, respectively. The reference frame adopted to express the field quantities is shown in Figure 2. The tapers of the antennas are defined as

$$x = \pm c_a \cdot \exp\left[c_b\left(y - 10\right)\right]. \quad (1)$$

The values of the antenna geometrical parameters are shown in Table 1.

A commercial Finite Integration Technique (FIT) electromagnetic simulation software CST MWS is used to analyze the radiative performances of the Vivaldi antenna. The antenna is excited by a UWB signal in the frequency band 3.1–10.6 GHz, which is a Gaussian pulse in the frequency band 0–3.75 GHz modulated by a cosine wave carrier at the frequency

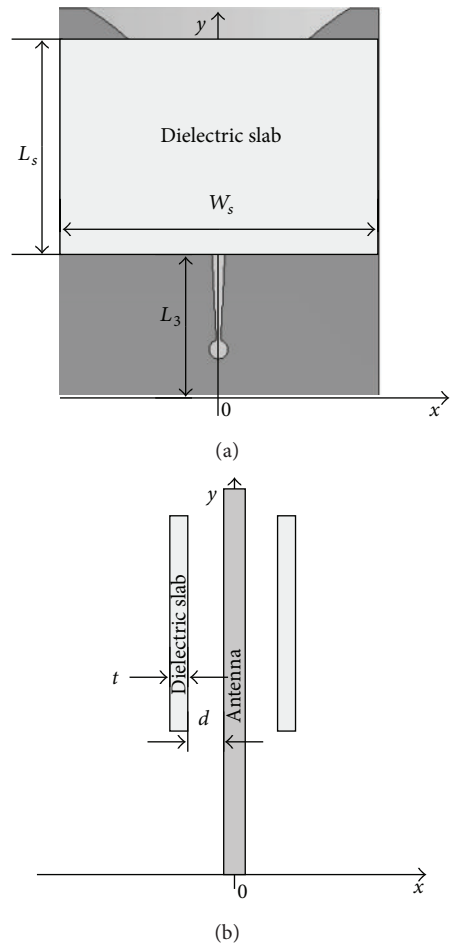

Figure 6: Geometry of the improved Vivaldi antenna: (a) top view and (b) lateral view.

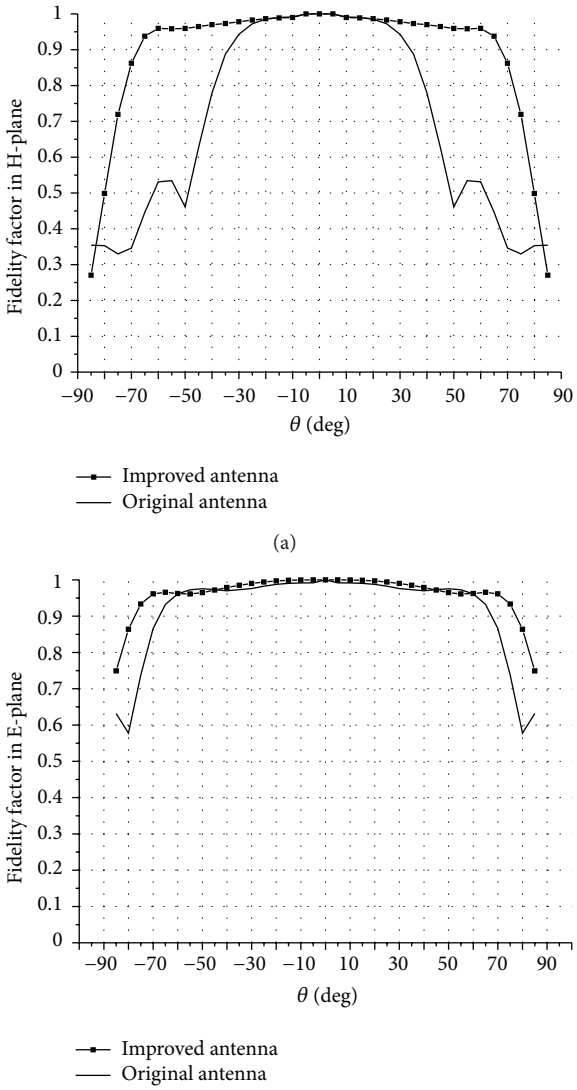

Figure 7: (a) Simulation results of fidelity factor in H-plane ($\varphi = 90^\circ$) and (b) simulation results of fidelity factor in E-plane ($\varphi = 0^\circ$).

6.85 GHz. The waveform of excitation signal is shown in Figure 3. A set of probes have been placed at a distance of 1000 mm from the antenna on a plane around the antenna and spaced by 5 degrees to detect the time-domain signal radiated by the antenna. Since the Vivaldi antenna has quite good cross-polar property, only the copolar radiation signals are considered. The normalized signal waveforms at the main beam direction and other directions computed in the E- and H-planes are shown in Figures 4 and 5, respectively.

The fidelity factor between the signal at the main beam direction $S_1(t)$ and the signal in an arbitrary angular direction $S_2(t)$ is defined as the normalized cross-correlation between them and can be calculated by [3]

$$\text{fidelity} = \max_{\tau} \frac{\int_{-\infty}^{+\infty} S_1(t-\tau)\, S_2(t)\, dt}{\sqrt{\int_{-\infty}^{+\infty} \|S_1(t)\|^2 dt \int_{-\infty}^{+\infty} \|S_1(t)\|^2 dt}}. \quad (2)$$

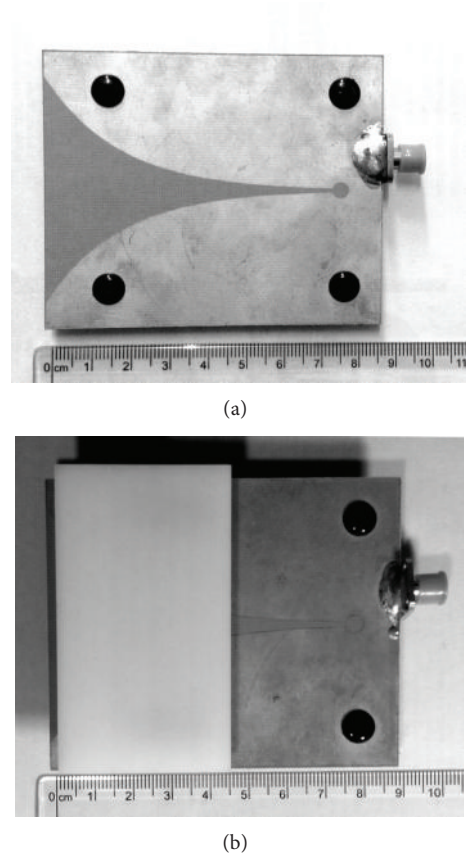

Figure 8: (a) Picture of the original antenna and (b) picture of the improved antenna.

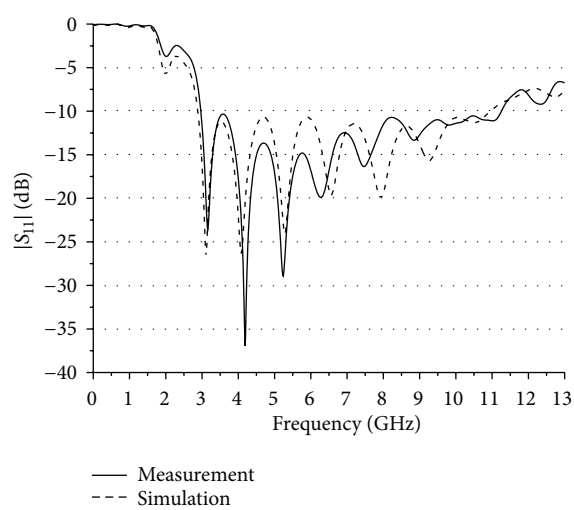

Figure 9: $|S_{11}|$ of improved antenna.

The fidelity factor results computed in E- and H-planes are listed in Table 2.

From Table 2, it appears that the fidelity factor in H-plane degrades quickly as the angle between the antenna's main beam and the observation point is larger than 35 degrees.

Table 1: Geometrical parameters of the original Vivaldi antenna.

Parameter	Value	Unit
W	70	mm
L	85	mm
L_1	10	mm
L_2	12.25	mm
W_f	0.85	mm
R_1	2.07	mm
R_2	3.3	mm
α	46	°
C_a	0.4440	
C_b	0.0559	

Table 2: Computed fidelity factor of the original antenna in H-plane and E-plane.

H-plane ($\varphi = 90$)		E-plane ($\varphi = 0$)	
θ (degree)	Fidelity factor	θ (degree)	Fidelity factor
0	1	0	1
5	0.99998	5	0.99182
10	0.99157	10	0.99154
15	0.99012	15	0.99040
20	0.98533	20	0.98758
25	0.97260	25	0.98263
30	0.94303	30	0.97626
35	0.88816	35	0.97320
40	0.77987	40	0.97004
45	0.62700	45	0.97318
50	0.46141	50	0.97558
55	0.53453	55	0.97288
60	0.53101	60	0.96154
65	0.44638	65	0.93226
70	0.34619	70	0.86615
75	0.33003	75	0.73830
80	0.35294	80	0.57766
85	0.35444	85	0.63184

And this distortion will cause poor performance degradation while the beam is scanning out of this range.

To improve the signal fidelity factor in a larger angular region, two dielectric slabs with relative dielectric constant ε_r and thickness t, which parallel the antenna substrate, are added to the original Vivaldi antenna. The distance between the slabs and antenna substrate is d. The structure of the proposed antenna is shown in Figure 6.

The dielectric slabs play a role as a spatial filter, which have the angular-dependant effect on the incident wave. So, by proper tuning of ε_r, t, and d, the quality of the radiated wave can be restored. This effect can be used to optimize the antenna fidelity factor in the angular operational region. Besides the parameters above, the length of the slabs L_s and the position of the slabs along the y-axis L_3 also can be considered as optimization parameters because they decide the angular range covered by the slabs.

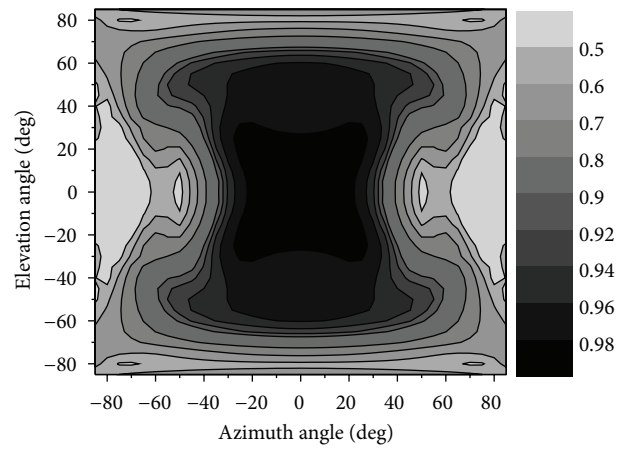

(a)

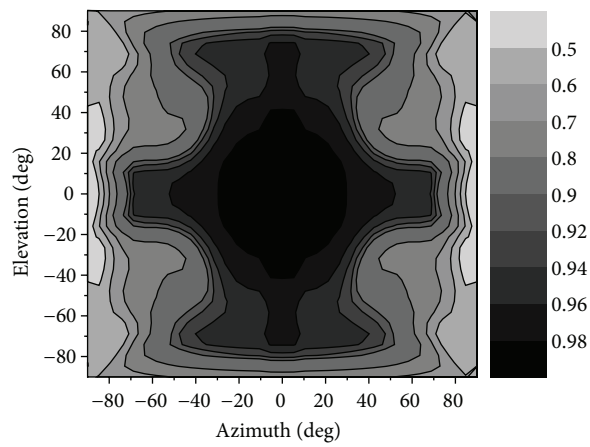

(b)

Figure 10: (a) Fidelity factor test results of the original antenna and (b) fidelity factor test results of the improved antenna.

3. Antenna Simulation and Measurement

The polyformaldehyde, having a relative dielectric constant $\varepsilon_r = 3.8$, is chosen for the realization of the two dielectric slabs thanks to its intrinsic characteristics, consisting in the easy machining and good temperature characteristics. The structure of the Vivaldi antenna is optimized with the goal of the better fidelity factor in H-plane and in E-plane using Genetic Algorithms optimizer in CST MWS. The criterion of the fidelity factor is set to 0.9. The optimal parameters of the dielectric slabs are listed in Table 3.

The fidelity factor of improved antenna computed in E-plane and H-plane is listed in Table 4 and compared with the results of the original antenna as shown in Figure 7.

The fidelity factor in H-plane has been improved significantly. The available range of the original antenna in H-plane is 70 degrees, and the improved antenna has an available range wider than 135 degrees, which has been improved by about 97%. Besides that, the available range in E-plane has been improved from 136 degrees to 156 degrees, which is not such remarkable as that in H-plane.

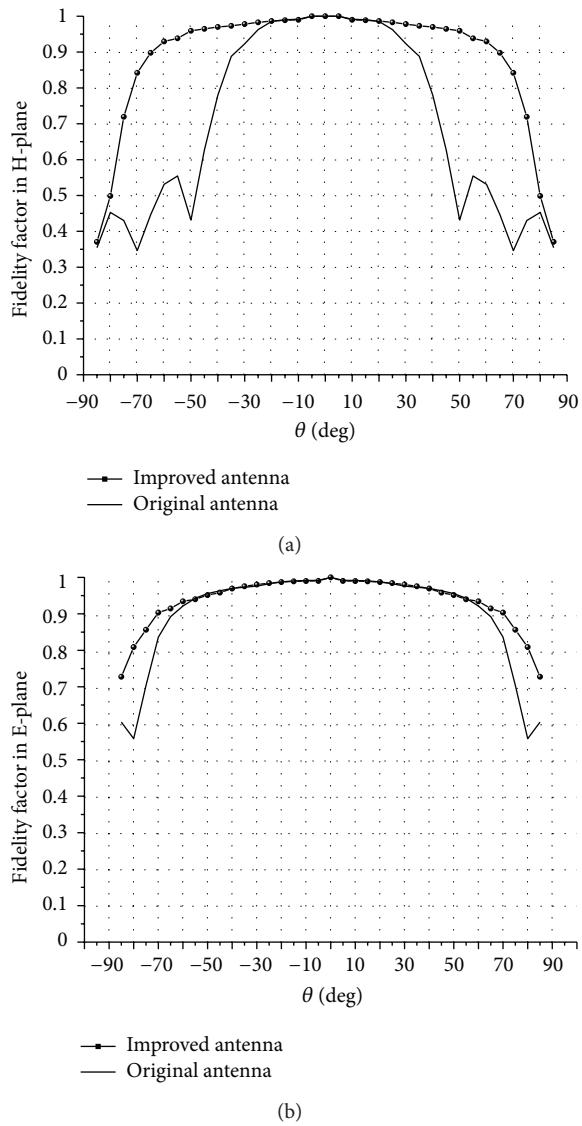

Figure 11: (a) Measurement results of fidelity factor in H-plane and (b) measurement results of fidelity factor in E-plane.

Table 3: The geometrical parameters of the dielectric slabs.

Parameter	Value	Unit
t	4.4	mm
W_s	40	mm
L_3	43	mm
d	9.15	mm
L_s	70	mm

The prototypes of the two considered antennas are shown in Figure 8, while the numerical and measurement results concerning the frequency behavior of the parameter $|S_{11}|$ of the new antenna are reported in Figure 9.

The measurement of fidelity factor was carried out in an enclosed anechoic chamber. The measured antenna is installed on a rotating platform. A wideband probe is used to receive the transient signal radiated by the antenna under test when changing the azimuth and the elevation angle of the antenna. The fidelity factors, calculated in the upper half-plane are plotted in Figure 10. The measurement results of the fidelity factor in E-plane and H-plane are shown in Figure 11.

Table 4: Fidelity factor of the improved antenna computed in E-plane and H-plane.

H-plane ($\varphi = 90$)		E-plane ($\varphi = 0$)	
θ (degree)	Fidelity factor	θ (degree)	Fidelity factor
0	1	0	1
5	0.99995	5	0.99995
10	0.98976	10	0.99973
15	0.98881	15	0.99888
20	0.98655	20	0.99709
25	0.98285	25	0.99421
30	0.97808	30	0.99023
35	0.97300	35	0.98521
40	0.97008	40	0.97907
45	0.96478	45	0.97186
50	0.95924	50	0.96504
55	0.95839	55	0.96137
60	0.95966	60	0.96244
65	0.93783	65	0.96566
70	0.86216	70	0.96156
75	0.71946	75	0.93351
80	0.49866	80	0.86404
85	0.27054	85	0.74927

The original Vivaldi antenna shows its good fidelity factor characteristics in a side-ways H-shape area with azimuth angle scanning less than 35 degrees in H-plane and elevation angle less than 65 degrees in E-plane, respectively. The improved Vivaldi antenna shows its good fidelity factor characteristics in a cross-shape area with azimuth angle scanning better than 65 degrees in H-plane and elevation angle better than 70 degrees in E-plane, respectively, which is extended in horizontal direction significantly.

4. Conclusion

In this paper, a new method to improve the fidelity factor of a planar Vivaldi UWB antenna has been proposed. Two dielectric slabs, which play the role of a spatial filter suitable to restore the signal waveform in time domain, are added to the original Vivaldi antenna. By tuning the dimensions and the relative position of the dielectric slabs, the fidelity factor in the half space is optimized. The angular available range in H-plane with the fidelity factor greater than the value of 0.9 has been improved by 95% and the available angular range in E-plane has been improved by 14%.

Acknowledgments

The authors would like to express their sincere gratitude to CST Ltd., Germany, for providing a free package of CST MWS

software. This work was supported in part by the key program of the National Natural Science Foundation of China under Grant 61032003 and the National Basic Research Program of China under Grant 2009CB320402.

References

[1] Y. Q. Zhang, Y. X. Guo, and M. S. Leong, "A novel multilayer UWB antenna on LTCC," *IEEE Transactions on Antennas and Propagation*, vol. 58, no. 9, pp. 3013–3019, 2010.

[2] T. A. Vu, M. Z. Dooghabadi, S. Sudalaiyandi et al., "UWB Vivaldi antenna for impulse radio beamforming," in *Proceedings of the 27th Norchip Conference*, pp. 1–5, Trondeim, Norway, November 2009.

[3] E. Pancera, T. Zwick, and W. Wiesbeck, "Spherical fidelity patterns of UWB antennas," *IEEE Transactions on Antennas and Propagation*, vol. 59, no. 6, pp. 2111–2119, 2011.

[4] F. Gross, *Frontiers in Antennas: Next Generation Design & Engineering*, McGraw-Hill, 2011.

[5] G. Cappelletti, D. Caratelli, R. Cicchetti, and M. Simeoni, "A low profile printed drop-shaped dipole antenna for wide-band wireless applications," *IEEE Transactions on Antennas and Propagation*, vol. 59, no. 10, pp. 3526–3535, 2011.

[6] A. A. Gheethan and D. E. Anagnostou, "Dual band-reject UWB antenna with sharp rejection of narrow and closely-spaced bands," *IEEE Transactions on Antennas and Propagation*, vol. 60, no. 4, pp. 2071–2076, 2012.

[7] L. Desrumaux, A. Godard, M. Lalande, V. Bertrand, J. Andrieu, and B. Jecko, "An original antenna for transient high power UWB arrays: the Shark antenna," *IEEE Transactions on Antennas and Propagation*, vol. 58, no. 8, pp. 2515–2522, 2010.

[8] L. R. Lewis, M. Fassett, and J. Hunt, "A broadband stripline array element," in *Proceedings of the IEEE Antennas and Propagation Symposium Digest*, pp. 335–337, Atlanta, Ga, USA, 1974.

[9] Y. Li and A. Chen, "Design and application of Vivaldi antenna array," in *Proceedings of the 8th International Symposium on Antennas, Propagation and EM Theory (ISAPE '08)*, pp. 267–270, Kunming, China, November 2008.

[10] A. Z. Hood, T. Karacolak, and E. Topsakal, "A small antipodal vivaldi antenna for ultrawide-band applications," *IEEE Antennas and Wireless Propagation Letters*, vol. 7, pp. 656–660, 2008.

[11] J. Bai, S. Shi, and D. W. Prather, "Ultra-wideband slot-loaded antipodal Vivaldi antenna array," in *Proceedings of the IEEE International Symposium on Antennas and Propagation (APSURSI '11)*, pp. 79–81, Spokane, Wash, USA, 2011.

[12] J. Zhang, J. Wang, and W. Hu, "Analysis of UWB signal distortion in transmitting/receiving antenna systems," in *Proceedings of the 9th International Symposium on Antennas Propagation and EM Theory (ISAPE '10)*, pp. 163–166, Guangzhou, China, December 2010.

[13] K. Trott, B. Cummings, R. Cavener, M. Deluca, J. Biondi, and T. Sikina, "Wideband phased array radiator," in *Proceedings of the IEEE International Symposium on Phased Array Systems & Technology*, pp. 383–386, Boston, Mass, USA, October 2003.

[14] D. Carsenat and C. Decroze, "UWB antennas beamforming using passive time-reversal device," *IEEE Antennas and Wireless Propagation Letters*, vol. 11, pp. 779–782, 2012.

[15] M. A. Elmansouri and D. S. Filipovic, "Pulse distortion and mitigation thereof in spiral antenna-based UWB communication systems," *IEEE Antennas and Wireless Propagation Letters*, vol. 59, no. 10, pp. 3863–3871, 2011.

[16] G. Quintero, J. F. Zurcher, and A. K. Skrivervik, "System fidelity factor: a new method for comparing UWB antennas," *IEEE Transactions on Antennas and Propagation*, vol. 59, no. 7, pp. 2502–2512, 2011.

[17] E. Pancera and W. Wiesbeck, "Fidelity based optimization of UWB antenna-radiation for medical applications," in *Proceedings of the IEEE International Symposium on Antennas and Propagation (APSURSI '11)*, p. 2411, Spokane, Wash, USA, July 2011.

Hindawi Publishing Corporation
International Journal of Antennas and Propagation
Volume 2013, Article ID 941924, 9 pages
http://dx.doi.org/10.1155/2013/941924

Review Article

Dual-Band Integrated Antennas for DVB-T Receivers

Andrea D'alessandro,[1] Roberto Caso,[1] Marcos R. Pino,[2] and Paolo Nepa[1]

[1] *Department of Information Engineering, University of Pisa, I-56122 Pisa, Italy*
[2] *Department of Electrical Engineering, University of Oviedo, 3203 Gijón, Spain*

Correspondence should be addressed to Roberto Caso; roberto.caso@iet.unipi.it

Received 6 December 2012; Accepted 30 March 2013

Academic Editor: Renato Cicchetti

An overview on compact Planar Inverted-F Antennas (PIFAs) that are suitable for monitor-equipped devices is presented. In particular, high efficiency PIFAs (without any dielectric layer) with a percentage bandwidth (%BW) greater than 59% (470–862 MHz DVB-T band) are considered. In this context, two PIFA configurations are reviewed, where a dual-band feature has been obtained, in the 3300–3800 MHz (14% percentage bandwidth) WiMAX and 2400–2484 MHz (2.7% percentage bandwidth) WLAN IEEE 802.11b,g frequency bands, respectively, to also guarantee web access to on-demand services. The two PIFAs fill an overall volume of $225 \times 31 \times 20\,\text{mm}^3$ and $207 \times 12 \times 8\,\text{mm}^3$, respectively. They are composed of a series of branches, properly dimensioned and separated to generate the required resonances. Finally, to show the extreme flexibility of the previous two configurations, a novel dual-band L-shape PIFA has been designed. A reflection coefficient less than −6 dB and −10 dB and an antenna gain of around 2 dBi and 6.3 dBi have been obtained in the 470–862 MHz DVB-T band and the 2400–2484 MHz WLAN band, respectively. The L-shape PIFA prototype can be obtained by properly cutting and folding a single metal sheet, thus resulting in a relatively low-cost and mechanically robust antenna configuration.

1. Introduction

Many countries already switched their terrestrial television broadcasting from analog to Digital Video Broadcasting-Terrestrial (DVB-T) [1]; besides, the demand for digital television reception is increasing also for mobile terminals, such as smart phones and notebooks, which include web access through Wireless Local Area Networks (WLANs) as well. Due to the severe space limitations of typical monitor-equipped devices, dual-band compact integrated antennas for DVB-T and WLAN applications are more attractive than a couple of distinct single-band antennas. Several wide-band antennas suitable for DVB-T applications (percentage bandwidth greater than 59%) have been recently presented [2–16]. Among them, PIFAs are those more suitable for integration into multifunctions devices with a high density of electronic circuits; indeed, their own ground plane acts as an electromagnetic shield and the 3D structure helps in enlarging impedance bandwidth. Also, multiple frequency bands can be achieved by adding more resonating paths [17]. A linear-shape PIFA working in the DVB-T and WIMAX frequency bands has been presented in [18]. Moreover, an alternative layout for a dual-band linear-shape PIFA has been more recently proposed in [19], for an antenna operating in the DVB-T and WLAN frequency bands. Since the PIFAs in [18, 19] cannot be made shorter than 20 cm, while still getting an acceptable input impedance matching at the DVB-T frequency band, some other layout modifications are needed for integration into those devices with a length of the monitor sides not greater than 13–15 cm, or when part of the space along the monitor border is occupied by a webcam or a microphone. In such cases, a possible modification of the antenna layout with respect to that in [18, 19] is based on conforming the antenna to the shape of one of the device corners (a few preliminary simulation results were presented in [20]). In this paper, both numerical simulations and experimental results for an L-shape PIFA layout derived from that in [19] are presented, to show that the modified layout can be a valuable solution for monitor-equipped devices with an extent smaller than 15 cm × 15 cm. Simulation results have been derived by using CST Microwave Studio commercial tool.

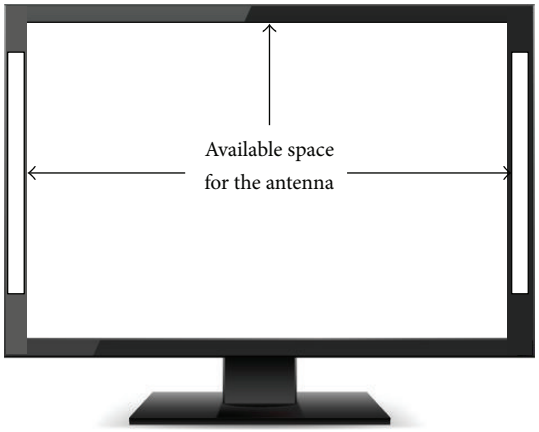

Figure 1: Example of a typical monitor chassis; the available space for the antenna is highlighted in a light color.

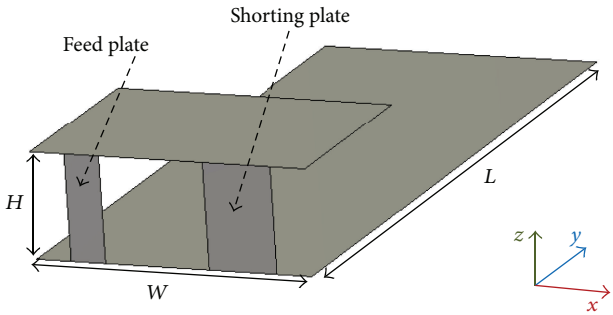

Figure 2: A PIFA where bandwidth enlargement can be achieved by optimizing the widths of the feeding and shorting plates [12].

2. Overview on Wideband and High Efficiency Compact Planar Inverted-F Antennas

In Figure 1, a typical TV chassis is shown, where possible spaces available to locate an antenna are also highlighted. A number of DTV wideband antennas have been recently presented [2–11], which are mainly low-cost, low-profile, and easy-fabrication printed monopoles and patch-alike antennas. Printed monopoles require a careful positioning inside devices with high circuitry density, as they are quite sensitive to the presence of nearby metal parts. On the other hand, patch-alike antennas and PIFAs are suitable for integration because their ground plane also acts as a shield.

In this section, a review of some high efficiency (without any dielectric layer) PIFAs will be presented. In particular, antennas with a percentage bandwidth greater than 59% (i.e., the DVB-T %BW) have been taken into account. These antennas are suitable to be integrated into devices, such as a monitor or a TV chassis, where relatively large volumes are often available along their borders.

In [12], a PIFA with a percentage bandwidth of 65% and operating in the 1.6–3 GHz band for mobile applications (GSM, PCS, DCS, UMTS, WLAN, WiMax, and Bluetooth) has been presented. A so large impedance bandwidth can be

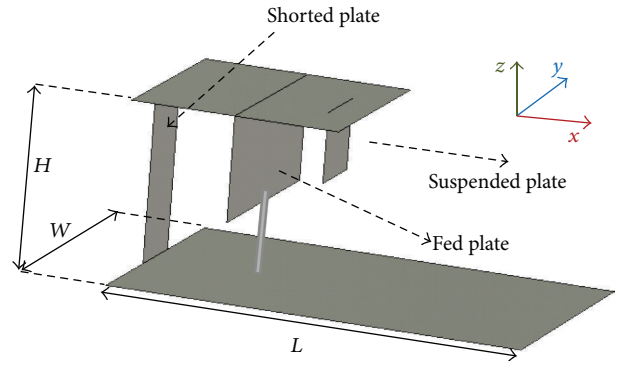

Figure 3: A PIFA consisting of a planar rectangular monopole top-loaded with a rectangular patch attached to two rectangular plates, one is shorted to the ground and the other is suspended [13].

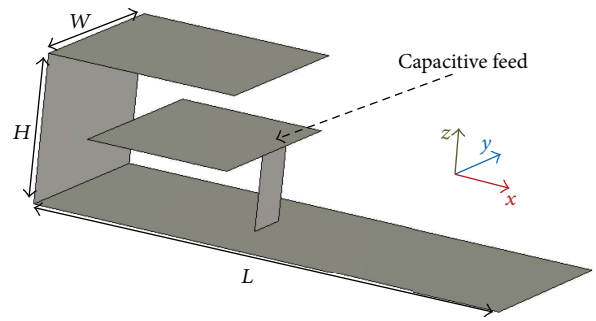

Figure 4: A PIFA where a large impedance bandwidth has been obtained by using a capacitive feeding [14].

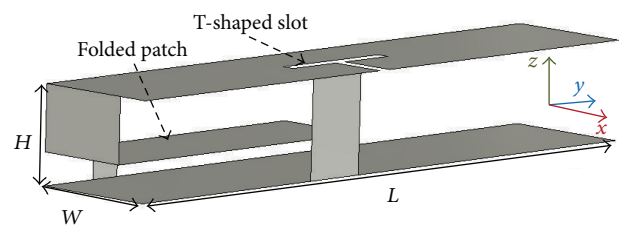

Figure 5: The inclusion of a T-shaped slot as well as a folded patch results in a wide impedance bandwidth in the PIFA presented in [15].

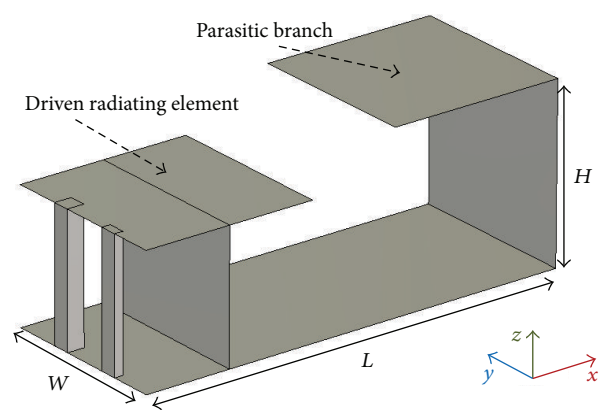

Figure 6: A PIFA characterized by a driven (fed) radiating element separated by a small gap from a parasitic branch [16].

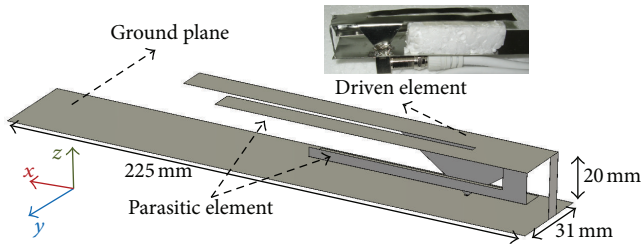

Figure 7: *Conf. A*: 3D view.

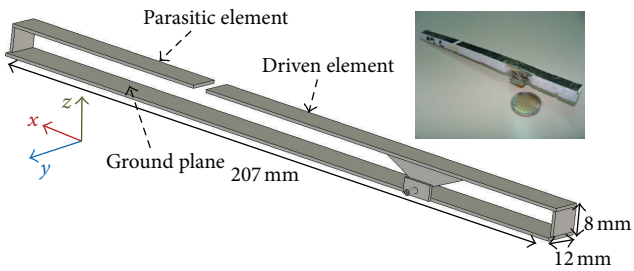

Figure 8: *Conf. B*: 3D view.

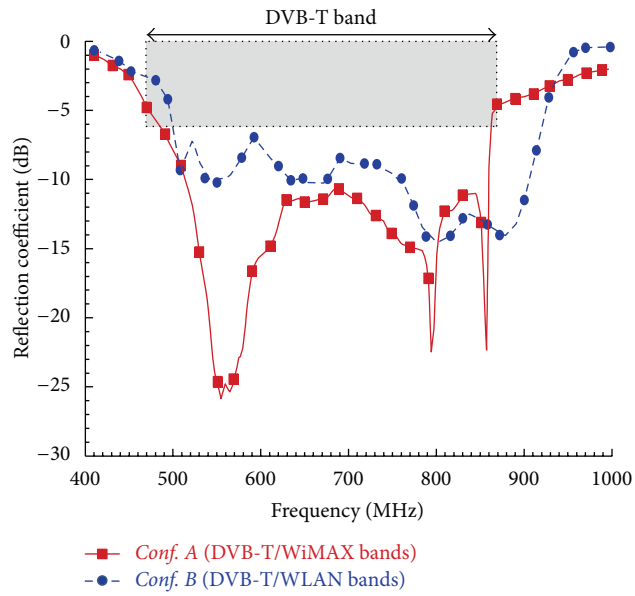

Figure 9: Measured reflection coefficient for the two PIFAs in [16, 18], in the DVB-T band.

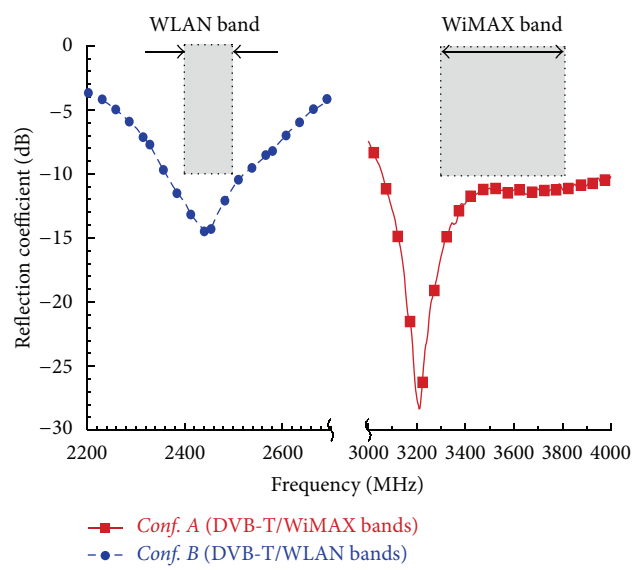

Figure 10: Measured reflection coefficient for the two PIFAs in [16, 18], in the WiMAX and WLAN bands, respectively.

achieved by optimizing the widths of the feeding and shorting plates (Figure 2).

In [13], a PIFA configuration has been presented (Figure 3) which is made of a planar rectangular monopole top-loaded with a rectangular patch attached to two rectangular plates, one shorted to the ground and the other suspended. The fabricated antenna prototype has a measured impedance bandwidth of 125% (reflection coefficient lower than −10 dB in the 3–13 GHz band). The radiator size is $20 \times 10 \times 7.5\ \text{mm}^3$, making the antenna electrically small over most of the band and suitable for integration in mobile devices.

In [14], a capacitive feed is used to improve impedance characteristics (Figure 4). By changing three parameters (the area of the feed plate, the separation from the radiating top plate, and probe placement on the feed plate), antenna resonances can be controlled. The proposed design exhibits an impedance bandwidth ranging from 1.18 GHz to 2.24 GHz (61.92%).

In [15], a modified PIFA (Figure 5) with a compact size of 34 mm × 8.0 mm × 8.0 mm has been proposed. The uniqueness of this design is the inclusion of both a T-shaped slot and a folded patch. The compact PIFA has a very wide 77% 10-dB impedance bandwidth (a larger bandwidth up to 81.3% has been measured on the prototype).

A UWB PIFA for the 2.4–6.2 GHz band (88.4% relative bandwidth), which is characterized by a driven (fed) radiating element separated by a small gap from a parasitic branch (Figure 6), has been presented in [16].

Starting from the previous configurations, two high efficiency PIFAs have been presented in [18–20] for DVB-T band. A dual band functionality has been obtained by adding a new path in the antenna layout [18] or by using the small gap between the feed element and the parasitic one [19, 20].

Figure 7 shows the layout, the antenna prototype, and the main parameters of the PIFA proposed in [18] (named as *Conf. A* as shown in Figure 7).

Conf. A antenna (Figure 7) is composed of a series of branches, properly dimensioned and separated to generate the required resonances. The antenna exhibits a multiband functionality between 470 MHz and 862 MHz (59% percentage bandwidth) and between 3300 MHz and 3800 MHz (14% percentage bandwidth) for DVB-T and WiMAX applications, respectively. The final layout resulted from an optimization process focused to reduce the overall antenna dimensions as much as possible. The prototypes were fabricated with

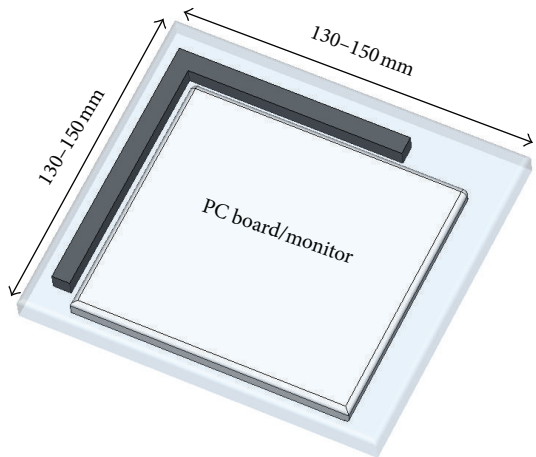

Figure 11: Example of a 3D view of a typical monitor chassis. The available space for the antenna is dark highlighted.

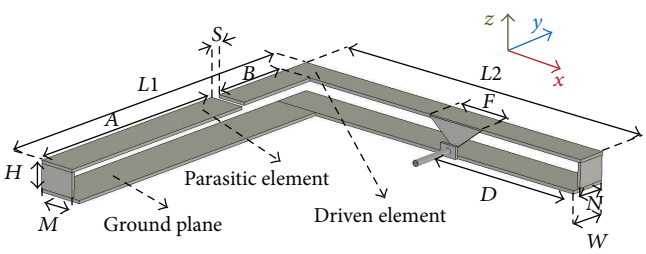

Figure 12: Geometry of the proposed dual-band L-shape PIFA.

a 0.4 mm thick aluminum foil, properly cut and folded. This simplifies the antenna fabrication and avoids any soldering, except for that at the antenna connector.

The extent of the antenna proposed in [16] was also reduced in terms of wavelength in [19, 20], for the DVB-T and WLANs bands (named as *Conf. B* as shown in Figure 8).

The driven PIFA element acts as the primary element, governing the lowest resonant frequency, while the upper resonant frequency close to the DVB-T band is controlled by the parasitic element. Moreover, the separating gap helps in controlling a third resonance around 2.45 GHz in the IEEE 802.11b,g band for WLANs. Thus, as an improvement of the solution in [16], the proposed PIFA exhibits a dual band functionality. Moreover, if compared with [16], a significant reduction of 63% and 87% was achieved for the electrical thickness (H) and width (W), respectively (the electrical size is referred to the wavelength at the DVB-T band center frequency, where $\lambda = 448$ mm) at the cost of only 9% length (L) increase.

The 50 Ω-impedance matching was met for the two configurations (*Conf. A* and *Conf. B*) by optimizing the feeding plate shapes (the triangular plates connecting the feeding cables to the radiating elements in Figures 7 and 8) and the position of the shorting strip. The two PIFAs occupy an overall volume of $225 \times 31 \times 20$ mm^3 and $207 \times 12 \times 8$ mm^3, respectively. These radiating elements are relatively large with respect to antennas printed or mounted on high permittivity

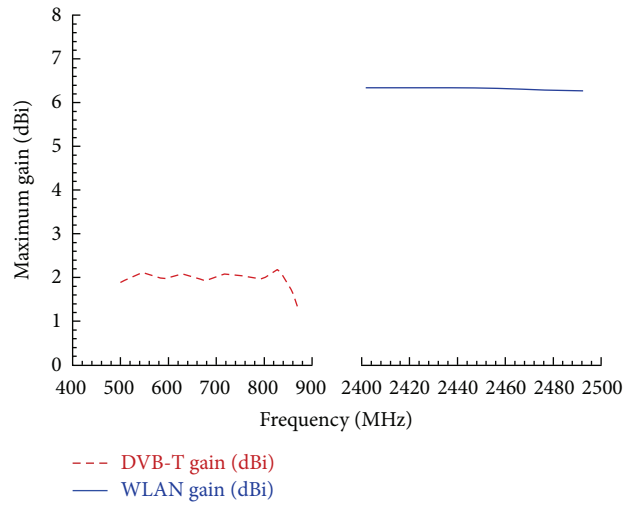

Figure 13: Simulated gain for the proposed dual-band L-shape PIFA as a function of frequency.

substrates, but, at the same time, they can guarantee higher gains and radiation efficiencies.

As shown in Figures 9 and 10, the measured reflection coefficients for *Conf. A* and *Conf. B* PIFAs are below −6 dB in the whole DVB-T band for both configurations and less than −10 dB in the WiMAX and IEEE 802.11b,g bands, respectively. The previous values are typical thresholds for integrated antennas for such communication standards.

The resonances in the DVB-T band for the two antenna configurations are mainly due to the plates of length L and the branches of length A and B. The PIFA height H is a critical parameter for obtaining the antenna impedance matching. For the *Conf. A* antenna, gain lies between 2.8 and 3.3 dBi in the lower band and between 3.2 dBi and 4.0 dBi in the WiMAX band.

The gain for the *Conf. B* is between 2.4 dBi and 3.3 dBi in the DVB-T band and between 4.4 dBi and 4.8 dBi in the WLAN band. The relatively high values obtained for the gain are due to the absence of a lossy dielectric under the radiating plate. A further analysis consisted in measuring the reflection coefficient variations when a metallic obstacle is located close to the antenna [19]. In particular, a large metallic plate (300 mm × 400 mm) was positioned in the vicinity of the antenna, at distances of 1 cm, 2 cm, and 3 cm. The numerical results demonstrated that the reflection coefficient variations are minimal. The robustness of the solution in terms of reflection coefficient variations with respect to the presence of near metal parts has been analyzed and checked through measurements too.

3. A Novel Dual-Band L-Shape Planar Inverted-F Antenna (PIFA)

Starting from the dual-band linear-shape PIFA described in [19], a modified layout suitable to be integrated along the corner of a compact monitor-equipped device (as shown in Figure 11) is here presented.

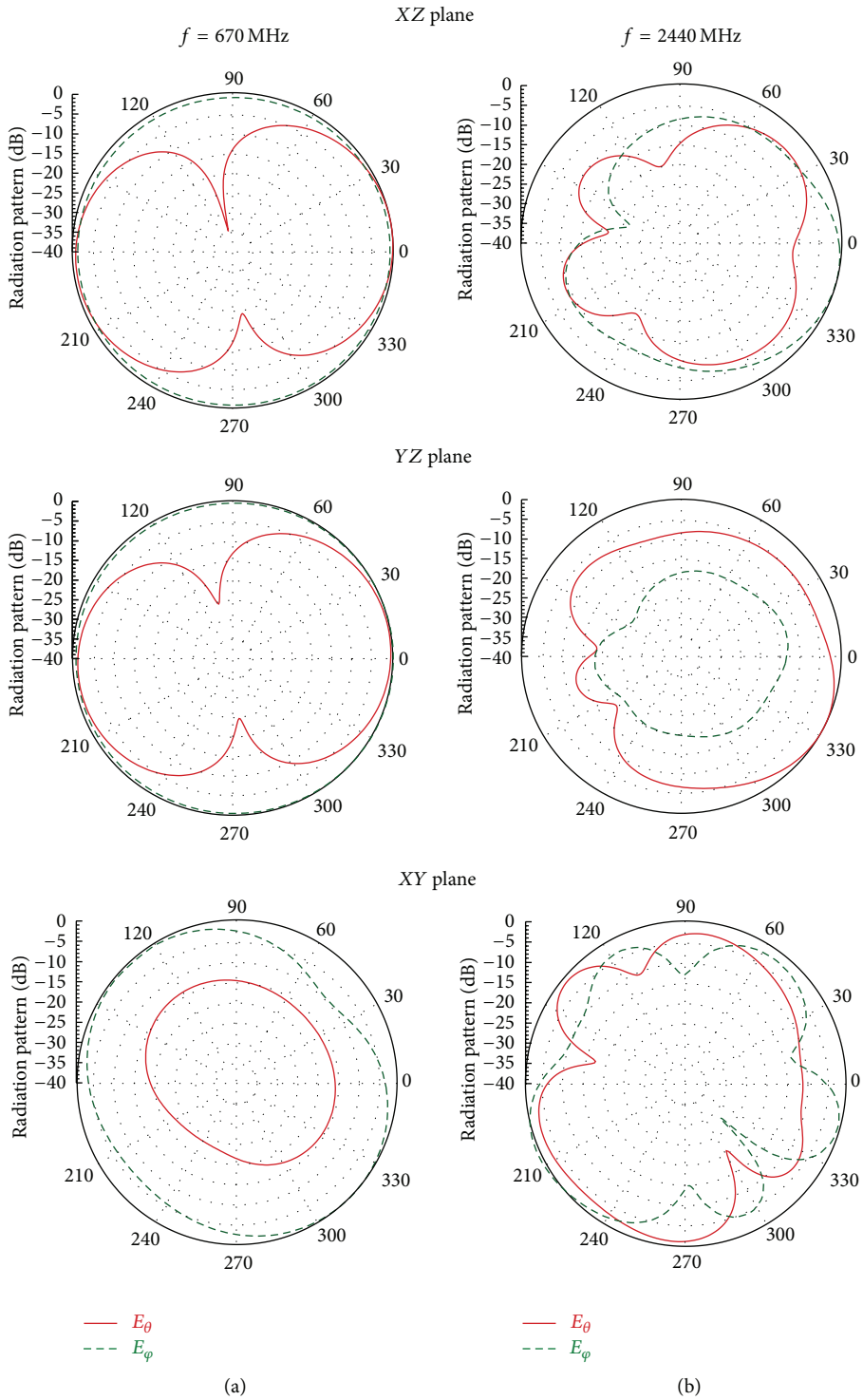

Figure 14: Simulated radiation patterns (E_θ and E_φ components normalized to the electric field amplitude at $\theta = 0$) for the proposed dual-band L-shape PIFA: (a) 670 MHz (central frequency for the DVB-T band); (b) 2440 MHz (central frequency for the IEEE 802.11b,g band).

In [18–20], it has been verified that the total length L of a linear PIFA is a key parameter to achieve impedance matching at DVB-T band, and it should be greater than 20 cm to get satisfactory VSWR performance in the whole DVB-T frequency range.

It is worth noting that the new L-shape antenna configuration cannot be obtained by simply bending the antenna in [19], since all the basic antenna geometrical parameters need to be modified to optimize antenna performance (Figure 12).

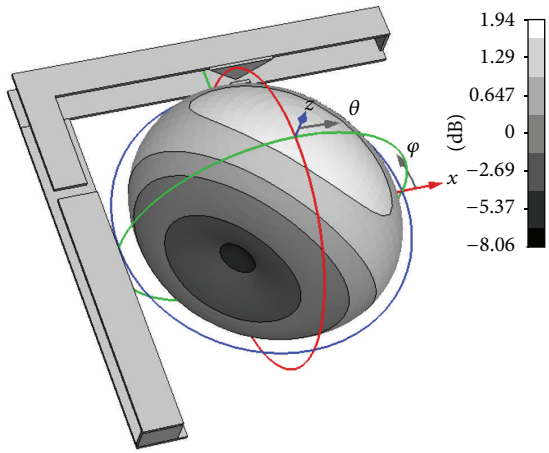

Figure 15: Simulated 3D antenna gain (dBi) for the dual-band L-shape PIFA at 670 MHz.

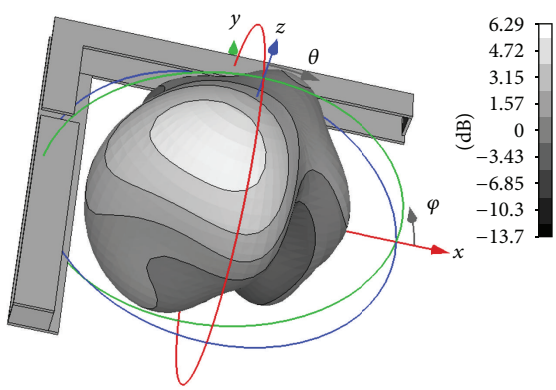

Figure 16: Simulated 3D antenna gain (dBi) for the dual-band L-shape PIFA at 2440 MHz.

Table 1 shows the values of all geometrical parameters of the optimized L-shape PIFA.

In particular, the driven and parasitic elements jointly contribute to determine the two resonances at the DVB-T band. They can be controlled by varying the following parameters: *W*, *H*, *L1* and *L2*. Also, the sum of the arm lengths, *L1* and *L2*, must be retained greater than 20 cm. The width and the height of the radiating element have been set at 13 mm and 8 mm, respectively, as in [19]. Furthermore, the gap *S* between the two elements mainly affects the antenna reflection coefficient at the IEEE 802.11b,g band. The distance between the two radiating elements, *S*, and the distance of the feeding point from the edge, *D*, represent the most effective design parameters for antenna tuning. *M* and *N* variations cause the resonant frequency to shift in the IEEE 802.11b,g band; also, the reflection coefficient values increase at the DVB-T frequencies. As for the PIFAs in [18–20], the L-shape PIFA can be made out of a cut and bent single metal sheet.

3.1. Numerical Results for the Dual-Band L-Shape PIFA. Simulation results have been derived by using CST Microwave Studio commercial tool. The simulated reflection coefficient is below −6 dB and −10 dB in the DVB-T and WLAN bands, respectively. The simulated antenna gain (Figure 13) is between 1.8 dBi and 2.2 dBi in the DVB-T band and between 6.2 dBi and 6.4 dBi in the WLAN band; a radiation efficiency greater than 95% has been obtained at both frequency bands due to the absence of dielectric substrates.

Table 1: Dual-band L-shape PIFA dimensions (mm).

L1	120
L2	116
W	13
H	8
S	3.3
A	76.5
M	12
B	30.2
N	10
D	47
F	20

The radiation pattern modifications have been analyzed and compared to those of the linear-shape PIFA in [19]. The simulated radiation patterns in the principal planes, *XZ*, *YZ*, and *XY*, are shown in Figure 14 (E_θ and E_φ components, with all of them normalized to the electric field amplitude at $\theta = 0$), when evaluated at the center frequency of the bands of interest. In the DVB-T band, the L-shape geometry causes a 45° rotation of the radiation pattern in the *XY* plane, as also apparent form the antenna gain 3D plots shown in Figures 15 and 16. In the other two principal planes (*XZ* and *YZ*), a 10° displacement from broadside of the E_θ component maximum occurs; the E_φ component exhibits an almost omnidirectional radiation pattern.

The radiation patterns in Figure 17 show that L-shape PIFA radiates a linearly polarized field in the $\varphi = +45°$ plane. Also, it radiates as a combination of two orthogonal linear radiators that are fed in-phase. At higher frequency, in the WLAN band, a larger number of lobes is present, as expected since the antenna is electrically long at 2.4 GHz (see Figures 14 and 16).

3.2. Experimental Results for the Dual-Band L-Shape PIFA. A prototype was realized with a 0.4 mm thick adhesive copper tape, cut and folded around a polystyrene block to obtain the final 3D structure. Results in terms of simulated and measured reflection coefficient are shown in Figure 18. The measured reflection coefficient is below −6 dB and −10 dB in the DVB-T and WLAN bands, respectively. Measurements on the radiation patterns have been performed at the anechoic chamber of the Department of Electrical Engineering of the University of Oviedo. The antenna prototype is shown in Figure 19 when it is mounted on the rotating platform for radiation pattern measurement.

The measured radiation patterns for the *XZ* and *YZ* planes, at 670 MHz and 2440 MHz, are compared with numerical simulations in Figures 20 and 21. Discrepancies between simulations and measurements are probably due

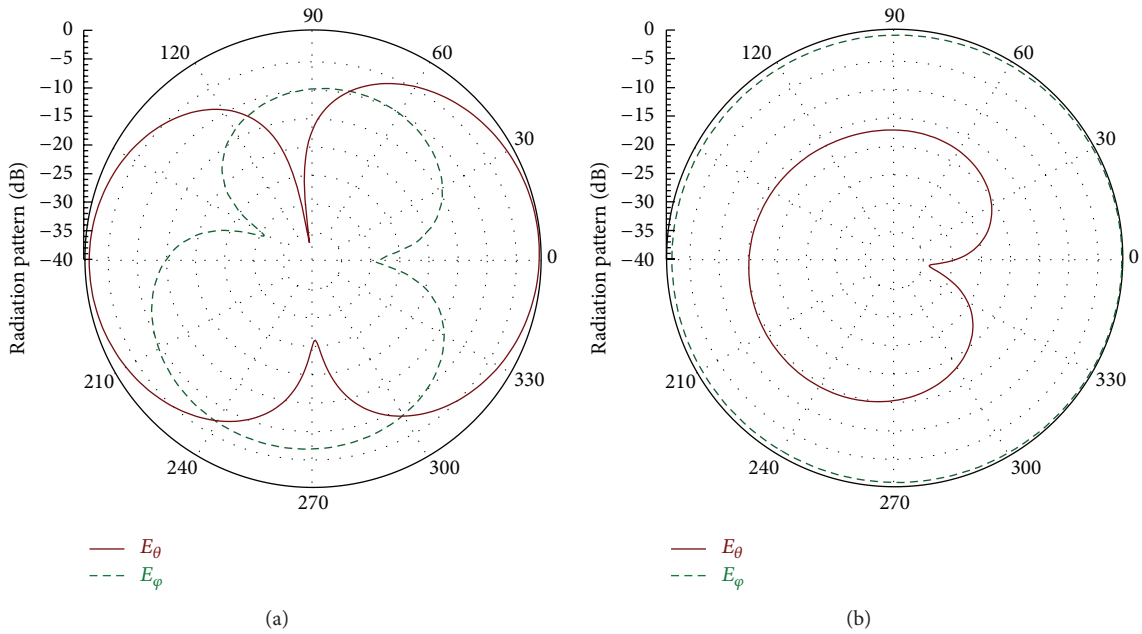

Figure 17: Simulated radiation patterns (E_θ and E_φ components normalized to the electric field amplitude at $\theta = 0$) for the proposed dual-band L-shape PIFA at 670 MHz: (a) $\varphi = 45^\circ$ plane; (b) $\varphi = -45^\circ$ plane.

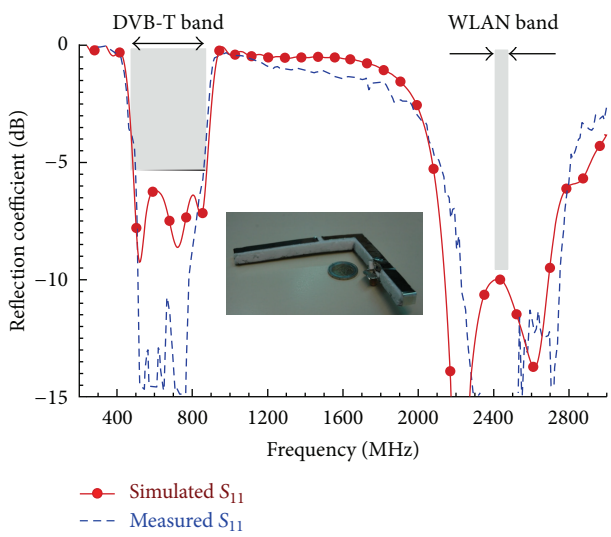

Figure 18: Simulated and measured reflection coefficient for the proposed dual-band L-shape PIFA.

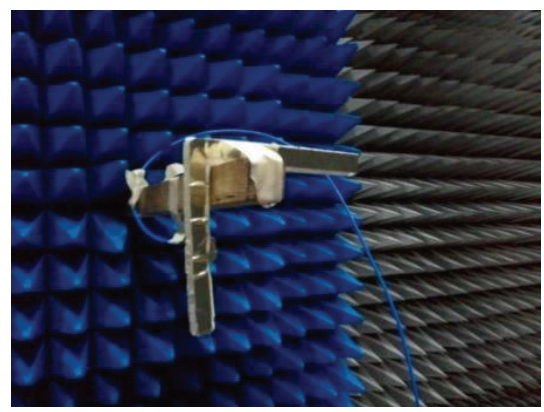

Figure 19: Antenna prototype mounted on the rotating platform for radiation pattern measurements.

to the limited mechanical robustness of the homemade prototype and the manufacturing inaccuracies. The measured antenna gain is about 1 dBi and 5 dBi for the DVB-T and the WLAN band, respectively (it is about 1 dB less than simulated results).

4. Conclusions

Starting from an overview on compact Planar Inverted-F Antennas, a dual-band L-shape Planar Inverted-F Antenna operating in both the DVB-T band (470–862 MHz) and the WLAN IEEE 802.11b,g band (2400–2484 MHz) has been presented. It has been designed to meet space requirements typically required for integration along the corner of display-equipped devices. A prototype was realized and characterized. The L-shape PIFA can be obtained by properly cutting and folding a single metal sheet, thus resulting in a relatively low-cost and mechanically robust antenna configuration.

Although the final design here shown has been obtained by assuming specific requirements on the maximum length of the two arms of the L-shape PIFA (less than 15 cm for both arms), it has been numerically and experimentally verified that VSWR performance at the extremely large DVB-T frequency band can be still met by properly tuning antenna geometrical parameters, when the arm length requirements change less than 10% with respect to the lengths in Table 1.

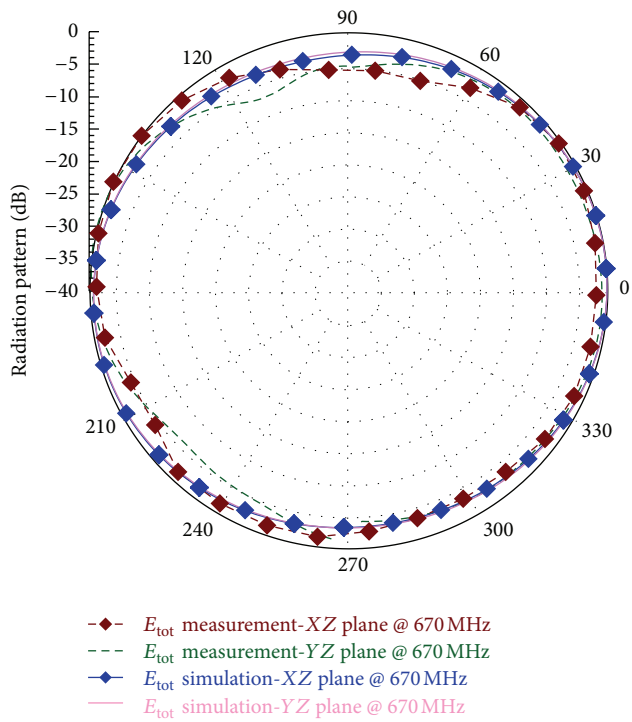

Figure 20: Simulated and measured radiation patterns (total E-field for the XZ and YZ planes) for the proposed dual-band L-shape PIFA at 670 MHz (central frequency for the DVB-T band).

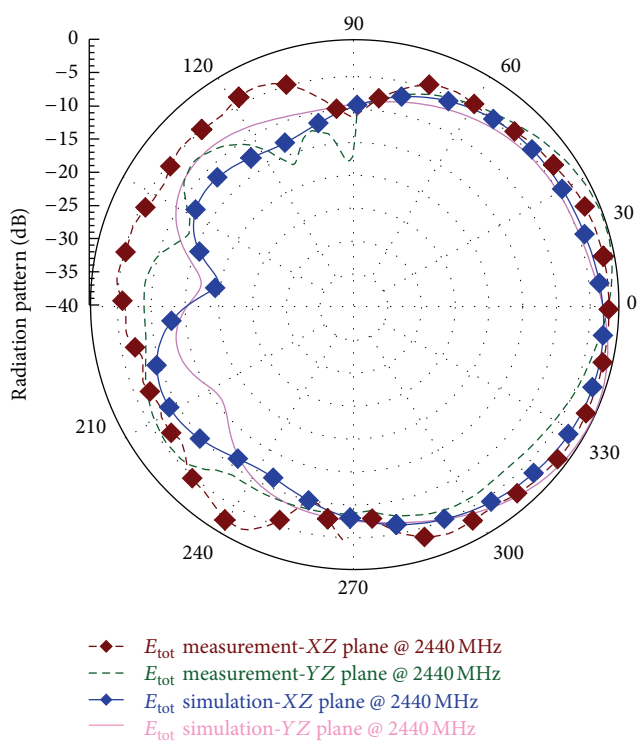

Figure 21: Simulated and measured radiation patterns (total E-field for the XZ and YZ planes) for the proposed dual-band L-shape PIFA at 2440 MHz (central frequency for the IEEE 802.11b,g band).

This confirms the robustness of the proposed L-shape PIFA design, which can be well optimized also when specific and demanding aesthetic/mechanical requirements must be met.

References

[1] DVB Project, http://www.dvb.org/.

[2] K. L. Wong, C. I. Lin, T. Y. Wu, and J. W. Lai, "A planar DTV receiving antenna for laptop applications," *Microwave and Optical Technology Letters*, vol. 42, no. 6, pp. 483–486, 2004.

[3] C. M. Su, L. C. Chou, C. I. Lin, and K. L. Wong, "Internal DTV receiving antenna for laptop application," *Microwave and Optical Technology Letters*, vol. 44, no. 1, pp. 4–6, 2005.

[4] Y. W. Chi and K. L. Wong, "Wideband printed dipole antenna for DTV signal reception," in *Proceedings of IEEE Region 10 Conference (TENCON '07)*, pp. 1–4, November 2007.

[5] W. S. Chen, Y. T. Chen, H. T. Chen, and J. S. Kuo, "A wideband printed monopole antenna for wireless applications," in *Proceedings of IEEE International Symposium on Antennas and Propagation and USNC/URSI National Radio Science Meeting (APSURSI '09)*, June 2009.

[6] C. Yang, J. Kim, H. Kim, J. Wee, B. Kim, and C. Jung, "Quad-band antenna with high isolation MIMO and broadband SCS for broadcasting and telecommunication services," *IEEE Antennas and Wireless Propagation Letters*, vol. 9, pp. 584–587, 2010.

[7] C. Y. Huang, B. M. Jeng, and J. S. Kuo, "Grating monopole antenna for DVB-T applications," *IEEE Transactions on Antennas and Propagation*, vol. 56, no. 6, pp. 1775–1776, 2008.

[8] C. Y. Huang, B. M. Jeng, and C. F. Yang, "Wideband monopole antenna for DVB-T applications," *Electronics Letters*, vol. 44, no. 25, pp. 1448–1450, 2008.

[9] L. Low, J. Batchelor, R. Heaton, and N. Chen, "Dual patches microstrip fed antenna with wide bandwidth," in *Proceedings of the Loughborough Antennas and Propagation Conference (LAPC '09)*, pp. 429–432, November 2009.

[10] M. Koubeissi, Mouhamadou, C. Decroze, D. Carsenat, and T. Monédière, "Triband compact antenna for multistandard terminals and user's hand effect," *International Journal of Antennas and Propagation*, vol. 2009, Article ID 491262, 7 pages, 2009.

[11] J. K. Wee, J. W. Park, I. S. Yeom, B. G. Kim, and C. W. Jung, "Compact DVB-H antenna with broad dual-band operation for PMP applications," *IEEE Antennas and Wireless Propagation Letters*, vol. 9, pp. 580–583, 2010.

[12] H. T. Chattha, Y. Huang, and Y. Lu, "PIFA bandwidth enhancement by changing the widths of feed and shorting plates," *IEEE Antennas and Wireless Propagation Letters*, vol. 8, pp. 637–640, 2009.

[13] C. See, H. Hraga, R. Abd-Alhameed, N. McEwan, J. Noras, and P. Excell, "A low-profile ultra-wideband modified planar inverted-F antenna," *IEEE Transactions on Antennas and Propagation*, vol. 61, no. 1, pp. 100–108, 2012.

[14] C. Suárez-Fajardo, J. O. Gómez-Sará, and M. Ferrando-Bataller, "Broadband PIFA with capacitive feed," in *Proceedings of IEEE International Symposium on Antennas and Propagation and USNC/URSI National Radio Science Meeting (APSURSI '09)*, pp. 1–4, June 2009.

[15] H. Chaobin and Z. Qi, "A compact wideband PIFA for dual-band WLAN applications," in *Proceedings of the International Conference on Microwave and Millimeter Wave Technology (ICMMT '12)*, vol. 4, pp. 1–4, May 2012.

[16] C. H. See, R. A. Abd-Alhameed, D. Zhou, and P. S. Excell, "A planar inverted-f-l antenna (pifla) with a rectangular feeding plate for lower-band uwb applications," *IEEE Antennas and Wireless Propagation Letters*, vol. 9, pp. 149–151, 2010.

[17] P. Nepa, G. Manara, A. A. Serra, and G. Nenna, "Multiband PIFA for WLAN mobile terminals," *IEEE Antennas and Wireless Propagation Letters*, vol. 4, no. 1, pp. 349–350, 2005.

[18] R. Caso, A. D'Alessandro, A. A. Serra, P. Nepa, and G. Manara, "An integrated dual-band PIFA for DVB-T and WiMAX applications," *IEEE Antenna and Wireless Propagation Letters*, vol. 10, pp. 1027–1030, 2011.

[19] R. Caso, A. D'Alessandro, A. A. Serra, P. Nepa P, and G. Manara, "A compact dual-band PIFA for DVB-T and WLAN applications," *IEEE Transaction on Antennas and Propagation*, vol. 60, no. 4, pp. 2084–2087, 2012.

[20] R. Caso, A. D'Alessandro, A. A. Serra, P. Nepa, and G. Manara, "Dual-band integrated G-PIFA antenna for DVB-T and WLAN applications," in *Proceedings of IEEE International Symposium on Antennas and Propagation, Spokane (AP-S '11)*, Washington, DC, USA, July 2011.

Hindawi Publishing Corporation
International Journal of Antennas and Propagation
Volume 2013, Article ID 396459, 10 pages
http://dx.doi.org/10.1155/2013/396459

Research Article

Wireless Sensing for the Respiratory Activity of Human Beings: Measurements and Wide-band Numerical Analysis

Lorenzo Scalise,[1] Valter Mariani Primiani,[2] Paola Russo,[2] Alfredo De Leo,[2] Desar Shahu,[2] and Graziano Cerri[2]

[1] *Dipartimento di Ingegneria Industriale e Scienze Matematiche (DIISM), Università Politecnica delle Marche, Via Brecce Bianche, 60131 Ancona, Italy*
[2] *Dipartimento di Ingegneria dell'Informazione (DII), Università Politecnica delle Marche, Via Brecce Bianche, 60131 Ancona, Italy*

Correspondence should be addressed to Paola Russo; paola.russo@univpm.it

Received 5 December 2012; Revised 11 March 2013; Accepted 20 March 2013

Academic Editor: Renato Cicchetti

An electromagnetic sensing system for the measurement of the respiratory activity is presented. The aims are to demonstrate the feasibility of the proposed approach and in particular to evaluate the effect on the measured signal of the distance between the subject and the sensing apparatus. Moreover, an electromagnetic model of the system, including the monitored subject, is proposed as a tool to solve the problem of selecting working parameters for system design. The sensing system is based on the measurement of the phase variation of the reflection coefficient caused by the respiratory activity. The phase signal compared with the thorax displacement measured by a reference instrument shows a high correlation ($R = 0.97$) for different subject postures (sitting, standing, and lying) and a reduction of the signal amplitude with the distance −0.11 dB/cm is reported. The numerical simulations performed on a wide-band highlight the frequencies where the method exhibits the highest sensitivity to thorax movements. The sensitivity can be further improved by reducing the antenna beamwidth. Despite the signal amplitude reduction, the proposed system makes it possible to correctly operate at distances up to 2.5 m.

1. Introduction

Daily clinical practice often requires the monitoring of important physiological parameters of the patient (respiratory and heart rates, arterial pressure, oxygen saturation, etc.) and commonly known as vital signs. From home recovery to intensive care monitoring, vital signs need to be continuously measured and presented to patient carers or used to activate alarms or therapeutic procedures [1]. In order to measure these quantities, the use of invasive procedures based on contact transducers or electrodes [1] is typically required. However, these procedures can limit the duration of monitoring, restrict the patient's movements, cause signal artifacts, and, in some cases, represent a risk for the patient (burns, microshocks, infections, etc.). It is therefore of great interest to explore the possibility to use wireless technologies for the measurement of vital signs that can avoid a direct contact with the patient's body. Some interesting wireless applications have recently been proposed for heart rate monitoring, based on optical methods that enable to precisely assess heart rate variability [2–5] or on electromagnetic waves [6].

Among vital signs, monitoring of respiratory activity and its rate is of particular importance since the cessation of the respiratory function can be a life-threat, especially for patients in critical conditions. This event can build up gradually and, in this case, the continuous monitoring of respiratory acts is fundamental for identifying and/or predicting such a dangerous event [7]. As far as noncontact respiratory rate monitoring is concerned, different approaches have been proposed [8–12]. Such minimally-invasive methods, mainly used for remote monitoring purposes and diagnosis of sleep disorders, are resistive, piezoelectric or inductive thoracic

belts [8, 9], transthoracic impedance transducers [11] or under-mattress pressure mats [12]. The main limitations of such methods are due to movement artifacts and the subject's position (i.e., for pressure mats the subject has to lie on the bed); in particular, the use of chest belts is strongly limited in the case of patients with reduced expired/inspired air exchange and is not applicable for long and medium-term monitoring purposes [8].

As a consequence, the possibility to monitor the respiratory activity with a noncontact method has been an object of numerous recent investigations [13–19]. Laser Doppler vibrometry has demonstrated to be valid and reliable during *in-vivo* tests [13–15], whereas a second alternative approach is electromagnetic (EM) sensing [16–23]. The first EM approaches proposed [16, 17] were not adopted because of the bulky, complex, and rather expensive hardware. With a progressive reduction of dimensions and costs of radiofrequency components and systems, the interest in this sensing technique has rapidly increased. At present, there are two main categories of noncontact vital sign electromagnetic detection systems: ultra-wideband (UWB) pulse radar and continuous wave (CW) Doppler radar. Recent examples of pulsed UWB radar [18–20] were adopted to precisely measure respiration and heartbeat. Echo signals using mono [22] and double antenna [23] CW systems are measured at different working frequencies aiming to detect vital signs. These recent works are of extreme interest in view of a future transfer of this approach to wireless, market-ready monitoring systems. In [24], a novel, wireless, low-cost, and wearable Doppler radar system composed of textile materials and capable of detecting moving objects behind a barrier is presented; the on-body system is capable of detecting multiple moving subjects in indoor environments, including through-wall scenarios.

The majority of these papers demonstrate the possibility to measure a time signal synchronous to the respiratory rhythm and proportional to the variation of the thorax volume caused by inspiration/expiration acts. The great interest on the EM sensing of the respiratory activity is due to the wireless feature of the technique, realized with small antennas illuminating from a distance. Moreover, it is important to underline that, in order to operate, the antenna does not need to be accurately pointed toward a specific part of the subject's body (as for laser-based methods), but it can generally illuminate the region where the monitored subject is positioned [22–25]. Finally, it is worth noting that EM sensing makes it possible to measure through clothes or fabric (bed sheets, blankets, clothes, etc.) without signal disturbances [19]; such a characteristic is a valuable aspect especially in the case of patients who are forced to stay in bed or noncollaborative or unconscious subjects (neonates in incubators, burn-injured, or postoperative patients).

The aim of this paper is therefore to propose an electromagnetic (EM) method for the detection of the respiratory activity and the measurement of the respiratory rate, based on the measurement of the EM signal backscattered by the monitored subject. In particular, the phase variation of the input reflection coefficient of an antenna illuminating the subject during its normal respiratory activity is analyzed in the frequency domain. This approach makes it possible investigate the backscattered signal over a wide frequency range. The availability of a wide band characterization will make it possible to optimally choose the operating frequency if a continuous wave (CW) system is sought or to properly choose the frequency content to build up an optimal pulse if an UWB technology is used. Many parameters contribute to the system performance, and for a good system design, the quantitative assessment of the received signal in dependence on the distance and on the subject posture (standing, sitting, or laying in front of the measurement apparatus) is essential. This is particularly important for the definition of the parameters at the design stage of the system. Such dependences have been investigated using a dedicated experimental set-up able to operate in frequency domain. The EM model was developed and tested to provide the voltage at the input/output port of the transmitting/receiving antenna as a function of the antenna characteristics and of the interaction between the radiated field and the monitored body. In particular, the model made it possible to perform a wide frequency band analysis of the system sensitivity, and a parametric study with respect to the antenna radiating characteristic. The design of an "ad hoc" antenna (i.e., printed antennas [26, 27]) and systems, characterized by reduced costs and increased sensitivity and portability (i.e., market available system [28]) based on the results obtained in this paper, is left to a future step.

2. Experimental Set-Up and Testing Conditions

2.1. Experimental Set-Up. The measurement method used for the detection of the respiratory activity is schematically reported in Figure 1 [22]. A vectorial network analyzer (VNA) (HP 8753D) is used to generate the output signal at 6 GHz (1 mW) to feed the antenna. The VNA measures the reflection coefficient of the antenna (S_{11}) which depends on the antenna itself and on the reflected signal backscattered from the body.

The reflection coefficient is a complex quantity, so it is possible to use both amplitude and phase time variations to gain information about the respiratory activity of the subject positioned in front of the antenna. In order to have a sufficiently sensitive system, phase variations were used. In fact, being the thorax displacement (ΔD) due to the respiratory activity a small percentage of the total distance, the amplitude variation is small. On the other hand, ΔD is a significant fraction of the wavelength used ($\lambda = 5\,\text{cm}$), therefore the variation of the phase of the reflected signal (ΔP) is easily detectable.

VNA performs a continuous measurement of the reflection coefficient S_{11} (modulus and phase) of the antenna, after a proper calibration procedure, over a time interval that can be chosen by the user (Sweep time). Thanks to this continuous wave (CW) operating modality, the output frequency remains the same during the instrument sweep and therefore the reflection coefficient variations can be ascribed only to the subject's respiratory activity.

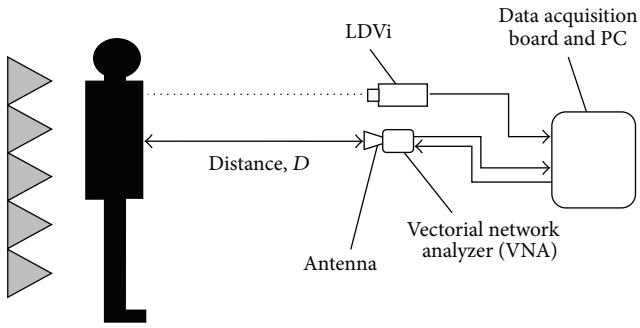

Figure 1: Scheme of the experimental set-up.

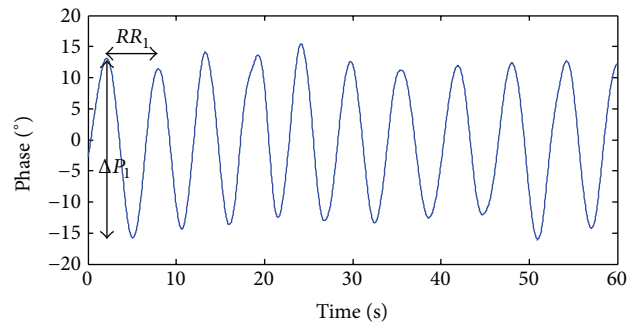

Figure 2: Time domain response of the S_{11} phase signal measured at 50 cm from the subject's thorax during regular respiration (time window 60 s); ΔP_1 is the phase variation measured during the first respiratory act, RR_1 is the 1st respiratory period.

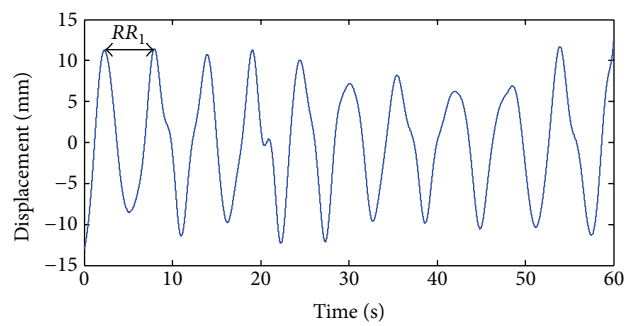

Figure 3: Distance variation ΔD of the subject's thorax (sternum) measured by LDVi at 50 cm during regular respiration (time window 60 s); RR_1 is the 1st respiratory period.

The subject is positioned inside a space delimited by pyramidal absorbers (Emerson & Cuming Eccosorb VHP-18-NRL) to avoid unwanted reflections; the distance between the subject and the absorbers is about 1.5 m, while the distance from the antenna and the chest of the subject (D in Figure 1) can be varied as well as the position of the subject with respect to the main lobe. The presence of absorbing material is not essential for the final application of the technique, but it is here used to reproduce a well controllable electromagnetic environment and to isolate the set-up area from other coexisting laboratory activities. A broadband, double ridge, horn antenna (model AH System SAS 571) has been used to transmit/receive the electromagnetic waves. The antenna, which is well matched on the frequency range 0.7–18 GHz, exhibits a half power beam of about 41° in H plane and 66° in the E plane, at 6 GHz.

A laser Doppler vibrometer (LDVi) was used for the measurement of the respiratory acts, as a reference instrument. LDVi was proved [13–15] to accurately provide the oscillations of the skin surface in correspondence to the respiratory acts.

The phase of the S_{11} signal was sampled at 26 Hz (maximum available data sampling), while the velocity signal from the LDVi was initially sampled at 1 kHz. On both signals, the phase of S_{11} measured by the proposed system and the LDVi signal, a wavelet filter (dB8, 5th order for the S_{11} signal and 10th level for the LDVi) was applied in order to reject the disturbances caused by motion artifacts, high frequency noise, and heartbeats [22]. The LDVi velocity signal was integrated to obtain the surface displacement time history. As a final step, the LDVi displacement signal was down-sampled to the same sampling frequency of the S_{11} signal (26 Hz). Examples of the S_{11} phase and LDVi displacement signals simultaneously measured are reported in Figures 2 and 3, respectively.

In this case, the subject was sitting and normally breathing; the antenna was placed at a distance $D = 50$ cm. The variation of the displacement due to the respiratory activity is reported on Figure 3, and it is evident how such variation of the displacement produces a variation in the phase of the reflection coefficient simultaneously recorded by the measurement system proposed (Figure 2). It is also possible to note how the operating frequency (6 GHz) exhibits a sufficiently small wavelength (5 cm) to make thorax excursions (Figure 3) detectable.

2.2. Testing Conditions. We operated our tests on a single male volunteer, aged 22, with a body index mass (BMI, [1]) of 19.59 [kg/m^2].

The measurement apparatus and the subject were held at 5 measurement distances: 50, 100, 150, 200, and 250 cm. The subject assumed three postures: standing, sitting and lying (on a semirigid bed). While for the standing and sitting postures; the antenna was kept in front of the subject for the laying posture, the subject was asked to assume three positions: supine, prone, and lateral. Each test had a duration of 60 s and, for each distance and position, it was repeated 3 times. A total of 2880 s of acquisition time were recorded. During measurement, the subject was asked to breathe normally.

In order to correlate the amplitude of the signal measured by the e.m. system and the distance D, we have measured the peak-to-peak phase variation $\overline{\Delta P}$, mean of the ΔP_i values measured on all the 3 tests repeated for each distance in correspondence with the respiratory acts (in Figure 2, the ΔP_1 value is reported for the first respiratory act).

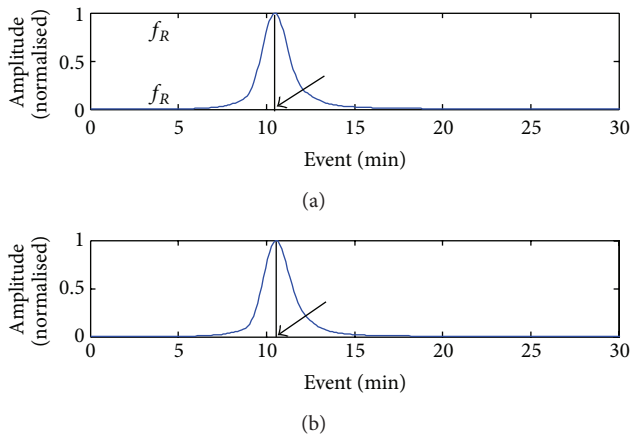

Figure 4: (a) Power spectrum of S_{11} phase signal (same data of Figure 2). (b) Power spectrum of the displacement signal measured by the LDVi (same data of Figure 3).

As a second parameter describing the quality of the measurement condition, we have defined [22] the quantity signal-to-noise ratio (SNR), according to the following formula:

$$\mathrm{SNR}_{\mathrm{dB}} = 20\,\mathrm{Log}_{10}\left(\frac{\overline{\Delta P}}{V_n}\right), \tag{1}$$

where $\overline{\Delta P}$ is the mean of the ΔP values measured from the phase of the S_{11} signal (filtered) and V_n is the RMS (root mean Square) of the phase of the S_{11} signal (noise), measured without the presence of the subject.

The mean respiratory frequency (f_R) for each test has been calculated for both systems (Figure 4) from the power spectrum of the measured signals (after removal of the DC component).

3. Results

The possibility to use the proposed experimental set-up for the detection of the respiratory activity is proved by the trace shown in Figure 5, where a time sequence of 37 s of the S_{11} phase signal is reported for the case of the subject sitting in front of the system at the distance D of 20 cm (Figure 5). For this demonstrative test, the tidal volume of the subject was simultaneously measured using a reference instrument (spirometer, MLT 1000L ADI), and this is also reported in Figure 5. For this test, the volunteer was asked to follow a specific respiratory rhythm (about 10 s of high respiration rate, followed by 10 s of apnea, and finally slow/normal respiratory rhythm).

From Figure 5, it is evident how the S_{11} phase signal is highly correlated with the instantaneous value of the tidal volume simultaneously measured by the spirometer. The $\overline{\Delta P}$ value (mean and standard deviation) measured for each distance D tested is illustrated in Figure 6 for the three postures: sitting, standing, and supine (only at D = 100 cm and D = 150 cm). Some signal spikes, due to rapid movement artifacts, are visible on the first part of S_{11} phase signal;

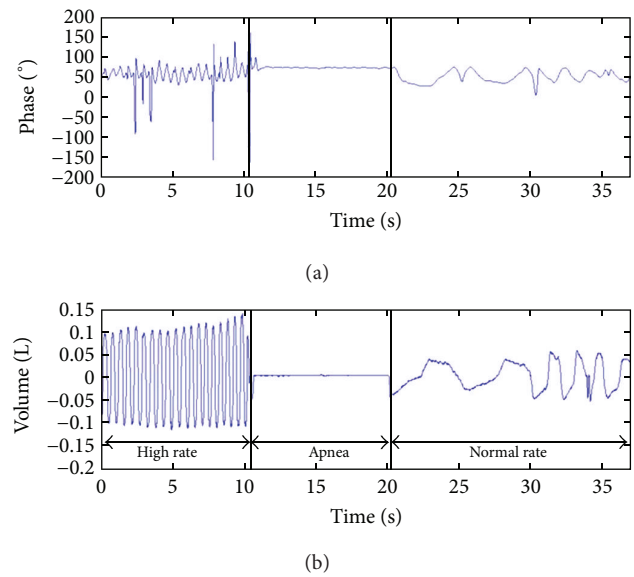

Figure 5: Comparison of the S_{11} phase signal (a) and spirometer signal (b) subject sitting, distance D = 20 cm.

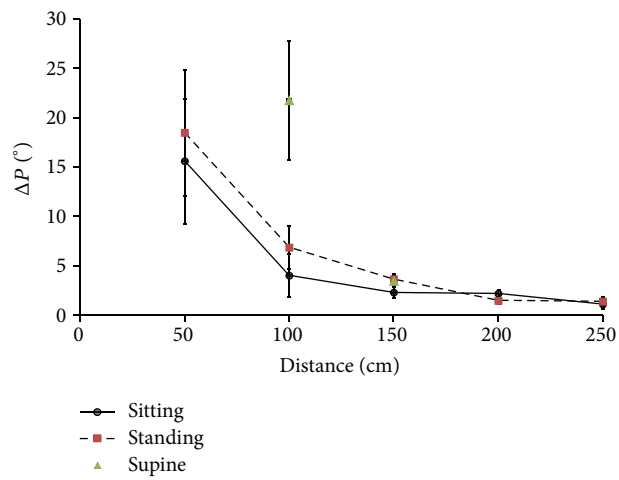

Figure 6: Mean and standard deviation of ΔP in function of the distance D for sitting, standing, and lying postures.

the same phenomena are not detected by the spirometer measuring the subject air flow.

From the results obtained, it is possible to observe that, for both the postures, there is a reduction of $\overline{\Delta P}$ as the distance D is increased.

The system exhibits the maximum phase variation for the closest distances (19° at 50 cm, standing) while, even still detectable, a minimum phase variation is reported for the longer distances tested (1° at 250 cm). It is also possible to note how, for all the distances D, the measured data are all compatible, highlighting the absence of the dependence of $\overline{\Delta P}$ on the posture. The only exception is reported for the supine posture at 100 cm where $\overline{\Delta P}$ reaches the highest value measured (21°); this is probably due to the fact that the supine posture (the subject was lying on a semi-rigid

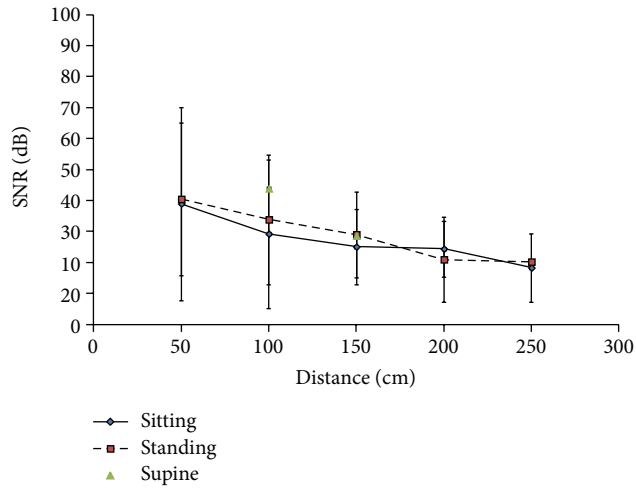

FIGURE 7: SNRs values (mean and standard deviation) in the function of D and for each of the postures.

bed) accentuated the thorax excursion during the normal respiratory acts.

From Figure 6, it is also possible to observe the $\overline{\Delta P}$ reduction of 74% and 63% between the data measured at 50 cm and the data measured at 100 cm, for sitting and standing postures, respectively. This signal reduction is due to the fact that the radiated beam for $D > 80$ cm, according to the radiating antenna pattern characteristics, is no longer focused exclusively on the subject thorax, but some of the incident power is also transmitted to the background, and it does not contribute to the generation of the reflected signal.

The SNRs of the signals measured, calculated according to (1), are shown in Figure 7 for the tested postures.

As for $\overline{\Delta P}$, it is evident how the greater D, the lower SNR, and this is confirmed for all the postures. The highest value (39 dB) is obtained at the distance of 50 cm for the standing posture, while the lowest (18 dB) is reported when the subject is sitting at 250 cm. It is also possible to note how the SNRs values are compatible for all the distances, confirming that posture is not a significant parameter.

From the data measured, it is possible to estimate an SNR loss of −0.11 dB/cm when the subject is standing in front of the antenna and of −0.9 dB/cm when the subject is sitting. Such values make it possible to estimate an SNR reduction of more than 27 dB for distances >3 m, independently from the subject's posture (sitting or standing).

In Figure 8, the scatter plot of the mean respiratory frequencies (f_R) measured by the LDV and the proposed system, together with the fitting line (mean square), is shown for standing, sitting, and supine postures. In this case, the correlation coefficient calculated between the two systems is 0.97.

Finally in Figure 9, we illustrate the case of the subject lying ($D = 100$ cm) and assuming 3 positions: supine, prone and lateral. Also in this case, a good value for the correlation coefficients calculated between the two systems is verified: 0.94, 0.93, and 0.98 for supine, prone, and lateral positions, respectively.

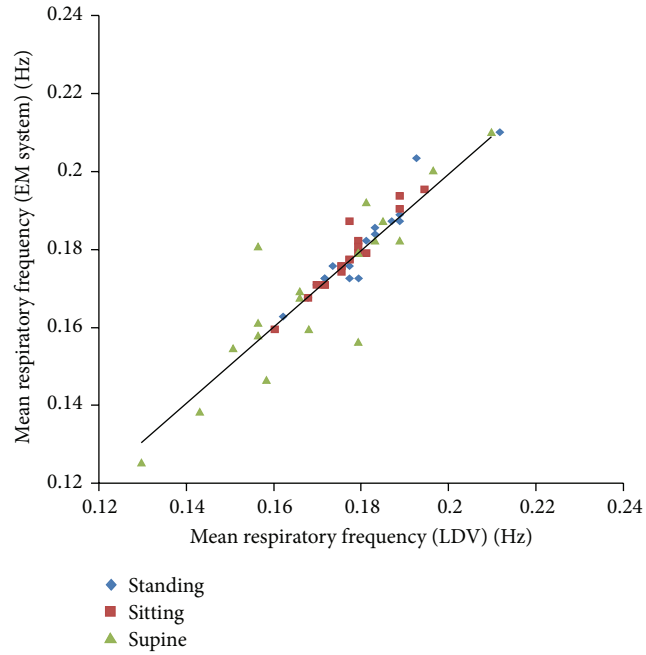

FIGURE 8: Scatter plot of mean respiratory frequencies (f_R): LDVi versus proposed method (subject position: standing, sitting, and supine).

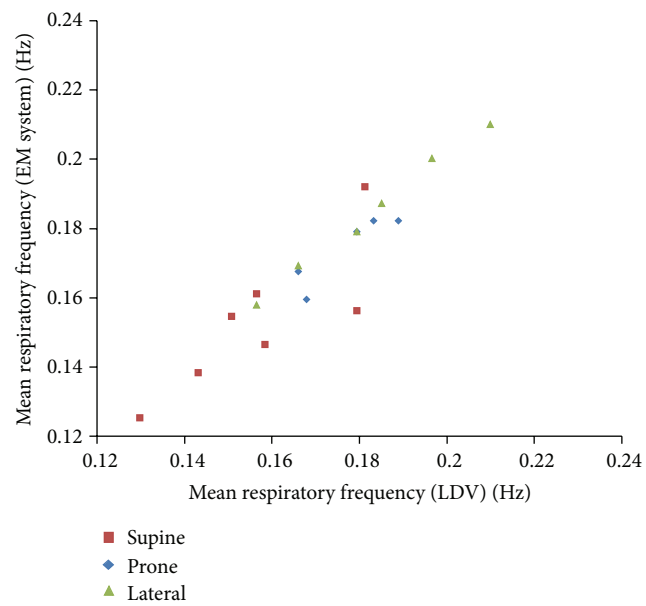

FIGURE 9: Scatter plot of mean respiratory frequencies (f_R): LDVi versus proposed method (supine, prone, and lateral; $D = 100$ cm).

4. Electromagnetic Model for Wide Band Analysis

An electromagnetic model of the interaction between the monitored subject and the electromagnetic system is proposed. The aim is to provide a characterization of the field scattered by the thorax of a subject during its normal

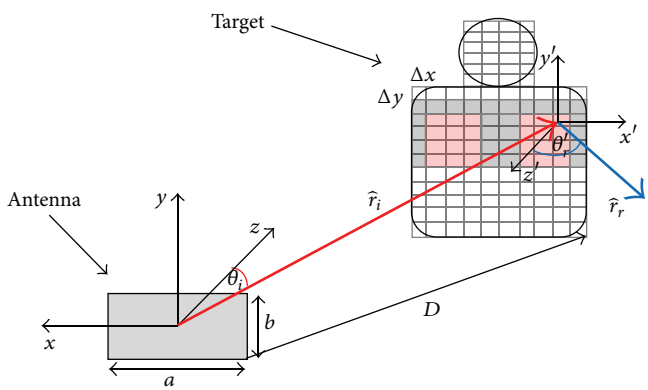

FIGURE 10: Geometry of the antenna and the target.

respiratory activity and to evaluate variations of the received signal (S_{11}) in a wide frequency band (2–12 GHz).

More in general, the model proposed can be used to analyze the influence of some important parameters (working frequency, antenna field pattern, etc.) on amplitude and phase variations of the measured signal ΔP (sensitivity) with the goal of optimizing the future design of e.m. systems using the same working principle.

Figure 10 illustrates the geometry of the scenario of interest which is composed by an antenna radiating toward a target placed at a distance D. The target is a simplified representation of a human thorax, where a subarea of the total target (colored region in Figure 10) may change its relative position along the z direction with respect to the remaining part of the target (the white region in the figure). In particular, to highlight the effect on the phase variation of the complex movement of an actual thorax, two different areas have been introduced to characterize larger and smaller amplitude of displacement (red and gray areas in Figure 10, resp.). The antenna is an equivalent ideal aperture antenna, having a radiation pattern with the same beamwidth of the actual antenna. The aperture has a uniform y-directed field distribution E_0, and its dimensions ($a \times b$) are chosen so to provide the desired half power beamwidth $\Delta\theta$ and $\Delta\varphi$ in the E and H planes, respectively (as reported later).

The dominant y-component of the incident electric field, radiated by the aperture in the direction $\hat{r}_i$ (referred to a spherical system associated to the Cartesian system x, y, z) and assuming far field conditions is given by [25]

$$E_y^i = j\frac{abE_0 e^{-j(2\pi r_i/\lambda)}}{\lambda r_i}\cos(\theta_i)\frac{\sin(X_i)}{X_i}\frac{\sin(Y_i)}{Y_i}, \quad (2)$$

where:

$$X_i = \frac{\pi a}{\lambda}\sin(\theta_i)\cos(\varphi_i),$$
$$Y_i = \frac{\pi b}{\lambda}\sin(\theta_i)\sin(\varphi_i). \quad (3)$$

$r_i\theta_i, \varphi_i$ are the coordinates of the observation point in the spherical system centered on the aperture.

The field radiated by the aperture impinges on the body's surface from the incident direction $\hat{r}_i$ and is partially reflected in the direction $\hat{r}_r$, as shown in Figure 10. The received signal (S_{11}) is calculated evaluating the electric field coupled back with the antenna.

In this simplified model, to account for the amplitude and phase variations of the incident field, the body surface facing the antenna is subdivided in n subareas ($n = 134$), and each subarea is considered as a radiating aperture with a uniform field distribution. The reflected electric field is calculated considering the oblique incidence of a plane wave on a dielectric interface, and its value is

$$E_y^- = \rho_{\mathrm{TM}}E_{\theta_i}^i\cos\theta_r'\sin\varphi_r' - \rho_{\mathrm{TE}}E_{\varphi_i}^i\cos\varphi_r', \quad (4)$$

where θ_r', φ_r' define the direction of the reflected wave in the local coordinate system (x', y', z') centered in the nth subarea, ρ_{TM}, ρ_{TE} are the reflection coefficients of the transverse components of the electric field on the incidence plane [25] and depend on the incidence angle and on the dielectric properties of the body; $E_{\theta_i}^i$ and $E_{\varphi_i}^i$ are the incident electric field components in spherical coordinate system.

Similarly to physical optic approach, the interaction among the fields of adjacent subareas is assumed to be negligible. The subarea dimensions Δx and Δy are chosen so that the transmitting aperture antenna can be considered in the far field zone of the radiating nth element; the E_y field component radiated by this element is

$$E_{ny} = j\frac{\Delta x\Delta y E_y^- e^{-j(2\pi r_r/\lambda)}}{\lambda r_r}\cos(\theta')\frac{\sin(X_n)}{X_n}\frac{\sin(Y_n)}{Y_n}, \quad (5)$$

where

$$X_n = \frac{\pi\Delta x}{\lambda}\left[\sin(\theta')\cos(\varphi') - \sin(\theta_r')\cos(\varphi_r')\right],$$
$$Y_n = \frac{\pi\Delta y}{\lambda}\left[\sin(\theta')\sin(\varphi') - \sin(\theta_r')\sin(\varphi_r')\right], \quad (6)$$

being r', θ', φ' the spherical coordinates of the observation point expressed in a local coordinate system (x', y', z') centred in the nth subarea, and θ_r', φ_r' the direction of the reflected wave. The total field scattered by the body and received by the antenna is

$$E_y^{\mathrm{sc}} = \sum_{n=1}^{N} E_{ny}. \quad (7)$$

The knowledge of the signal received by the antenna makes it possible to evaluate the S_{11} scattering parameters of the antenna:

$$S_{11} = \Gamma_{\mathrm{ant}} + \Gamma_{\mathrm{sc}}\sqrt{\frac{\left(1 - |\Gamma_{\mathrm{ant}}|^2\right)\eta}{Z_0 ab}}\,\vec{l}_{\mathrm{eff}}\cdot\hat{y}\frac{Z_0}{Z_{\mathrm{ant}} + Z_0}, \quad (8)$$

where Γ_{ant} and Z_{ant} are, respectively, the reflection coefficient and the input impedance of the antenna radiating in free space, Z_0 is the characteristic impedance of the line feeding the antenna, η is the free space wave impedance, and l_{eff} is the effective length of the antenna, $\Gamma_{\mathrm{sc}} = E_y^{\mathrm{sc}}/E_0$.

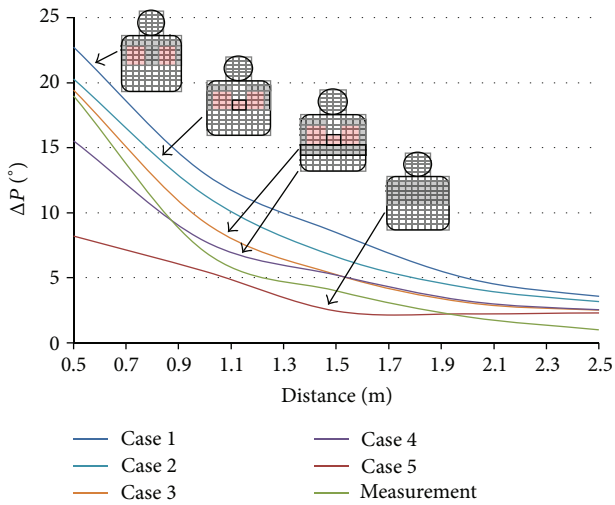

Figure 11: Maximum phase variation for different type of breathing movements simulated and measured.

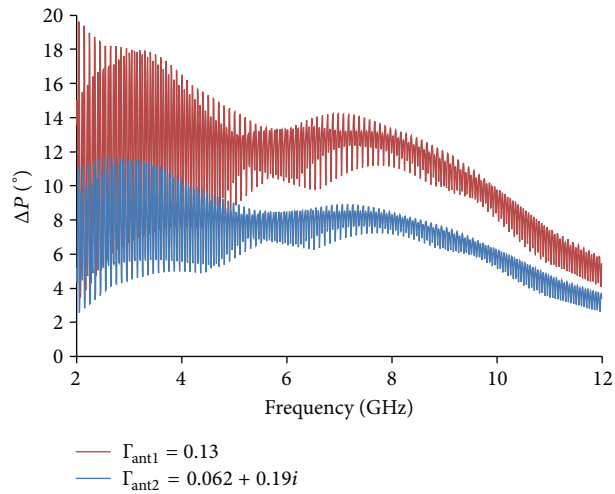

Figure 12: Phase variation (numerical model) as function of the emitted frequency and for two antenna reflection coefficients.

The model results were applied using the same testing conditions used for the measurements of Figure 6. The antenna used for the measurements has $\Gamma_{\text{ant}} = 0.062 + 0.19i$ at the working frequency $f = 6$ GHz. The data implemented for the model are $\Delta x = \Delta y = 5$ cm; conductivity of the body $\sigma_{\text{body}} = 1$; relative permittivity of the body $\varepsilon_{\text{body}} = 70$; half power beamwidth: $\Delta\theta = 66^\circ$, $\Delta\varphi = 41^\circ$ (from which the aperture dimensions are derived: $a = \lambda/0.79$, $b = \lambda/1.229$). The distance between the aperture antenna and the colored subareas of Figure 10 was changed in a few steps as: $D - k\Delta d$, where $\Delta d = 1$ mm for the gray area and $\Delta d = 2$ mm for the red area of Figure 10, and $k = 0.10$. The chest displacement chosen is typical for human breathing (see e.g., Figure 3). In Figure 11, the results obtained with the model and the measurement of Figure 6 (standing) are reported. In the same figure, it is possible to see the model results obtained changing the breathing behavior of the subject. In particular, for case 1, 2, 3, and 5 the grey zones and the red zones have, respectively, a maximum displacement of 1 cm, and 2 cm, whereas for case 4 the grey and the red zones have respectively a maximum displacement of 1 cm and 1.8 cm.

Figure 11 shows how the complexity of the mechanism involved in the respiration acts affects the electromagnetic results. The phase variation depends strongly on the way of breathing, that is, on the position variations of the points on the thorax surface. Moreover, these variations are differently detected by the antenna because it weights the surface movements with its radiation pattern. From the same figure it is possible to see that the model is very sensitive to the different thorax movements, and it predicts correctly the order of magnitude of the phase variations due to breathing. A direct comparison of the measurements and the model results would require a precise knowledge of the displacement of each point of the thorax of the subject under measurement.

The proposed model allows to investigate the influence of the frequency, and the radiation beamwidth of the antenna has been carried out.

Considering the subject placed at a distance D of 150 cm, with the numerical model (using case 1), it is possible to infer the phase variations due to the respiratory acts at different working frequencies in the interval 2–12 GHz, maintaining the other experimental parameters as described previously. In Figure 12, we report the phase variation at a target distance D of 150 cm in function of the emitted frequency and for two antenna matching conditions:

$$\Gamma_{\text{ant1}} = 0.13, \qquad \Gamma_{\text{ant2}} = 0.062 + 0.19i. \tag{9}$$

The maximum phase variation exhibits an oscillating behavior with a period that depends on the distance between the antenna and the target. This behavior depends on how the reflected signal and the antenna reflection coefficient combine at different frequencies. Figure 13 shows the S_{11} on the complex plane during a respiratory act for 5 different frequencies. These frequencies are chosen in the range of the highest variations. It is clearly evident that the two components in (8) combine differently and that, in particular, there are two frequencies (2.72 and 2.78 GHz) that have a larger phase variation then the others.

Figure 12 also shows that the phase ΔP depends on the frequency and that there are some frequencies where it can reach a maximum value; therefore, these frequencies can be chosen to obtain a more sensitive system. The same figure also shows the phase variation for two different antenna reflection coefficients. It is interesting to note that the matching of the antenna plays an important role in the value of the phase variation amplitude ΔP and that the higher the impedance matching, the greater is the phase variation. This behavior is due to the signal backscattered by the antenna itself, which combines together with the signal coming from the target masking the information on respiratory movements.

A similar analysis can be conducted modifying the directivity of the antenna (beamwidth). We have kept all the test parameters equal to the ones used for case 1 of Figure 11, but three different half power beamwidths are considered:

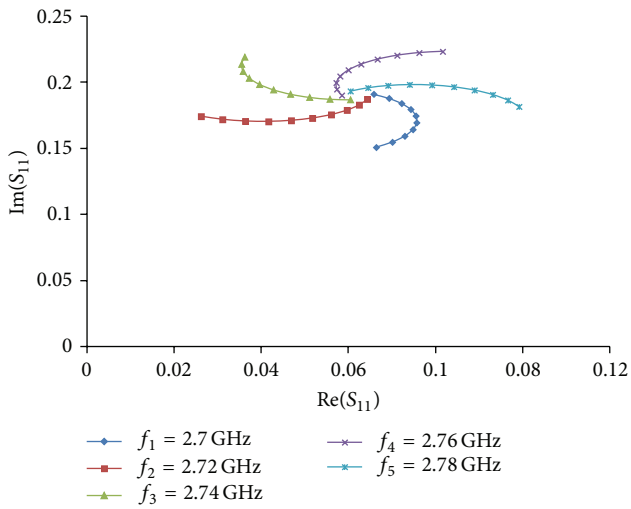

FIGURE 13: S_{11} at the input port of the antenna in the complex plane for 5 different frequencies.

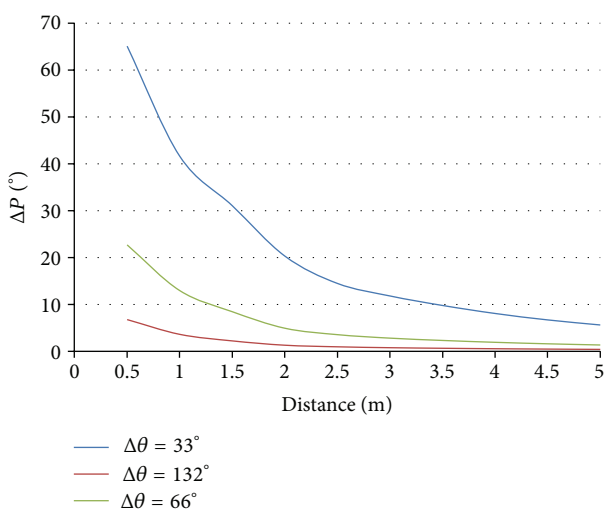

FIGURE 14: Effect of the half power beamwidth ($\Delta\theta\Delta\phi$) on the phase variation for increasing distances D.

(1) $\Delta\theta = 66^\circ$, $\Delta\varphi = 41^\circ$ (2) $\Delta\theta = 33$, $\Delta\varphi = 20$, (3) $\Delta\theta = 132^\circ$, and $\Delta\varphi = 82^\circ$.

In Figure 14, the phase variation of the received signal for the three cases is illustrated, when the target is placed at different distances.

It can be seen that the beamwidth greatly affects the sensitivity of the system, in particular when the target is placed near the antenna. This result is due to the focalization effect of the increasing directivity which increases the reflected signal level because most of the radiated power is intercepted by the moving part of the target.

It is also possible to observe that, with the target placed at a distance of 150 cm from the antenna, the phase variation of the reflected signal for $\Delta\theta = 33^\circ$ is considerably greater with respect to the case of $\Delta\theta = 66^\circ$. This effect is not so evident away from the antenna, where the free space attenuation of the signal is increased and where, for all the three cases, the target is partially radiated by the incident power.

As a consequence, it is possible to note that while an increase in frequency does not significantly influence the value of the detected phase variations caused by respiratory activity, the reduction of the antenna beamwidth appears to positively influence the phase of the signal detected (S_{11}) during respiration.

5. Discussion and Conclusions

A wireless noncontact approach to the problem of the measuring of the respiratory activity of human subjects has been proposed, using an electromagnetic sensing system. This method is based on the measurement of the phase variations of the reflection coefficient S_{11} caused by the displacement of the thorax surface, and an electromagnetic model has been proposed to reproduce the system response. The model is based on a frequency domain approach, and it is an useful tool for investigating the influence of the parameters on the system performances.

The proposed method is not only limited to a CW monitoring, as it has been demonstrated by the wideband frequency domain analysis carried out with the electromagnetic model. In fact, useful information about the design of an UWB pulse monitoring system can be also easily achieved from the obtained results. For example, from the results shown in the previous section, it can be inferred that the most suitable pulse for a pulse monitoring system should have the significant part of its spectrum in the range 2–4 GHz to maximize sensitivity or the range 4–6 GHz for a flat response.

The solution proposed is feasible for brief as well as for prolonged observation time which is the main limitation of the systems available for respiration monitoring [8, 20]. Change of the respiration frequencies as well as apneas can be clearly detected (Figure 5). Good correlations ($R = 0.97$) with the gold standards are also reported for the measured mean respiration frequencies.

The measurement system proposed presents also a reduced sensitivity to the subject posture. Standing, sitting, and laying postures have been investigated and they guarantee good correlations ($R = 0.94$, 0.93, and 0.98) also for different laying positions (supine, prone, and lateral), meaning that, when lying, the subject observed is free to assume any position during the test, while this is not possible for currently available measurement systems [8, 20] which have, in fact, this strong limitation.

In detail, the experimental investigations have highlighted the dependence of the signal amplitude (phase variation in °) on target distance. The 74% of signal reduction has been reported when the subject was measured at 1 m, with respect to the case of the subject standing at 0.5 m. While for longer distances the signal amplitude is always <5°. More in detail, we have explored the dependence of the quality of the measured (in particular the signal SNR) on the distance between antenna and subject, D. A reduction in the SNR with distance D has been reported (in the order of −0.11 dB/cm). From our tests, it is shown that despite the fact

that at 2.5 m the SNR is reduced (about the 50%) in respect to the signal measured at 25 cm, it is still sufficiently high to allow a correct detection of the respiratory activity. In the case where a minimum operating SNR is requested, a possible solution could be to improve the emitted power (1 mW in our case) or to use a narrower radiating beam for the antenna. Although the quality of the signal can be reduced in some conditions (longer distances), the SNR is still sufficiently high (>18 dB) to provide reliable data.

The possible implementation of the proposed measurement approach could make use of market ready technologies which are not designed for laboratory use and are available at lower costs [28]. In general such devices are not optimized for the scopes considered in this paper (i.e., measurement of respiratory rate), and therefore they could be improved by the results reported.

Testing in "neutral" laboratory conditions (presence of e.m. absorbers), surrounding the subject under test, is a limitation of our study, and in this preliminary work it has been decided to better focus on the phenomenon, reducing the effect of interfering inputs such as the clutter due to environmental conditions. For future applications, the electromagnetic scattering of the surroundings and in general the clutter received at the antenna need to be analyzed. Moreover, for longer time exposure (some hours), automatic recalibration of the system could be introduced to reduce the effect of electronic circuit drift. In practice, in the case of an hospitalized patient, most of the received signal can be considered as static clutter, and signals variations are only due to the respiratory activity. In more complex situations a dedicated postprocessing will be needed to discriminate between patient's respiration from other nonstatic reflections. This aspect will be taken into account under consideration in our future research activity as well as the need for specifically designed antenna providing precisely shaped radiation patterns.

The method proposed in this paper has been tested only on one motionless person; if two or more subjects will be simultaneously illuminated by the antenna, the sensor will detect a composition of their signals. This can be a limitation of the method investigated, and attempts to resolve this problem have been recently proposed by placing more than one sensor and therefore using spatial diversity [27].

A possible future aspect to be investigated is related to the fact that, from a clinical point of view, "respiratory activity" also includes other aspects such as the depth (flow, volume) of the single air acts. The possibility to calibrate the thorax displacement measured by a laser Doppler vibrometer to the flow or volume exchanged during respiration has been demonstrated [14]. This possibility has been recently explored also for microwave sensors [29]. Such possibility could be studied also for the here proposed em approach.

Different applications of electromagnetic noncontact sensing of human beings can also be considered in the fields of security, rescue in emergency situations, elderly remote care, and so forth. Such perspective has aroused the attention of the scientific community on the potentiality of these kinds of sensors.

Acknowledgments

The authors would like to thank Dr. Paolo Marchionni and Dr. Ilaria Ercoli for their help in the laboratory sessions.

References

[1] J. G. Webster, *Medical Instrumentation Application and Design*, John Willey & Sons, Boston, Mass, USA, 1992.

[2] L. Scalise and U. Morbiducci, "Non-contact cardiac monitoring from carotid artery using optical vibrocardiography," *Medical Engineering and Physics*, vol. 30, no. 4, pp. 490–497, 2008.

[3] U. Morbiducci, L. Scalise, M. De Melis, and M. Grigioni, "Optical vibrocardiography: a novel tool for the optical monitoring of cardiac activity," *Annals of Biomedical Engineering*, vol. 35, no. 1, pp. 45–58, 2007.

[4] M. De Melis, U. Morbiducci, and L. Scalise, "Identification of cardiac events by optical vibrocardiograpy: comparison with phonocardiography," in *Proceedings of the 29th Annual International Conference of IEEE-EMBS, Engineering in Medicine and Biology Society (EMBC '07)*, pp. 2956–2959, August 2007.

[5] M. De Melis, U. Morbiducci, L. Scalise et al., "A preliminary study for the evaluation of large artery stiffness: a non contact approach," *Artery Research*, vol. 2, no. 3, pp. 100–101, 2008.

[6] S. Bakhtiari, T. W. Elmer, N. M. Cox et al., "Compact millimeter-wave sensor for remote monitoring of vital signs," *IEEE Transactions on Instrumentation and Measurement*, vol. 61, no. 3, pp. 830–841, 2011.

[7] M. I. Bierman, "Respiratory monitoring," in *Comprehensive Respiratory Care*, D. E. Dantzkner, N. R. Macintyre, and E. D. Bakow, Eds., W. B. Saunders Company, Philadelphia, Pa, USA, 1995.

[8] M. Folke, L. Cernerud, M. Ekström, and B. Hök, "Critical review of non-invasive respiratory monitoring in medical care," *Medical and Biological Engineering and Computing*, vol. 41, no. 4, pp. 377–383, 2003.

[9] X. Zhu, W. Chen, T. Nemoto et al., "Real-time monitoring of respiration rhythm and pulse rate during sleep," *IEEE Transactions on Biomedical Engineering*, vol. 53, no. 12, pp. 2553–2563, 2006.

[10] K. Watanabe, T. Watanabe, H. Watanabe, H. Ando, T. Ishikawa, and K. Kobayashi, "Noninvasive measurement of heartbeat, respiration, snoring and body movements of a subject in bed via a pneumatic method," *IEEE Transactions on Biomedical Engineering*, vol. 52, no. 12, pp. 2100–2107, 2005.

[11] K. P. Cohen, W. M. Ladd, D. M. Beams et al., "Comparison of impedance and inductance ventilation sensors on adults during breathing, motion, and simulated airway obstruction," *IEEE Transactions on Biomedical Engineering*, vol. 44, no. 7, pp. 555–566, 1997.

[12] D. I. Townsend, M. Holtzman, R. Goubran, M. Frize, and F. Knoefel, "Measurement of torso movement with delay mapping using an unobtrusive pressure-sensor array," *IEEE Transactions on Instrumentation and Measurement*, vol. 60, no. 5, pp. 1751–1760, 2011.

[13] L. Scalise, P. Marchionni, and I. Ercoli, "Optical method for measurement of respiration rate," in *Proceedings of the IEEE International Workshop on Medical Measurements and Applications (MeMeA '10)*, pp. 19–22, May 2010.

[14] L. Scalise, P. Marchionni, and I. Ercoli, "A non contact, optical procedure for precise measurement of respiration rate and flow,"

in *Biophotonics: Photonic Solutions for Better Health Care II*, vol. 77150 of *Proceedings of SPIE*, April 2010.

[15] L. Scalise, I. Ercoli, P. Marchionni, and E. P. Tomasini, "Measurement of respiration rate in preterm infants by laser Doppler vibrometry," in *Proceedings of the IEEE International Workshop on Medical Measurement and Applications (MeMeA '11)*, pp. 657–661, 2011.

[16] J. C. Lin, "Non-invasive microwave measurement of respiration," *Proceedings of the IEEE*, vol. 63, no. 10, p. 1530, 1975.

[17] E. Greneker, "Radar sensing of heartbeat and respiration at a distance with applications of the technology," *Radar*, vol. 97, pp. 150–154, 1997.

[18] J. C. Lin, "Microwave sensing of physiological movement and volume change: a review," *Bioelectromagnetics*, vol. 13, no. 6, pp. 557–565, 1992.

[19] C. Gu, C. Li, J. Lin, J. Long, J. Huangfu, and L. Ran, "Instrument-based noncontact doppler radar vital sign detection system using heterodyne digital quadrature demodulation architecture," *IEEE Transactions on Instrumentation and Measurement*, vol. 59, no. 6, pp. 1580–1588, 2010.

[20] J. C. Y. Lai, Y. Xu, E. Gunawan et al., "Wireless sensing of human respiratory parameters by low-power ultrawideband impulse radio radar," *IEEE Transactions on Instrumentation and Measurement*, vol. 60, no. 3, pp. 928–938, 2011.

[21] C. Li, J. Ling, J. Li, and J. Lin, "Accurate doppler radar noncontact vital sign detection using the RELAX algorithm," *IEEE Transactions on Instrumentation and Measurement*, vol. 59, no. 3, pp. 687–695, 2010.

[22] L. Scalise, A. De Leo, V. Mariani Primiani, P. Russo, D. Shahu, and G. Cerri, "Non contact monitoring of the respiration activity by electromagnetic sensing," in *Proceedings of the IEEE International Workshop on Medical Measurement and Applications (MeMeA '11)*, pp. 418–422, 2011.

[23] F. Soldovieri, I. Catapano, L. Crocco, L. N. Anishchenko, and S. I. Ivashov, "A feasibility Study for Life SignsMonitoring via a Continuous-Wave Radar," *International Journal on Antenna and Propagation*, vol. 2012, Article ID 420178, 5 pages, 2012.

[24] S. Agneessens, P. Van Torre, F. Declercq et al., "Design of a wearable, low-cost, through-wall doppler radar system," *International Journal on Antenna and Propagation*, vol. 2012, Article ID 840924, 9 pages, 2012.

[25] C. A. Balanis, *Antenna Theory: Analysis and Design*, John Wiley & Sons, New York, NY, USA, 2005.

[26] P. Bernardi, R. Cicchetti, S. Pisa, E. Pittella, E. Piuzzi, and O. Testa, "Design and realization of a UWB radar for breath activity monitoring," in *Proceedings of the International Symposium on Electromagnetic Compatibility (EMC EUROPE '12)*, pp. 1–6, 2012.

[27] L. W. Chua, "A new UWB antenna with excellent time domain characteristics," in *Proceedings of the 8th European Conference on Wireless Technology*, pp. 551–554, October 2005.

[28] https://www.novelda.no/content/development-kits.

[29] D. Dei, G. Grazzini, G. Luzi et al., "Non-contact detection of breathing using a microwave sensor," *Sensors*, vol. 9, no. 4, pp. 2574–2585, 2009.

Hindawi Publishing Corporation
International Journal of Antennas and Propagation
Volume 2013, Article ID 869170, 14 pages
http://dx.doi.org/10.1155/2013/869170

Review Article

Recent Developments in Reconfigurable and Multiband Antenna Technology

N. Haider, D. Caratelli, and A. G. Yarovoy

Microwave Sensing, Signals and Systems, Delft University of Technology, Mekelweg 4, 2628 CD, Delft, The Netherlands

Correspondence should be addressed to N. Haider; s.n.haider@tudelft.nl

Received 7 December 2012; Accepted 30 January 2013

Academic Editor: Renato Cicchetti

A comparative analysis of various reconfigurable and multiband antenna concepts is presented. In order to satisfy the requirements for the advanced systems used in modern wireless and radar applications, different multiband and reconfigurable antennas have been proposed and investigated in the past years. In this paper, these design concepts have been classified into three basic approaches: tunable/switchable antenna integration with radio-frequency switching devices, wideband or multiband antenna integration with tunable filters, and array architectures with the same aperture utilized for different operational modes. Examples of each design approach are discussed along with their inherent benefits and challenges.

1. Introduction

Traditionally wireless systems are designed for single predefined mission. Therefore, the antennas of these systems also possess some fixed parameters such as frequency band, radiation pattern, polarization, and gain. Recently reconfigurable antennas (RAs) have gain tremendous research interest for many different applications, for example, cellular radio system, radar system, satellite communication, airplane, and unmanned airborne vehicle (UAV) radar, smart weapon protection. In mobile and satellite communications, reconfigurable antennas are useful to support a large number of standards (e.g., UMTS, Bluetooth, WiFi, WiMAX, DSRC) to mitigate strong interference signal and to cope with the changing environmental condition. On the other hand, in radar applications, reconfigurability at antenna level is often needed for multifunctional operation. This feature is achieved by utilizing antenna array systems that can be quickly adapted according to the mission. Therefore, a control over operating frequency, beam pointing direction, polarization, antenna gain, and so forth is required. A single RA can replace a number of single-function antennas. Thereby overall size, cost, and complexity of a system can be reduced while improving performance such as radar cross-section (RCS). This paper gives a comparative analysis of various concepts that has been utilized to design reconfigurable antennas.

2. Design Concepts for Reconfigurable Antennas

In recent time, many interesting and novel concepts have been developed to achieve adaptable antenna properties. Key aspects of some outstanding concepts will be addressed in the following sections. In our discussion, we mainly focus on antenna design with frequency agility. Some examples of antenna structures with polarization, bandwidth, and pattern reconfigurable property will be addressed as well.

There are basically three design approaches for achieving antenna frequency agility which are as follows:

(a) antennas integrated with electronic switches, mechanical actuators, tunable materials for reconfigurability in terms of circuital characteristics and/or radiation properties;

(b) ultrawideband (UWB) or multiband antennas integrated with tunable filters;

(c) reconfigurable/multiband arrays where the same aperture is utilized for different operational modes.

Table 1: Comparison of tunable components.

Tunable component	Advantages	Disadvantages
MEMS	Reduced insertion loss, good isolation, extremely high linearity, low power losses, consumes little or almost no DC power, wide bandwidth	Need high-control voltage (50–100 V), poor reliability due to mechanical movement within the switch (0.2–100 μs), slow switching speed, discrete tuning, limited lifecycle
PIN Diode	Needs very low driving voltage, high tuning speed (1–100 ns), high power handling capability, very reliable since there are no moving part, extremely low cost	Needs high DC bias current in their on state which consumes a significant amount of DC power, nonlinear behavior, poor quality factor, discrete tuning
Varactor	The current flow through the varactor is small compared to PIN diode or MEMS, continuous tuning	Varactors are nonlinear and have low dynamic range, and complex bias circuitry are required

3. Tunable/Switchable Antenna Technology

Frequency reconfiguration has become important for many modern communication systems. Therefore, there has been a notable advancement in adaptable antenna technology. Among them utilizing the same antenna aperture for different frequencies will provide the most compact solution. Relatively narrowband antennas with tunable or switchable properties are the best solution when the size and efficiency are important issues. This approach reduces the requirements of the front-end filter compared to a UWB or multiband antenna.

Frequency reconfigurable antennas are often realized by employing radio frequency (RF) microelectromechanical systems (MEMS), varactors, or PIN diodes. A comparison of these components is provided in Table 1. The MEMS components have some advantages over PIN or varactor diodes, such as reduced insertion loss, low noise figure, high quality factor, extremely high linearity, low power losses, and negligible direct-current (DC) power consumption. Recent advancements in MEMS technology enable the realization of MEMS with high switching speed and compact size. In [1], a switching time of 225 ns has been reported, and in [2] MEMS with dimensions as small as few μm have been shown. However, integrating a large number of lumped components (e.g., MEMS, varactor) in the radiating element might increase the power loss, noise, and complexity of the biasing circuitry. Furthermore, the power handling capability and the lifetime of these components are also important issues to take into account during the design stage.

In the following sections, some examples of reconfigurable antennas, operating mostly at the lower portion of the microwave spectrum, have been discussed. In this paper, the references are selected based on the applied technologies and design concepts.

3.1. Frequency Tuning with MEMS Switches. Reconfigurable antenna design with RF MEMS switches has gain tremendous research interest [3–12]. A dual-band tunable rectangular slot antenna was presented in [3]. In this design, the frequency tuning was achieved by utilizing the RF MEMS variable capacitor on a stub as depicted in Figure 1. The DC voltage of the MEMS is applied between the RF signal line and the ground plane which eliminated the need for additional bias lines. Simulation and experimental results predicted that the resonance frequencies of the antenna can be shifted from 10.22 GHz to 10.57 GHz and from 7.7 GHz to 8.7 GHz. However, in this design, independent tuning in both frequency bands is not achieved.

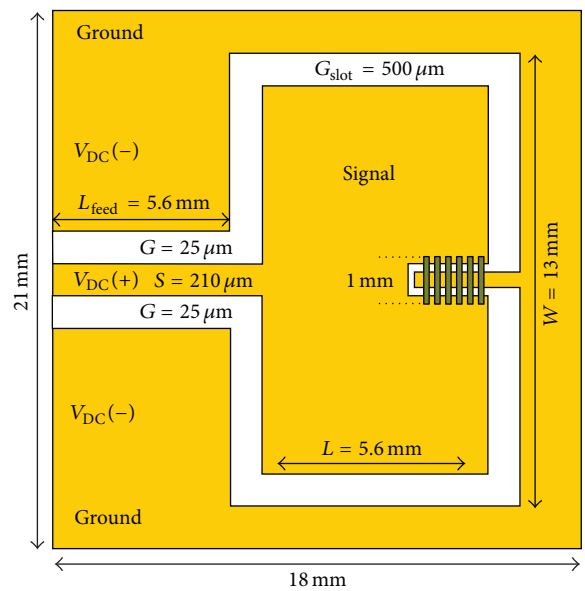

Figure 1: Slot-ring antenna loaded with MEMS [3].

A capacitive MEMS loaded PIFA antenna (see Figure 2) has been studied in [4]. The outcome of this study confirmed that the antenna is capable of operating over a bandwidth of more than one octave while improving the performance in terms of specific absorption rate.

A well-known example of frequency tuning with MEMS is the pixel antenna concept (see Figure 3) which allows for switching in frequency band, polarization, and/or scan angle [5]. The disadvantage of this approach is the need of many switches which will increase the cost and the power loss, as well as the complexity of the biasing circuit.

In [7], the topology of a reconfigurable microstrip patch antenna using RF-MEMS has been presented (see Figure 4). In this study, the production cost of the antenna on quartz substrate has been reduced using only two lithographic steps.

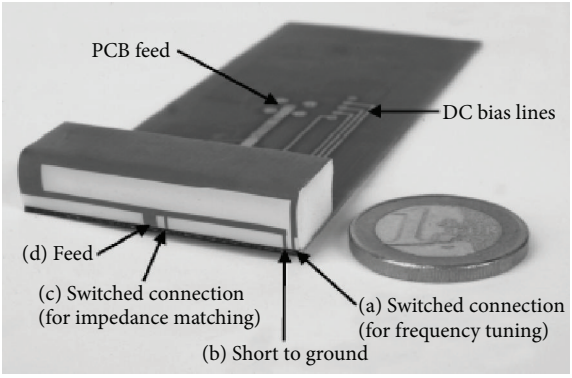

Figure 2: Frequency switchable PIFA antenna with MEMS [4].

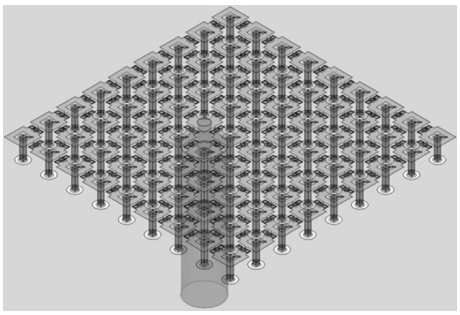

Figure 3: Frequency reconfigurable pixel patch antenna [6].

Therefore, this antenna has potential to be fabricated as an integrated antenna system on the chip (SoC). The results presented in [7] confirmed that the operational band of the antenna can be switched between 5.25 GHz and 5.6 GHz. However, due to the high ohmic losses in the aluminum, this antenna structure is characterized by poor radiation efficiency.

The antenna proposed in [8] provides frequency and polarization reconfigurability. By properly selecting the ON/OFF state of different RF-MEMS (Figure 5), the antenna can be configured into right-handed circular polarization (RHCP), left-handed circular polarization (LHCP), or linear polarization. Furthermore, the resonance frequency for linear polarization shifts depending if all the MEMS are in ON state or OFF state. The proposed design provides impedance bandwidth of 9% relative to 10 dB return loss level when configured for linear polarization. For circular polarization, the fractional bandwidth is 11% although, it is to be noticed, the −3 dB axial ratio bandwidth is only 1.6%.

3.2. Frequency Tuning with Varactors. Integrating varactors in an antenna structure is a common way for achieving frequency agility [13–18]. In [13], a new and simple antenna topology for frequency and polarization diversity is presented (Figure 6). In this design, the resonating microstrip radiator consists of several smaller patches which are interconnected by varactors. These varactors are independently biased to change the electrical lengths of the corresponding patches

Figure 4: Frequency switchable antenna based on MEMS technology [7].

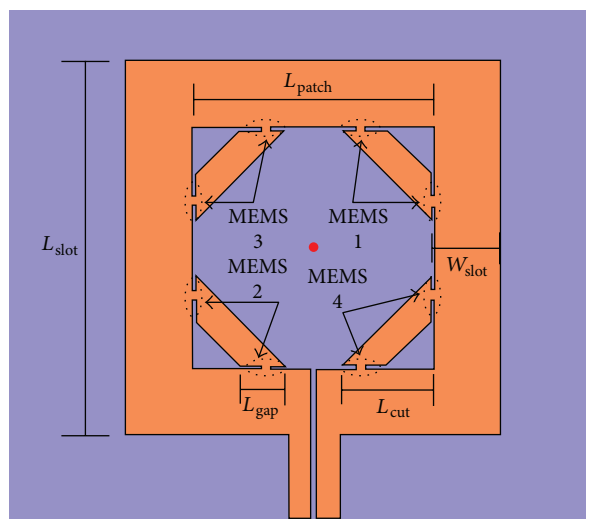

Figure 5: Frequency and polarization agile patch antenna [8].

and thereby change the resonant frequency of the corresponding modes. In addition, unbalanced biasing of varactor sets electrically shifts the feed point out of the antenna center. In this way, the real part of the feed-point impedance has been modified to obtain the desired optimal impedance matching. The angular position of the feed point defines the antenna polarization state. So, the whole microstrip structure can be adjusted in terms of electrical size, shape, and feed-point location, while maintaining its well-known characteristics.

A differentially fed microstrip antenna with frequency tuning capability has been presented in [14] where varactor diodes have been utilized to tune the operational band (see Figure 7). In [17], adjustable high impedance surface (HIS) using varactor diodes has been utilized in an active reflectarray (Figure 8). The reflection phase coefficient of these unit cells can be controlled by changing the capacitance

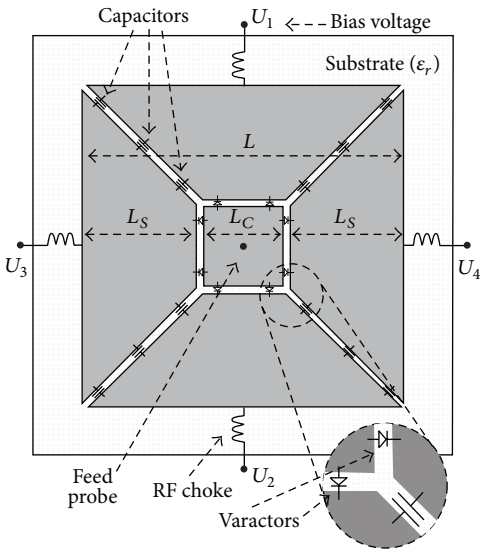

Figure 6: Varactor-loaded patch antenna [13].

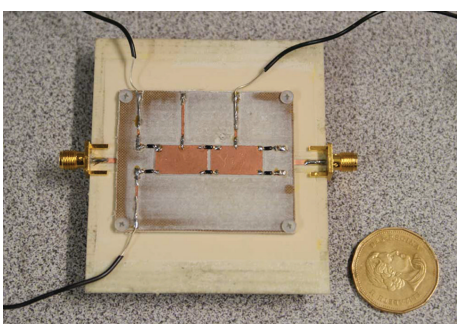

Figure 7: Frequency tunable differentially fed patch antenna [14].

values of these varactors. This ability to change the phase of the reflection coefficient of the unit cell gives the possibility to reconfigure the radiation pattern of the array.

3.3. Frequency Tuning with PIN Diodes. Many antenna engineers use PIN diode as the switching component [18–29]. In [18], a reconfigurable meander radiator is proposed which is composed of three PIN diodes and one varactor diode (see Figure 9). In this respect, the varactor diode is useful to adjust the resonant frequency in a fine way. It has been demonstrated that, by properly selecting the state of the diodes, the resonant frequency can be tuned from 470 MHz to 1080 MHz.

In the study presented in [19], a switchable Vivaldi antenna has been demonstrated to provide either a narrow- or wideband frequency response. As it can be noticed in Figure 10, ring slots bridged by PIN diode switches have been inserted in the radiating element to obtain a narrowband resonating behavior at different frequencies. On the other hand, the PIN diodes are deactivated wherein a wideband operation is desired.

A frequency reconfigurable L/S band phased-array antenna has been studied in [20, 21]. As illustrated in Figure 11, square-ring loaded probe-fed reconfigurable patch elements were arranged in such a way that half wavelength element spacing has been maintained at both frequency bands and hence provides wide angle scanning at both bands.

In [22], a polarization reconfigurable slot antenna is proposed. Here the antenna polarization can be switched between vertical and horizontal polarization by changing the feeding structure between CPW feed and slotline feed. The geometry of the antenna is presented in Figure 12. The operating modes of the CPW-to-slotline transition are shown in Figure 13. When PIN 1 is ON and PIN 2 is OFF, the structure operates in the CPW mode. The slotline mode is activated when PIN 2 is ON and PIN 1 is OFF. In this case, the right slotline is used to feed the horizontal polarization. The electric field distribution of this design for two orthogonal polarizations is presented in Figure 14.

The proposed method provides polarization agility with single feed line. The test result of this structure indicates a wideband operation (>25%). However, the reduced polarization purity is a limiting factor. Furthermore, the implementation of the PIN diode in the CPW line might degrade the antenna performance.

3.4. Mechanically Reconfigurable Antennas. The antenna topologies discussed above utilized lumped tunable components. More recently for applications where RF switches are not desired due to the additional power losses in the switches and complexity of the bias lines, mechanically reconfigurable antennas are being investigated [30–32]. Mechanically reconfigurable antennas are promising devices which can provide reduced RF loss, higher isolation, and better linearity with respect to antenna structures integrated with electronic switches. Nevertheless, practical issues, such as the total size and overall complexity of the system, need to be considered. In [30], a rotatable antenna has been designed for cognitive radio to tune the operational band from 2 to 10 GHz.

Mechanically reconfigurable antennas have also been used to achieve pattern diversity with a single radiating element. For systems which do not require fast pattern reconfiguration, this approach is attractive to replace the need of expensive phased array. In [31], a square ring antenna with a bendable parasitic plate has been used for machine-to-machine (M2M) communications (see Figure 15).

3.5. Frequency Reconfigurability by Tunable Materials. Reconfigurability with tunable material is a very new research area and still facing challenges such as reliability, efficiency, and proper modeling. However, in recent times many researches are carried out in this region and notable achievements have been reported [33–38]. Ferroelectric dielectric materials can be used for reconfigurable antennas as their permittivity changes with the applied DC bias voltage (see Figure 16) [33]. Disadvantage of this type of material is the large bias voltage required to change the dielectric constant and high losses of the material. However, some results indicated that this type of antenna can provide higher directivity, narrow main lobe, and lower side lobes level than conventional phased array.

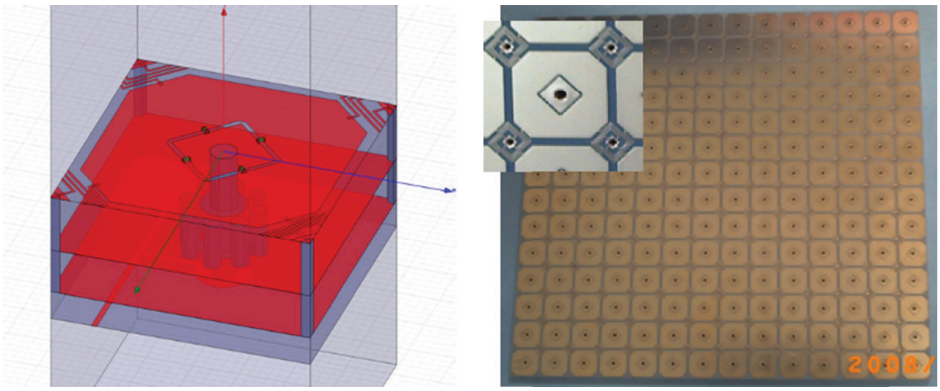

(a) (b)

Figure 8: Basic geometry of the unit cell (a) and the array structure (b) of an adjustable high impedance surface [17].

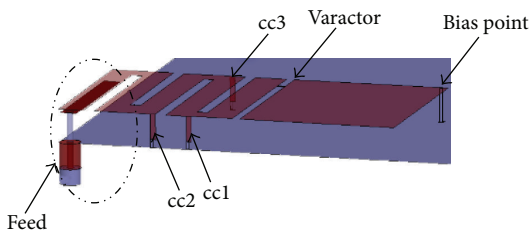

Figure 9: Reconfigurable meander antenna loaded with PIN diodes (cc1, cc2, and cc3) [18].

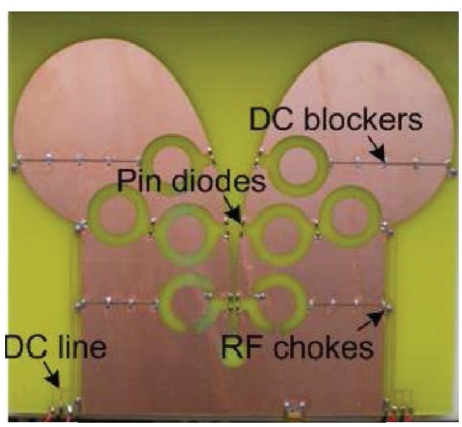

Figure 10: Switchable Vivaldi antenna [19].

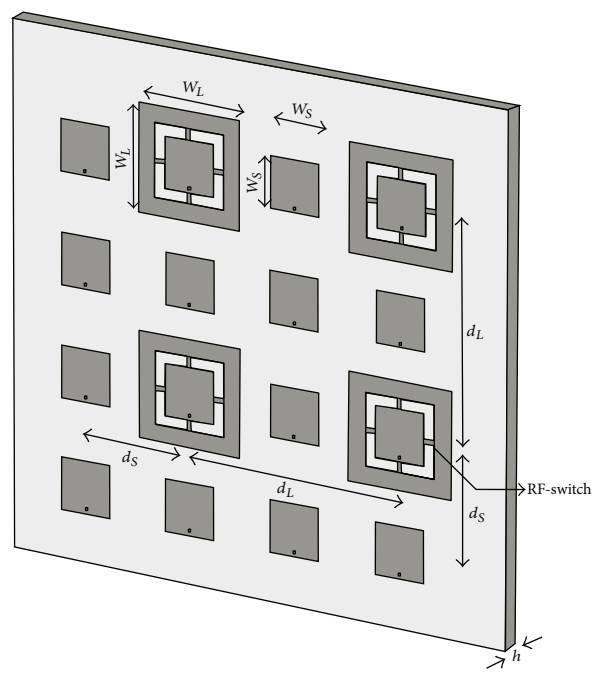

Figure 11: Reconfigurable ring-loaded patch antenna array [20].

In [34], a waveguide slot antenna with reconfigurable aperture is presented (see Figure 17). The reconfigurable aperture consists of a number of surface PIN diodes (SPIN). The conductivity of SPIN changes proportionally to the plasma density. These SPIN diodes can be activated or deactivated to produce the desired radiation pattern. Therefore, additional flexibility can be achieved compared to conventional waveguide slot antennas. In this design, plasma regions which have relatively high electrical conductivity can be temporarily created inside a silicon substrate. This way a different antenna configuration can be created. For this, a semiconductor chip has been used which contains the PIN structures. The chip acts as a planar dielectric waveguide and electromagnetic waves can propagate in it. It has been claimed in [34] that the plasma of carriers created by forward biased PIN structures locally affects the wave propagation velocity and helps to steer the beam within a wide steering angle.

Another example of reconfigure antenna with tunable material property is the plasma antenna. Metal-like conductive plasma channels in high-resistivity silicon can be activated by the injection of a suitable DC current [35]. The proposed structure is illustrated in Figures 18 and 19. One metal on alumina and three identical plasma islands constitute the monopole antenna. The plasma channels are

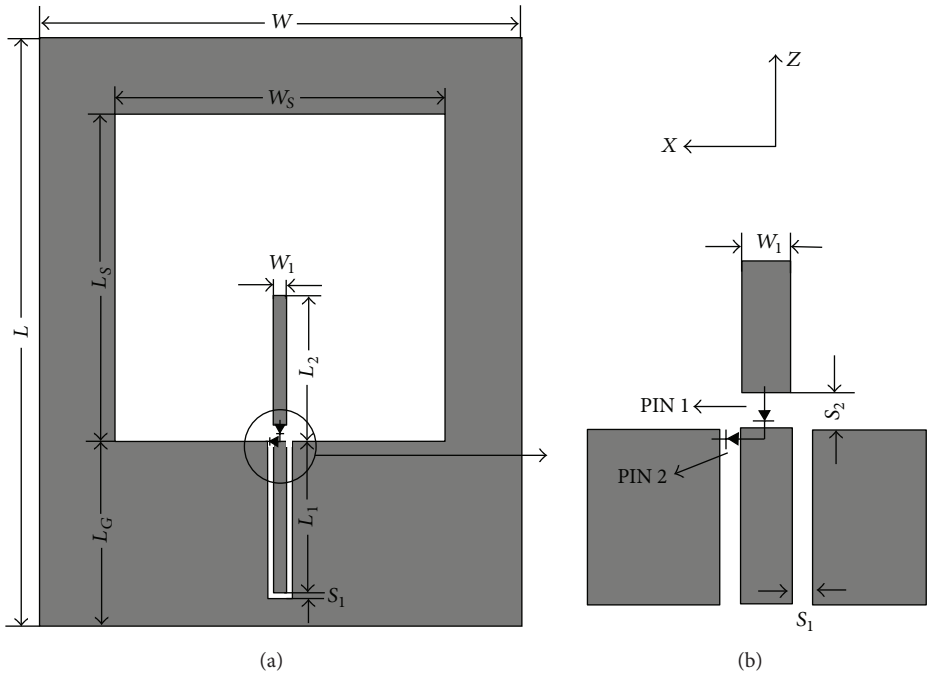

Figure 12: Geometry of a reconfigurable slot antenna [22].

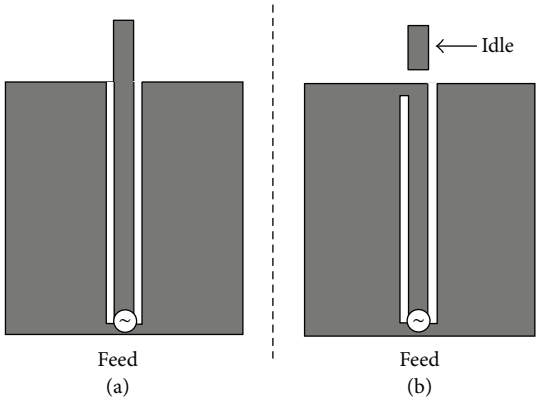

Figure 13: Feeding structure of the reconfigurable slot antenna: (a) CPW mode; (b) slotline mode [22].

realized by using high-resolution silicon fabrication technology. It has been pointed out in [35] that these reconfigurable antennas enable frequency hopping, beam shaping, and steering without the complexity of RF feed structures. The approach presented in [35] can provide high resolution due to the advancements in semiconductor technology.

A new approach which has recently gained a lot of research interest is the liquid crystal tunable antennas. The permittivity of a liquid crystal can be varied with DC bias voltage. Liquid crystals (LCs) are substances whose phase of matter has properties of both a conventional liquid and a solid crystal. The dielectric permittivity of an LC can be varied by orienting its molecules with an electrostatic or magnetostatic field or by surface interaction with a mechanically rubbed polyamide film. Researches of Sheffield University have demonstrated an LC tunable microstrip patch antenna at 5 GHz [36] with a tuning range of 4–8% (see Figure 20). However, due to the high losses in the LC material, the antenna suffered from poor efficiency (20–40%).

It is, however, to be noticed that, while the electromagnetic behavior of LCs is well understood at optical frequencies, the use of LCs at microwave and millimeter-wave frequencies requires first their electromagnetic characterization in terms of dielectric properties at these frequencies. The available literature on this topic is limited to a few LC mixtures. Overall it appears that a careful design of the mixture is of crucial importance for the applicability of this type of material in reconfigurable devices. Besides the above-mentioned reconfigurable concepts, other promising research areas are emerging, such as the exploitation of microfluidics [39, 40], optical controls [41, 42], and graphene [43, 44] in reconfigurable antennas.

4. Wideband Antenna Integration with Tunable Filters

In Section 4, some examples of reconfigurable antenna with tunable or switchable components have been provided. Another approach is to use ultrawideband or multiband antenna elements [45–60]. In this approach, one needs antenna solutions which feature good performance (good impedance matching, radiation pattern, gain, etc.) for the whole bandwidth of interest and a tunable filter will be used to select the operational frequency band. Furthermore, for phased-array application, unidirectional radiation is required.

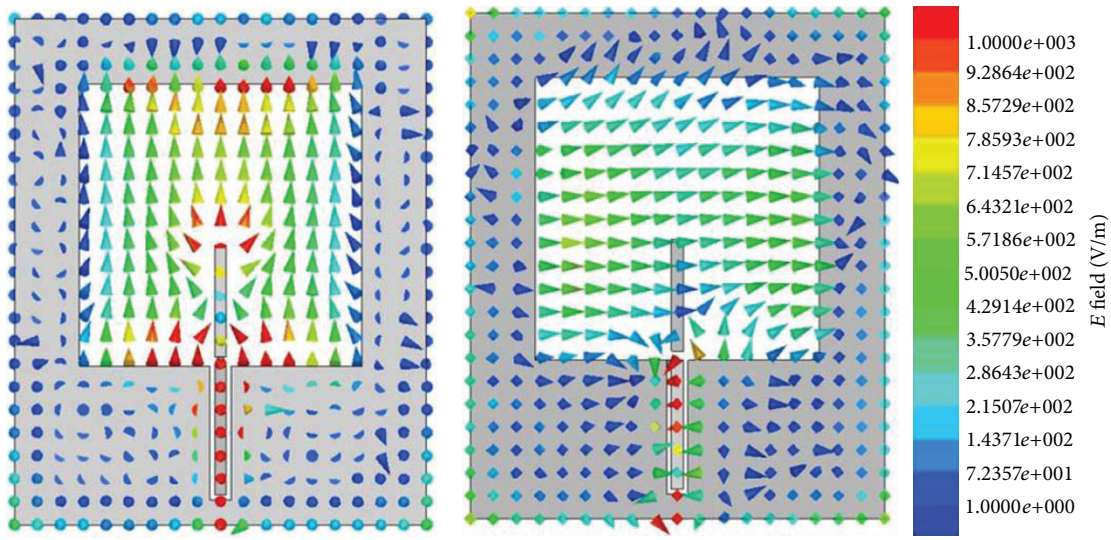

(a) (b)

Figure 14: Electric field distribution within the reconfigurable slot antenna: (a) CPW mode; (b) slot-line mode [22].

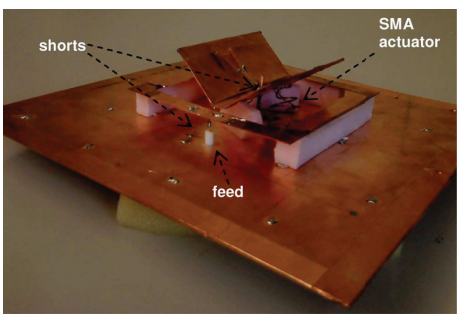

Figure 15: Reconfigurable square ring-patch antenna with dual-flap ground-shorted parasitic patch [31].

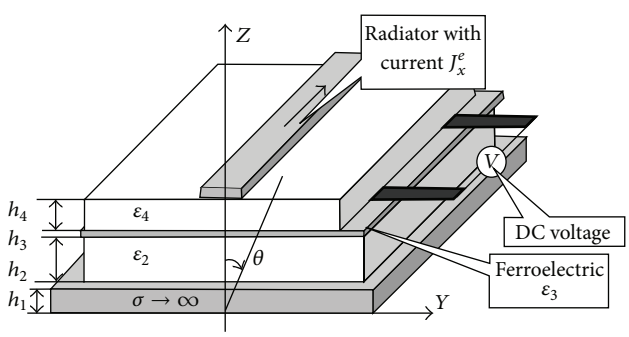

Figure 16: Ferroelectric antenna concept [33].

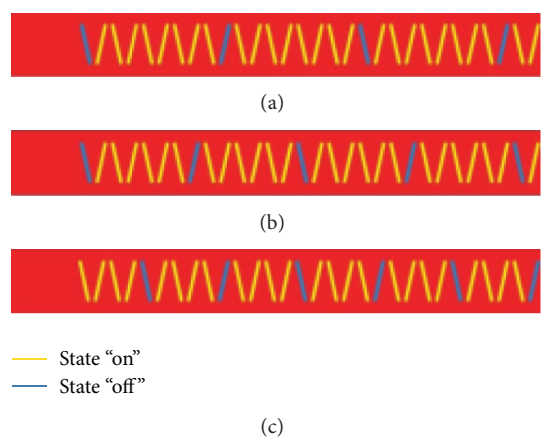

Figure 17: Slotted waveguide antenna [34].

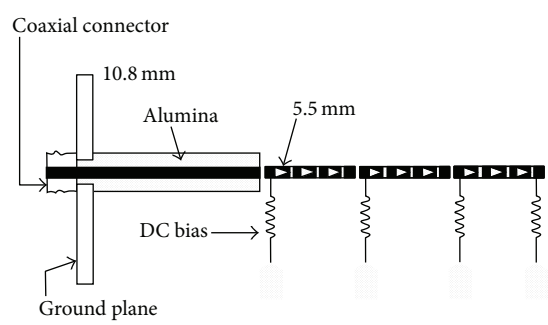

Figure 18: Assembled monopole unit [35].

There has been a lot of broadband antenna design for different applications. For instance, transversal electromagnetic (TEM) horn or dielectric filled waveguide antenna can provide extremely wide bandwidth with directive radiation pattern. End fire wideband antennas, such as antipodal Vivaldi antennas and linear tapered slot antenna (LTSA) can also be used for phased array. Dual polarized Vivaldi antenna arrays (see Figure 21), can be designed for more than 10:1 bandwidths while scanning 45° or more. But to date, the high cross-polarization and high mutual coupling

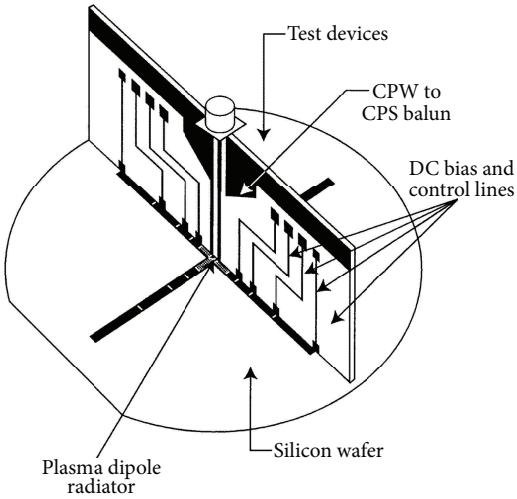

Figure 19: Monolithic dipole on a silicon wafer [35].

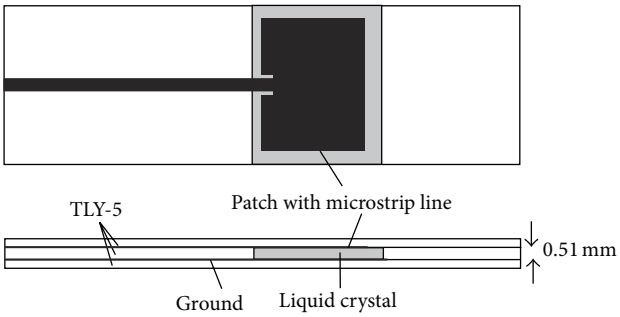

Figure 20: LC tunable microstrip patch antenna [36].

between the elements have been a major limiting factor. Other potential candidates of UWB phased-array element are the 3D monopole antenna (fat monopole, tab monopole, cylindrical monopole) and dielectric resonator or dielectric lens antenna. Nevertheless, there are some challenges when UWB antenna element is utilized in multifrequency radar system. Firstly, antenna performance should be good and consistent over a very wide frequency band. Furthermore, this approach requires filters with very high out-of-band noise rejection capability.

An alternative solution is to place the filter in the radiating element itself. This will relax the preselect filter requirements. An example of this design approach is provided by the reconfigurable Vivaldi antenna presented in [16], where a bandpass filter is integrated in the feeding line of the radiating structure resulting in a frequency switchable filtenna. As shown in Figure 22, a varactor diode is inserted within the filter structure in order to provide frequency reconfiguration capability. This concept is attractive since it does not require the insertion of switching component directly in the radiating element.

In [47], a directive UWB antenna with large fractional bandwidth has been designed for full-polarimetric array. As depicted in Figure 23 in this study linearly polarized antennas are grouped together and fed in such a way that

Figure 21: Dual-polarized Vivaldi array [45].

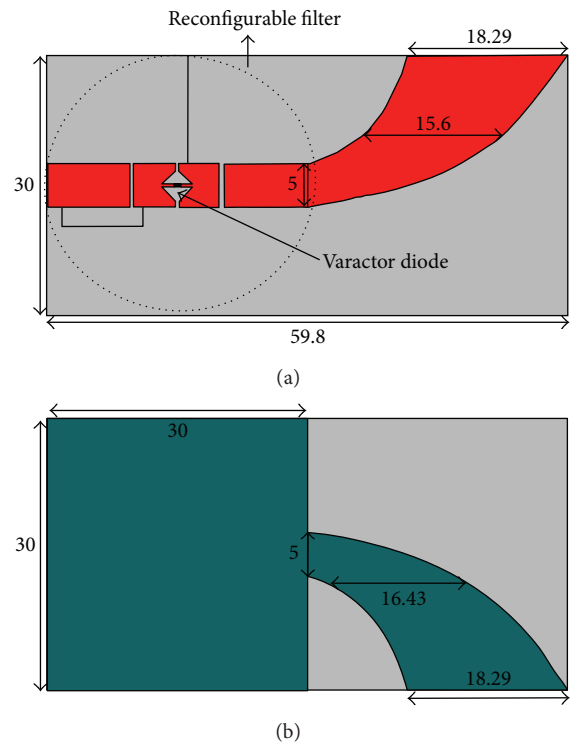

Figure 22: Frequency reconfigurable filtenna: (a) top layer and (b) bottom layer [16].

they can radiate fields in two orthogonal planes while maintaining their wideband properties. A nondispersive wideband antenna has been used as the radiating element. The antenna concept is based on the combination of the electromagnetic characteristics of a loop and a planar monopole [48, 49].

5. Reconfigurable Array Structures

In the two approaches detailed in the previous sections, the same radiating element is used for different frequency

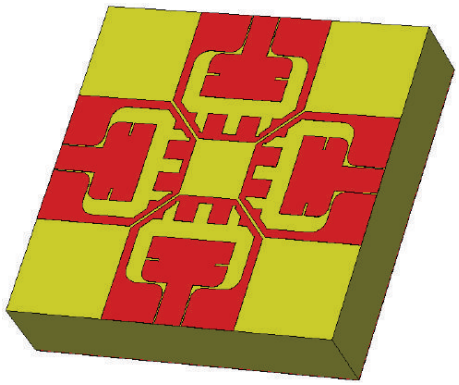

Figure 23: Dual-polarized UWB subarray [47].

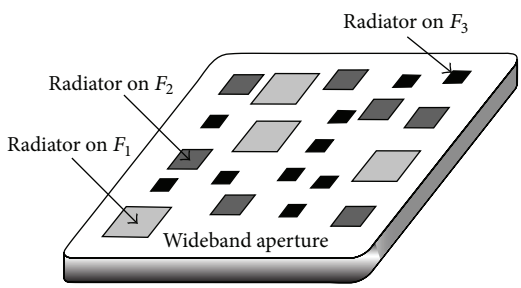

Figure 24: Shared aperture antenna [61].

bands. An alternative solution is to employ different radiating elements for different antenna performances. Advantages of this approach are the simple configuration and frequency jumps that can be extremely large. However, for this approach separate antenna arrays and feeding networks are required which will increase the total size.

5.1. Shared Aperture Antennas. The shared aperture antenna is one example of the mentioned design concept. In this approach, the idea is to share the physical area of the antenna aperture between different subarrays. The concept is illustrated in Figure 24. Here interleaved matrix of radiators is used [61]. This concept can be utilized for multifrequency, multifunction, and multipolarization applications. The advantage of shared aperture antenna is possibility to perform multiple tasks, achieve narrow beam width, avoid amplitude tapering, and so forth. The main challenges related to shared aperture antenna is to design subarrays which satisfies their requirements and placing the elements on the same aperture while avoiding any physical overlapping.

Another notable example of multiband array is presented in [62]. Here an interleaved phased array is utilized with waveguide element and wideband tapered element (see Figure 25). The array operates in triband and C, X and Ku band. The waveguide element operates at Ku band and the wideband "bunny ear" element operates at C to X band. In this design, the two types of elements are orthogonally polarized and therefore isolation between them is very high. However, the coupling between two adjacent wideband

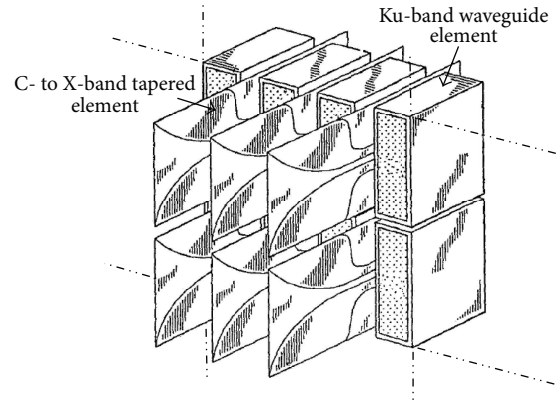

Figure 25: Multiband phased-array antenna with interleaved elements [62].

elements is very high, this being the major limiting factor for the array performance.

5.2. Multilayer Antennas. An alternative solution of shared aperture antenna is multilayer antenna array. In [63], a dual-frequency dual-polarized array antenna is presented (see Figure 26). Two planar arrays are incorporated for simultaneous S- and X-band operation. Rectangular ring resonator and circular patches are used as the radiating elements at S and X bands, respectively. These circular patches are combined to form the array using a series-fed structure to save the space of the feeding line network. The S-band elements are placed on the top substrate, and a foam layer is used to separate the array. One of the important design considerations for any multilayer array is that the antennas operating at different bands should be nearly transparent to each other to avoid performance degradation.

For reflector antennas frequency agility can be achieved by mounting several feed horns about the focus (with some degradation of pattern characteristics). Reflector type antenna has very high efficiency but requires mechanical movement to steer its beam. Furthermore, it is not flat and not easy to integrate on a host platform, and is significantly bulkier than planar antennas. As a result reflectarray antennas are often used. These are low cost, low profile, and high gain antennas with the beam scanning capability of a phased-array antenna. However, the disadvantage of reflectarray is the limited bandwidth caused by the narrow bandwidth of the elements and the different phase lengths needed at each frequency for beam steering. Dual frequency reflectarray can be designed by using dual layers of radiating elements [64]. An example of dual frequency reflectarray is presented in Figure 27.

Another notable example of multiband array is presented in [65]. As the S-band elements, dipoles are used while square patches are used as the X-band element (see Figure 28). The dual frequency ratio is here 1 : 3. The measured bandwidth of VSWR < 2 are 8.9% for S band and 17% for X band. The disadvantage of this approach is the complex fabrication process due to the five substrate layers. Furthermore, every

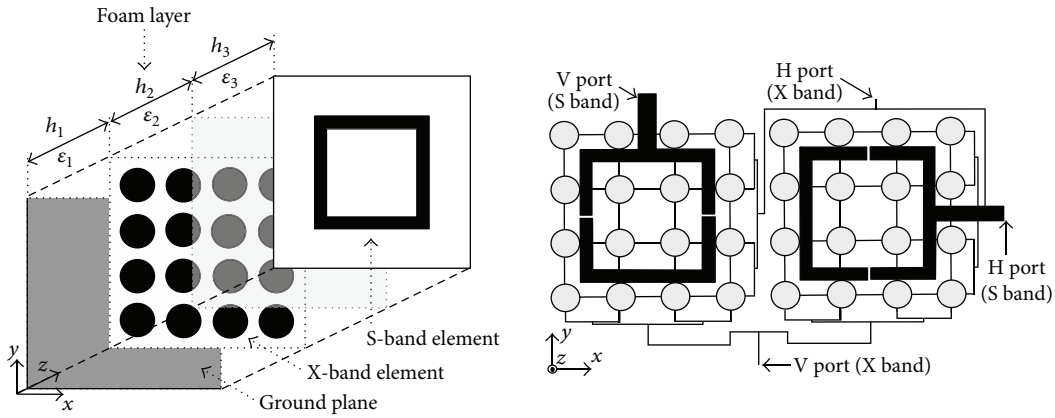

Figure 26: A dual-polarized planar-array antenna for S and X band [63].

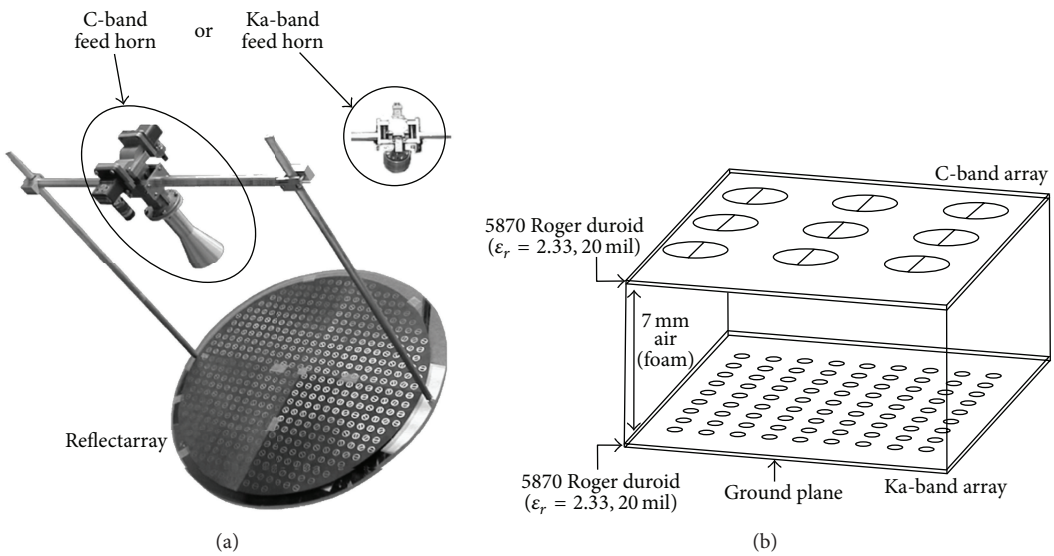

Figure 27: Dual-layer reflectarray topology [64].

dual-polarized antenna element of both bands has two coaxial connectors beneath the substrates of the antenna. Therefore, a large number of connectors is required for the array structure. As stated in [65], a dual-polarized 2×1 S-band or 7×4 X-band array will need 60 coaxial connectors.

6. Conclusions

Reconfigurable antennas have their applications in numerous areas such as communications and surveillance. They possess the properties to modify the relevant circuital characteristics and/or radiation properties in real time. The implementation of several functionalities on the same antenna requires topological reconfigurability to achieve radiation pattern and frequency agility. In particular, parameters such as the shape and size of the array and the grid spacing should be changed to adapt to the requirements set by the considered functionality. Moreover, digital beam forming in transmit and receive would offer great flexibility in the definition of the field of view and coverage. This requires both the possibility to choose the most suited beam-forming algorithm and corresponding calibration procedure. The antenna element can be reconfigured to obtain frequency, polarization, and/or radiation pattern agility. Frequency agility can be intended either as the ability to switch between different operating frequency bands (linked to the sensor application), for example, in a multifunctional system, or to tune the centre frequency of the instantaneous bandwidth within the total operating bandwidth of a specific communication or sensing functionality. The first case requires reconfigurability not only at antenna element level, with switching components such to obtain proper antenna operation within the aimed frequency bands, but also at array topology level, to correspondingly adapt the array spacing. The second case considers narrow-band elements whose centre frequency is tuned with tunable components or substrates. Polarization agility refers to the ability to change the polarization of the transmitted/received electromagnetic field, for example, between two orthogonal

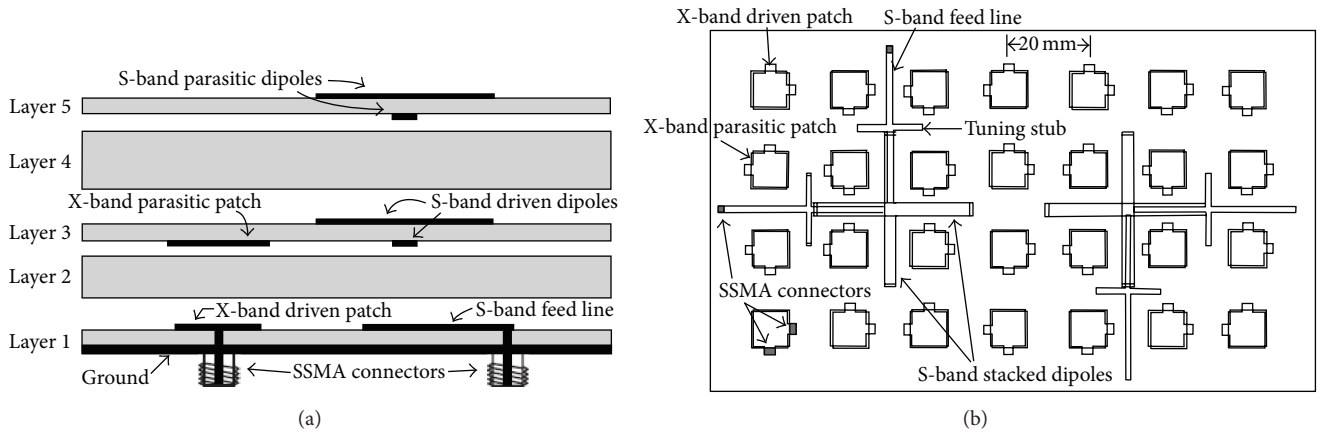

Figure 28: Dual-band dual-polarized antenna array: (a) side view and (b) top view [65].

linear polarizations or between linear and circular polarization. Polarization agility is an asset to implement on the same hardware platform functionalities with different polarization requirements, such as communication (typically circular) and surveillance (typically linear). Enabling technologies for antenna reconfigurability are switches, variable capacitances, and tunable substrates. These technologies are especially suitable for antennas realized in printed technology. A radiating element in printed technology consists of a metallic surface to which an electric signal is coupled through a guiding line. Switches such as PIN diodes and RF MEMS are typically used to electrically connect/disconnect metallic parts in order to introduce (discretized) changes in the geometry of the total radiating surface. The power handling capability and the lifetime of the switches are important issues. MEMS switches have some advantages over PIN diodes, such as lower insertion loss, lower noise figure, higher quality factor, higher linearity, lower power losses, and very little DC power consumption. However, they show higher actuation voltage and longer switching time. Recent advances in MEMS technology enable the realization of MEMS with improved switching speed and compact size. Varactor diodes provide a capacitance that can be continuously tuned by acting on the diode bias voltage. In view of this, they are typically used as a load to tune the resonance frequency of the antenna element. MEMS with capacitance variable in a given range represent a topic of research but currently available prototypes are not yet sufficiently reliable. Tunable materials, such as ferrite, ferroelectric materials, and liquid crystals are materials whose dielectric properties can be changed by applying an electric or magnetic field. Therefore, they can be used as antenna substrates to uniformly vary the size of the radiating surface therewith obtaining, for example, a change in the resonant frequency or beam steering. At least three approaches can be identified to obtain an antenna able to cover different frequency bands, for example, corresponding to different functionalities: by using very wideband technology, by considering frequency tunable antenna elements, or by implementing dual (multi-) layered arrays. Moreover, if frequency agility is required also filtering of out-of-band signals should be reconfigurable.

Tunable/Switchable Antenna Technology. Among different radiators, an adaptive element will provide the most compact solution and therefore can be easily realized in a dense array. Tunable or switchable narrowband antennas are the best solution when the size and efficiency are important issues. This approach reduces the requirements of the front-end filter compared to a UWB or multiband approach. An adaptive antenna can be realized by changing the physical structure of the radiator, for example, through switches or varactor diodes. However, integrating large number of lumped components (e.g., MEMS, diodes) in the radiating element might increase the power loss, noise, and complexity of the biasing circuitry. For this reason, an alternative approach consists in implementing the switch at the level of the matching network, which is typically located under the ground plane (for antenna in printed circuit board) between the antenna element and the TR module. More recently, antennas which are tuned by varying substrate properties have gained some research interest. Ferrite, ferroelectric material, and liquid crystal are used for these tunable antennas. However, these researches are still at a preliminary state and are facing challenges like reliability, efficiency, accurate control of the material property, and proper modeling.

Wideband Antenna Integration with Tunable Filters. An UWB or multiband antenna makes it possible to cover a very wide bandwidth which can encompass all desired frequencies of operation. Most of the proposed radiating elements are evolutions of the tapered slot antenna and have a three-dimensional geometry. Consequently, the main design challenges include feeding network, mutual coupling, and the need of filters for multifunctional operations. An alternative solution is to place the filter in the radiating element itself. This will relax the preselect filter requirements.

Reconfigurable Arrays. This approach involves fully populated individual arrays placed together in a manner as to minimize the interference of one (array) over the other. Elements for both arrays can be combined into individual modules. For the dual layer approach to minimize performance degradation the top array should be nearly transparent to the bottom

layer. Therefore, the structure of the radiating element should be carefully considered. Moreover, if these arrays have to be made reconfigurable, the corresponding bias lines at different layers would affect the performance of the other layers.

Acknowledgment

This study is conducted as part of the Sensor Technology Applied in Reconfigurable Systems for Sustainable Security (STARS) project. For further information: http://www.starsproject.nl/.

References

[1] G. N. Nielson, M. J. Shaw, O. B. Spahn et al., "High-speed, sub-pull-in voltage MEMS switching," SANDIA REPORT SAND2008-0211, 2008.

[2] N. Biyikli, Y. Damgaci, and B. A. Cetiner, "Low-voltage small-size double-arm MEMS actuator," *Electronics Letters*, vol. 45, no. 7, pp. 354–356, 2009.

[3] K. Topalli, E. Erdil, O. A. Civi, S. Demir, S. Koc, and T. Akin, "Tunable dual-frequency RF MEMS rectangular slot ring antenna," *Sensors and Actuators A*, vol. 156, no. 2, pp. 373–380, 2009.

[4] K. R. Boyle and P. G. Steeneken, "A five-band reconfigurable PIFA for mobile phones," *IEEE Transactions on Antennas and Propagation*, vol. 55, no. 11, pp. 3300–3309, 2007.

[5] W. H. Weedon, W. J. Payne, and G. M. Rebeiz, "MEMS-switched reconfigurable antennas," in *Proceedings of the IEEE International Symposium on Antennas and Propagation*, pp. 654–657, 2001.

[6] A. Grau and F. De Flaviis, "A distributed antenna tuning unit using a frequency reconfigurable PIXEL-antenna," in *Proceedings of the 4th European Conference on Antennas and Propagation (EuCAP '10)*, pp. 1–5, April 2010.

[7] A. Vasylchenko, X. Rottenberg, B. X. Broze, M. Nuytemans, W. De Raedt, and G. A. E. Vandenbosch, "A frequency switchable antenna based on MEMS technology," in *Proceedings of the 4th European Conference on Antennas and Propagation (EuCAP '10)*, pp. 1–3, April 2010.

[8] J. Balcells, Y. Damgaci, B. A. Cetiner, J. Romeu, and L. Jofre, "Polarization reconfigurable MEMS-CPW antenna for mm-wave applications," in *Proceedings of the 4th European Conference on Antennas and Propagation (EuCAP '10)*, April 2010.

[9] A. Grau, J. Romeu, M. J. Lee, S. Blanch, L. Jofre, and F. De Flaviis, "A Dual-Linearly-polarized MEMS-reconfigurable antenna for narrowband MIMO communication systems," *IEEE Transactions on Antennas and Propagation*, vol. 58, no. 1, pp. 4–17, 2010.

[10] S. Yang, H. K. Pan, A. E. Fathy, S. El-Ghazaly, and V. K. Nair, "A novel reconfigurable mini-maze antenna for multi-service wireless universal receiver using RF MEMS," in *Proceedings of the IEEE MTT-S International Microwave Symposium Digest*, pp. 182–185, June 2006.

[11] C.-Y. Chiu, J. Li, S. Song, and R. D. Murch, "Frequency-reconfigurable pixel slot antenna," *IEEE Transactions on Antennas and Propagation*, vol. 60, no. 10, pp. 4921–4924, 2012.

[12] D. E. Anagnostou, G. Zheng, L. Feldner et al., "Silicon-etched re-configurable self-similar antenna with RF-MEMS switches," in *IEEE Antennas and Propagation Society Symposium*, vol. 2, pp. 1804–1807, June 2004.

[13] T. Korošec, P. Ritoša, and M. Vidmar, "Varactor-tuned microstrip-patch antenna with frequency and polarisation agility," *Electronics Letters*, vol. 42, no. 18, pp. 1015–1016, 2006.

[14] S. V. Hum and H. Y. Xiong, "Analysis and design of a differentially-fed frequency agile microstrip patch antenna," *IEEE Transactions on Antennas and Propagation*, vol. 58, no. 10, pp. 3122–3130, 2010.

[15] C. R. White and G. M. Rebeiz, "Single- and dual-polarized tunable slot-ring antennas," *IEEE Transactions on Antennas and Propagation*, vol. 57, no. 1, pp. 19–26, 2009.

[16] Y. Tawk, J. Costantine, and C. G. Christodoulou, "A varactor-based reconfigurable filtenna," *IEEE Antennas and Wireless Propagation Letters*, vol. 11, pp. 716–719, 2012.

[17] P. Ratajczak, J.-M. Baracco, and P. Brachat, "Adjustable high impedance surface for active reflectarray applications," in *Proceedings of the 2nd European Conference on Antennas and Propagation (EuCAP '07)*, pp. 1–6, November 2007.

[18] F. Canneva, J. M. Ribero, and R. Staraj, "Tunable antenna for DVB-H band," in *Proceedings of the 4th European Conference on Antennas and Propagation (EuCAP '10)*, pp. 1–3, April 2010.

[19] M. R. Hamid, P. Gardner, P. S. Hall, and F. Ghanem, "Switched-band Vivaldi antenna," *IEEE Transactions on Antennas and Propagation*, vol. 59, no. 5, pp. 1472–1480, 2011.

[20] N. Haider, D. P. Tran, A. G. Roederer, and A. G. Yarovoy, "Reconfigurable L/S band phased array," *Electronics Letters*, vol. 47, no. 23, pp. 1265–1266, 2011.

[21] N. Haider, D. P. Tran, and A. G. Yarovoy, "A new concept for frequency reconfigurable phased-array element," in *Proceedings of the Antennas and Propagation Conference (LAPC '11)*, pp. 1–4, Loughborough, UK, November 2011.

[22] Y. Li, Z. Zhang, W. Chen, and Z. Feng, "Polarization reconfigurable slot antenna with a novel compact CPW-to-slotline transition for WLAN application," *IEEE Antennas and Wireless Propagation Letters*, vol. 9, pp. 252–255, 2010.

[23] D. Piazza, N. J. Kirsch, A. Forenza, R. W. Heath, and K. R. Dandekar, "Design and evaluation of a reconfigurable antenna array for MIMO systems," *IEEE Transactions on Antennas and Propagation*, vol. 56, no. 3, pp. 869–881, 2008.

[24] D. Piazza, P. Mookiah, M. D'Amico, and K. R. Dandekar, "Experimental analysis of pattern and polarization reconfigurable circular patch antennas for MIMO systems," *IEEE Transactions on Vehicular Technology*, vol. 59, no. 5, pp. 2352–2362, 2010.

[25] J. Ollikainen, O. Kivekäs, and P. Vainikainen, "Low-loss tuning circuits for frequency-tunable small resonant antennas," in *Proceedings of the 13th IEEE International Symposium on Personal, Indoor and Mobile Radio Communications (PIMRC '02)*, vol. 4, pp. 1882–1887, September 2002.

[26] T.-Y. Han and C.-T. Huang, "Reconfigurable monopolar patch antenna," *Electronics Letters*, vol. 46, no. 3, pp. 199–200, 2010.

[27] D. Peroulis, K. Sarabandi, and L. P. B. Katehi, "Design of reconfigurable slot antennas," *IEEE Transactions on Antennas and Propagation*, vol. 53, no. 2, pp. 645–654, 2005.

[28] S.-X. Cao, X.-X. Yang, B. Gong, and B.-C. Shao, "A reconfigurable microstrip antenna with agile polarization using diode switches," in *IEEE International Symposium on Antennas and Propagation (APSURSI '11)*, pp. 1566–1569, July 2011.

[29] A. C. K. Mak, C. R. Rowell, and R. D. Murch, "Low cost reconfigurable landstorfer planar antenna array," *IEEE Transactions on Antennas and Propagation*, vol. 57, no. 10, pp. 3051–3061, 2009.

[30] Y. Tawk, J. Costantine, K. Avery, and C. G. Christodoulou, "Implementation of a cognitive radio front-end using rotatable controlled reconfigurable antennas," *IEEE Transactions on Antennas and Propagation*, vol. 59, no. 5, pp. 1773–1778, 2011.

[31] S. J. Mazlouman, A. Mahanfar, C. Menon, and R. G. Vaughan, "Square ring antenna with reconfigurable patch using shape memory alloy actuation," *IEEE Transactions on Antennas and Propagation*, vol. 60, no. 12, pp. 5627–5634, 2012.

[32] J. T. Bernhard, E. Kiely, and G. Washington, "A smart mechanically actuated two-layer electromagnetically coupled microstrip antenna with variable frequency, bandwidth, and antenna gain," *IEEE Transactions on Antennas and Propagation*, vol. 49, no. 4, pp. 597–601, 2001.

[33] J. Modelski and Y. Yashchyshyn, "Semiconductor and ferroelectric antennas," in *Proceedings of the Asia-Pacific Microwave Conference (APMC '06)*, pp. 1052–1059, December 2006.

[34] Y. Yashchyshyn, J. Marczewski, K. Derzakowski, J. W. Modelski, and P. B. Grabiec, "Development and investigation of an antenna system with reconfigurable aperture," *IEEE Transactions on Antennas and Propagation*, vol. 57, no. 1, pp. 2–8, 2009.

[35] A. E. Fathy, A. Rosen, H. S. Owen et al., "Silicon-based reconfigurable antennas—concepts, analysis, implementation, and feasibility," *IEEE Transactions on Microwave Theory and Techniques*, vol. 51, no. 6, pp. 1650–1661, 2003.

[36] L. Liu and R. J. Langley, "Liquid crystal tunable microstrip patch antenna," *Electronics Letters*, vol. 44, no. 20, pp. 1179–1180, 2008.

[37] Y. Yashchyshyn and J. Modelski, "Reconfigurable semiconductor antenna," in *Proceedings of the 9th International Conference: The Experience of Designing and Application of CAD Systems in Microelectronics (CADSM '07)*, pp. 146–150, February 2007.

[38] A. Gaebler, A. Moessinger, F. Goelden et al., "Liquid crystal-reconfigurable antenna concepts for space applications at microwave and millimeter waves," *International Journal of Antennas and Propagation*, vol. 2009, Article ID 876989, 7 pages, 2009.

[39] D. Rodrigo, L. Jofre, and B. A. Cetiner, "Circular beam-steering reconfigurable antenna with liquid metal parasitics," *IEEE Transactions on Antennas and Propagation*, vol. 60, no. 4, pp. 1796–1802.

[40] S. A. Long and G. H. Huff, "A substrate integrated fluidic compensation mechanism for deformable antennas," in *Proceedings of the NASA/ESA Conference on Adaptive Hardware and Systems (AHS '09)*, pp. 247–251, August 2009.

[41] Y. Tawk, J. Costantine, S. Hemmady, G. Balakrishnan, K. Avery, and C. G. Christodoulou, "Demonstration of a cognitive radio front end using an optically pumped reconfigurable antenna system (OPRAS)," *IEEE Transactions on Antennas and Propagation*, vol. 60, no. 2, pp. 1075–1083, 2012.

[42] R. N. Lavallee and B. A. Lail, "Optically-controlled reconfigurable microstrip patch antenna," in *Proceedings of the IEEE International Symposium on Antennas and Propagation*, pp. 1–4, July 2008.

[43] I. Llatser, C. Kremers, D. N. Chigrin et al., "Characterization of graphene-based nano-antennas in the terahertz band," in *Proceedings of the 6th European Conference on Antennas and Propagation (EUCAP '12)*, pp. 194–198, March 2012.

[44] Y. Huang, L. S. Wu, M. Tang, and J. Mao, "Design of a beam reconfigurable THz antenna with graphene-based switchable high-impedance surface," *IEEE Transactions on Nanotechnology*, vol. 11, no. 4, pp. 836–842, 2012.

[45] M. Stasiowski and D. Schaubert, "Broadband array antenna," in *Proceedings of the Antenna Applications Symposium*, pp. 42–59, September 2008.

[46] A. Kumar, "Monopole arrays are electronically steerable," *Microwaves & RF*, vol. 45, no. 9, pp. 88–94, 2006.

[47] N. Haider, B. Yang, D. P. Tran, and A. G. Yarovoy, "UWB antenna element for a full-polarimetric antenna array," in *Proceedings of the 4th European Conference on Antennas and Propagation (EuCAP '10)*, pp. 1–5, April 2010.

[48] N. Haider, D. Caratelli, D. P. Tran, and A. G. Yarovoy, "Directive electric-magnetic antenna for UWB applications," *Microwaves, Antennas & Propagation, IET*. In press.

[49] N. Haider, D. Caratelli, and A. G. Yarovoy, "Circuital characteristics and radiation properties of an UWB electric-magnetic planar antenna for Ku-band applications," *Radio Science*, vol. 48, 2013.

[50] S. Nikolaou, N. D. Kingsley, G. E. Ponchak, J. Papapolymerou, and M. M. Tentzeris, "UWB elliptical monopoles with a reconfigurable band notch using MEMS switches actuated without bias lines," *IEEE Transactions on Antennas and Propagation*, vol. 57, no. 8, pp. 2242–2251, 2009.

[51] D. Manteuffel, M. Arnold, Y. Makris, and Z. N. Chen, "Concepts for future multistandard and ultra wideband mobile terminal antennas using multilayer LTCC technology," in *Proceedings of the IEEE International Workshop on Antenna Technology (iWAT '09)*, pp. 1–4, March 2009.

[52] G. M. Brzezina, L. Roy, and L. MacEachern, "LTCC ultra-wideband antenna with transceiver integration capability," in *Proceedings of the European Microwave Conference*, vol. 3, pp. 2011–2014, October 2005.

[53] R. Erickson, R. Gunnarsson, T. Martin et al., "Wideband and wide scan phased array micro- strip patch antennas for small platforms," in *Proceedings of the 2nd European Conference on Antennas and Propagation (EuCAP '07)*, pp. 1–6, November 2007.

[54] T. Aboufoul, A. Alomainy, and C. Parini, "Reconfigured and notched tapered slot UWB antenna for cognitive radio applications," *International Journal of Antennas and Propagation*, vol. 2012, Article ID 160219, 8 pages, 2012.

[55] M. Martínez-Vázquez, O. Litschke, M. Geissler, D. Heberling, A. M. Martínez-González, and D. Sánchez-Hernández, "Integrated planar multiband antennas for personal communication handsets," *IEEE Transactions on Antennas and Propagation*, vol. 54, no. 2, pp. 384–391, 2006.

[56] G. Srivatsun and S. S. Rani, "Compact multiband planar fractal cantor antenna for wireless applications: an approach," *International Journal of Antennas and Propagation*, vol. 2012, Article ID 839520, 6 pages, 2012.

[57] J. J. Heikkinen and M. A. Kivikoski, "Directive dual-band CP shorted ring-slot antenna," in *Proceedings of the IEEE International Symposium on Antennas and Propagation*, pp. 1–4, July 2008.

[58] D. Caratelli, R. Cicchetti, G. Bit-Babik, and A. Faraone, "A perturbed E-shaped patch antenna for wideband WLAN applications," *IEEE Transactions on Antennas and Propagation*, vol. 54, no. 6, pp. 1871–1874, 2006.

[59] D. Caratelli, R. Cicchetti, G. Bit-Babik, and A. Faraone, "Circuit model and near-field behavior of a novel patch antenna for WWLAN applications," *Microwave and Optical Technology Letters*, vol. 49, no. 1, pp. 97–100, 2007.

[60] G. Cappelletti, D. Caratelli, R. Cicchetti, and M. Simeoni, "A low-profile printed drop-shaped dipole antenna for wide-band wireless applications," *IEEE Transactions on Antennas and Propagation*, vol. 59, no. 10, pp. 3526–3535, 2011.

[61] C. I. Coman, I. E. Lager, and L. P. Ligthart, "The design of shared aperture antennas consisting of differently sized elements," *IEEE Transactions on Antennas and Propagation*, vol. 54, no. 2, pp. 376–383, 2006.

[62] R. S. Chu, K. M. Lee, and A. T. S. Wang, "Multiband phased-array antenna with interleaved tapered-elements and waveguide radiators," in *Proceedings of the AP-S International Symposium & URSI Radio Science Meeting*, vol. 3, pp. 1616–1619, July 1996.

[63] S. H. Hsu, Y. J. Ren, and K. Chang, "A dual-polarized planar-array antenna for S-band and X-band airborne applications," *IEEE Antennas and Propagation Magazine*, vol. 51, no. 4, pp. 70–78, 2009.

[64] C. Han, C. Rodenbeck, J. Huang, and K. Chang, "A C/Ka dual frequency dual layer circularly polarized reflectarray antenna with microstrip ring elements," *IEEE Transactions on Antennas and Propagation*, vol. 52, no. 11, pp. 2871–2876, 2004.

[65] X. Qu, S.-S. Zhong, and Y.-M. Zhang, "Dual-band dual-polarised microstrip antenna array for SAR applications," *Electronics Letters*, vol. 42, no. 24, pp. 1376–1377, 2006.

Hindawi Publishing Corporation
International Journal of Antennas and Propagation
Volume 2013, Article ID 914734, 6 pages
http://dx.doi.org/10.1155/2013/914734

Research Article

Sparse Channel Estimation for MIMO-OFDM Two-Way Relay Network with Compressed Sensing

Aihua Zhang,[1,2] Shouyi Yang,[1] and Guan Gui[3]

[1] *School of Information Engineering, Zhengzhou University, Zhengzhou 450001, China*
[2] *School of Electronic and Information Engineering, Zhongyuan University of Technology, Zhengzhou 450007, China*
[3] *Department of Communication Engineering, Graduate School of Engineering, Tohoku University, Sendai 980-8579, Japan*

Correspondence should be addressed to Aihua Zhang; zhah00@yahoo.com.cn

Received 30 September 2012; Revised 7 February 2013; Accepted 12 February 2013

Academic Editor: Antonio Faraone

Accurate channel impulse response (CIR) is required for equalization and can help improve communication service quality in next-generation wireless communication systems. An example of an advanced system is amplify-and-forward multiple-input multiple-output two-way relay network, which is modulated by orthogonal frequency-division multiplexing. Linear channel estimation methods, for example, least squares and expectation conditional maximization, have been proposed previously for the system. However, these methods do not take advantage of channel sparsity, and they decrease estimation performance. We propose a sparse channel estimation scheme, which is different from linear methods, at end users under the relay channel to enable us to exploit sparsity. First, we formulate the sparse channel estimation problem as a compressed sensing problem by using sparse decomposition theory. Second, the CIR is reconstructed by CoSaMP and OMP algorithms. Finally, computer simulations are conducted to confirm the superiority of the proposed methods over traditional linear channel estimation methods.

1. Introduction

Two-way relay network (TWRN) has attracted great attention because it can improve spectral efficiency unlike a one-way relay network [1]. In a typical TWRN, two terminals, $\mathbb{T}_1$ and $\mathbb{T}_2$, exchange information through the assistance of an intermediate relay $\mathbb{R}$ via amplify-and-forward (AF). The TWRN requires two time slots to exchange their information. At the first time slot, both terminals send their data to the relay simultaneously, and then $\mathbb{R}$ amplifies the superimposed signal and broadcasts it to the end terminals during the second time slot. After receiving the signal from $\mathbb{R}$, the end nodes remove their own interference and perform a coherent detection process to recover the data transmitted from the other node. Compared with the basic single-antenna relay channel, the multiple-input multiple-output (MIMO) relay channel provides the high capacity of MIMO communication with the coverage extension capability of relay nodes. MIMO relay channel is one of the most promising solutions as it increases channel capacity and network reliability and effectively combats multipath fading. Furthermore, the orthogonal frequency-division multiplexing (OFDM) modulation technique provides efficient bandwidth utilization and robustness against time-dispersive channels. Therefore, the MIMO-OFDM-TWRN is a promising technique for next-generation wireless communication systems.

The MIMO-OFDM-TWRN system faces more challenges because channel estimation is required not only for data detection but also for self-data cancellation at the two terminals. Linear channel estimation methods have been proposed for MIMO-OFDM-TWRN. In [2], channel estimation by using least squares (LS) was proposed, and the block-based training design method was considered to achieve the optimal linear channel estimator. In addition, channel information estimation which uses the expectation conditional maximization (ECM) algorithm was proposed in [3]. However, both proposed methods do not take advantage of channel sparsity, and they result in performance loss of MIMO-OFDM-TWRN. In the development of channel modeling, numerous measurements demonstrated that multipath wireless channels tended to exhibit a cluster or sparse structure in which majority of the channel taps end up

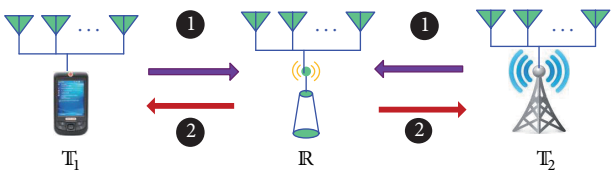

Figure 1: MIMO-OFDM-TWRN: (1) multiaccess stage, (2) broadcasting stage.

being either zero or below the noise floor, especially when operating at large bandwidths and signaling durations and/or with numbers of antenna elements [4–6]. In addition, with the theoretical development of compressed sensing (CS) [7], numerous researchers have proposed sparse channel estimation methods for point-to-point (P2P) communication systems, including single-antenna [8] or multiple-antenna [9] systems. Sparse channel estimation methods [10, 11] on cooperative networks have also been investigated. All channel estimation methods are limited to either single-antenna or multiple-antenna systems for traditional P2P transmission and single-antenna relay channel. To the best of our knowledge, corresponding work has not been conducted for MIMO-OFDM-TWRN.

In this study, we focus on the TWRN with multiple antennas at relay $\mathbb{R}$ and both end nodes, which is modulated by OFDM. We introduce the MIMO-OFDM-TWRN channel model and formulate composite channels estimation as a compressed sensing problem by using sparse decomposition theory. Then, the composite channel is reconstructed by CoSaMP [12] and OMP [13] algorithms. Finally, we verify the proposed methods via computer simulations. This study contributes to the field by introducing a sparse channel estimation technique with compressed sensing for MIMO-OFDM-TWRN and the use of the sparse structure information in the CIR by the end users.

The remainder of this paper is organized as follows. Section 2 describes the system model. Section 3 provides details on the proposed algorithm. The simulation results are reported in Section 4, and the conclusions are provided in Section 5.

2. System Model

2.1. Relay Transmission Model. Figure 1 shows a typical TWRN with two source nodes, $\mathbb{T}_1$ and $\mathbb{T}_2$, and one relay node, $\mathbb{R}$. The two terminal users exchange information with the assistance of the relay node. $\mathbb{T}_1$ and $\mathbb{T}_2$ each have N_T antennas, and $\mathbb{R}$ has N_R antennas. The bidirectional communication is performed in two phases, as shown in Figure 1. In phase I, $\mathbb{T}_1$ and $\mathbb{T}_2$ send their signal simultaneously to the relay node $\mathbb{R}$. Then, the relay amplifies the received signals and broadcasts them to the source nodes $\mathbb{T}_1$ and $\mathbb{T}_2$ in phase II.

The channel between the mth antenna of $\mathbb{T}_i$ and the rth antenna of $\mathbb{R}$ is assumed to be a quasi-static frequency-selective fading channel with an impulse response denoted by $\mathbf{h}^i_{r,m} = [h^i_{r,m}(0), h^i_{r,m}(1), \ldots, h^i_{r,m}(L-1)]^T \in C^{L\times 1}$, where $i = 1, 2$ and L is the channel length. All channels $\mathbf{h}^i_{r,m}$, $(i = 1, 2;\ m = 1, \ldots, N_T;\ r = 1, \ldots, N_R)$ are assumed as zero-mean circularly symmetric complex Gaussian random variables with variance $(\sigma^i_{r,m})^2$ and are independent of each other. The average transmission powers of $\mathbb{T}_1$, $\mathbb{T}_2$, and $\mathbb{R}$ are P_1, P_2, and P_R, respectively. For the time being, we assume perfect synchronization among three terminals.

2.2. Received Signals at the Relay Node and the End Users. The training signal vectors transmitted from the mth antenna of $\mathbb{T}_1$ and $\mathbb{T}_2$ are denoted by s^i_m. We assume that $E\{\|\mathbf{s}^i_m\|^2\} = P_i$. In phase I, the signal vectors $\mathbf{s}^1_m$ and $\mathbf{s}^2_m$ are processed by an inverse fast Fourier transform as $\tilde{\mathbf{s}}^i_m = \mathbf{F}^H\mathbf{s}^i_m = [\tilde{s}^i_m(0), \tilde{s}^i_m(1), \ldots, \tilde{s}^i_m(N-1)]$, where F is the discrete Fourier transformation (DFT) matrix with the (m, n)th entity given by $\mathbf{F} = 1/\sqrt{N}e^{-j2\pi mn/N}$, $(m, n = 0, 1, \ldots, N)$. To avoid inter-block interference, $\tilde{\mathbf{s}}^i_m$ is the cyclic prefix (CP) of length L_p added before being transmitted, and L_p should satisfy $L_p \geq L-1$. The received signal vector at the node $\mathbb{R}$ after removing CP can be written as

$$\mathbf{y}_R = \mathbf{H}^1\tilde{s}^1 + \mathbf{H}^2\tilde{s}^2 + \mathbf{w}, \tag{1}$$

where

$$\begin{gathered}
\tilde{\mathbf{s}}^1 = \left[\left(\tilde{s}^1_1\right)^T, \left(\tilde{s}^1_2\right)^T, \ldots \left(\tilde{s}^1_{N_T}\right)^T\right]^T, \\
\tilde{\mathbf{s}}^2 = \left[\left(\tilde{s}^2_1\right)^T, \left(\tilde{s}^2_2\right)^T, \ldots \left(\tilde{s}^2_{N_T}\right)^T\right]^T, \\
\mathbf{H}^1 = \begin{bmatrix} \mathbf{H}^1_{1,1} & \mathbf{H}^1_{1,2} & \cdots & \mathbf{H}^1_{1,N_T} \\ \mathbf{H}^1_{2,1} & \mathbf{H}^1_{2,2} & \cdots & \mathbf{H}^1_{2,N_T} \\ \vdots & \vdots & \vdots & \vdots \\ \mathbf{H}^1_{N_R,1} & \mathbf{H}^1_{N_R,2} & \cdots & \mathbf{H}^1_{N_R,N_T} \end{bmatrix}, \\
\mathbf{H}^2 = \begin{bmatrix} \mathbf{H}^2_{1,1} & \mathbf{H}^2_{1,2} & \cdots & \mathbf{H}^2_{1,N_T} \\ \mathbf{H}^2_{2,1} & \mathbf{H}^2_{2,2} & \cdots & \mathbf{H}^2_{2,N_T} \\ \vdots & \vdots & \vdots & \vdots \\ \mathbf{H}^2_{N_R,1} & \mathbf{H}^2_{N_R,2} & \cdots & \mathbf{H}^2_{N_R,N_T} \end{bmatrix}, \\
\mathbf{w} = \left[\mathbf{w}^T_1\mathbf{w}^T_2\cdots\mathbf{w}^T_{N_R}\right]^T.
\end{gathered} \tag{2}$$

The matrix $\mathbf{H}^i_{r,m}$ is an $N\times N$ circulant matrix in which the first column takes the form $\mathbf{h}^i_{r,m} = [h^i_{r,m}(0)h^i_{r,m}(1)\cdots h^i_{r,m}(L-1)0_{1\times(N-L)}]^T$. The noise vector $\mathbf{w}$ is a complex Gaussian random vector with zero mean and covariance matrix $E\{\mathbf{w}\mathbf{w}^H\} = N_0\mathbf{I}_N$.

In phase II, the vector y_R is amplified by a real factor β, and $\beta^2E\{\mathbf{y}^H\mathbf{y}\} = N_R \times P_R$. The factor β is given by

$$\beta = \sqrt{\frac{P_R}{\sum_{r=1}^{N_R}\sum_{m=1}^{N_T}\sum_{l=0}^{L-1}\left[\sigma^1_{r,m}(l) + \sigma^2_{r,m}(l)\right] + N_0}}, \tag{3}$$

where $\sigma^i_{r,m}(l) = E[|\mathbf{h}^i_{r,m}(l)|^2]$, $i = 1, 2$.

The vector $\beta \mathbf{y}_R$ is CP-added before being transmitted back to $\mathbb{T}_1$ and $\mathbb{T}_2$. Only the channel estimation problem at $\mathbb{T}_1$ is considered in this study. A similar procedure can be applied at $\mathbb{T}_2$. The received signal at $\mathbb{T}_1$, which is from relay $\mathbb{R}$ after removing CP, can be written as [3]

$$\mathbf{y}_{T_1} = \beta \mathbf{G}\left(\mathbf{H}^1 \tilde{s}^1 + \mathbf{H}^2 \tilde{s}^2\right) + \mathbf{n}_{T_1}, \tag{4}$$

where

$$\mathbf{G} = \begin{bmatrix} \mathbf{H}^1_{1,1} & \mathbf{H}^1_{2,1} & \cdots & \mathbf{H}^1_{N_R,1} \\ \mathbf{H}^1_{1,2} & \mathbf{H}^1_{2,2} & \cdots & \mathbf{H}^1_{N_R,2} \\ \vdots & \vdots & \vdots & \vdots \\ \mathbf{H}^1_{1,N_T} & \mathbf{H}^1_{2,N_T} & \cdots & \mathbf{H}^1_{N_R,N_T} \end{bmatrix} \tag{5}$$

and $\mathbf{n}_{T_1} = \beta \mathbf{G}\mathbf{w} + \mathbf{n}$, $\mathbf{n} = [n_1^T n_2^T \cdots n_{N_R}^T]^T$.

According to the matrix theory, matrices $\mathbf{H}^i_{r,m}$ can be decomposed as $\mathbf{H}^i_{r,m} = \mathbf{F}^H \Lambda^i_{r,m} \mathbf{F}$ [14], where $\mathbf{\Lambda}^i_{r,m} = \operatorname{diag}\{\mathbf{H}^i_{r,m}(0), \mathbf{H}^i_{r,m}(1), \ldots, \mathbf{H}^i_{r,m}(N-1)\}$ and $\mathbf{H}^i_{r,m}(c) = \sum_{l=0}^{L-1} \mathbf{h}^i_{r,m} e^{-j(2\pi lc/N)}$, $(c = 0, 1, \ldots, N-1)$

$$\begin{aligned} \beta \mathbf{H}^1_{r_1,m_1} \mathbf{H}^1_{r_2,m_2} &= \mathbf{F}^H \beta \mathbf{\Lambda}^1_{r_1,m_1} \mathbf{\Lambda}^1_{r_2,m_2} \mathbf{F}, \\ \beta \mathbf{H}^1_{r_1,m_1} \mathbf{H}^2_{r_2,m_2} &= \mathbf{F}^H \beta \mathbf{\Lambda}^1_{r_1,m_1} \mathbf{\Lambda}^2_{r_2,m_2} \mathbf{F}, \end{aligned} \tag{6}$$

where r_1 and $r_2 = 1, 2, \ldots, N_R$, and m_1 and $m_2 = 1, 2, \ldots, N_T$. Equations (6) are two circulant matrices that have the first columns of $[\beta(\mathbf{h}^1_{r_1 m_1} * \mathbf{h}^1_{r_2 m_2}) 0_{1\times(N-2L+1)}]^T$ and $[\beta(\mathbf{h}^1_{r_1 m_1} * \mathbf{h}^2_{r_2 m_2})\, 0_{1\times(N-2L+1)}]^T$. Thus, by normalizing DFT of $\mathbf{y}_{T_1}$, system model (4) can be rewritten as

$$\begin{aligned} \mathbf{y}_1 &= (\mathbf{I} \otimes \mathbf{F})\, y_{T_1} \\ &= \sum_{r=1}^{N_R} \sum_{m=1}^{N_T} \beta \mathbf{\Lambda}^1_{r_1,m_1} \left(\mathbf{\Lambda}^1_{r_2,m_2} s^1 + \mathbf{\Lambda}^2_{r_2,m_2} s^2\right) + \mathbf{F} n_{T_1}. \end{aligned} \tag{7}$$

From (7), we define composite channels g and q, which are given, respectively, as

$$\begin{aligned} \mathbf{g} &= \beta\left(\mathbf{h}^1_{r,m} \otimes \mathbf{h}^1_{r,n}\right), \\ \beta \mathbf{\Lambda}^1_{r_1,m_1} \mathbf{\Lambda}^1_{r_2,m_2} &= \operatorname{diag}(\mathbf{W}\mathbf{g}), \\ \mathbf{q} &= \beta\left(\mathbf{h}^1_{r,m} \otimes \mathbf{h}^2_{r,n}\right), \\ \beta \mathbf{\Lambda}^1_{r_1,m_1} \mathbf{\Lambda}^2_{r_2,m_2} &= \operatorname{diag}(\mathbf{W}\mathbf{q}). \end{aligned} \tag{8}$$

Then, (7) can be expressed as

$$\mathbf{y}_1 = \mathbf{S}\mathbf{k} + \mathbf{F}\mathbf{n}_{T_1}, \tag{9}$$

where $\mathbf{S} = [\mathbf{s}^1 \mathbf{s}^2]$, $\mathbf{k} = [\mathbf{g}^T \mathbf{q}^T]$, and $\mathbf{W}$ is a matrix which takes the first $(2L-1)$ columns of $\sqrt{N}\mathbf{F}$.

3. Sparse Channel Estimation

3.1. Overview of Compressed Sensing. Compressed sensing (CS) describes a new signal acquisition theory in which sparse high dimensional vectors can be accurately recovered from a small number of linear observations. CS has been applied in various areas, such as imaging, radar, speech recognition, and data acquisition. In communications, an immediate application of CS is wireless sparse multipath channel estimation. Detailed descriptions can be found in [7].

In this paper, we consider the linear model as (9). According to the CS, if an unknown signal vector satisfies the sparse or approximate sparse requirements, the conditions under which CS succeeds depends on the structure of the measurement matrix $\mathbf{S}$. Thus, these kinds of unknown signals can be robustly reconstructed from observation signal $\mathbf{y}_1$. However, the sparsest solution is always a nondeterministic polynomial-time hard (NP-hard) problem. According to recent theoretical results, the observation signal can be used to efficiently recover any "sparse enough" signal provided that the matrix $\mathbf{S}$ satisfies the so-called restricted isometric property (RIP) [15, 16]. We suppose that $\mathbf{S}$ is a $n \times p$ complex-valued measurement matrix that has unit ℓ_2-norm columns. The $\mathbf{S}$ satisfies the RIP of order d with parameter $\delta_d \in (0, 1)$, which can satisfy the inequality

$$(1 - \delta_d)\, \|\mathbf{k}\|_2^2 \le \|\mathbf{S}\mathbf{k}\|^2 \le (1 + \delta_d)\, \|\mathbf{k}\|_2^2, \tag{10}$$

where $\|\mathbf{k}\|_2^2$ denotes the ℓ_2-norm, which is given by $\|\mathbf{k}\|_2^2 = \sum |\mathbf{h}^i_{r,m}|^2$. If (10) is satisfied, the training sequence is said to satisfy the RIP of order d, and the accurate channel estimator with high probability can be obtained by using CS methods. Although verifying whether a given matrix satisfies this condition is difficult, many matrices satisfy the restricted isometry constant (RIC) with high property and few measurements. In particular, it has been shown exponentially with high probability that the random Gaussian, Bernoulli, and partial Fourier matrices satisfy the RIC with a number of measurements that are nearly linear in the sparsity level.

3.2. Compressed Channel Estimation (CCE). Since the channel impulse responses $\mathbf{h}^i_{r,m}$ are sparse enough, their cooperation convoluted channel g and q have been verified to be sparse or approximate sparse [17]. In this case, we use two greedy algorithms, that is, orthogonal matching pursuit (OMP) [13] and compressive sampling matching pursuit (CoSaMP) [12], which select each dominant coefficient in channel through iteration. We also present the LS channel estimator for comparison. The LS estimator (known position) is given by numerous practical algorithms for channel estimation. The LS estimator is expressed as

$$\hat{\mathbf{k}} = \begin{cases} \mathbf{S}_T^{\dagger} \mathbf{y}_1, & T \subseteq \operatorname{supp}(\mathbf{k}), \\ 0, & \text{others}, \end{cases} \tag{11}$$

where $\operatorname{supp}(\mathbf{k})$ denotes the nonzero taps that support the channel vector $\mathbf{k}$, $\mathbf{S}_T$ is the submatrix constructed from the columns of $\mathbf{S}$, and T denotes the selected subcolumns which correspond to the nonzero index set of the convoluted

channel vector h. The mean square error (MSE) of the LS estimator $\widehat{\mathbf{k}}$ is given by

$$\widehat{\mathbf{k}} \triangleq \mathbf{S}^{\dagger}\mathbf{y}_1 = \mathbf{k} + \mathbf{S}^{\dagger}\mathbf{F}\mathbf{n}_T, \tag{12}$$

where $\mathbf{S}^{\dagger}$ is the pseudo-inverse of $\mathbf{S}$ and is given by $\mathbf{S}^{\dagger} = (\mathbf{S}^H\mathbf{S})^{-1}\mathbf{S}^H$. The MSE of the LS channel estimate is given by $\mathrm{MSE} = E\{\|\widehat{\mathbf{k}} - \mathbf{k}\|^2\} = E\{\|\mathbf{S}^{\dagger}\mathbf{F}\mathbf{n}_T\|^2\}$, which can also be written as

$$\mathrm{MSE}\left(\widehat{\mathbf{k}}\right) = \sigma_n^2 \operatorname{tr}\left\{\left(\mathbf{S}^{\dagger}\mathbf{S}\right)^{-1}\right\}. \tag{13}$$

By utilizing CS recovery algorithms for compressive channel estimation, we propose CCE-OMP and CCE-CoSaMP. The two estimation methods for convoluted channels are described as follows.

3.2.1. CoSaMP Estimator $\widehat{\mathbf{k}}_{\mathrm{CoSaMP}}$. Given y_1, F and W, and training signal matrix $\mathbf{S} = \mathrm{diag}(\mathbf{F}\mathbf{s}^i)\mathbf{W}$, the maximum number of dominant channel coefficients is assumed as d. The CCE-CoSaMP is performed as follows.

Initialization. We set the nonzero coefficient index as $T_0 = \emptyset$, the residual estimation error $\mathbf{r}_0 = \mathbf{y}_1$, and the initialize iteration counter as $l = 1$.

Identification. We select a column index n_l of $\mathbf{S}$ that is most correlated with the residual

$$n_l = \left|\langle r_{l-1}, \mathbf{S}_n\rangle\right|, \qquad T_l = T_{l-1} \cup n_l. \tag{14}$$

We use the LS method to calculate a channel estimator as $\mathbf{T}_{\mathrm{LS}} = \arg\min \|\mathbf{y}_1 - \mathbf{S}\mathbf{k}\|$ and select a maximum of T dominant taps denoted by $\mathbf{k}_{\mathrm{LS}}$. The positions of the selected dominant taps in this substep are denoted by T_{LS}.

Merge. The positions of the dominant taps are merged by $T_l = T_{\mathrm{LS}} \cup T_l$.

Estimation. We compute the best coefficient for approximating the channel vector with chosen columns

$$\mathbf{k}_l = \arg\min_k \left\|\mathbf{y} - \mathbf{S}_{T_l}\mathbf{k}\right\|_2. \tag{15}$$

Pruning. We select the T_l largest channel coefficients

$$k_l = [k]_d \tag{16}$$

and replace the left taps $T \setminus T_l$ by zero.

Iteration. We update the estimation error

$$\mathbf{r}_l = \mathbf{y} - \widetilde{\mathbf{X}}_{T_l}\mathbf{k}_l. \tag{17}$$

We increase the iteration counter k. We repeat (14) to (17) until the stopping criterion holds, and then set $\widehat{\mathbf{k}}_{\mathrm{CoSaMP}} = \mathbf{k}_l$.

3.2.2. OMP Estimator $\widehat{\mathbf{k}}_{\mathrm{OMP}}$. Given the received signal $\mathbf{y_1}$, $\mathbf{W}$, $\mathbf{F}$, and $\mathbf{s}^i$, the CCE-OMP estimator runs as follows.

Initialize. We set the nonzero coefficient index as $T_0 = \emptyset$, the residual estimation error $\mathbf{r}_0 = \mathbf{y}_1$, and the initialize iteration counter as $l = 1$.

Identification. We select a column index n_l of $\mathbf{s}^i$ that is most correlated with the residual

$$\begin{aligned} n_l &= \left|\mathbf{r}_{l-1}, \mathbf{S}_n\right|, \\ T_l &= \mathrm{T}_{l-1} \cup n_l, \\ \mathbf{k}_l &= \arg\min_k \left|\mathbf{y}_1 - \mathbf{S}_{T_l}\right|. \end{aligned} \tag{18}$$

Estimation. We compute the best coefficient for approximating the channel vector with chosen columns

$$\mathbf{k}_l = \arg\min_k \left\|\mathbf{y}_1 - \mathbf{S}_{T_l}\mathbf{k}\right\|_2. \tag{19}$$

Iteration. We update the estimation error

$$\mathbf{r}_l = \mathbf{y}_1 - \mathbf{S}_{T_l}\mathbf{k}_l. \tag{20}$$

We increase the iteration counter l. We repeat (18) to (20) until the stopping criterion holds, and then set $\widehat{\mathbf{k}}_{\mathrm{OMP}} = \mathbf{k}_l$.

4. Simulation Results

In this section, we present the simulation results and analyze the performance of compressive channel estimation in a MIMO-OFDM two-way relay network. We compare the performance of the proposed estimators with that of an LS-based linear estimator and adopt 10,000 independent Monte Carlo runs for averaging. We consider the MIMO relay network with $N_{\mathrm{T}} = N_R = 2$ antennas; the number of carriers is 128. All channels have the same length ($P = 32$), and the positions of the nonzero channel taps are randomly generated. QPSK modulation is used. Transmit power is set as $P_1 = P_2 = P$, and AF relay power is set as $P_R = P$. The signal-to-noise ratio is defined as a as $10\log(P/\sigma_n^2)$. When the number of nonzero taps in cooperation channels $\mathbf{h}_{r,m}^i$, ($i = 1, 2$; $r = 1, 2, \ldots, N_R$; $m = 1, 2, \ldots, N_T$) is changed, the simulation results are shown in Figures 2 to 5.

The channel estimators are evaluated via the average MSE, which is defined by

$$\text{average MSE}\ (\Delta\mathbf{k}) = \frac{\left\|\mathbf{k} - \widehat{\mathbf{k}}\right\|_2^2}{M\,(2L-1)}, \tag{21}$$

where $\mathbf{k}$ and $\widehat{\mathbf{k}}$ denote the channel vector and its estimator, respectively, M is the number of Monte Carlo runs, and $(2L-1)$ is the overall length of channel vector k. In Figure 2, the number of nonzero taps of $\mathbf{h}_{r,m}^i$, ($i = 1, 2$) is set to 2, and the cooperation convoluted channel also has sparsity. Figure 2 shows that the performance of the proposed CCE methods is significantly better than that of the LS estimator and is close to the ideal LS estimator by using the known position of the channel. In Figure 3, the number of nonzero taps of $\mathbf{h}_{r,m}^i$, ($i = 1, 2$) is set as 4.

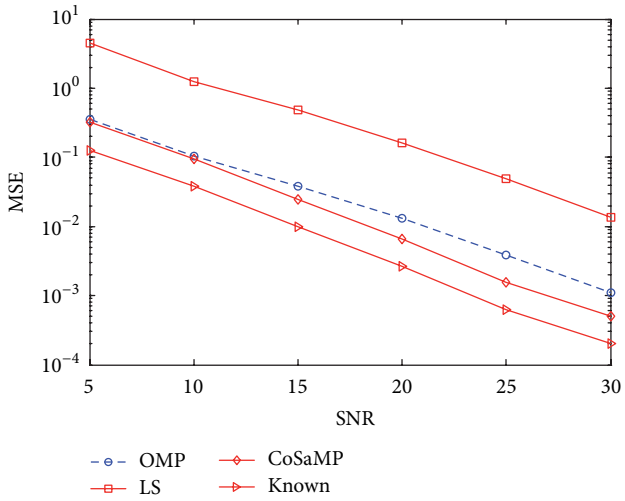

Figure 2: MSE performance of channel estimation at $\mathbb{T}_1$ for the case when $d = 2$.

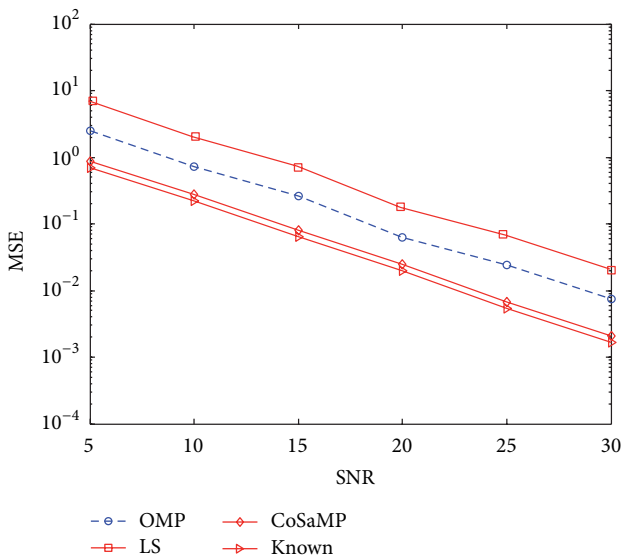

Figure 3: MSE performance of channel estimation at $\mathbb{T}_1$ when $d = 4$.

A comparison between the simulation results in the two figures (Figures 2 and 3) shows that the proposed estimators can exploit the channel sparseness. Notably, if channels are dense rather than sparse, all proposed estimators will have the same performance as the LS estimator.

We also compare the performance of the proposed CCE-CoSaMP estimator with that of the ECM estimator algorithm in this section. Figures 4 and 5 show that when channel impulse responses $\mathbf{h}_{r,m}^{i}$ are sparse enough, the proposed CCE estimator performs significantly better than the ECM algorithm. However, as the number of nonzero taps of all the channels increases, the performance of CCE-CoSaMP is closer to that of the ECM algorithm.

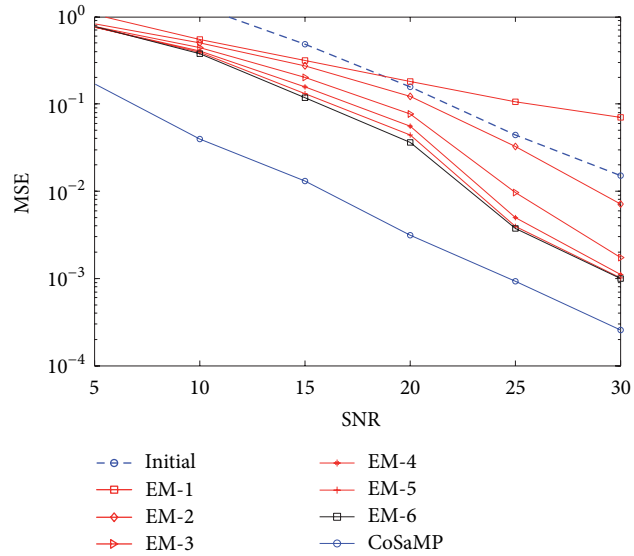

Figure 4: MSE performance of channel estimation at $\mathbb{T}_1$ for when channel impulse responses $\mathbf{h}_{r,m}^{i}$ are sparse enough ($d = 2$).

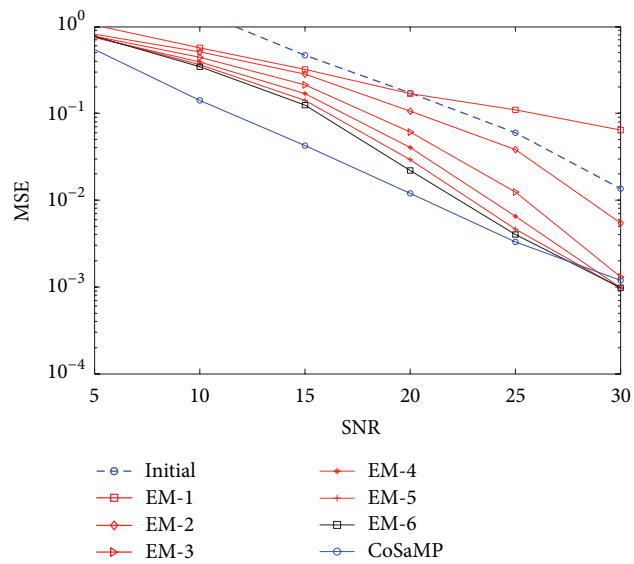

Figure 5: MSE performance of channel estimation at $\mathbb{T}_1$ for when channel impulse responses $\mathbf{h}_{r,m}^{i}$ are sparse ($d = 4$).

5. Conclusion

This paper investigated the channel estimation problem in sparse multipath MIMO two-way relay networks that adopt the OFDM technique. To address the shortcomings of conventional linear channel estimation methods, we proposed compressed channel estimation methods for MIMO-OFDM two-way relay networks under the AF protocol. The sparseness of convoluted sparse channels was demonstrated by a measure function. The proposed methods exploited the sparsity in the MIMO TWRN channel. The simulation results confirmed the superior performance of the proposed method

compared with conventional linear methods, for example, LS and ECM.

Acknowledgment

This study is funded by the National Natural Science Foundation of China (Grant nos. 61071175, 61202499, 61271421, and 61152004).

References

[1] P. Larsson, N. Johansson, and K. E. Sunell, "Coded bi-directional relaying," in *Proceedings of the 63rd IEEE Vehicular Technology Conference (VTC '06)*, pp. 851–855, May 2006.

[2] Z. Fang and J. Shi, "Least square channel estimation for two-way relay MIMO-OFDM systems," *ETRI Journal*, vol. 33, no. 5, pp. 806–809, 2011.

[3] T. H. Pham, Y. C. Liang, H. K. Garg, and A. Nallanathan, "Joint channel estimation and data detection for MIMO-OFDM two-way relay networks," in *Proceedings of the 53rd IEEE Global Communications Conference (GLOBECOM '10)*, Miami, Fla, USA, December 2010.

[4] W. U. Bajwa, A. Sayeed, and R. Nowak, "Sparse multipath channels: modeling and estimation," in *Proceedings of the 13th IEEE Digital Signal Processing Workshop and 5th IEEE Signal Processing Education Workshop (DSP/SPE '09)*, pp. 320–325, Marco Island, Fla, USA, January 2009.

[5] N. Czink, X. Yin, H. Özcelik, M. Herdin, E. Bonek, and B. H. Fleury, "Cluster characteristics in a MIMO indoor propagation environment," *IEEE Transactions on Wireless Communications*, vol. 6, no. 4, pp. 1465–1474, 2007.

[6] Y. Zhou, M. Herdin, A. M. Sayeed, and E. Bonek, "Experimental study of MIMO channel statistics and capacity via the virtual channel representation," Tech. Rep., University of Wisconsin-Madison, February 2007.

[7] D. L. Donoho, "Compressed sensing," *IEEE Transactions on Information Theory*, vol. 52, no. 4, pp. 1289–1306, 2006.

[8] W. U. Bajwa, J. Haupt, G. Raz, and R. Nowak, "Compressed channel sensing," in *Proceedings of the 42nd Annual Conference on Information Sciences and Systems (CISS '08)*, pp. 19–21, Princeton, NJ, USA, 2008.

[9] W. U. Bajwa, J. Haupt, A. M. Sayeed, and R. Nowak, "Compressed channel sensing: a new approach to estimating sparse multipath channels," *Proceedings of the IEEE*, vol. 98, no. 6, pp. 1058–1076, 2010.

[10] A. Zhang, G. Gui, and S. Yang, "Compressive channel estimation for OFDM cooperation networks," *Research Journal of Applied Sciences*, vol. 4, no. 8, pp. 897–901, 2012.

[11] G. Gui, Z. Chen, Q. Meng, Q. Wan, and F. Adachi, "Compressed channel estimation for sparse multipath two-way relay networks," *International Journal of Physical Sciences*, vol. 6, no. 12, pp. 2782–2788, 2011.

[12] D. Needell and J. A. Tropp, "CoSaMP: iterative signal recovery from incomplete and inaccurate samples," *Communications of the ACM*, vol. 53, no. 12, pp. 93–100, 2010.

[13] J. A. Tropp and A. C. Gilbert, "Signal recovery from random measurements via orthogonal matching pursuit," *IEEE Transactions on Information Theory*, vol. 53, no. 12, pp. 4655–4666, 2007.

[14] R. M. Gray, "Toeplitz and circulant matrices: a review," *Foundations and Trends in Communications and Information Theory*, vol. 2, no. 3, pp. 155–239, 2006.

[15] E. J. Candès, "The restricted isometry property and its implications for compressed sensing," *Compte Rendus de l'Academie des Sciences, Paris, Series I*, vol. 346, no. 9-10, pp. 589–592, 2008.

[16] E. J. Candes and T. Tao, "Decoding by linear programming," *IEEE Transactions on Information Theory*, vol. 51, no. 12, pp. 4203–4215, 2005.

[17] G. Gui, W. Peng, A. Mehbodniya, and F. Adachi, "Compressed channel estimation for sparse multipath non-orthogonal amplify-and-forward cooperative networks," in *Proceedings of the 75th IEEE Vehicular Technology Conference (VTC '12)*, Yokohama, Japan, May 2012.

Hindawi Publishing Corporation
International Journal of Antennas and Propagation
Volume 2013, Article ID 924768, 6 pages
http://dx.doi.org/10.1155/2013/924768

Research Article

Planar Ultrawideband Antenna with Photonically Controlled Notched Bands

Drasko Draskovic, Jean Raphaël Olivier Fernandez, and César Briso Rodríguez

Universidad Politécnica de Madrid, 28031 Madrid, Spain

Correspondence should be addressed to Drasko Draskovic; drasko.draskovic@upm.es

Received 7 December 2012; Accepted 29 January 2013

Academic Editor: Diego Caratelli

A design of a planar microstrip-fed ultrawideband (UWB) printed circular monopole antenna with optically controlled notched bands is presented. The proposed antenna is composed of a circular ultrawideband patch, with an etched T-shaped slot controlled by an integrated silicon switch. The slot modifies the frequency response of the antenna suppressing 3.5–5 GHz band when the switch is in open state. The optical switch is controlled by a low-power near-infrared (808 nm) laser diode, which causes the change in the frequency response of the antenna generating a frequency notch. This solution could be expanded to include several notches in the antenna frequency response achieving a fully reconfigurable UWB antenna. The antenna could be remotely controlled at large distances using optical fiber. The prototype antenna has been fully characterized to verify these design concepts.

1. Introduction

Ultrawideband (UWB) antennas with filtering properties are demanded in many practical applications, owing to the coexistence of UWB systems with other wireless standards, such as WLAN (5.15–5.35 and 5.725–5.825 GHz), WiMAX (3.5 GHz), X-band downlink satellite communication systems (7.25–7.75 GHz), or ITU (8.025–8.4 GHz). The antenna with filtering properties is employed in order to mitigate the devastating interference as well as to remove the requirement of additional bandstop filters. Reconfigurable antennas can have reconfigurable frequency, radiation pattern, polarization, or a combination of these properties. Planar antennas with reconfigurable band notches have been proposed [1–3]. Notched bands were introduced using split ring resonators (SRRs) and complementary split ring resonators (CSRRs). Electronic switches were mounted across or along the resonators to activate the corresponding band notches. Optical switches were introduced in the designs of the frequency and beam reconfigurable antenna [4] and frequency reconfigurable antenna [1]. The ultrawideband planar antenna with photonically controlled notched bands using silicon switch is presented in this paper.

Photonic devices have been considered enabling technologies for future RF and microwave devices and subsystems. The research of optically controlled microstrip switches started in 1970s [5, 6] and is continuing throughout to today. References have reported devices fabricated from coplanar waveguides and microstrip transmission lines printed on silicon substrate [7, 8]. Simple microwave switches have been applied in designs of antennas, filters, phase shifters, and couplers [9–11]. The main advantage of optically controlled microwave circuits is high level of isolation between the controlling electronic circuit and the microwave circuit. Typically the highly resistive silicon wafer in these devices is illuminated by a near-infra-red laser or a light-emitting diode (LED), with the optical power of few milliwatts. Devices that have proved themselves ideal for implementation of silicon switches are reconfigurable antennas and cryogenic components [12]. The main advantage in reconfigurable antenna design is the elimination of biasing lines that can modify the radiation pattern of the antenna. Several notches controlled with optical switches can be easily included in one antenna to control the frequency response and radiation pattern.

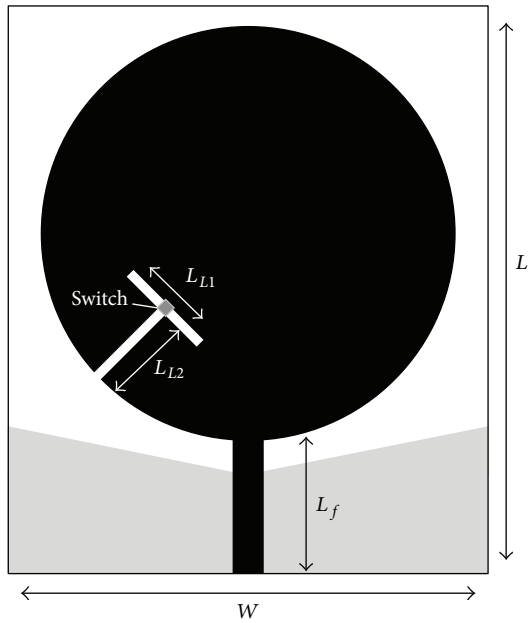

Figure 1: The design geometry of the proposed ultrawideband antenna.

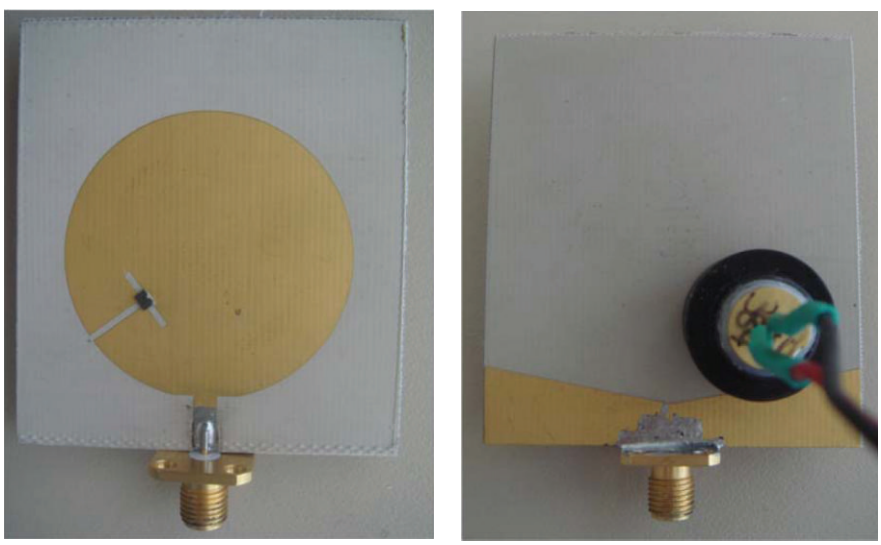

(a) (b)

Figure 2: Front and back views of the antenna prototype.

2. Antenna Design

The design presented in this paper, shown in Figure 1, is based on the design of a monopole UWB antenna with an etched T-shaped slot and with a partial ground plane designed to be used for UWB from 3.1 to 10.6 GHz. The antenna is based on a Taconic substrate with the dielectric constant 3.5 and thickness of 1.524 mm. The radius of the circle is 18.3 mm, and the other dimensions are as follows: $L = 50$ mm, $W = 50$ mm, $L_f = 7.5$ mm, $L_{L1} = 11.7$ mm, and $L_{L2} = 8.6$ mm.

The antenna includes a slot controlled with the optical switch. This slot can be designed to generate a notch at the desired frequency, and also the bandwidth of the notch can be controlled with the resistivity of the switch. It is also possible to introduce additional slots that would result in multiple notches.

The optical switch is made placing a silicon dice over the slot of the resonator. The dimensions of the dice of silicon wafer are 1 mm × 1 mm. When the switch is mounted, the slot resonator is causing the band notch in a frequency response of the antenna when the laser diode is turned off and the switch is in OFF state. When the laser diode is activated and the switch is in ON state, the additional resonance is cancelled

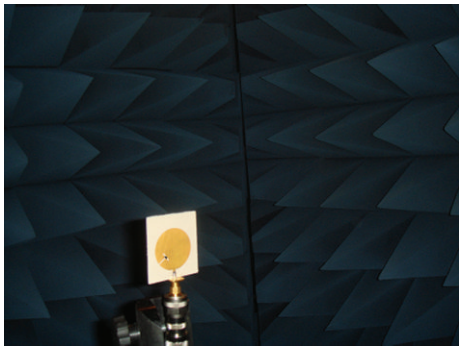

Figure 3: Antenna measurement in the anechoic chamber.

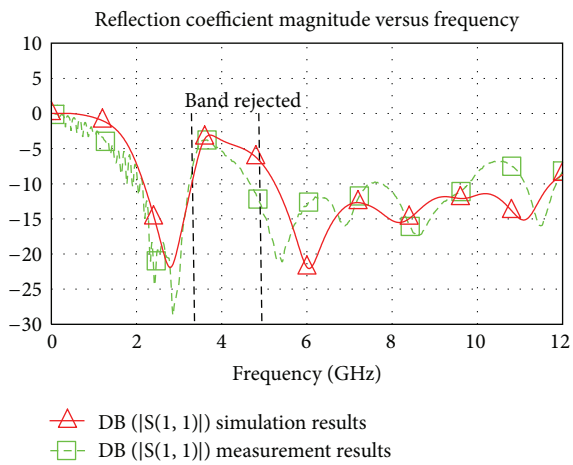

Figure 4: Simulation and measurement of return loss of the antenna when the switch is OFF and the slot generates a notch from 3.5 to 5 GHz.

and the notch disappears. In this case, antenna operates in full ultrawideband frequency range.

The dice is made of highly resistive silicon placed on the top of the microstrip gap and photoinduced with a near-infrared laser diode. The silicon wafer used in the design is highly resistive (around 6,000 Ohm cm), type N, doped with Phosphorus, with 111 crystal orientation, 0.3 mm thick, single side polished. The light was focused using a 200 mW 808 nm near-infrared laser diode module attached to the back of the ground of the antenna. A 0.5 mm hole was drilled through the substrate, which allows laser light to reach silicon dice. A prototype shown in Figure 2 was fabricated to verify the performance.

3. Simulation and Experimental Results

Electromagnetic simulations of the ultrawideband antenna were performed using CST Studio Suite, and the switch was modelled with different material conductivities for OFF and ON states. Switch conductivities were 10 and 350 S/m, respectively. These values of switch conductivities were extracted from the measurements of the individual switch placed over a gap of a $50'\Omega$ microstrip transmission line built on the same

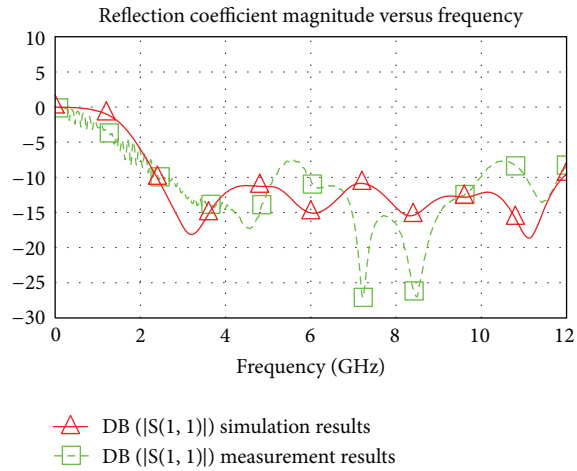

Figure 5: Simulation and measurement of return loss of the antenna when the switch is ON, and the slot disappears. The antenna covers all UWB from 3.1 to 10 GHz.

Table 1: Gain versus frequency with and without notch.

Frequency	Notch "on" gain	Notch "off" gain
3.1 GHz	2.5 dB	2.7 dB
4 GHz	−3 dB	3.0 dB
6.85 GHz	3 dB	3.5 dB
10 GHz	2.1 dB	2.2 dB

Table 2: Polarization purity change in presence of T-slot.

Frequency	Polarization purity change (dB)
3.1 GHz	0.96 dB
5.66 GHz	3.28 dB
6.85 GHz	2.72 dB

substrate. Measurements of the antenna were performed in the anechoic chamber as shown in Figure 3. Antenna return loss simulation and measurement results are shown in states when the switch is OFF and ON in Figures 4 and 5. It can be clearly seen in Figure 4 how the band from 3.5 to 5 GHz is rejected when the switch is ON and the antenna is working from 3.1 to 10.6 GHz with return losses better than 10 dB that fulfils the FCC criterion [13].

Gain, efficiency, and radiation pattern measurements of the antenna at different frequencies were performed in a large far field anechoic chamber. The results of the gain measured with and without notch are given in Table 1. Gain significantly reduces when the notch is activated. The average efficiency of the antenna is 70% and reduces to 60% when the switch is ON. We performed measurements of the influence of T-slot on polarization purity by measuring antenna polarization purity with slot and without it. The results are summed up in Table 2. We found that in both cases antenna exhibits good polarization purity.

The simulated and measured E-plane- and H-plane-normalized radiation patterns at 3.1 GHz and 6.85 GHz for

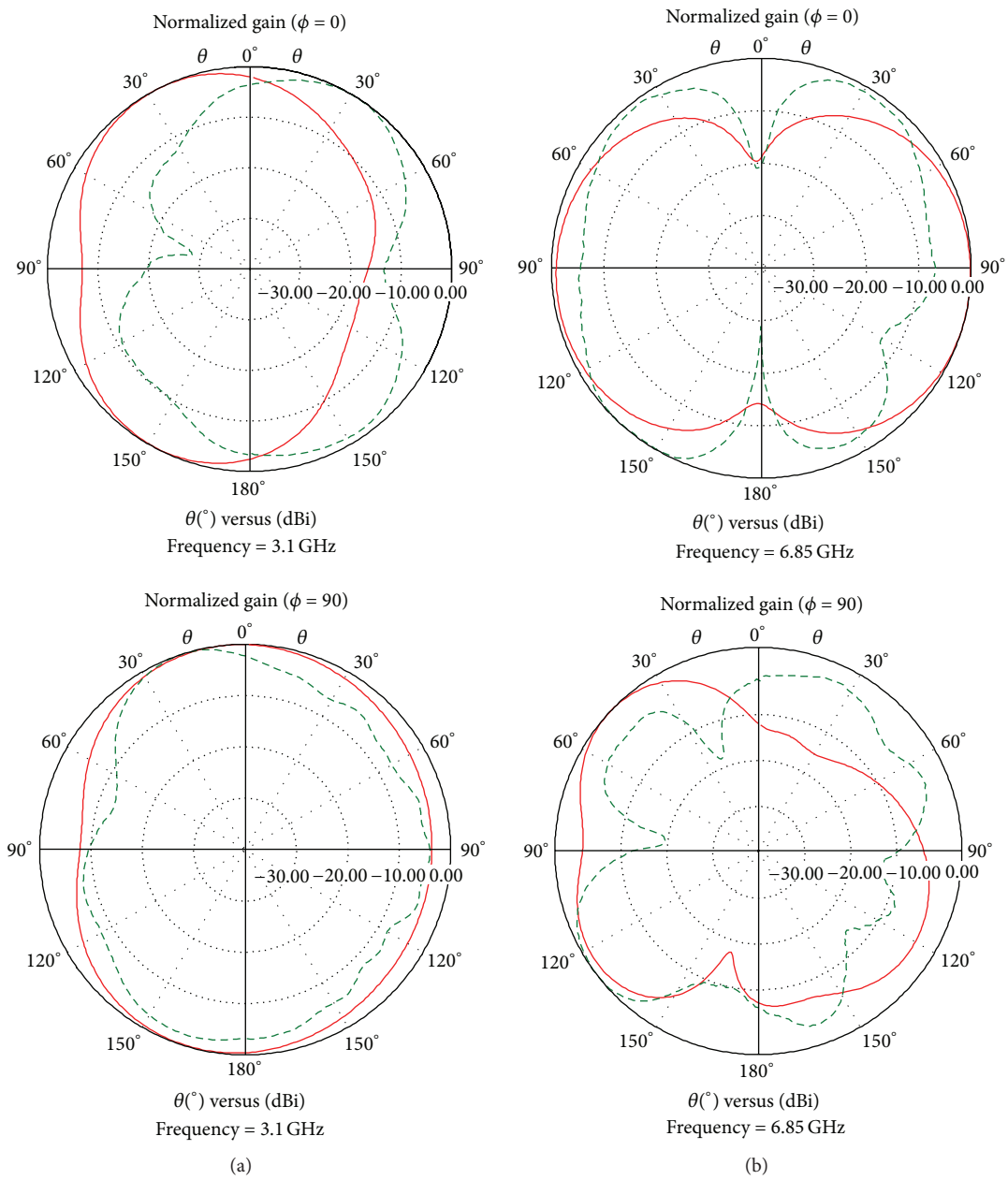

Figure 6: Simulated (solid) and measured (dashed) E-plane and H-plane radiation patterns for the center frequency: (a) 3.1 GHz and (b) 6.85 GHz for OFF state of the switch.

both switch states are plotted in Figures 6 and 7, respectively. Radiation pattern is quite omnidirectional and fits fairly well with CST simulations. There are some differences that can be caused by the feeding SMA connector and small parasitic capacitance (0.2 pF) of the silicon switch.

4. Conclusion

The design of a new ultrawideband monopole antenna with an etched T-shaped slot with integrated silicon switch and photonically controlled band notch has been presented. The photoconductive silicon switch was mounted across the T-shaped slot resonator and used to activate and deactivate the notch in the antenna response.

The main advantage of this ultrawideband antenna with filtering properties is the elimination of the undesired band. In our case a 3.5 to 5 GHz band has been chosen, and a controlled reduction of the antenna gain has been achieved. The band notch switching has been successfully demonstrated through simulation and measurements. The other advantage of this reconfigurable ultrawideband antenna is the elimination of biasing lines that could interfere with the operation of the antenna. Applications requiring sensing

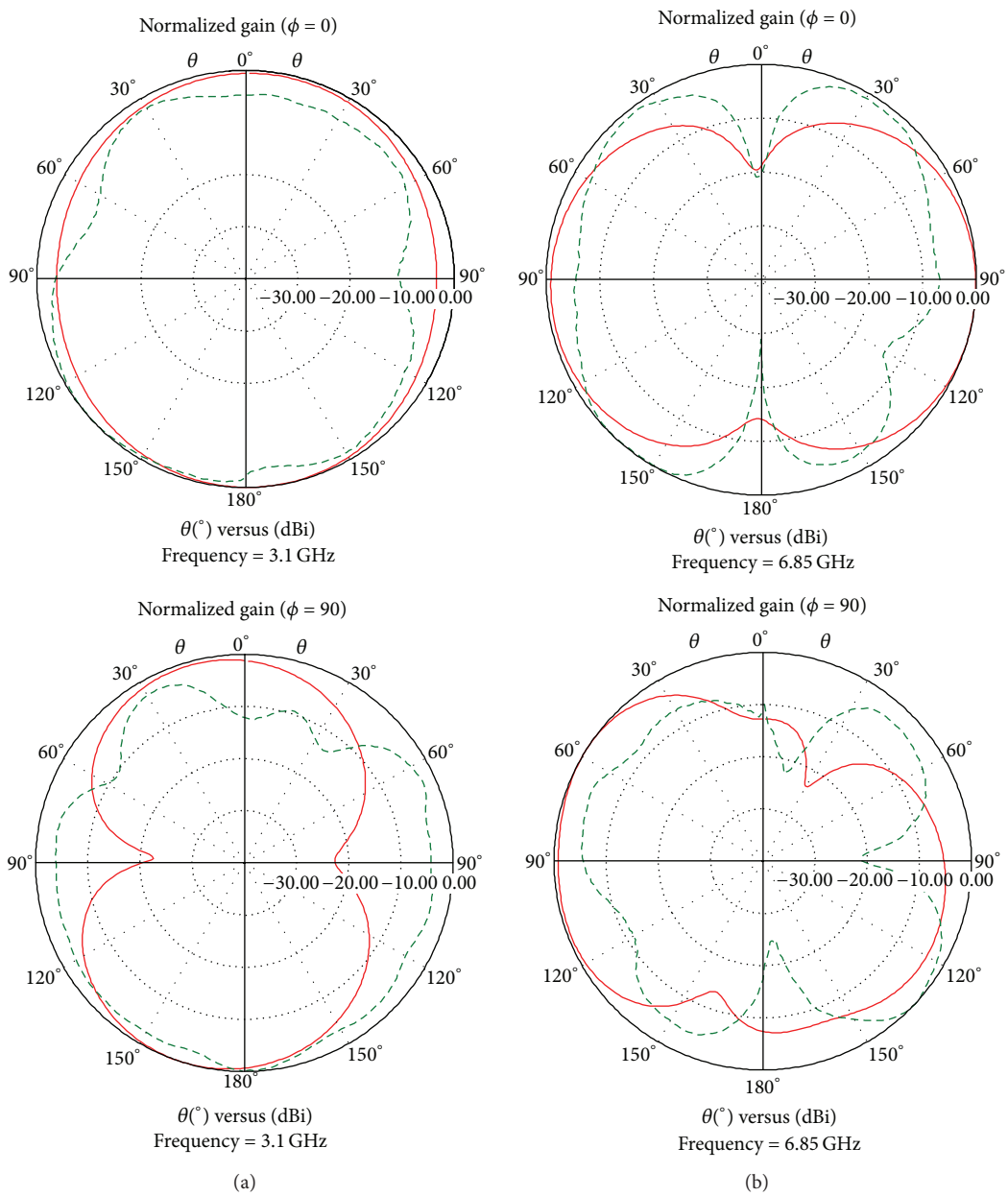

Figure 7: Simulated (solid) and measured (dashed) E-plane and H-plane radiation patterns for the center frequency: (a) 3.1 GHz and (b) 6.85 GHz for ON state of the switch.

and frequency band switching such as cognitive radio could benefit from the proposed reconfigurable antenna.

References

[1] Y. Tawk, A. R. Albrecht, S. Hemmady, G. Balkrishnan, and C. G. Christodoulou, "Optically pumped frequency reconfigurable antenna design," *IEEE Antennas and Wireless Propagation Letters*, vol. 9, pp. 280–283, 2010.

[2] Y. Zhang, W. Hong, C. Yu, Z. Q. Kuai, Y. D. Don, and J. Y. Zhou, "Planar ultrawideband antennas with multiple notched bands based on etched slots on the patch and/or split ring resonators on the feed line," *IEEE Transactions on Antennas and Propagation*, vol. 56, no. 9, pp. 3063–3068, 2008.

[3] M. Al-Husseini, J. Costantine, C. G. Christodoulou, S. E. Barbin, A. El-Hajj, and K. Y. Kabalan, "A reconfigurable frequency-notched UWB antenna with split-ring resonators," in *Proceedings of Asia-Pacific Microwave Conference (APMC '10)*, pp. 618–621, December 2010.

[4] C. J. Panagamuwa, A. Chauraya, and J. C. Vardaxoglou, "Frequency and beam reconfigurable antenna using photoconducting switches," *IEEE Transactions on Antennas and Propagation*, vol. 54, no. 2, pp. 449–454, 2006.

[5] D. H. Auston, "Picosecond optoelectronic switching and gating in silicon," *Applied Physics Letters*, vol. 26, no. 3, pp. 101–103, 1975.

[6] W. Platte, "Spectral dependence of microwave-power transmission in laser-controlled solid-state microstrip switches," *IEE*

Journal on Solid-State and Electron Devices, vol. 2, no. 4, pp. 97–103, 1978.

[7] J. R. Flemish and R. L. Haupt, "Optimization of a photonically controlled microwave switch and attenuator," *IEEE Transactions on Microwave Theory and Techniques*, vol. 58, no. 10, pp. 2582–2588, 2010.

[8] Y. Horii and M. Tsutsumi, "Scattering parameters of semiconductor microstrip line under laser spot illumination," in *Proceedings of the IEEE MTT-S International Microwave Symposium Digest*, vol. 1–3, pp. 1675–1678, June 1996.

[9] D. Draskovic, C. Panagamuwa, J. C. Vardaxoglou, and D. Budimir, "Frequency reconfigurable RF circuits using photoconducting switches," *International Journal of RF and Microwave Computer-Aided Engineering*, vol. 20, no. 1, pp. 15–21, 2010.

[10] D. Draskovic, C. Panagamuwa, D. Budimir, and J. C. Vardaxoglou, "Frequency switchable dual-band branch-line couplers," in *Proceedings of the 39th European Microwave Conference (EuMW '09)*, pp. 133–136, Rome, Italy, October 2009.

[11] D. Draskovic and D. Budimir, "Optically reconfigurable dual-band compact branch-line couplers," in *Proceedings of the 2nd European Conference on Antennas and Propagation (EuCAP '07)*, pp. 11–16, Edinburgh, UK, November 2007.

[12] K. F. Raihn, N. O. Fenzi, E. R. Soares, and G. L. Matthaei, "Optical switch for high temperature superconducting microwave band reject resonators," in *Proceedings of the IEEE MTT-S International Microwave Symposium*, vol. 1–3, pp. 187–190, May 1995.

[13] C. H. Lee, P. S. Mak, and A. P. DeFonzo, "Optical control of millimeter-wave propagation in dielectric wave-guides," *IEEE Journal of Quantum Electronics*, vol. 16, no. 3, pp. 277–288, 1980.

Hindawi Publishing Corporation
International Journal of Antennas and Propagation
Volume 2013, Article ID 291064, 7 pages
http://dx.doi.org/10.1155/2013/291064

Research Article

Safety Aspects of People Exposed to Ultra Wideband Radar Fields

Marta Cavagnaro, Stefano Pisa, and Erika Pittella

Department of Information Engineering, Electronics and Telecommunications, Sapienza University of Rome, Rome 00184, Italy

Correspondence should be addressed to Marta Cavagnaro; cavagnaro@die.uniroma1.it

Received 5 October 2012; Accepted 24 December 2012

Academic Editor: Renato Cicchetti

The safety aspects of people exposed to the field emitted by ultra wideband (UWB) radar, operating both in the spatial environment and on ground, for breath activity monitoring are analyzed. The basic restrictions and reference levels reported in the ICNIRP safety guideline are considered, and the compliance of electromagnetic fields radiated by a UWB radar with these limits is evaluated. First, simplified analytical approaches are used; then, both a 3-dimensional multilayered body model and an anatomical model of the head have been used to better evaluate the electromagnetic absorption when a UWB antenna is placed in front of the head. The obtained results show that if the field emitted by the UWB radar is compliant with spatial and/or ground emission masks, then both reference levels and basic restrictions are largely satisfied.

1. Introduction

Ultra wideband radars have unique features suitable for a large variety of biomedical sensing applications, as for example, the continuous monitoring of breath activity, the monitoring of internal organ movements, the measurement of the heart rate variability, and the pregnancy monitoring.

The first UWB radar for remote sensing was patented in 1994 by McEwan at the Lawrence Livermore National Laboratory (LLNL) [1]. This kind of radar is constituted by a pulse generator, a UWB receiver, a timing circuitry, a signal processor, and UWB antennas. The pulse generator is based on a pulse repetition interval generator with a repetition rate in the range 1–10 MHz followed by a step-like generator producing a fast rise-time edge. Then, one or more impulse-shaping networks convert the fast edge in a signal whose time dependence is Gaussian-like or a higher derivative of the Gaussian pulse [2]. Subsequently, the signal is sent to the transmitting UWB antenna and it is radiated toward the target. Once reflected by the target, the impulse is received by the same or a different UWB antenna, detected by a suitable receiving section [3, 4], and processed to evaluate the distance between the antenna and the target.

In accordance with the previous description, the UWB radar radiated signal is a pulse train with a repetition rate in the 1–10 MHz range. Due to the particular applications of UWB radar in medicine, crucial points to investigate are the assessment of the UWB radar radiated field and the study of the compliance with safety guidelines. To this end, since the foreseen applications of the UWB radar are both on ground and inside a spatial environment, the maximum value of the radiated field used in this study will be settled considering the emission masks of the Federal Communications Commission (FCC) [5], defined on imaging systems, and of the space environment [6], referring to the electromagnetic compatibility of the electronic apparatuses [7].

The safety issue related to the exposure of humans to the electromagnetic field emitted by the UWB radar can be evaluated following the guidelines issued by ICNIRP (International Commission on Non-Ionizing Radiation Protection) [8] and referenced in the European regulations [9]. ICNIRP guideline was published in 1998 [8] and recently reconfirmed in the frequency range 100 kHz–300 GHz [10]. This guideline defines basic restrictions, which are restraining values directly linked to health effects, and reference levels, which are limits on the electromagnetic field impinging on

the subject. Moreover, a distinction between workers, that is, people who are exposed to the electromagnetic field due to their work, and the general population is done, with lower limits settled for this last category of people.

In this work, the safety assessment related to the exposure of people to UWB radar fields is tackled in several ways.

An analytical study is performed first to evaluate the compliance of the UWB radar with ICNIRP safety guidelines under the hypothesis that the maximum allowable levels, extrapolated by FCC and spatial emission masks, are used. Then, this analysis is refined simulating a realistic scenario in which a multilayered body model is placed in front of a UWB antenna. Finally, an anatomical model of the head is taken into account in the presence of the same UWB antenna.

The paper is organized as follows: in Section 2, the ICNIRP guideline is introduced. In Section 3, the compliance of the UWB radar with ICNIRP limits is examined, using a model of the radar for the estimation of the radiated field and using a worst case analytical approach to test compliance with basic restrictions. In Section 4, the electromagnetic absorption is evaluated considering a 3-dimensional multilayered body model and an anatomical model of the human head. Eventually, in Section 5, conclusions are drawn.

2. Limits and Exposure Levels

According to FCC [5], a UWB radar used for medical purposes should emit an electromagnetic field whose spectrum covers the 3.1–10.6 GHz band. In this frequency band, the main effect that the electromagnetic field can produce inside the human body is the temperature increase, related to the power absorption [8].

Into the safety guidelines, thermal effects of electromagnetic field are associated to the SAR, defined as the power absorbed per unit mass and measured in W/kg [8]. Accordingly, in the 100 kHz–10 GHz band, the ICNIRP guideline settles limits (named "basic restrictions") on the SAR considering both the SAR as averaged over the whole body (SAR_{WB}) and the SAR as averaged over 10 g in the head and trunk ($SAR_{10\,g}$) and in the limbs ($SAR_{10\,gL}$), as reported in Table 1. These values are averaged over 6 min [8]. When near field exposures are considered, since the electromagnetic field distribution may be highly inhomogeneous, and there could be a direct coupling between the electromagnetic field source and the exposed humans, the SAR limits must be considered.

For far field exposure, ICNIRP gives reference levels in terms of electromagnetic field values derived from the basic restrictions through dosimetry considerations.

Reference levels are defined as unperturbed field values spatially averaged over the entire body of the exposed individual. The electric field, magnetic field, and power density reference levels for the general population in the frequency range from 2 GHz to 300 GHz are settled to 61 V/m, 0.16 A/m, and 10 W/m^2, respectively [8].

Moreover, since the field radiated by the UWB radar is constituted by a pulse train, exposure limits have to be considered for short-term effects, with particular reference to the microwave hearing effect [8]. These limits are settled in terms of specific energy absorption (SA) and temporal peak of the electric field. According to ICNIRP, "*for pulsed exposures in the frequency range 0.3 to 10 GHz and for localized exposure of the head, in order to limit or avoid auditory effects caused by thermoelastic expansion, an additional basic restriction is recommended. This is that the SA* [defined as the time integral of SAR] *should not exceed 10 mJ/kg for workers and 2 mJ/kg for the general public, averaged over 10 g tissue*." (note no. 7, Table 4 in [8]). Furthermore, "*although little information is available on the relation between biological effects and peak values of pulsed fields, it is suggested that, for frequencies exceeding 10 MHz,* S_{eq} [i.e., the power density] *as averaged over the pulse width should not exceed 1,000 times the reference levels or that field strengths should not exceed 32 times the field strength reference levels*".

Table 1: ICNIRP basic restrictions in the 100 kHz–10 GHz band [7].

	SAR_{WB} (W/kg)	$SAR_{10\,g}$ (W/kg)	$SAR_{10\,gL}$ (W/kg)
Workers	0.4	10	20
General population	0.08	2	4

3. Compliance Evaluations

Since in the considered application (i.e., remote monitoring of the breath activity) the exposed subject is mainly in the antenna far field region, reference levels must be considered for safety purposes. On the other hand, because the subject under investigation could move during monitoring, it may happen that the subject could find himself close to the antenna thus taking up the reactive field. Consequently, also basic restrictions have been taken into account. Furthermore, for some particular body positions, the UWB signal could impinge on the subject head; therefore, also SA estimation has been considered [11–13].

To compare the radiated field, the SAR, and the SA values produced by the UWB radar with the limits reported in the ICNIRP standard, three safety factors have been defined as follows:

$$\mathrm{SE} = \left(\frac{E_{\mathrm{REF}}}{E_{\mathrm{COMP}}}\right)^2, \qquad \mathrm{SS} = \frac{\mathrm{SAR}_{\mathrm{REF}}}{\mathrm{SAR}_{\mathrm{COMP}}}, \qquad \mathrm{SW} = \frac{\mathrm{SA}_{\mathrm{REF}}}{\mathrm{SA}_{\mathrm{COMP}}}, \tag{1}$$

where E_{REF} is the electric field reference value reported in the ICNIRP standard, E_{COMP} is the computed radiated field, $\mathrm{SAR}_{\mathrm{REF}}$ and $\mathrm{SA}_{\mathrm{REF}}$ are the values of the SAR and SA settled in the ICNIRP guideline, and $\mathrm{SAR}_{\mathrm{COMP}}$ and $\mathrm{SA}_{\mathrm{COMP}}$ are the computed SAR and SA, respectively. According to the definition, the higher the value of the safety factor, the lower the exposure of the subject.

3.1. Reference Levels in relation to FCC Emission Masks. In the FCC regulations, emission masks are based on EIRP

measured on a specified bandwidth. According to FCC [5], for UWB medical imaging systems, the radiated emissions between 3.1 GHz and 10.6 GHz shall not exceed the EIRP value of −41.3 dBm, when measured using a resolution bandwidth of 1 MHz. Correspondingly, the value reported at a given frequency indicates the maximum allowed EIRP within a bandwidth of 1 MHz, centered on that frequency.

To evaluate the maximum amplitude of the source signal allowed by FCC emission mask, the UWB radar model presented in [14] has been used. Simulations have been performed by using the half-heart shaped UWB antenna introduced in [15], by considering a source with a repetition rate of 1 MHz and various time behaviors of the signal. In particular, the Gaussian pulse is given by

$$V_S(t) = V_0 e^{-(1/2)((t-t_0)/\sigma)^2}, \tag{2}$$

with $\sigma = 100$ ps, and it has been considered together with its first 4 derivatives. For each pulse, the maximum amplitude V_0 that gives rise to an EIRP in compliance with the FCC emission mask has been computed (see legend in Figure 1).

By considering the fourth derivative of the Gaussian pulse, whose maximum amplitude in compliance with FCC is equal to 1 V, the total EIRP ($\mathrm{EIRP}_{\mathrm{TOT}}$) value has been computed by the following formula:

$$\mathrm{EIRP}_{\mathrm{TOT}} = \frac{1}{1\,\mathrm{MHz}} \int_{f_L}^{f_H} \mathrm{EIRP}(f)\, df, \tag{3}$$

finding a value of 1.76 μW. The electric field intensity value 1 m far from the antenna can be evaluated by

$$E_{\mathrm{rms}}^2 = \frac{\mathrm{EIRP}_{\mathrm{TOT}} 120\pi}{4\pi(1.0)^2} \tag{4}$$

and is equal to 0.007 V/m. This electric field value is well below the 61 V/m reference level defined by ICNIRP. In this case, the safety factor is $\mathrm{SE} = 7.6 \cdot 10^7$.

Eventually, considering the electric field time behavior obtained at a distance of 1 m from the radar with the same excitation conditions (in particular considering the fourth derivative of the Gaussian pulse with an amplitude of 1 V), the computed electric field peak value is equal to 0.57 V/m. According to ICNIRP, this value should not exceed 32 times the field strength reference level (61 V/m) and hence 1952 V/m. The corresponding safety factor SE is about $1.2 \cdot 10^7$.

3.2. Reference Levels in relation to Space Environment Emission Masks. Regarding the electromagnetic compatibility masks of the spatial environment [6], the compliance with Columbus and NASA masks for narrowband emission has been verified for the same UWB radar model previously introduced [14]. Simulations have been performed by using the half-heart shaped antenna [15], a source with a repetition rate of 1 MHz having the time behaviors of a Gaussian pulse with $\sigma = 100$ ps and of its first 4 derivatives. Also in this case, for each pulse, the maximum amplitude, that gives rise to an electric field in compliance with both Columbus and NASA masks, has been computed. The values are reported in Figure 2.

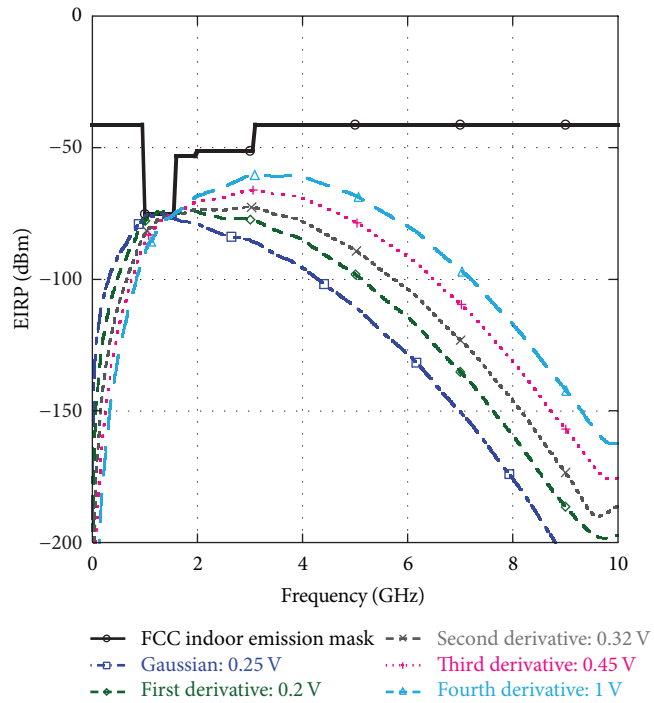

Figure 1: Computed EIRP for various pulse shapes achieved with a real UWB antenna. The maximum pulse amplitude that gives rise to EIRP in compliance with FCC indoor emission mask is reported.

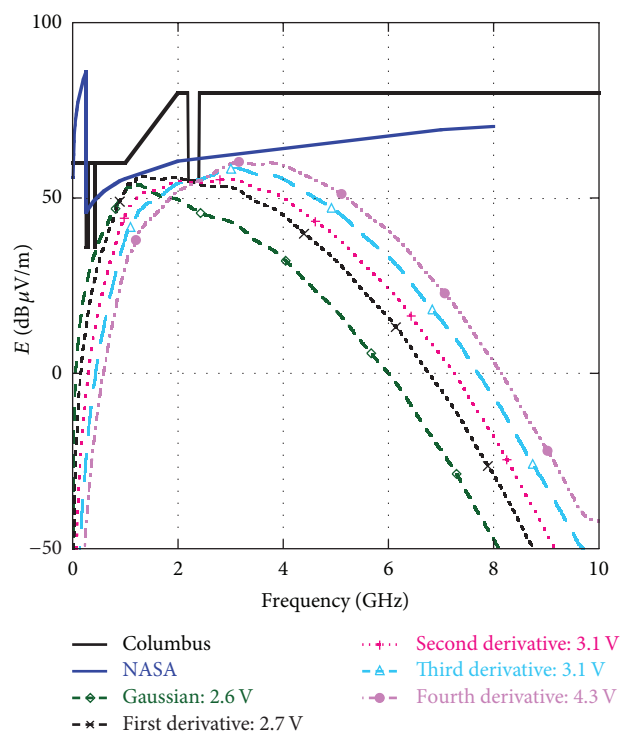

Figure 2: Computed E-field for various pulse shapes. The maximum pulse amplitude that gives rise to an E-field level in compliance with Columbus and NASA emission mask is reported.

In this case, by considering the fourth derivative of the Gaussian pulse, the maximum EIRP evaluated from (3) is 32.5 μW. Correspondingly, the maximum electric field intensity value, evaluated from (4), is equal to 0.03 V/m. The safety factor value is SE = $4.1 \cdot 10^6$. Finally, the electric field time behavior has a peak value equal to 2.48 V/m so that the SE is about $0.62 \cdot 10^6$.

From the values shown in Figures 1 and 2, it can be noted that the maximum voltage of the pulse generator that gives rise to an electric field that meets the space environment masks is higher than the one that complies with the FCC mask.

3.3. Whole Body SAR. Taking into account the radiated power when the fourth derivative of the Gaussian pulse is applied with its maximum allowable value (see Figures 1 and 2), the $\mathrm{SAR_{WB}}$ have been computed, considering a worst case condition in which a man weighting 72.4 kg (M) absorbs all the radiated power. In this case, the whole body averaged SAR, namely, the power absorbed per unit mass, is

$$\mathrm{SAR_{WB}} = \frac{P_{\mathrm{RAD}}}{M} = \frac{1.76\,\mu\mathrm{W}}{72.4\,\mathrm{kg}} = 2.43 \cdot 10^{-8}\ \mathrm{W/kg}, \quad (5)$$

in the case of FCC mask, and

$$\mathrm{SAR_{WB}} = \frac{P_{\mathrm{RAD}}}{M} = \frac{32.5\,\mu\mathrm{W}}{72.4\,\mathrm{kg}} = 4.49 \cdot 10^{-7}\ \mathrm{W/kg}, \quad (6)$$

in the case of Columbus and NASA masks.

As it can be noted from (5) and (6), the computed SAR values are well below the 0.08 W/kg limit provided by ICNIRP for general population. Regarding the SS safety factor, we obtain

$$\begin{aligned} \mathrm{SS} &= \frac{0.08}{2.43 \cdot 10^{-8}} = 3.3 \cdot 10^6, \\ \mathrm{SS} &= \frac{0.08}{4.49 \cdot 10^{-7}} = 0.18 \cdot 10^6, \end{aligned} \quad (7)$$

for FCC and spatial masks, respectively.

3.4. SAR Averaged over 10 g. By supposing that the same radiated power is all absorbed in 10 g mass of the exposed subject, the $\mathrm{SAR_{10\,g}}$, in the case of FCC mask fulfillment, is given by

$$\mathrm{SAR_{10\,g}} = \frac{P_{\mathrm{RAD}}}{M} = \frac{1.76\,\mu\mathrm{W}}{0.01\,\mathrm{kg}} = 1.76 \cdot 10^{-4}\ \mathrm{W/kg}, \quad (8)$$

while for the spatial masks case, we obtain

$$\mathrm{SAR_{10\,g}} = \frac{P_{\mathrm{RAD}}}{M} = \frac{32.5\,\mu\mathrm{W}}{0.01\,\mathrm{kg}} = 3.25 \cdot 10^{-3}\ \mathrm{W/kg}. \quad (9)$$

Also, in this case, the computed SAR value is well below the limit value established by ICNIRP for general population and for the SAR averaged over 10 g mass, that is, 2 W/kg. In this case, the SS values are given by

$$\begin{aligned} \mathrm{SS} &= \frac{2}{1.76 \cdot 10^{-4}} = 1.1 \cdot 10^4, \\ \mathrm{SS} &= \frac{2}{3.25 \cdot 10^{-3}} = 6.1 \cdot 10^2, \end{aligned} \quad (10)$$

for FCC and spatial masks, respectively.

3.5. SA Evaluations. In order to take into account the possibility that the exposed subject stands with the head in front of the radar antenna, the specific energy absorption has been calculated, starting from the SAR averaged over 10 g mass. In particular, since the SA is defined as the time integral of SAR over a signal period T [8], it can be obtained as

$$\mathrm{SA} = \int_0^T \mathrm{SAR}\,dt = \mathrm{SAR} \cdot T. \quad (11)$$

For a period T of 1 μs (equivalent to a pulse repetition frequency of 1 MHz), we obtain

$$\mathrm{SA} = 1.76 \cdot 10^{-4} \cdot 10^{-6} = 1.76 \cdot 10^{-10}\ \mathrm{J/kg}, \quad (12)$$

in the case the radar is used on ground, and:

$$\mathrm{SA} = 3.25 \cdot 10^{-3} \cdot 10^{-6} = 3.25 \cdot 10^{-9}\ \mathrm{J/kg}, \quad (13)$$

if the radar operates in the spatial environment.

The computed SA values are well below the limit value established by ICNIRP for the general population that is equal to 2 mJ/kg. The safety factors (SW) values are

$$\begin{aligned} \mathrm{SW} &= \frac{2}{1.76 \cdot 10^{-7}} = 1.1 \cdot 10^7, \\ \mathrm{SW} &= \frac{2}{3.25 \cdot 10^{-6}} = 0.61 \cdot 10^6 \end{aligned} \quad (14)$$

for FCC and spatial masks, respectively.

4. SA Evaluations in 3D Human Models

To better evaluate the specific energy absorption, both a multilayered planar model, similar to that studied in [16], and a 3D anatomical model of the head have been considered.

The model used in [16] was derived from the Visible Human (VH) data set [17]. However, other human body models are available for electromagnetic dosimetry studies. In particular, the so-called "Virtual population" comprises a man (Duke, 34-year-old), a woman (Ella, 26-year-old), and several children [18]. While the VH model represents a relatively big man (1.80 m tall and 103.0 kg weight), Duke, being 1.77 m tall and weighting 72.4 kg, is closer to the "standard man" dimensions.

Starting from the Duke model, a section passing through the head has been considered in order to build a multilayered body model whose tissues and corresponding thicknesses are shown in Table 2. Moreover, the whole Duke's head has been taken into account.

Table 2: Tissues and corresponding thicknesses of a section of the head of the Duke model.

	Duke model	
	Tissue	Thickness (mm)
1	Skin	3
2	Fat	8
3	Muscle	10
4	Bone	6
5	Brain	50

4.1. SA Evaluations in a 3D Multilayered Model. Specific energy absorption (SA) has been computed by electromagnetic simulations exposing the multilayered model derived from the Duke to the field radiated by the half-heart shaped antenna [15]. The antenna has been excited with a voltage source whose time behavior is the fourth derivative of the Gaussian pulse with amplitude 1 V (Figure 3). The electric field as a function of the time has been computed in correspondence with 15 different positions within the layered model, as shown in Figure 3.

Starting from the field values, the SA has been computed according the following relationship:

$$\mathrm{SA} = \int_0^T \frac{J(t)\,E(t)}{\rho} \cdot dt. \tag{15}$$

Figure 4 shows the calculated SA profile in the Duke skin layer (plane xz of Figure 3), while Figure 5 shows the values of the SA computed in the various tissues as a function of the distance from the antenna (direction y of Figure 3). The figures show that the highest value of the SA is found in the skin, right in front of the antenna, and it is equal to 5.9 pJ/kg. By considering a worst case approach in which the 10 g averaged SA is supposed to be equal to the peak SA, a value well below the limit of 2 mJ/kg established by ICNIRP for the general public is obtained.

4.2. SA Evaluations in the Duke Anatomical Model of the Head. To study a more realistic condition, an electromagnetic analysis has been performed considering the anatomical Duke model of the head exposed to the heart-shaped UWB antenna. In particular, the UWB antenna has been placed 5 cm far from the head in correspondence with a Duke's eye (see Figure 6).

Figure 7 shows the SA profile computed in the various tissues of the Duke head as a function of the distance from the antenna. As it can be noted from the figure, the highest value of the SA, in correspondence with the eye lens, is equal to $7.9 \cdot 10^{-2}$ pJ/kg that is well below the value of 2 mJ/kg for the general public established by ICNIRP.

As regarding the computation of the whole body SAR and the SAR as averaged over 10 g for the Duke's model, the considerations reported in Sections 3.3 and 3.4 can be applied, respectively.

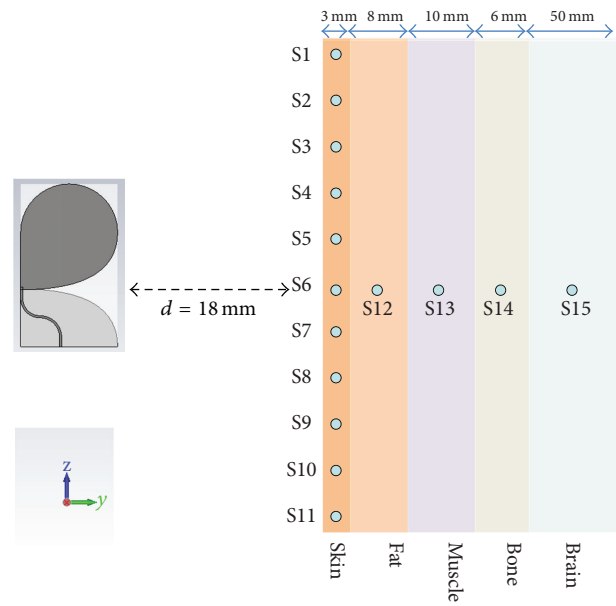

Figure 3: UWB antenna in the presence of the multilayered body model.

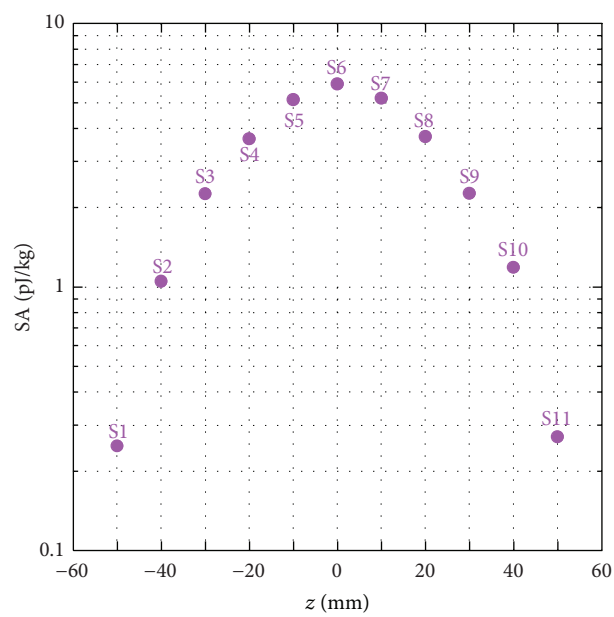

Figure 4: SA evaluated inside the skin tissue.

5. Conclusions

This paper addresses the safety aspects of people exposed to the field emitted by ultra wideband radar operating both in the spatial environment and on ground.

The compliance with ICNIRP SAR and SA limits and field exposure levels has been evaluated considering the emission mask issued by the FCC and those to be considered in space environment.

The comparison of the computed electric field values with reference levels issued by ICNIRP reveals that the peak values

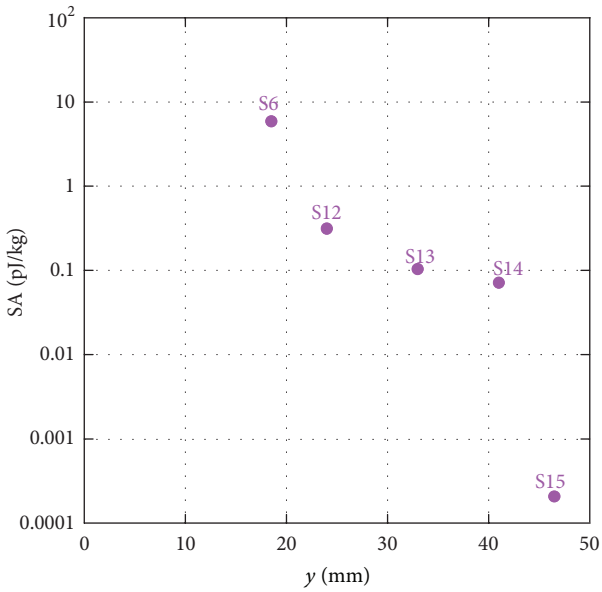

Figure 5: SA evaluated inside the various tissues of the considered multilayered body model.

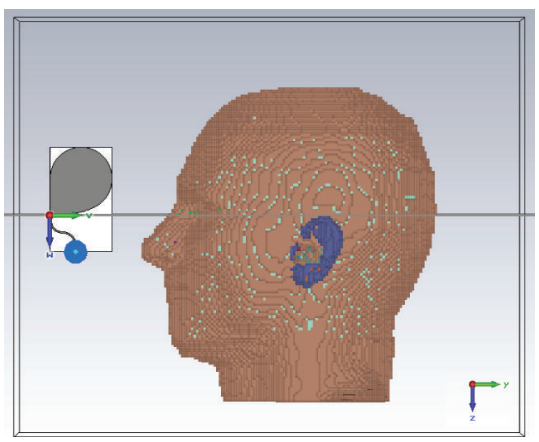

Figure 6: UWB antenna and the anatomical model of the Duke's head.

give rise to lower safety factors with respect to RMS values. Moreover, the safety factor achieved satisfying FCC emission mask is higher than the one evaluated filling the spatial masks.

On the basis of the conducted analysis, the parameter that gives rise to the lower safety factor is the SAR averaged over 10 g of mass. However, in this case, it has been supposed that all the radiated power is absorbed in 10 g mass, which is quite an unrealistic hypothesis.

Furthermore, the SA evaluation conducted considering a 3D electromagnetic model of the Duke placed close a UWB antenna has shown that also, in this case, ICNIRP restrictions are largely satisfied.

In particular, numerical results concerning SA show that simulated values are two-order magnitude lower than the analytical ones evaluated in a worst case condition.

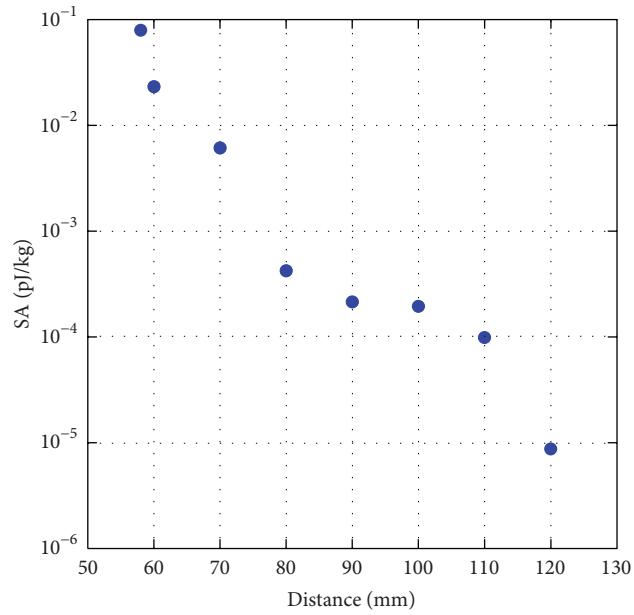

Figure 7: SA evaluated inside the head tissues as a function of the distance from the UWB antenna.

Acknowledgment

This research is funded by the Italian Space Agency (ASI), under Contract no. I/009/11/0 (NIMURRA Project).

References

[1] T. E. McEwan, "Ultra-wideband radar motion sensor," US Patent 5,36,070, 1994.

[2] J. R. Andrews, "UWB signal sources, antennas and propagation," Application Note AN-14a, Picosecond Pulse Labs, Boulder, Colo, USA, 2003.

[3] J. D. Taylor and T. E. McEwan, "The micropower impulse radar," in *Ultra-Wideband Radar Technology*, J. D. Taylor, Ed., pp. 155–164, CRC Press, Boca Raton, Fla, USA, 2001.

[4] J. Dederer, B. Schleicher, F. A. T. Santos, A. Trasser, and H. Schumacher, "FCC compliant 3.1–10.6 GHz UWB pulse radar system using correlation detection," in *Proceedings of the IEEE MTT-S International Microwave Symposium, (IMS '07)*, pp. 1471–1474, Honolulu, Hawaii, USA, June 2007.

[5] FCC02-48, "Revision of part 15 of the commission's rules regarding ultra-wideband transmission systems," 2002.

[6] International Space Station, "Space station electromagnetic emission and susceptibility requirements," Revision F, 2001.

[7] P. Russo, V. M. Primiani, A. De Leo, and G. Cerri, "Radiated emission of breath monitoring system based on UWB pulses in spacecraft modules," in *Proceedings of the ESA Workshop on Aerospace EMC*, pp. 1–6, Venice, Italy, May 2012.

[8] ICNIRP, "Guidelines for limiting exposure to time-varying electric, magnetic, and electromagnetic fields (up to 300 GHz)," *Health Physics*, vol. 74, no. 4, pp. 494–523, 1998.

[9] Commission of European Communities, *Council Recommendation on Limits for Exposure of the General Public to Electromagnetic Fields: 0 Hz–300 GHz*, EC, Brussels, Belgium, 1998.

[10] ICNIRP, "ICNIRP statement on the 'Guidelines for limiting exposure to time-varying electric, magnetic, and electromagnetic fields (UP to 300 GHz)'," *Health Physics*, vol. 97, no. 3, pp. 257–258, 2009.

[11] Q. Wang and J. Wang, "SA/SAR analysis for multiple UWB pulse exposure," in *Proceedings of the 2008 Asia-Pacific Symposium on Electromagnetic Compatibility and 19th International Zurich Symposium on Electromagnetic Compatibility (APEMC '08)*, pp. 212–215, Singapore, May 2008.

[12] S. Allen, J. C. Lin, J. B. Anderson et al., "ICNIRP statement on EMF-emitting new technologies," *Health Physics*, vol. 94, no. 4, pp. 376–392, 2008.

[13] V. De Santis, M. Feliziani, and F. Maradei, "Safety assessment of UWB radio systems for body area network by the FD_2TD method," *IEEE Transactions on Magnetics*, vol. 46, no. 8, pp. 3245–3248, 2010.

[14] S. Pisa, P. Bernardi, M. Cavagnaro, E. Pittella, and E. Piuzzi, "A circuit model of an ultra wideband impulse radar system for breath activity monitoring," *International Journal of Numerical Modelling*, vol. 25, no. 1, pp. 46–63, 2012.

[15] E. Pittella, P. Bernardi, M. Cavagnaro, S. Pisa, and E. Piuzzi, "Design of UWB antennas to monitor cardiac activity," *Applied Computational Electromagnetics Society Journal*, vol. 26, no. 4, pp. 267–274, 2011.

[16] E. M. Staderini, "UWB radars in medicine," *IEEE Aerospace and Electronic Systems Magazine*, vol. 17, no. 1, pp. 13–18, 2002.

[17] M. J. Ackerman, "The visible human project," in *Proceedings of the IEEE*, vol. 86, no. 3, pp. 504–511, March 1998.

[18] A. Christ, W. Kainz, E. G. Hahn et al., "The virtual family—development of surface-based anatomical models of two adults and two children for dosimetric simulations," *Physics in Medicine and Biology*, vol. 55, no. 2, pp. N23–N38, 2010.

Hindawi Publishing Corporation
International Journal of Antennas and Propagation
Volume 2013, Article ID 151864, 6 pages
http://dx.doi.org/10.1155/2013/151864

Research Article

Planar Printed Shorted Monopole Antenna with Coupled Feed for LTE/WWAN Mobile Handset Applications

Do-Gu Kang and Youngje Sung

Department of Electronic Engineering, Kyonggi University Yeongtong-gu, Suwon-si, Gyeonggi-do, Republic of Korea

Correspondence should be addressed to Youngje Sung; yjsung@kgu.ac.kr

Received 28 June 2012; Accepted 6 December 2012

Academic Editor: Antonio Faraone

A shorted monopole antenna with coupled feed for LTE/WWAN mobile handset applications is described. The basic resonance of the shorted monopole combines with the resonance formed by the coupling between the coupling strip and the feeding pad to cover the LTE700, GSM850, and GSM900 bands. Both the feeding pad and the coupling strip operate with the shorting strip as a loop antenna. The resonance of the loop antenna and the harmonics of the shorted monopole combine to cover the GSM1800, GSM1900, UMTS, and LTE2300 bands. A stable and omnidirectional radiation pattern with reasonable gain has been observed over the operating bandwidth.

1. Introduction

Technological advancements and the diversity of needs in wireless communication are leading to the development of antennas for smaller, lighter, and more multifunctional mobile handsets [1]. Consequently, planar monopoles [2–4] enabling pentaband WWAN (wireless wide area network) operation have been developed. The WWAN band covers the GSM850 (824–894 MHz), GSM900 (880–960 MHz), GSM1800 (1710–1880 MHz), GSM1900 (1850–1990 MHz), and UMTS (1920–2170 MHz) bands. These developed planar monopoles are, respectively, a monopole with coupled strips [2], a CPW-fed LI-shaped monopole [3], and a coupled-fed shorted monopole [4]. Recently, coupled-fed shorted monopoles covering not only the WWAN band but also the LTE band have been developed. The LTE band covers LTE700 (698–798 MHz), LTE2300 (2300–2400 MHz), and LTE2500 (2500–2690 MHz) [5, 6]. These monopoles operating in the WWAN/LTE bands are, respectively, a monopole with a tuning stub [5] and a monopole with a chip inductor-loaded shorted strip [6].

In this paper, a shorted monopole antenna with coupled feed for LTE/WWAN bands is proposed. The base resonance of the shorted monopole combines with the resonance formed by the coupling between the feeding pad and the coupling strip to include the LTE700, GSM850, and GSM900 bands. The loop antenna is formed by both the coupled feed structure and the shorting strip. The loop resonance and a harmonic element combine to cover the GSM1800, GSM1900, UMTS, and LTE2300 bands. Therefore, the proposed structure covers the LTE700, LTE2300, GSM850, GSM900, GSM1800, GSM1900, and UMTS bands.

2. Antenna Geometry

Figure 1 shows the proposed antenna which consists of a long radiator (AB), a coupling strip (BC), a feeding pad, and a shorting strip. l_1 denotes the total length of the long radiator. l_2 denotes the length of the part generating the coupled feed, and g denotes the gap between the feeding pad and the coupling strip; these are the two parameters that affect the coupled feed. l_3 denotes the length of the feeding pad. The antenna covers an area of $18 \times 49\,\text{mm}^2$ on the upper surface of an FR4 substrate with a 0.6 mm thick. The total area of the substrate is $118 \times 49\,\text{mm}^2$; the ground (GND) found on the lower surface of the substrate covers an area of $100 \times 49\,\text{mm}^2$.

3. Simulated and Measured Results

Figure 2 shows the simulated and measured reflection coefficients for the proposed antenna and reference 1. The

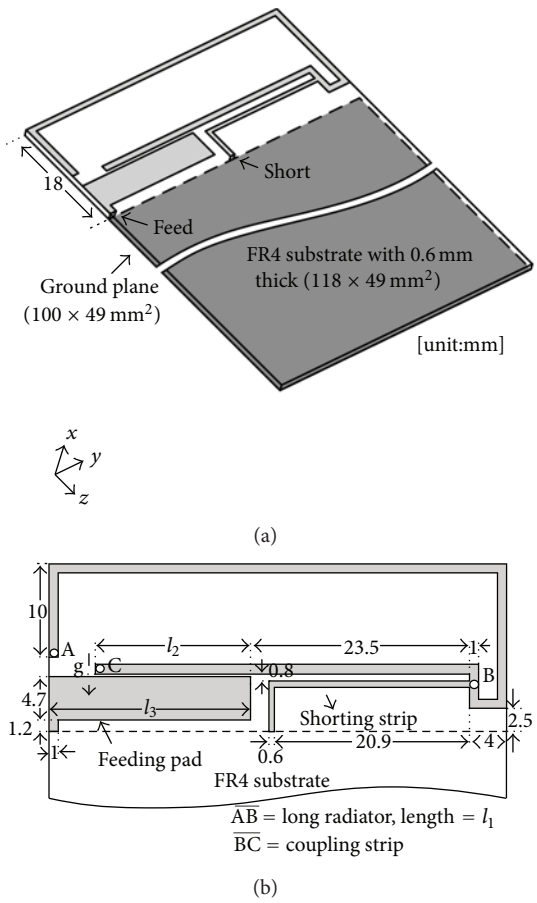

Figure 1: (a) 3D geometry of the proposed antenna. (b) The antenna geometry as seen from above.

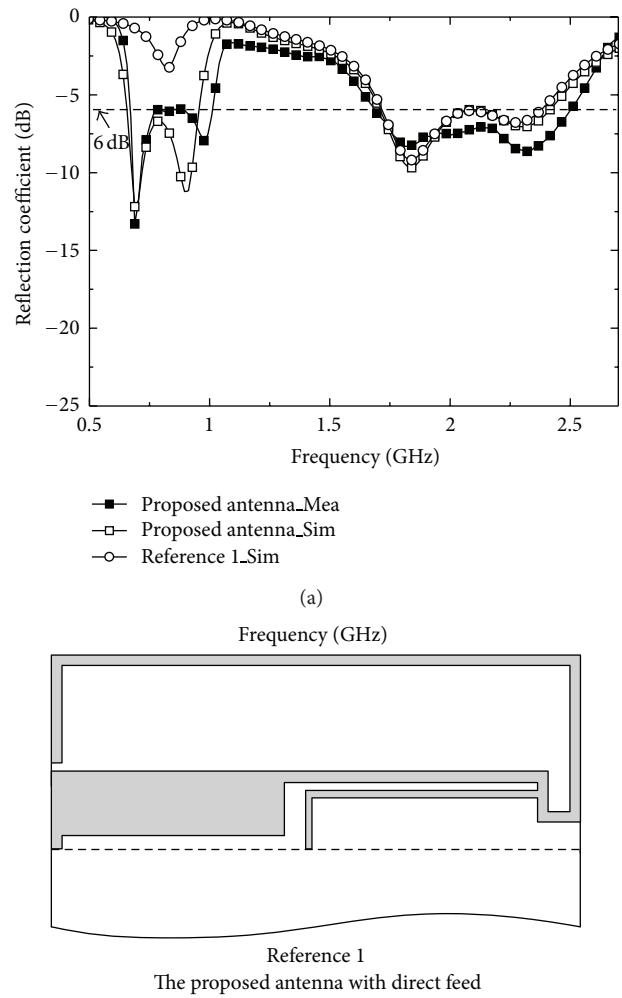

Figure 2: Simulated and measured reflection coefficients for the proposed antenna and reference 1.

parameters for the proposed antenna were set to $l_1 = 78$ mm, $l_2 = 16.5$ mm, $g = 0.3$ mm, and $l_3 = 21.5$ mm. The prototype of the proposed antenna is based on the foregoing optimized parameters and is fabricated as shown in Figure 3. The simulation was carried out through HFSS. The simulated results were nearly identical to the measured results. The proposed antenna has four resonant frequencies (f_1, f_2, f_3, and f_4). The low band covers the LTE700, GSM850, and GSM900 bands, and the high band covers the GSM1800, GSM1900, UMTS, and LTE2300 bands. All the bands operated properly with a −6 dB bandwidth which is a widely used value for internal WWAN antennas in practical mobile phone application.

If the proposed antenna's result is compared to reference 1′s (the proposed antenna with direct feed) result, the effect of the coupled feed can be observed. The matching characteristics of the base resonance were improved by the coupled feed that increases the electrical length. Therefore, the resonance frequency decreased. The resonance combined with the second resonance that was formed by the coupled feed. The two resonances form dual resonance. Therefore, the proposed antenna achieves a low wideband through the coupled feed.

Figure 3: Fabricated prototype of the proposed antenna.

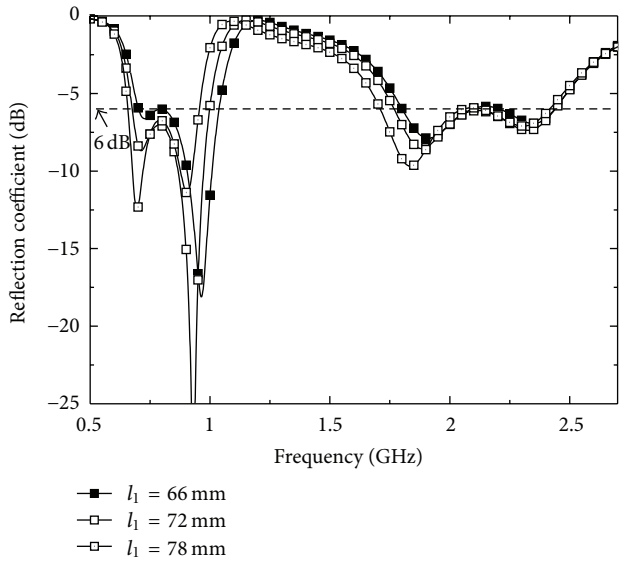

Figure 4: Simulated reflection coefficients relative to changes in the total length of the long radiator l_1.

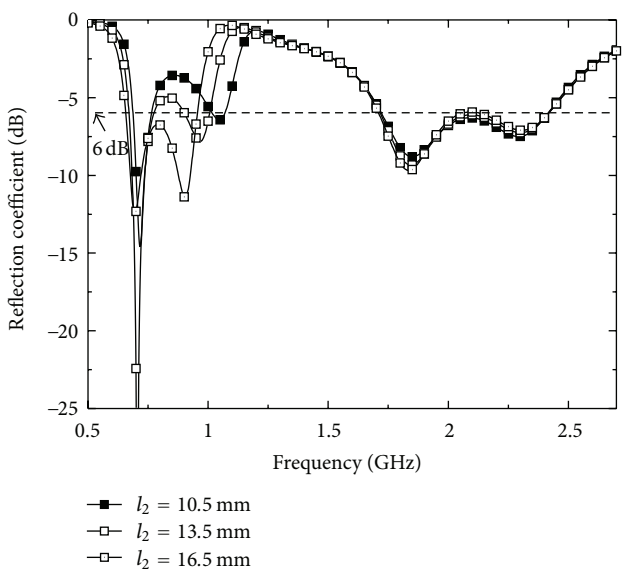

Figure 5: Simulated reflection coefficients relative to changes in the length of the part generating the coupled feed l_2.

Figure 4 shows the simulated reflection coefficients relative to the changes in the total length l_1 of the long radiator. The base resonance f_1 is formed by the long radiator's length which was a resonance length of $\lambda/4$ at f_1 (0.69 GHz). Further, f_3 decreased, which proves that f_3 is a harmonic of f_1. As l_1 increased, the lower edge of the high band decreased from 1.8 to 1.71 GHz. Thus, the antenna covers the GSM1800 band. Therefore, considering the high band, l_1 was selected as 78 mm.

Figure 5 shows the simulated reflection coefficients relative to the changes in length l_2 of the part generating the coupled feed l_2. Because l_2 affects the coupled feed, the

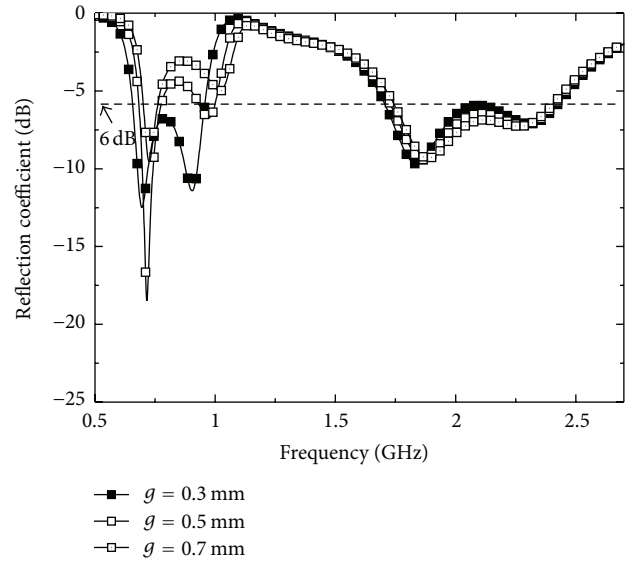

Figure 6: Simulated reflection coefficients relative to changes in the gap between feeding pad and coupling strip g.

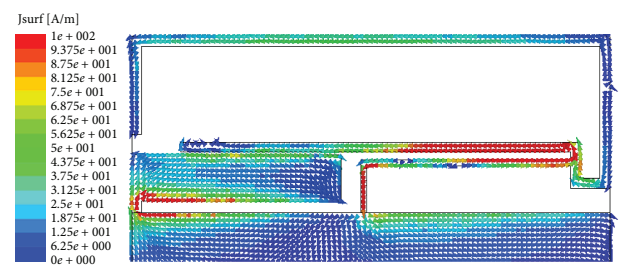

Figure 7: Surface current distribution simulated on the proposed antenna's radiator and GND at f_4 = 2.3 GHz.

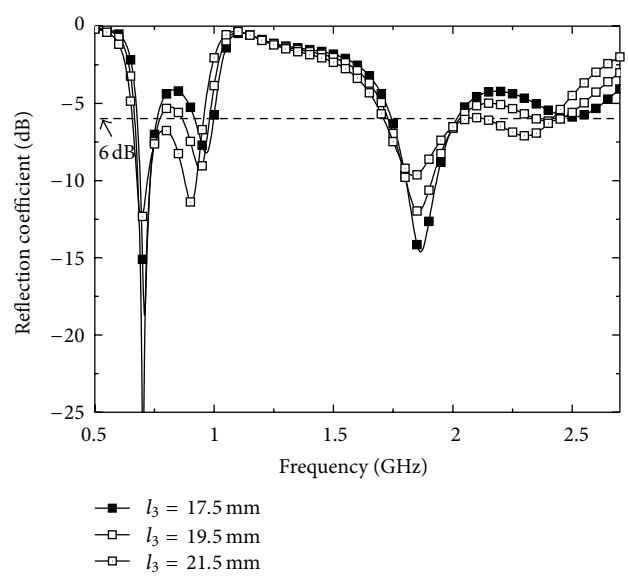

Figure 8: Simulated reflection coefficients relative to changes in the length of the feeding pad l_3.

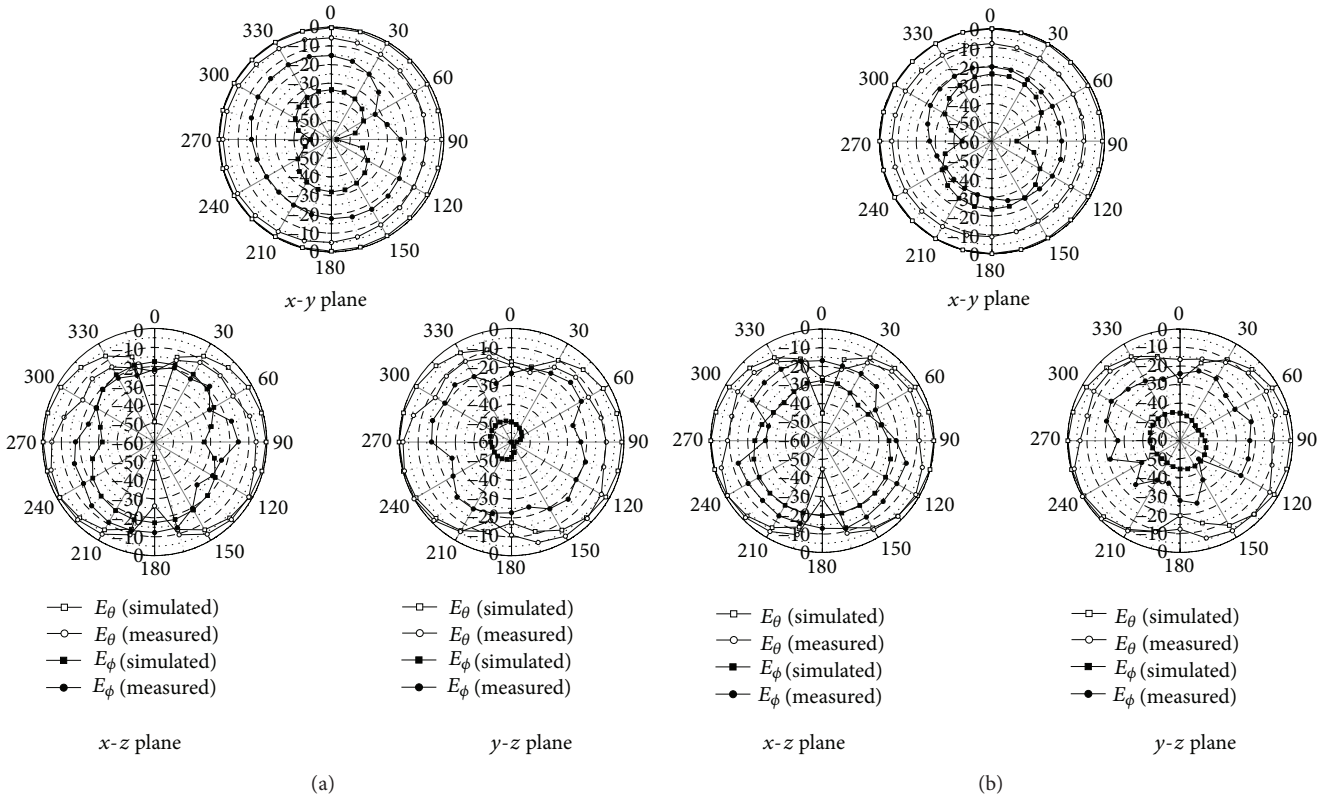

Figure 9: Simulated and measured 2D radiation patterns of proposed antenna: (a) $f_1 = 0.69$ GHz, (b) $f_2 = 0.9$ GHz.

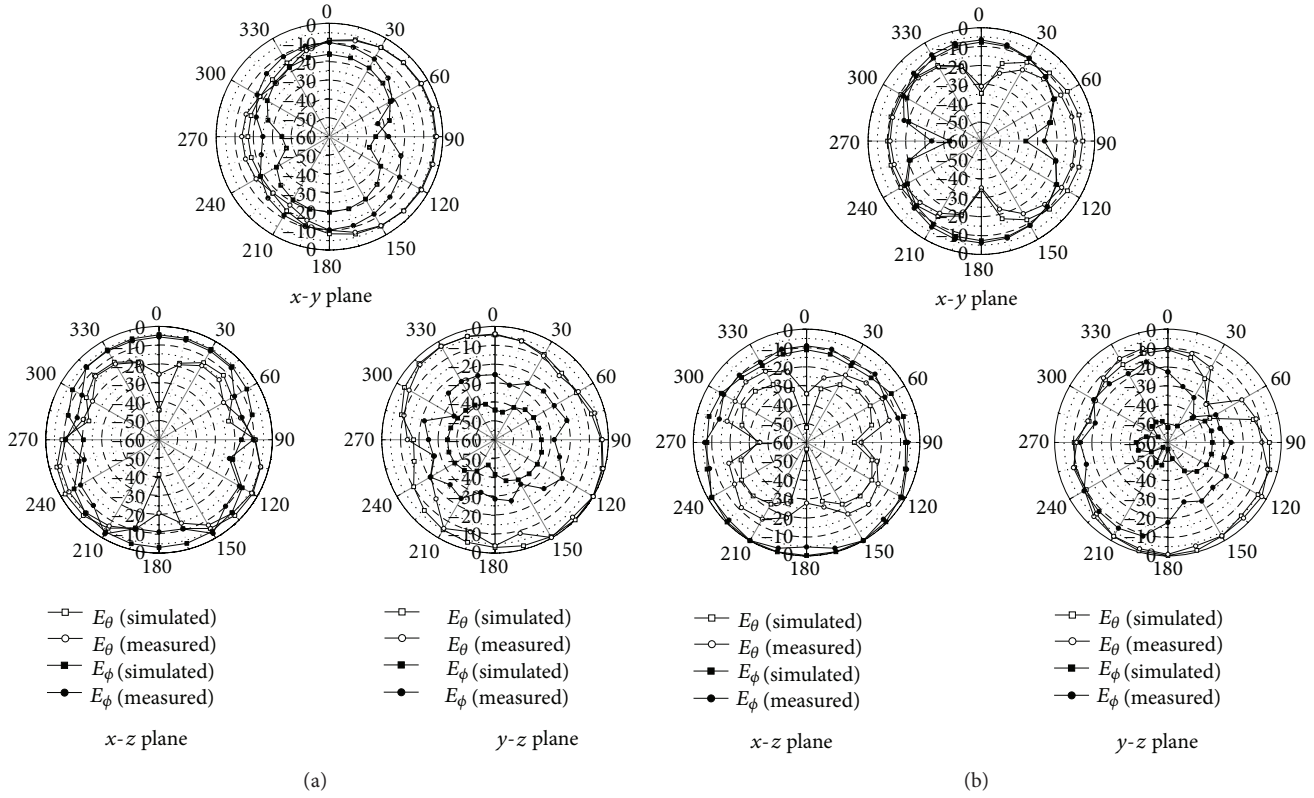

Figure 10: Simulated and measured 2D radiation patterns of proposed antenna: (a) $f_3 = 1.82$ GHz, (b) $f_2 = 2.3$ GHz.

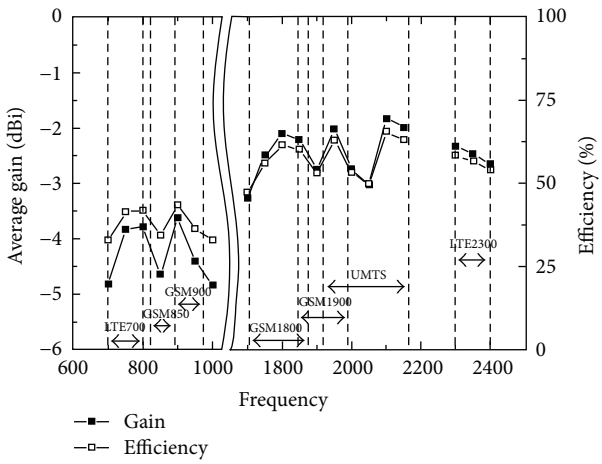

Figure 11: Measured average gain and efficiency of the proposed antenna.

resonance formed by the coupled feed was affected as l_2 changed. The base resonance formed by the long radiator further combined with the resonance formed by the coupled feed as l_2 increased. l_2 was selected as 16.5 mm to allow the antenna to have low wideband characteristics.

Figure 6 shows the simulated reflection coefficients relative to the changes in gap g between the feeding pad and the coupling strip. As g decreased, the matching of f_2 improved in the state the matching between f_1 and f_2 improved. Thus, considering the low band, g was selected as 0.3 mm.

Figure 7 shows the surface current distribution simulated on the proposed antenna's radiator and GND at f_4 = 2.3 GHz. The red area indicates a strong field, whereas the blue area indicates a weak field. The maximum current is located at the beginning of the feeding pad, and the null of the current is located at the end. The coupled gap was electrically connected. The maximum current on the coupling strip generated the maximum current on the shorting strip's end. The null is located between the maximum current on the shorting strip's end and the maximum current on the shorting strip's beginning. Through these findings, the path from the feeding pad to the coupled gap was combined with the path from the coupling strip to the shorting strip, which was the path of the loop operating at the λ resonant length. Therefore, f_4 was the resonant frequency of the loop antenna.

Figure 8 shows the simulated reflection coefficients relative to the changes in length l_3 of the feeding pad. As l_3 increased, the matching characteristics between f_1 and f_2 improved with a decrease of f_2. Because l_3 affected the length of the coupled feed, its effect was analogous to the effect of l_2 and g in the low band. Further, the matching characteristics between f_3 and f_4 improved with a decrease of f_4. To take into consideration the effect of both the high band and low band, l_3 was set to 21.5 mm. When a parameter study of l_3 was compared with other parameter studies, it showed that f_4 was relatively more transferred by l_3. This is because l_3 resides in the loop path.

Figures 9 and 10 show the simulated and measured 2D radiation patterns of the proposed antenna at f_1 = 0.69 GHz, f_2 = 0.9 GHz, f_3 = 1.82 GHz, and f_4 = 2.3 GHz. The radiation pattern was measured on the x- y, x- z, and y- z planes, on the basis of the direction of the antenna placement shown in Figure 1(a). The measured co-pols closely matched the simulated co-pols; the measured cross-pols were higher than the simulated cross-pols. The reason for this is that the GND was extended by the cabling used to measure the radiation pattern. Dipole-like radiation patterns with omnidirectional radiation in the azimuthal plane (x- y plane) are observed at two resonances of the low band in Figure 9. Conversely, more nulls and changes occurred in the radiation pattern observed for the two high band resonances in Figure 10. The obtained radiation patterns were analogous to the radiation patterns of WWAN mobile phone antennas [7, 8]. In addition, stable radiation patterns were obtained in both the low band and the high band. Figure 11 shows the measured average gain and efficiency of the proposed antenna. At the LTE700/GSM850/GSM900 band, the average gain varies from −4.8 to −3.6 dBi. At the GSM1800/GSM1900/UMTS band, it varies from −3.2 to −1.8 dBi, while it varies from −2.6 to −2.3 dBi at the LTE2300 band.

4. Conclusions

In this work, a shorted monopole antenna with a coupled feed for LTE/WWAN mobile handset applications was proposed. The base resonance of the shorted monopole and the resonance formed by the coupled feed structure combine to form a low wideband. The coupled feed structure and the shorting strip generate the loop antenna. The loop resonance combines with the harmonic element, which forms a high wideband. Therefore, the proposed structure is suitable for seven-band mobile handset applications, covering the LTE700, GSM850, GSM900, GSM1800, GSM1900, UMTS, and LTE2300 bands. Good radiation characteristics for frequencies over the operating bands were observed.

Acknowledgment

This research was supported by Basic Science Research Program through the National Research Foundation of Korea (NRF) funded by the Ministry of Education, Science, and Technology (2010-0021222).

References

[1] P. Ciais, R. Staraj, G. Kossiavas, and C. Luxey, "Design of an internal quad-band antenna for mobile phones," *IEEE Microwave and Wireless Components Letters*, vol. 14, no. 4, pp. 148–150, 2004.

[2] H. W. Liu and C. F. Yang, "Miniature multiband monopole antenna for WWAN operation in laptop computer," *Electronics Letters*, vol. 46, no. 1, pp. 21–23, 2010.

[3] Y. Jee and Y. M. Seo, "Triple-band CPW-fed compact monopole antennas for GSM/PCS/DCS/WCDMA applications," *Electronics Letters*, vol. 45, no. 9, pp. 446–448, 2009.

[4] C.-T. Lee and S.-W. Su, "Compact and printed, standalone wireless wide area network antenna incorporating a conductive wire at low cost," *Microwave and Optical Technology Letters*, vol. 54, no. 1, pp. 109–113, 2012.

[5] S. C. Chen and K. L. Wong, "Small-size 11-band LTE/WWAN/WLAN internal mobile phone antenna," *Microwave and Optical Technology Letters*, vol. 52, no. 11, pp. 2603–2608, 2010.

[6] S. C. Chen and K. L. Wong, "Wideband monopole antenna coupled with a chip-inductor-loaded shorted strip for LTE/WWAN mobile handset," *Microwave and Optical Technology Letters*, vol. 53, no. 6, pp. 1293–1298, 2011.

[7] K. L. Wong and C. H. Huang, "Compact multiband PIFA with a coupling feed for internal mobile phone antenna," *Microwave and Optical Technology Letters*, vol. 50, no. 10, pp. 2487–2491, 2008.

[8] B. N. Kim, S. O. Park, J. K. Oh, and G. Y. Koo, "Wideband built-in antenna with new crossed c-shaped coupling feed for future mobile phone application," *IEEE Antennas and Wireless Propagation Letters*, vol. 9, pp. 572–575, 2010.

Hindawi Publishing Corporation
International Journal of Antennas and Propagation
Volume 2013, Article ID 684185, 6 pages
http://dx.doi.org/10.1155/2013/684185

Research Article

A Twin Spiral Planar Antenna for UWB Medical Radars

Giuseppe A. Zito,[1] Enrico M. Staderini,[2] and Stefano Pisa[3]

[1] *Gerontechnology and Rehabilitation Group, ARTORG Center for Biomedical Engineering Research, University of Bern, 3010 Bern, Switzerland*
[2] *Haute École d'Ingénierie et de Gestion du Canton de Vaud, Western Switzerland University of Applied Sciences (HES-SO), 1401 Yverdon-les-Bains, Switzerland*
[3] *Department of Information Engineering, Electronics and Telecommunications, Sapienza University of Rome, 00184 Rome, Italy*

Correspondence should be addressed to Stefano Pisa; pisa@die.uniroma1.it

Received 1 October 2012; Accepted 19 November 2012

Academic Editor: Renato Cicchetti

A planar-spiral antenna to be used in an ultrawideband (UWB) radar system for heart activity monitoring is presented. The antenna, named "twin," is constituted by two spiral dipoles in a compact structure. The reflection coefficient at the feed point of the dipoles is lower than −8 dB over the 3–12 GHz band, while the two-dipoles coupling is about −20 dB. The radiated beam is perpendicular to the plane of the spiral, so the antenna is wearable and it may be an optimal radiator for a medical UWB radar for heart rate detection. The designed antenna has been also used to check some hypotheses about the UWB radar heart activity detection mechanism. The radiation impedance variation, caused by the thorax vibrations associated with heart activity, seems to be the most likely explanation of the UWB radar operation.

1. Introduction

Ultrawideband radar systems transmit and receive ultrashort pulses having ultrawide bandwidth and very low power levels [1–5]. These properties make UWB radars safe for the exposed human being and compliant with other apparatuses in the environment, but at the same time increase the difficulty for the echo signal detection. For these reasons the radar antenna plays a crucial role in the UWB systems; in fact, it should combine the flat frequency response requirement on a wide band with directivity properties. Generally, a radiated beam directed towards the body is preferred for body-worn devices in order to minimize the "losses" towards the environment.

Some kinds of UWB antennas, as horn or Vivaldi antennas, have an high directivity [6–9]. However, for all these radiators the maximum directivity is in the same direction of the maximum size of the antenna. In order to realize a wearable radar system, a directivity in a direction perpendicular to the maximum size of the antenna is necessary. For this reason, other kinds of devices have to be investigated as, for example, spiral antennas. These antennas are constituted by two coplanar spirals that unwind with a given flare rate [10]. The main characteristic of spiral antennas is a radiated beam, very constant with the frequency, pointing in two opposite directions perpendicular to the spiral plan. An implementation of this antenna uses a perfect electric conducting (PEC) ground plane placed at a certain distance below the antenna to produce a unidirectional beam [11]. Finally, it is important to note that all the cited antennas can be used in a UWB radar to observe copolarized reflections. For the heart activity monitoring the use of cross-polarized antennas could be advantageous. In fact, with respect to copolarized radiators, cross-polarized antennas reduce the backscattering from planar surfaces, as the chest wall, and increase the backscattered field from asymmetric structures like the heart [12, 13].

Another open issue in UWB radar technique for heart activity monitoring is the physical rationale at the basis of the measured signals. After the first hypothesis, based on the far field operation, reported in the McEwan's patent [14], a wide set of hypotheses has been tested in [15]. Among others,

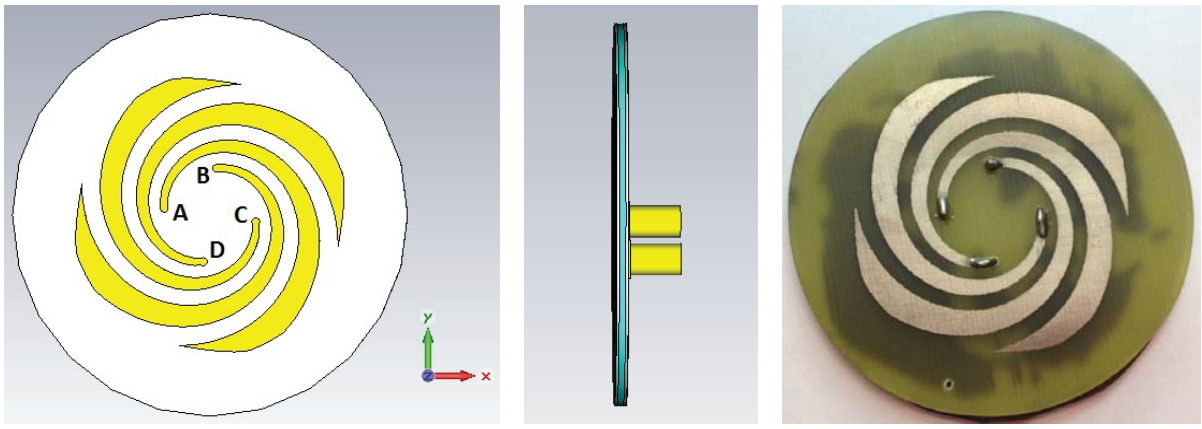

(a) (b) (c)

Figure 1: Geometry of the proposed twin spiral antenna. Frontal view (a) and lateral view (b). Antenna physical realization (c).

in [15] the blood perfusion in the skin layer and in all the thorax layers and the micromovements of the skin due to the heartbeat have been considered. However no definitive solution has been given to this problem.

In this paper a novel small-size directional twin cross-polarized planar spiral antenna for UWB systems is proposed. It is based on two twin spiral antennas rotated by 180° to each other on the same plane, one is used in transmission and the other in reception. Moreover, by using the designed antenna and a multilayer model of the human body, a theoretical study is performed for investigating the interaction mechanisms at the basis of the UWB radar operation.

2. Antenna Design

The main goal of the antenna design is to obtain, in the 3.1–10.6 GHz frequency range, issued by the federal communication commission (FCC) guidelines for medical applications [16], a reflection coefficient S_{11} and a coupling coefficient S_{21} lower than −8 dB and −20 dB, respectively.

The chosen antenna geometry is reported in Figure 1(a). The general equation for the upper and lower parts of the spiral arms on the x-y plane are

$$x(t) = a^{t/b}\cos(t)$$
$$y(t) = a^{t/b}\sin(t), \tag{1}$$

where "a" and "b" are parameters to be optimized to satisfy the design goals while "t" is the running variable. The final part of the lower line is closed with the higher part using a 4 point Spline. The other three arms of the antenna are obtained rotating the first arm of 90°, 180°, and 270° around z-axis.

The twin spiral geometry has been printed on a substrate having circular geometry, with a radius equal to 30 mm. The used substrate is a sheet of FR-4 having a relative permittivity $\varepsilon_r = 4.3$ and thickness $h = 0.4$ mm. In order to achieve an antenna pattern mainly in the direction of positive z-axis, an absorbing material and a reflecting plate have been placed behind the antenna. The absorbing material is ECCOSORB-FGM-40 with 1 mm thickness, the reflecting element is the copper plate of an FR-4 substrate. SMA connectors have been placed between point A in Figure 1 and the ground (port 1) and between point D and the ground (port 2) (see Figure 1(b)) while points B and C have been short circuited to the ground. In this manner a fully unbalanced structure is realized allowing an easy integration of this antenna in UWB radars with unbalanced TX/RX connections [17].

The antenna geometry has been optimized through parametric simulations using CST Microwave Studio software. In these simulations the antenna parameters (a and b in (1)) have been varied inside realistic ranges and magnitudes of the $S_{11}(f)$ and $S_{21}(f)$ scattering coefficients have been analyzed. Only geometries giving $S_{11}(f)$ magnitude lower than −8 dB ($\rho_{11} = 0.4$) and $S_{21}(f)$ magnitude lower than −20 dB ($\rho_{21} = 0.1$) between $f_1 = 3.1$ GHz and $f_2 = 10.6$ GHz have been considered and, among those selected, the one maximizing the cost function

$$C = \frac{1}{(f_2 - f_1)}\int_{f_1}^{f_2}\left(\frac{\rho_{11} - |S_{11}(f)|}{\rho_{11}}\right)\cdot\left(\frac{\rho_{21} - |S_{21}(f)|}{\rho_{21}}\right)df \tag{2}$$

has been chosen. The best value of (2) has been obtained with "a" equal to 2.55 and 2.75 for the lower and the upper lines of the arm, respectively, and "b" equal to 4.

3. Numerical Simulations and Measured Results

Figure 2 shows the return loss S_{11} (a) and the isolation S_{21} (b) as a function of the frequency obtained by means of CST simulations of the optimized antenna. The simulated results indicate that, according to the design goals, the antenna has a return loss lower than −8 dB and the S_{21} is always less than −20 dB in the 3.1–10.6 GHz frequency band.

The designed antenna has been realized (see Figure 1(c)) and the S_{11} and S_{21} scattering parameters have been measured by means of a vector network analyzer (PNA E8363B). The

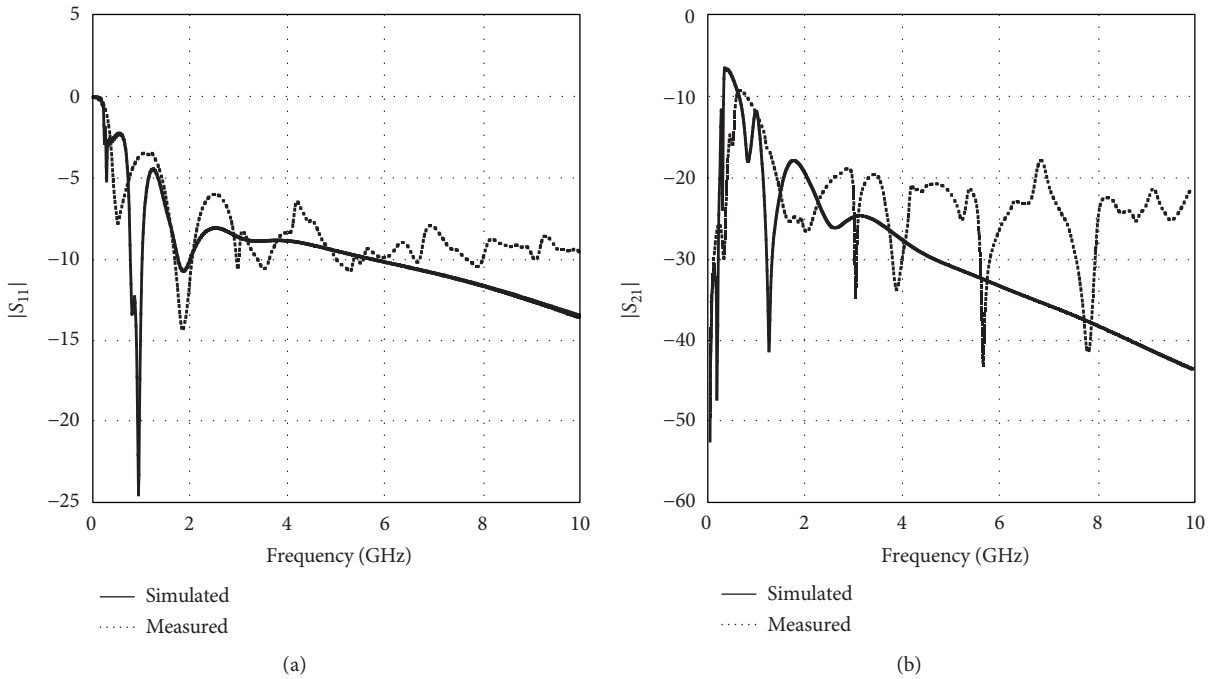

Figure 2: Return loss S_{11} (a) and isolation S_{21} (b) as a function of the frequency. Comparison between simulated and measured results.

obtained results are reported in Figures 2(a) and 2(b), respectively. The figures show that the S_{11} frequency behaviors are in a quite good agreement with simulations, while some discrepancies, probably due to the SMA connectors, are present in the S_{21} behavior.

Figure 3 shows the simulated antenna radiation pattern, on the x-z plane (a) and on the y-z plane (b) at 4, 6, 8, and 10 GHz. The plots highlight that the maximum radiation is on the z direction with a −3 dB aperture of about 70°. Notice that in Figure 3(a) the main lobe direction is deviated with respect the z axis of about 15°: this behavior was not present in simulations without SMA connectors.

An important parameter for characterizing a UWB antenna is the fidelity factor that is the peak value of the cross-correlation function between the signal $s_2(t)$ (electric field), at a given distance from the antenna, and the signal $s_1(t)$ (input voltage) [18]

$$F = \max_{\tau} \frac{\int_{-\infty}^{\infty} s_1(t)\, s_2(t+\tau)\, dt}{\sqrt{\int_{-\infty}^{\infty} s_1^2(t)\, dt}\sqrt{\int_{-\infty}^{\infty} s_2^2(t)\, dt}}, \tag{3}$$

where τ is the delay that maximizes F in (3).

The fidelity factor has been calculated in air at various distances from the antenna and for various directions. Results concerning the fidelity are summarized in Table 1. The values reported in the table highlight the very high fidelity factor of the proposed antenna.

Table 1: Simulated fidelity factor for the proposed twin antenna.

Probe position (cm)	Fidelity factor
$x = 0$; $y = 0$; $z = 10$	0.9803
$x = 0$; $y = 0$; $z = 5$	0.9732
$x = 4$; $y = 0$; $z = 0$	0.9283
$x = -4$; $y = 0$; $z = 0$	0.9680

4. Operating Principles

The first hypothesis on the UWB radar operating principle was proposed by McEwans [14] and was based on the far field detection of heart wall movements. In [15] the authors have evidenced that a UWB radar cannot detect the movements of the cardiac wall because of the strong attenuation of the UWB pulse in the thorax. A possible operating mechanism suggested in [15] is based on a near field interaction: the detected signal is not an echo, but the consequence of a change in the antenna radiation impedance at the same frequency of the heart rate.

To investigate this phenomenon, two possible mechanisms have been hypothesized, in particular the increase of the blood perfusion in the skin layer and in all the thorax layers, and the micromovements of the skin due to the heartbeat [15].

In order to study the influence of the blood perfusion on the antenna radiation impedance, first of all the alteration in the tissue dielectric properties due to the blood increase caused by heart activity has been quantified. For this purpose, a human body and lung volume of 70 and 5 liters, respectively, have been considered assuming a stroke volume of 80 mL flowing both in the lung and in the other tissues according to the big and small circulation concepts. Moreover, the whole blood content has been assumed equal to 5 liters uniformly distributed in the body. Notice that this is a rough

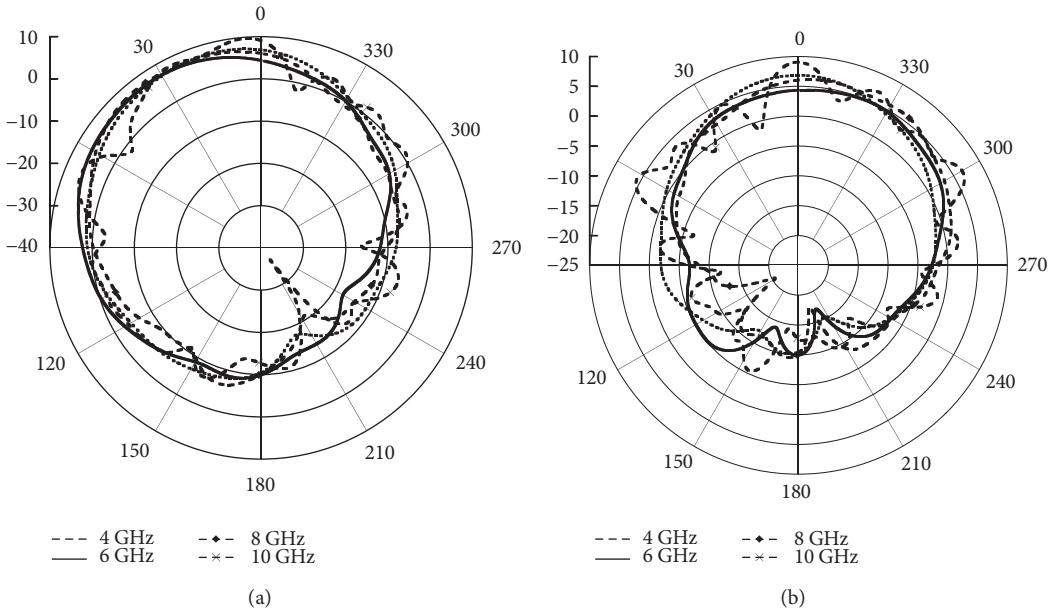

Figure 3: Antenna radiation pattern, on the x-z horizontal plane (a) and on the y-z vertical plane (b) at 4, 6, 8, and 10 GHz.

approximation because some organs as brain and muscles utilize more blood than fat and bones.

On the basis of these assumptions, the blood increase in the lungs and in all the other body tissues, between the end diastole and end systole, is about 20% and 2%, respectively. Finally, the tissues electrical parameters at the end of systole (ε_s and σ_s) have been calculated as an average between the value of the tissues electrical parameters at the end diastole (ε_d and σ_d) and the value of the blood (ε_b = 53.95 and σ_b = 5.39 S/m) weighted by the above reported percentages. The results are shown in Table 2.

In order to test the previously cited hypothesis on the radar operating principle a time domain simulation with the twin antenna in front of a model of the thorax has been performed (see Figure 4). In particular, the human body has been modeled by using a multilayer structure approximating the thorax of the visible human [19]. The considered geometry has been simulated by means of the CAD Microwave Studio by CST. The antenna was excited at one port by a Gaussian pulse with a 3–10 GHz bandwidth and the signal time behavior was recorded at the other port.

The comparison between the recorded signals, achieved by assigning to the various tissues the parameter values at the end diastole end at the end systole, shows signal differences of few microvolts, not detectable by a UWB radar.

Concerning the micromovements of the skin, according to [15], a displacement between the antenna and the skin of ±30 μm has been supposed and the structure has been simulated by means of Microwave Studio. In particular a reference situation with the antenna placed at 0.5 mm far from the body has been considered. Then the distance between the antenna and the body has been varied in the ±30 μm range. The signal received by the antenna at port 2, exciting at port 1 as in the previous study, is depicted in Figure 5. The figure shows that up to 1.5 ns all the signals are perfectly superimposed (the signal is inside the antenna) and then they split. The body micromovements are converted in delays that give rise to amplitude differences up to 20 mV (see Figure 5, absolute difference). In particular there is a direct correlation between the delays and the body micromovements.

It is worth noting that this effect is not directly connected to the spatial displacement, as in the classical radar analysis, but it is due to a modification of the complex antenna

Table 2: Tissues electrical parameters at the end of diastole (ε_d and σ_d) and at the end of systole (ε_s and σ_s).

	ε_d	ε_s	σ_d (S/m)	σ_s (S/m)
Skin	35.77	36.13	3.06	3.11
Muscle	49.54	49.63	4.04	4.07
Heart wall	50.27	50.34	4.86	4.87
Lung	44.86	46.68	3.94	4.23

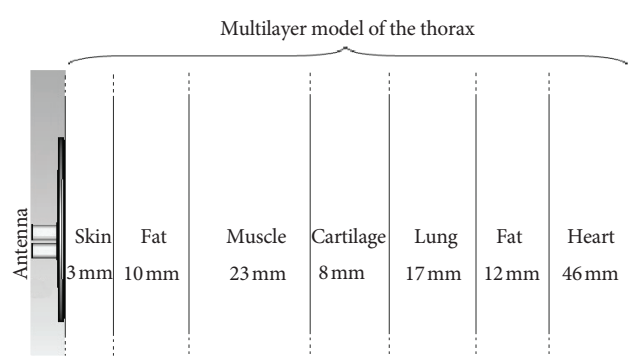

Figure 4: Twin antenna in front of a multilayer model of the thorax.

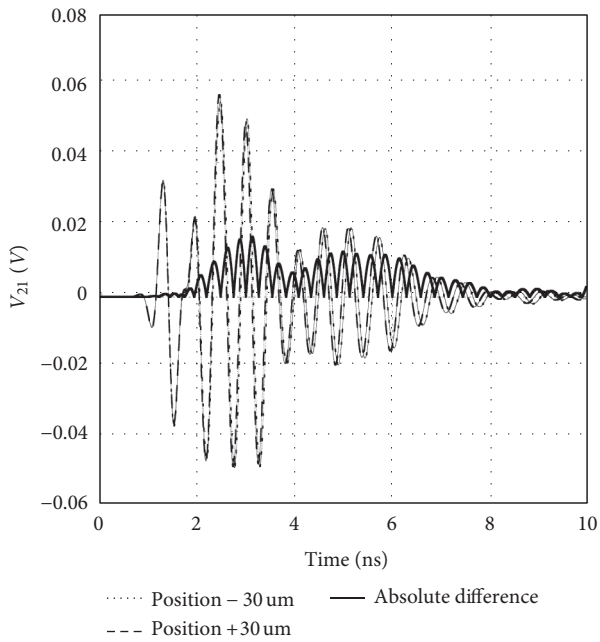

Figure 5: V_{21} simulated for different displacement between the thorax and the antenna.

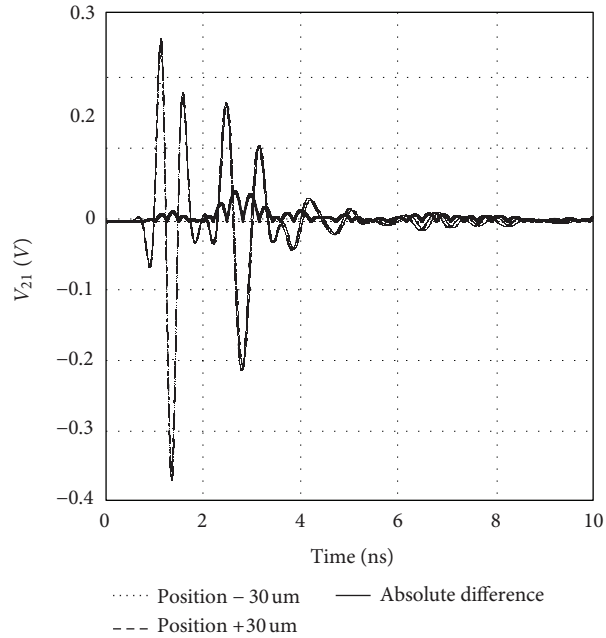

Figure 6: V_{11} simulated for different displacement between the thorax and the antenna.

radiation impedance. Moreover, it is interesting to note that the absolute difference signal can be recovered in more than one time point between 2 and 8 ns.

5. Discussion

The performed study has evidenced the ability of the twin antenna to detect heart activity by exiting the twin antenna at one port and measuring the reflections at the other port. A question arises: is this antenna operation better than the one in which the antenna transmits and receives with the same arms?

This issue has been studied by placing the antenna in front of the multilayer body model (see Figure 4), exciting the antenna with a Gaussian pulse with a 3–10 GHz bandwidth and measuring the signal at the transmitting arms (V_{11}) before and after a distance variation of 30 μm. The obtained results are reported in Figure 6 together with the absolute differences between the two signals.

The maximum voltage difference on the V_{11} signals is about 40 mV as compared with the 20 mV on V_{21} (see Figure 5), but the percentage difference, normalized respect to the maximum of the whole signal, is 16% for V_{11}, and 30% for V_{21}. Hence the signal variation V_{21} can be better evaluated than V_{11} by the sampling circuit used in the UWB radar.

In conclusion, the use of two cross-polarized radiating structures for the transmission and the reception of the UWB signals makes the proposed antenna better than a similar one using a single radiator. Moreover, with respect to similar realizations using two bow-tie, horn, or Vivaldi radiators [3] the proposed structure is very compact with a beam propagation axis perpendicular to the substrate. This makes the twin antenna easy to integrate in the UWB radar electronics and it makes easier the realization of a wearable radar.

6. Conclusions

The proposed twin antenna is a variation of the famous Archimedean spiral antenna, with two arms used for transmission and other two arms used for capturing the received echo.

The reflection coefficient at the feed point of the antenna is lower than −8 dB over the 3–12 GHz band while the two-antennas coupling is about −20 dB.

If inserted in a range gating UWB radar the antenna can be used to detect the heart rate activity.

In a UWB radar for heart rate activity monitoring, the measured signal is not related to an echo coming from the heart wall, but seems to be related to a change in the antenna radiating impedance as a consequence of the microdisplacements of the thorax in front of the antenna produced by the heart movements.

References

[1] T. E. McEwan, "Ultra-wideband radar motion sensor," United States Patent 5,361,070, 1994.

[2] E. M. Staderini, "UWB radars in medicine," *IEEE Aerospace and Electronic Systems Magazine*, vol. 17, no. 1, pp. 13–18, 2002.

[3] I. Y. Immoreev, S. Samkov, and T. H. Tao, "Short—distance ultrawideband radars," *IEEE Aerospace and Electronic Systems Magazine*, vol. 20, no. 6, pp. 9–14, 2005.

[4] S. Allen, J. C. Lin, J. B. Anderson et al., "ICNIRP statement on EMF-emitting new technologies," *Health Physics*, vol. 94, no. 4, pp. 376–392, 2008.

[5] S. Pisa, P. Bernardi, M. Cavagnaro, E. Pittella, and E. Piuzzi, "A circuit model of an ultra wideband impulse radar system for breath-activity monitoring," *International Journal of Numerical Modelling*, vol. 25, no. 1, pp. 46–63, 2012.

[6] P. J. Gibson, "The Vivaldi aerial," in *Proceedings of the 9th European Microwave Conference*, pp. 101–105, Brighton, UK, September 1979.

[7] E. Guillanton, J. Y. Dauvignac, C. Pichot, and J. Cashman, "A new design tapered slot antenna for ultra-wideband applications," *Microwave and Optical Technology Letters*, vol. 19, no. 4, pp. 286–289, 1998.

[8] E. Pittella, P. Bernardi, M. Cavagnaro, S. Pisa, and E. Piuzzi, "Design of UWB antennas to monitor cardiac activity," *Journal of the Applied Computational Electromagnetics Society*, vol. 26, no. 4, pp. 267–274, 2011.

[9] G. Cappelletti, D. Caratelli, R. Cicchetti, and M. Simeoni, "A low-profile printed drop-shaped dipole antenna for wideband wireless applications," *IEEE Transactions on Antennas and Propagation*, vol. 59, no. 10, pp. 3526–3535, 2011.

[10] S. Jacobsen, H. O. Rolfsnes, and P. R. Stauffer, "Characteristics of microstrip muscle-loaded single-arm Archimedean spiral antennas as investigated by FDTD numerical computations," *IEEE Transactions on Biomedical Engineering*, vol. 52, no. 2, pp. 321–330, 2005.

[11] L. Stutzman and G. A. Thiele, *Antenna Theory and Design*, Wiley, New York, NY, USA, 2nd edition, 1998.

[12] X. Yun, E. C. Fear, and R. H. Johnston, "Compact antenna for radar-based breast cancer detection," *IEEE Transactions on Antennas and Propagation*, vol. 53, no. 8, pp. 2374–2380, 2005.

[13] X. Yun, R. H. Johnston, and E. C. Fear, "Radar-based microwave Imaging for breast cancer detection: tumor sensing with cross-polarized reflections," in *Proceedings of the IEEE Antennas and Propagation Society Symposium 2004 Digest held in Conjunction with: USNC/URSI National Radio Science Meeting*, vol. 3, pp. 2432–2435, June 2004.

[14] T. E. McEwan, "Body monitoring and imaging apparatus and method," United States Patent 5,573,012.

[15] E. M. Staderini and G. Varotto, "On the UWB medical radars working principle," *International Journal of Ultra Wideband Communications and Systems*, vol. 2, no. 2, pp. 83–93, 2011.

[16] First Report and Order: Revision of Part 15 of the Commission's Rules Regarding Ultra-Wideband Transmission Systems Federal Communications Commission (FCC), ET Docket 98-153, 2002.

[17] H. A. Hjortland, D. T. Wisland, T. S. Lande, C. Limbodal, and K. Meisal, "CMOS impulse radar," in *Proceedings of the 24th Norchip Conference*, pp. 75–79, November 2006.

[18] D. Lamensdorf and L. Susma, "Baseband-pulseantenna techniques," *IEEE Antennas and Propagation Magazine*, vol. 36, no. 1, pp. 20–30, 1994.

[19] Visible Human Project, http://www.nlm.nih.gov/research/ visible/visible_gallery.html, 2012.

Hindawi Publishing Corporation
International Journal of Antennas and Propagation
Volume 2013, Article ID 945408, 8 pages
http://dx.doi.org/10.1155/2013/945408

Research Article

Structure-Based Evolutionary Programming Design of Broadband Wire Antennas

Giovanni Andrea Casula, Giuseppe Mazzarella, and Giorgio Montisci

Dipartimento di Ingegneria Elettrica ed Elettronica, Università di Cagliari, Piazza D'Armi, 09123 Cagliari, Italy

Correspondence should be addressed to Giuseppe Mazzarella; mazzarella@diee.unica.it

Received 3 October 2012; Revised 10 December 2012; Accepted 21 December 2012

Academic Editor: Renato Cicchetti

A design technique for wire antennas, based on the Structure-Based Evolutionary Programming, is used to design a broadband antenna with an end-fire radiation pattern and a very simple geometry, operating in the 3–16 GHz frequency band, namely, from the S band to the Ku band. The antenna has been analyzed with NEC-2 during the evolutionary process, looking for high gain, good input match, and robustness with respect to realization tolerances. The outcome of our design procedure shows a very good performance.

1. Introduction

Antenna design has been a matter of intuition and brute-force computation from the beginning (see e.g., [1, 2]). In the past literature, this task has been faced at different levels, from simple formulas [3] to sophisticated synthesis techniques [4–11], heuristic models [12, 13], or one of the different random optimization procedures proposed so far [14–18].

The traditional approach to the design of wire antennas starts by choosing a well-defined structure, whose parameters need to be suitably optimized. This requires, as a prerequisite, the choice of an antenna model which has proven able to comply with the design specifications. Successful proposals of broadband antennas are self-similar, so for those antennas the chosen model must be a self-similar one, either continuous, like a conical antenna, or discrete. The latter can be implemented either as an array [12] or as a prefractal antenna [19]. Of course, the final antenna could not fulfill exactly the model [13], but also such differences must be chosen externally. As a matter of fact, the choice of the model heavily constraints the whole design process. As a consequence, a significant skilled human interaction is required in the initial choice of the structure. The model could also be fine-tuned as the design proceeds, but this requires a skilled human interaction, too. The traditional approach is quite expensive, and therefore design techniques without human interaction are of interest, as long as they provide equal, or better, results. This can be achieved only when no initial structure is assumed, since this choice (which in a fully automated procedure cannot be further modified) can constraint too strongly the final solution.

Up to now, such a general tool has been sought for among random search procedures. Some of them are inspired by natural processes, either looking for an effective cooperative scheme, like Particle Swarm Optimization (PSO) [20], or aiming at exploring very different solution sets, like Genetic Algorithms (GA) [21–23]. As a matter of fact, the latter could be a good candidate for a valuable general tool, being inspired by Darwinian natural selection, since the variety of all living forms is known to everyone. However, despite of their strong premises, GA cannot fulfill this purpose since they still assume a completely defined antenna structure, and only an handful of parameters remains to be optimized. Borrowing the biological language, we can say that GA works at the nucleotide (i.e., bit) level and this strongly limits its effectiveness as a design tool.

On the other hand, the full power of evolution-inspired methods in the antenna design has been highlighted only when Genetic Programming (GP) or, more precisely, Structure-based Evolutionary Design (SED) [24] approaches have been proposed for simple wire antennas [25, 26], arrays [24], and FSS [27]. Evolutionary programming does not

require any antenna model, neither asks for a structure locked from the beginning. Instead, it considers a (virtually) infinite solution space, defined only by very loose constraints. If we require a wire antenna, SED is able to look for the final design among all possible wire antennas. As a matter of fact, SED can be used to automatically, and effectively, search, in this very huge solution space, for novel antenna configurations, which can be significantly more performant than antennas developed using standard techniques.

The strength of the SED resides in its description of each element of the solution space as the set of instructions needed to realize it. This description can be translated in a highly effective tree description [25] for computer implementation and allows the standard genetic operators (crossover, mutation) to reach an unparallel power. As a matter of fact, SED works at the organ level, so that *crossover* is the exchange of whole working parts of the individuals, while *mutation*, working on a subtree root, affects the whole sub-tree (as happens in the true natural selection). SED requires also a suitable fitness function, tailored to the problem at hand, and a time-effective analysis procedure.

To assess SED as a viable tool for robust design of broadband antennas, we consider here the design of a wideband wire antenna with an end-fire radiation pattern and a very simple geometry, operating in a range from S to Ku frequency bands, namely, from 3 GHz to 16 GHz, and reasonably matched at the input port. Apart from these simple "constraints," SED does not assume any other *a priori* information on the antenna structure. Rather, SED builds up the structure of the individual antennas as the procedure evolves. Therefore, SED solution space has the power of the continuum and allows exploring, and evaluating, general wire antenna configurations.

The solution space, namely, the set of admissible solutions in which the procedure looks for the optimum, is composed, in our case, of every broadband antenna with no limit on the number of wire segments, nor on the size or orientation, represented as real numbers. On the other hand, GA works on a given antenna model, so that its solution space is a discrete one and therefore is a very small subset of the SED solution space.

The most common broadband wire antennas are the log-periodic dipole arrays (LPDAs) [28–30], used in a wide range of applications due to their very wide bandwidth and their relatively narrow-beam characteristics. However, a wire LPDA operating in the bandwidth of the antenna proposed in this paper (namely, C, X, and Ku frequency bands) cannot be realized, because the corresponding dipoles would be too short at these frequencies. On the other hand, the broadband antenna designed here with SED can be easily scaled in order to work also at lower frequencies, keeping the same performances both in terms of input matching and of gain.

In order to compute the fitness, an analysis of each wire antenna generated by SED is needed. This has been performed using NEC-2 [31], a well-known, time-effective and well-assessed Method of Moments code. This software has been successfully used to model a wide range of wire antennas, with high accuracy (see, e.g., [32, 33]), and is now considered as one of the reference e.m. software (see, e.g., [26, 34]). For this reason, it has been used here. However, sometimes the SWR data of NEC-2 could have a reduced accuracy, therefore the final output of the design procedure has been validated, by testing it with HFSS [35], a commercial FEM code, since it has been shown that the results of this software are in very good agreement with experiment (see, e.g., [36]). As a matter of fact, although NEC is faster by orders of magnitude, NEC and HFSS results are in very good agreement, thus assessing our choice for the fitness evaluation.

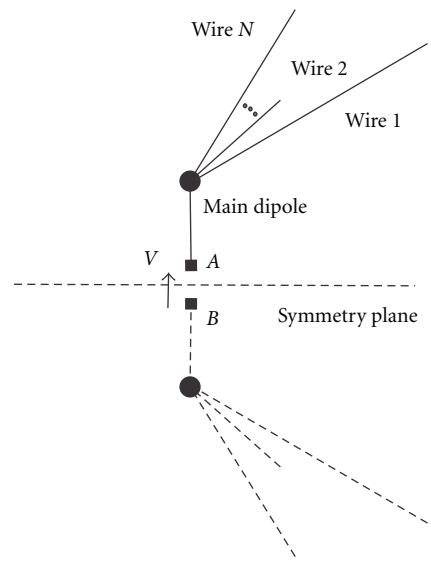

Figure 1: Wire antenna geometry.

2. Antenna Design and Fitness Function

The initial structure of each SED individual is depicted in Figure 1.

Each individual of the population (antenna) is composed by a principal vertical wire (the main dipole in Figure 1), connected to the feeding port on its bottom side, and by a number N (chosen by SED) of wires connected to the upper side of the main dipole with an arbitrary length and orientation in space. At the remote end of each of the N wires, we connect zero, one, or more further wires, still with arbitrary length and orientation, and so on, in an iterative manner. The structure is finally mirrored with respect to the horizontal plane, as indicated in Figure 1.

Each individual is built up using only four operations:

(a) add a wire according to the present directions and length;

(b) transform the end of the last added wire in a branching point;

(c) modify the present directions and length;

(d) stretch (or shrink) the last added wire.

In the first step of the evolutionary design, N individuals are randomly built. Then, an iterative procedure starts, where

the fitness of each individual is evaluated, and the next generation of the population is built assigning a larger probability of breeding to the individuals with the highest fitness. The iterative procedure ends when suitable stopping rules are met (i.e., when the individual antenna fulfills, within a predetermined tolerance, the specified requirements).

After each antenna has been generated, its geometrical coherency is verified, and incoherent antennas (e.g., an antenna with two elements too close, or even intersecting) are discarded. Then it is analysed by NEC-2 and its fitness is computed. The SED approach has been implemented in Java, while the analysis of each individual has been implemented in C++ (using the freeware source code Nec2cpp) and checked using the freeware tool 4nec2 [31].

The performance of each individual (antenna) of the population is evaluated by a proper fitness function, which is strongly dependent on the problem at hand, namely, by the electromagnetic behavior of the designed antenna, and must measure how closely the actual antenna meets the design specifications.

In the specific case of the broadband wire antenna of this paper, the fitness function has been selected in order to lead the evolution process toward a structure with a good input match in a frequency range as wide as possible (within S, C, X, and Ku bands), while keeping the highest end-fire gain and a reduced size.

Since improving one parameter usually results in worsening the other ones, the design technique has to handle a complicate trade-off between the conflicting objectives. The fitness structure is therefore a critical point in the design procedure, since only an appropriate choice can lead the design process to performing results, while largely reducing the computation time.

The chosen fitness has been built from the desired antenna performances [24] as

$$\text{Fitness} = \left[\left(1-\overline{\text{SWR}}\right)\cdot\alpha_{\text{SWR}} + \frac{G_{\text{MAX}}}{\overline{G}}\cdot\alpha_{\text{GAIN}}\right] \cdot\left(1+K_{\text{SIZE}}\cdot\frac{D_{\text{MAX}}}{D_{\text{ANT}}}\right), \tag{1}$$

where α_{SWR} and α_{GAIN} are suitable weights (whose values depend also on the input impedance of the actual antenna), $\overline{\text{SWR}}$, and $\overline{G}$ are, respectively, the mean values of the SWR and gain over the bandwidth of interest, D_{ANT} represents the actual antenna size, and D_{MAX} is the maximum allowed size for the antenna. Finally, K_{SIZE} is an appropriate weight which takes into account the requirement of a small size of the antenna. The values for the fitness weights have been obtained after a suitable local tuning, following an approach similar to the one described in detail in [24].

The weight α_{GAIN} in the fitness function (1) has the following expression:

$$\alpha_{\text{GAIN}} = \left(1+\alpha_{\text{Back}} * G_{\text{Back}}\right)\cdot\left(1+\alpha_{\text{Rear}} * G_{\text{Rear}}\right) \cdot\left(1+\alpha_{\text{Front}} * G_{\text{Front}}\right), \tag{2}$$

where G_{Back} is the gain computed in the back direction ($\theta = 90^\circ$, $\varphi = 180^\circ$), G_{Front} is the average gain computed in the front region ($|\theta| > 90^\circ + 2\Delta\vartheta$, $0^\circ + 2\Delta\varphi < \varphi < 90^\circ$, where $\Delta\vartheta$ and $\Delta\varphi$ indicate the main lobe amplitude), and G_{Rear} is the average gain computed in the rear region ($0^\circ \le |\vartheta| \le 180^\circ$, $90^\circ \le |\varphi| \le 180^\circ$). The weights α_{Back}, α_{Front} and α_{Rear} are chosen through a local tuning in order to get the maximum gain in the end-fire direction and an acceptable radiation pattern in the rest of the space. In the performed evolutionary process these parameters have the following values: $\alpha_{\text{Back}} = 0.12$, $\alpha_{\text{Front}} = 0.17$ and, $\alpha_{\text{Rear}} = 0.06$.

The weight α_{SWR} in the fitness function (1) is expressed using suitable parameters strictly related to the antenna input impedance, which are individually tuned. The resulting expression for α_{SWR} is

$$\alpha_{\text{SWR}} = \left(1+\alpha_{\text{IN}}\right)\cdot\left(1+\alpha_X\left|X_{\text{IN}}^A\right|\right)\cdot\left(1+\alpha_Q\frac{R_{\text{IN}}^A-\left|X_{\text{IN}}^A\right|}{R_{\text{IN}}^A}\right) \cdot\left(1+\alpha_{\text{Var}\,R}\cdot\sigma_R^2\right)\cdot\left(1+\alpha_{\text{Var}\,X}\cdot\sigma_X^2\right), \tag{3}$$

where

(i) $\alpha_{\text{IN}} = 50$ if $|X_{\text{IN}}^A| > R_{\text{IN}}^A$, and $\alpha_{\text{IN}} = 0$ otherwise (weight introduced in order to boost up structures with $R_{\text{IN}}^A > |X_{\text{IN}}^A|$);

(ii) $\alpha_X = 0.12$ (weight related to $|X_{\text{IN}}^A|$, introduced in order to force the evolution process to structures with an $|X_{\text{IN}}^A|$ as small as possible);

(iii) $\alpha_Q = 0.2$ (weight related to $R_{\text{IN}}^A - |X_{\text{IN}}^A|$, and introduced to advantage structures with a low Q factor);

(iv) $\alpha_{\text{Var}\,R} = \alpha_{\text{Var}\,X} = 0.03$ (weight related to the normalized mean square variation of R_{IN}^A and X_{IN}^A in the antenna required bandwidth, and introduced to advantage structures with a regular impedance behaviour);

and R_{IN}^A and X_{IN}^A are, respectively, the real part and the imaginary part of the antenna input impedance, while σ_R^2 and σ_X^2 are the normalized mean square variation of R_{IN}^A and of X_{IN}^A in the antenna required bandwidth. The two weights α_{IN} and α_Q are both connected to the Q factor of the antenna. However, α_{IN} gives a significant penalization to antennas with a large imaginary part of the input impedance, but it has a step-like behavior. Therefore, in order to get a further, smooth penalization to antennas with a large Q, we have added also the term with α_Q. We have observed that a combination of the two terms is more effective than either one separately.

The inclusion of ohmic losses into the gain computation, as well as the requirement of a good input match over all the required bandwidth, prevents from selecting superdirective solutions.

On the other hand, the requirement of a robust solution is not taken into account in the fitness, since we have found a different approach more efficient. The individuals associated with the highest fitness values, or very close to the

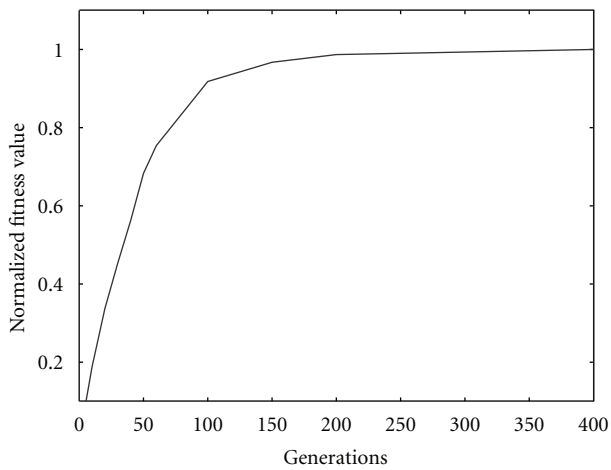

Figure 2: Plot of convergence of the designed antenna shown in Figure 3.

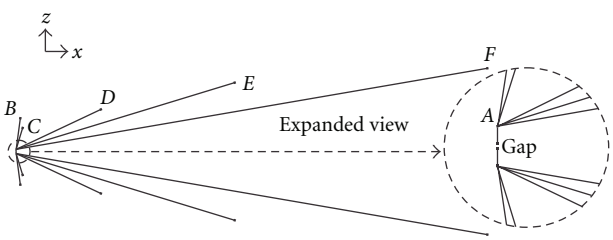

Figure 3: Geometry of the designed wire antenna.

best fitness value obtained so far, are perturbed (assigning random relocations to the elements) and analysed to assess their robustness with respect to random modifications of the structure. This random relocation allows to get robust structures with respect to both constructive errors and bad weather conditions (e.g., movements due to wind effect).

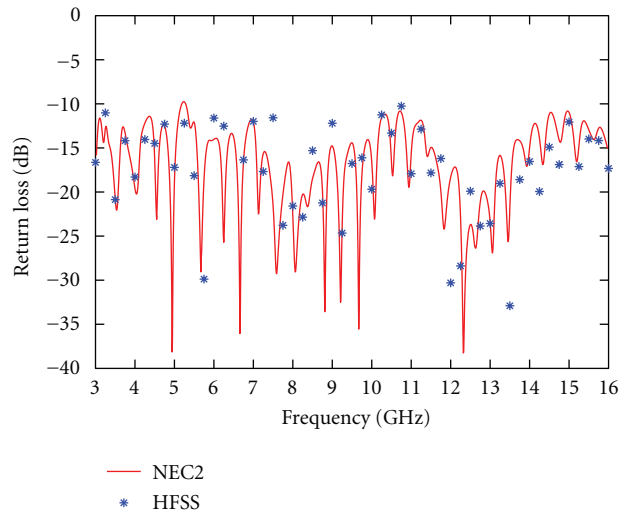

Figure 4: Frequency response of the designed antenna.

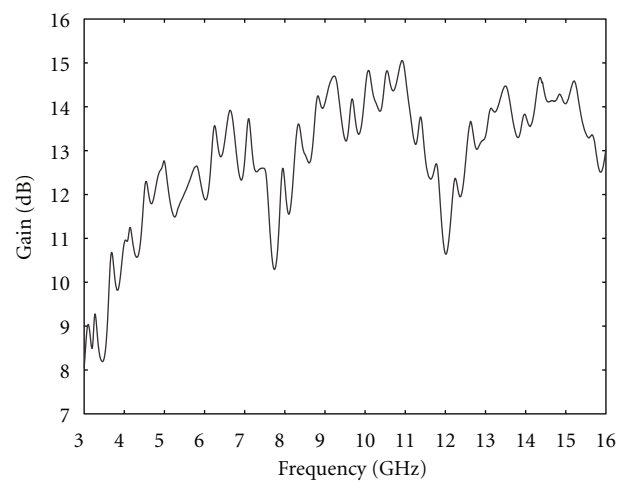

Figure 5: Simulated (NEC-2) Gain of the designed antenna.

3. Results

In order to test the procedure, we have designed a broadband wire antenna, with equal wire diameter (0.665 mm) and conductivity ($\sigma = 4 * 10^6$ S/m). We have required that the antenna has an input impedance of 200 Ω in the whole bandwidth, which is a typical characteristic impedance of bifilar lines [37]. The use of a bifilar line as a feeding network avoids the need of a balun to connect the balanced wire antenna to an unbalanced input, as provided for example by standard coaxial cables, having a typical input impedance of 50 Ω. On the other hand, the designed antenna can also be connected to a standard coaxial line using a commercial balun with an impedance transformation ratio of 4 : 1. In this case, since a balun with such large bandwidth (3–16 GHz) cannot be obtained, the operating bandwidth must be divided into a number of subbands, and an appropriate balun must be used in each subband.

The antenna has been designed using a population size of 1000 individuals, with a crossover rate set to 60%, and a mutation rate set to 40%. Its convergence plot is shown in Figure 2, and it appears that 250 generations are enough to reach convergence.

The best individual of the evolutionary process, obtained after several runs (e.g., a few tens) of the code, is shown in Figure 3, and the cartesian coordinates of each wire are reported in Table 1. This antenna is very easy to realize, consisting in only 12 metallic wires, and can be produced with a very low cost by the same technology used for Yagi and LPDA arrays.

In Figure 4 we show the input frequency response of the designed antenna using both NEC-2 and HFSS. It is clear that the antenna bandwidth (S11 < -10 dB) extends from 3 GHz up to well beyond 16 GHz. It is also clear that both NEC-2 and HFSS give essentially comparable results. This is also true for the radiation pattern. So, the use of NEC-2 in the design is fully assessed, and we will show only the NEC-2 results in the following.

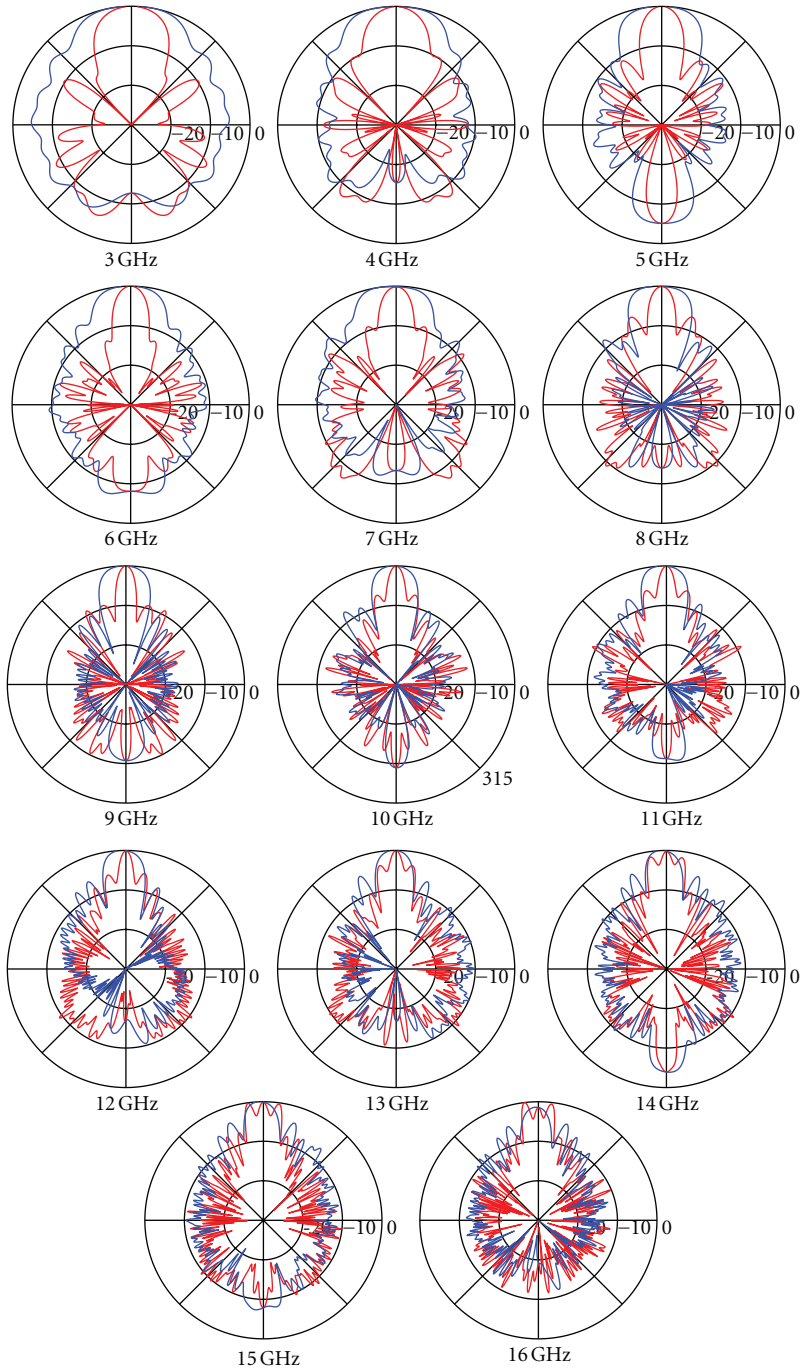

Figure 6: Simulated (NEC-2) normalized Far-Field pattern of the designed antenna. Blue line: E-Plane; red line: H-Plane.

In Figure 5 the end-fire Gain is reported. In the bandwidth 3–16 GHz, the mean Gain of the antenna is equal to 12.7 dB and the mean F/B ratio is about 11.6 dB.

In Table 2 the antenna gain, front-to-back ratio, and efficiency in the operating bandwidth are shown.

It is worth noting that the inclusion of ohmic losses into the gain computation is very important, since this prevents from selecting superdirective antennas during the evolution. As a matter of fact, the efficiency of the designed antenna is very good (greater than 97%, and with a mean value of 98.05%), despite of the relatively small electrical conductivity of the metal ($\sigma = 4 * 10^6$ S/m). Besides, while the maximum directivity is almost constant with respect to σ, the efficiency rapidly decreases [38]. It is therefore required to take into account in SED the actual conductivity of the antenna material, in order to discard individuals with low efficiency, which can result in unusable antennas.

Finally, the NEC-2 Far-Field-pattern in the operating frequency bandwidth is plotted in Figure 6. For each frequency, the E-Plane and the H-Plane are shown. The reported

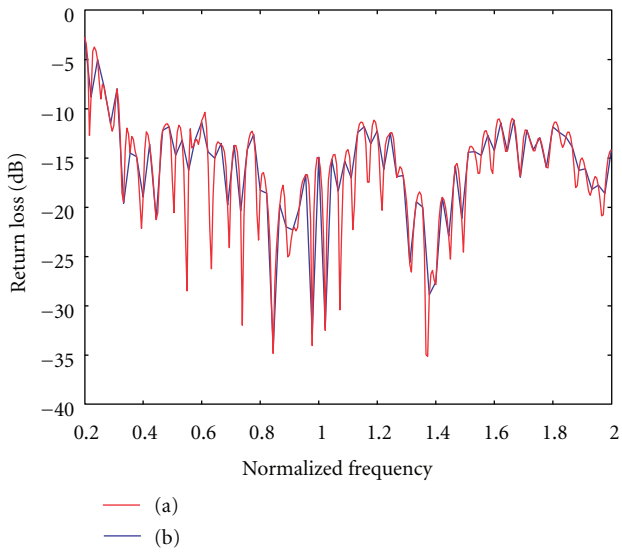

Figure 7: Simulated (NEC-2) Return Loss of the designed antenna at the center frequency of 8 GHz (a) and of the designed antenna scaled at the center frequency of 2 GHz (b).

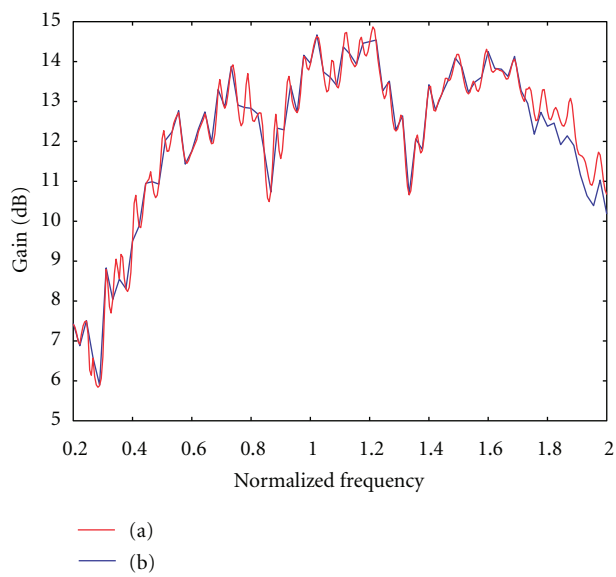

Figure 8: Simulated (NEC-2) Gain of the designed antenna at the center frequency of 8 GHz (a) and of the designed antenna scaled at the center frequency of 2 GHz (b).

radiation patterns confirm that the useful bandwidth of the designed antenna is 3–16 GHz, where the input matching is very good and the far-field is essentially end fire, with a good Gain and F/B ratio.

In order to evaluate the performance improvement of the broadband antenna proposed in this paper over standard solutions, we can compare it with wire log-periodic dipole arrays (LPDAs), the most popular broadband wire antennas [28–30]. However, a wire LPDA in the C frequency band (and beyond) cannot be realized because the dipole lengths would be too small with increasing frequency. On the other hand, the proposed antenna can be easily scaled in order to work at low frequencies, without degrading its performances.

Table 1: Cartesian coordinates of the ends of the wires for the antenna in Figure 2.

	X (mm)	Y (mm)	Z (mm)
A	0	0	2.00
B	1.97	2.38	30.25
C	2.07	3.35	20.82
D	60.25	5.85	39.50
E	156.25	5.85	68.00
F	340.00	5.85	86.25

Table 2: Radiation parameters for the antenna in Figure 2.

Freq (GHz)	Gain (dB)	F/B (dB)	Efficiency (%)
3	7.38	12.69	99.05
4	10.04	15.33	98.53
5	12.98	7.25	97.06
6	12.60	8.07	97.84
7	10.30	13.19	98.11
8	12.40	13.87	98.15
9	14.89	10.70	98.48
10	14.79	8.87	98.11
11	13.55	11.14	98.02
12	12.36	16.83	98.59
13	12.29	16.85	97.87
14	11.44	11.52	97.00
15	11.65	7.72	98.05
16	11.73	17.79	97.68

In Figures 7 and 8 we show, respectively, the return loss and the Gain, plotted with respect to the normalized frequency, of the antenna designed with SED within S, C, X, and Ku bands and of the same antenna scaled at the center frequency of 2 GHz. The simulations, performed with NEC-2, show a very similar behavior in the whole operating bandwidth, confirming that the proposed antenna can be easily scaled to work at any lower frequency.

Following [29, 30], a wire LPDA with the same bandwidth of our broadband antenna scaled at 2 GHz (Figures 7 and 8) will require at least 20 elements to get an average gain of only 8.5 dB, with the log period τ equal to 0.9. However, τ should be kept lower than 0.85 in order to ensure a good behaviour of the LPDA [30], and this constraint limits the gain of a standard LPDA to a value below 8 dB. This comparison shows that the proposed antenna allows significantly better performances with respect to standard LPDAs, with a little bit more complicated structure, but without requiring the typical twisted-cable feeding network of the LPDAs.

4. Conclusion

A new design technique for a wideband wire antenna has been presented. It is based on the Structure-based Evolutionary Design (SED), which exploits the concept of the

Evolutionary Programming. Since no a *priori* structure is assumed, a suitable fitness function allows to reach significant electrical performances with a simple geometry. Extension to multiobjective fitness is under consideration, but the results reported here show that its use is not required, except perhaps for very complicate requirements.

Inclusion of the ohmic losses and of a suitable robustness test leads to a small antenna size, while preventing from super directive solutions. The proposed approach can therefore be effectively employed also for different sets of requirements.

Conflict of Interests

The authors declare that there is no conflict of interests.

References

[1] S. Silver, *Microwave Antenna Theory and Design*, McGraw-Hill, 1949.

[2] R. S. Elliott, *Antenna Theory and Design*, Prentice-Hall, New York, NY, USA, 1981.

[3] R. E. Collin, *Antennas and Radiowave Propagation*, McGraw-Hill, 1986.

[4] H. J. Orchard, R. S. Elliott, and G. J. Stern, "Optimising the synthesis of shaped beam antenna patterns," *IEE Proceedings H*, vol. 132, no. 1, pp. 63–68, 1985.

[5] G. A. Casula and G. Montisci, "Design of dielectric-covered planar arrays of longitudinal slots," *IEEE Antennas and Wireless Propagation Letters*, vol. 8, pp. 752–755, 2009.

[6] O. M. Bucci, G. D'Elia, G. Mazzarella, and G. Panariello, "Antenna pattern synthesis. A new general approach," *Proceedings of the IEEE*, vol. 82, no. 3, pp. 358–371, 1994.

[7] G. Montisci, "Design of circularly polarized waveguide slot linear arrays," *IEEE Transactions on Antennas and Propagation*, vol. 54, no. 10, pp. 3025–3029, 2006.

[8] G. A. Casula, G. Mazzarella, and G. Montisci, "Effect of the feeding t-junctions in the performance of planar waveguide slot arrays," *IEEE Antennas and Wireless Propagation Letters*, vol. 11, pp. 953–956, 2012.

[9] G. A. Casula, G. Mazzarella, and G. Montisci, "A truncated waveguide fed by a microstrip as radiating element for high performance automotive anti-collision radars," *International Journal of Antennas and Propagation*, vol. 2012, Article ID 983281, 9 pages, 2012.

[10] S. Costanzo, G. A. Casula, A. Borgia et al., "Synthesis of slot arrays on integrated waveguides," *IEEE Antennas and Wireless Propagation Letters*, vol. 9, pp. 962–965, 2010.

[11] Z. Jin, G. Montisci, G. A. Casula, H. Yang, and J. Lu, "Efficient evaluation of the external mutual coupling in dielectric-covered waveguide slot arrays," *International Journal of Antennas and Propagation*, vol. 2012, Article ID 491242, 7 pages, 2012.

[12] R. Carrel, "The design of log-periodic dipole antennas," *IRE International Convention Record*, vol. 9, pp. 61–75, 1961.

[13] R. Mishra, R. Ghatak, and D. Poddar, "Design formula for Sierpinski Gasket pre-fractal planar-monopole antennas," *IEEE Antennas and Propagation Magazine*, vol. 50, no. 3, pp. 104–107, 2008.

[14] S. Congiu and G. Mazzarella, "A tri-band printed antenna based on a Sierpinski gasket," *Journal of Electromagnetic Waves and Applications*, vol. 21, no. 15, pp. 2187–2200, 2007.

[15] G. K. Mahanti, A. Chakrabarty, and S. Das, "Phase-only and amplitude-phase synthesis of dual-pattern linear antenna arrays using floating-point genetic algorithms," *Progress in Electromagnetics Research*, vol. 68, pp. 247–259, 2007.

[16] W. B. Wang, Q. Y. Feng, and D. Liu, "Application of chaotic particle swarm optimization algorithm to pattern synthesis of antenna arrays," *Progress in Electromagnetics Research*, vol. 115, pp. 173–189, 2011.

[17] S. A. Hosseini and Z. Atlasbaf, "Optimization of side lobe level and fixing quasi-nulls in both of the sum and difference patterns by using Continuous Ant Colony Optimization (ACO) method," *Progress in Electromagnetics Research*, vol. 79, pp. 321–337, 2008.

[18] K.-C. Lee, "Frequency-domain analyses of nonlinearly loaded antenna arrays using simulated annealing algorithms," *Progress in Electromagnetics Research*, vol. 53, pp. 271–281, 2005.

[19] B. Mhamdi, K. Grayaa, and T. Aguili, "Hybrid of particle swarm optimization, simulated annealing and tabu search for the reconstruction of two-dimensional targets from laboratory-controlled data," *Progress In Electromagnetics Research B*, no. 28, pp. 1–18, 2011.

[20] S. Baskar, A. Alphones, P. N. Suganthan, and J. J. Liang, "Design of Yagi-Uda antennas using comprehensive learning particle swarm optimization," *IEE Proceedings*, vol. 152, pp. 340–346, 2005.

[21] D. S. Linden and E. F. Altshuler, "Automating wire antenna design using genetic algorithms," *Microwave Journal*, vol. 39, no. 3, pp. 74–86, 1996.

[22] D. S. Linden and E. E. Altshuler, "Wire-antenna designs using genetic algorithms," *IEEE Antennas and Propagation Magazine*, vol. 39, no. 2, pp. 33–43, 1997.

[23] E. A. Jones and W. T. Joines, "Design of yagi-uda antennas using genetic algorithms," *IEEE Transactions on Antennas and Propagation*, vol. 45, no. 9, pp. 1386–1392, 1997.

[24] G. A. Casula, G. Mazzarella, and N. Sirena, "Evolutionary design of wide-band parasitic dipole arrays," *IEEE Transactions on Antennas and Propagation*, vol. 59, pp. 4094–4102, 2011.

[25] J. R. Koza, M. A. Keane, M. J. Streeter, W. Mydlowec, J. Yu, and G. Lanza, *Genetic Programming IV: Routine Human-Competitive Machine Intelligence*, Springer, 2003.

[26] J. D. Lohn, G. S. Hornby, and D. S. Linden, "An evolved antenna for deployment on NASA's space technology 5 mission," in *Genetic Programming Theory and Practice II*, Springer, 2005.

[27] L. Deias, G. Mazzarella, G. Montisci, and G. A. Casula, "Synthesis of artificial magnetic conductors using structure-based evolutionary design," submitted to *International Journal of Antennas and Propagation*.

[28] W. L. Stutzman and G. A. Thiele, *Antenna Theory and Design*, John Wiley, New York, NY, USA, 2nd edition, 1997.

[29] D. E. Isbell, "Log periodic dipole antennas," *IRE Transactions on Antennas and Propagation*, vol. 8, pp. 260–267, 1960.

[30] R. Carrel, "The design of log-periodic dipole antennas," *IRE International Convention Record*, pp. 61–75, 1961.

[31] G. J. Burke and A. J. Poggio, "Numerical Electromagnetics Code-Method of Moments," Tech. Rep. UCID-18834, Lawrence Livermore National Laboratory, 1981.

[32] G. J. Burke and A. J. Poggio, "Computer Analysis of the Twin-Whip," Tech. Rep. UCRL-52080, Lawrence Livermore Laboratory, Calif, USA, 1976.

[33] G. J. Burke and A. J. Poggio, "Computer Analysis of the Bottom-Fed FM Antenna," Tech. Rep. UCRL-52109, Lawrence Livermore Laboratory, Calif, USA, 1976.

[34] D. S. Linden and E. E. Altshuler, "Wire-antenna designs using genetic algorithms," *IEEE Antennas and Propagation Magazine*, vol. 39, no. 2, pp. 33–43, 1997.

[35] http://www.ansys.com/Products/Simulation+Technology/Electromagnetics/High-Performance+Electronic+Design/ANSYS+HFSS.

[36] S. R. Rengarajan, M. S. Zawadzki, and R. E. Hodges, "Waveguide-slot array antenna designs for low-average-sidelobe specifications," *IEEE Antennas and Propagation Magazine*, vol. 52, no. 6, pp. 89–98, 2010.

[37] B. C. Wadell, *Transmission Line Design Handbook*, Artech House, 1991.

[38] G. A. Casula, G. Mazzarella, and N. Sirena, "On the effect of the finite metal conductivity in the design of wire antennas using evolutionary design," in *Proceedings of the Antennas and Propagation Society International Symposium*, 2011.

Hindawi Publishing Corporation
International Journal of Antennas and Propagation
Volume 2013, Article ID 574128, 9 pages
http://dx.doi.org/10.1155/2013/574128

Research Article

A Compact UWB Antenna with a Quarter-Wavelength Strip in a Rectangular Slot for 5.5 GHz Band Notch

Pichet Moeikham, Chatree Mahatthanajatuphat, and Prayoot Akkaraekthalin

Faculty of Engineering, King Mongkut's University of Technology North Bangkok, 1518 Pracharat 1 Road, Bangsue, Bangkok 10800, Thailand

Correspondence should be addressed to Pichet Moeikham; moei76@hotmail.com

Received 9 September 2012; Revised 22 November 2012; Accepted 19 December 2012

Academic Editor: Renato Cicchetti

The limitation of the electromagnetic interferences (EMIs) caused by UWB radiating sources into WLAN/WiMAX communication systems operating in the frequency band located around 5.5 GHz requires the adoption of appropriate design features. To this purpose, a notch filter integrated into an UWB antenna, which is able to ensure a better electrical insulation between the two mentioned communication systems with respect to that already presented by the authors Moeikham et al. (2011), is proposed in this paper. The proposed filter, consisting in a rectangular slot including a quarter-wavelength strip integrated on the lower inner edge of the UWB radiating patch, is capable of reducing the energy emission in the frequency range between 5.1 and 5.75 GHz resulting in lower EMIs with sensible electronic equipments working in this frequency band. The antenna structure has no need to be tuned after inserting the rectangle slot with a quarter-wavelength strip. The proposed antenna has potential to minimize the EMIs at a frequency range from 5.1 to 5.75 GHz. The radiation patterns are given nearly omnidirectional in xy plane and likely bidirectional in yz plane at all frequencies by the proposed antenna. Therefore, this antenna is suitable to apply for various UWB applications.

1. Introduction

The ultra-wideband (UWB) monopole antenna has attracted much attention to design on a printed planar structure due to the fact that it could be designed with various shapes. Many inherent advantages exhibit on printed planar structure such as low profile, low cost, compact size, and ease for manufacture. Therefore, the printed planar antennas are popular rapidly. The printed antenna is preferably utilized with microstrip line or coplanar waveguide (CPW) as a feeding element. It is apparent in many pieces of literature that the compact UWB antennas based on the printed planar structure have been presented. For examples, the paper [1] presented development of a triangular CPW-fed printed antenna with specific ground plane shape. The antenna in [2] was designed by using a rectangular monopole M-shaped notch at the bottom patch with taper and T-shaped CPW feed. A taper shape slot and rectangular tuning stub fed by microstrip line was presented in [3]. The microstrip antenna combining the Giusepe Peano and Sierpinski Carpet fractal geometries was proposed [4]. In [5], a gradual curvature technique of central line and ground planes of CPW attached to rectangle patch was used for achieving ultra-wide impedance bandwidth. The paper [6] proposed a low-profile 3D antenna structure consisting of a bevel edge feed structure and a metal plate with folded strip. In [7], the microstrip line with balun structures was used as the feeding part of a low profile printed drop-shaped dipole antenna, resulting in a very wide impedance bandwidth suitable for multistandard WLAN/WIMAX/UWB wireless communications. Obviously, the printed planar antennas with various shapes using either microstrip line or CPW for feeding signal capably achieve ultra-wide impedance bandwidth. To confine fabrication tolerance and avoid using of via holes for some MMICs integration, the antenna design using one metallic side on dielectric substrate is proper and the CPW feeding structure possesses these vantages. In this paper, the CPW feeding structure has been chosen.

The frequency range belonging to 5.15–5.85 GHz has been assigned to the narrow band services including wireless local area network (WLAN) with the IEEE802.11a, HIPERLAN/2 standards and worldwide interoperability for microwave access (WiMAX) with the IEEE802.16e standard. Clearly this frequency range falls within the UWB band resulting in EMIs between both systems. To reject the EMIs for UWB systems, extra band-stop filters should be added. However, these elements lead to a need of more space, higher cost, and more complicate structures. To remedy these problems, an UWB antenna structure, suitable to minimize the EMIs with the R.F. systems working in the frequency band located around 5.5 GHz, is strongly desirable. Obviously, the challenge of feasible design for UWB antennas with compact size and the proper electrical characteristics of both frequency and time domain responses would be required. Especially, the potential reduction of EMIs from coexisting WLAN/WiMAX systems is also a necessary characteristic for the UWB antenna design.

Many techniques were employed to design the printed UWB antennas with notched band function. For examples, the technique of embedded one or more narrow slits on the radiating patch for achieving notched band function was proposed in [8–13], the narrow slit embedded on ground plane was used in [14, 15], while the spiral stub attached at feed line for band notching was also employed [15]. Parasitic strips coupled with the antennas were also proposed to reject the undesired frequencies [16–18]. In [19–23], a resonator inserted on the patch was proposed for achieving band notching. Additionally, a slit embedded on the ground plane of a printed discone UWB antenna was adopted to reject the undesired frequency bands [22], whereas the resonators nearby feeding line were employed for more notched bands [23]. The embedded narrow slits on the patch and ground plane with resonator on the opposite side of the radiating patch were presented in [24]. The other UWB slot antennas with band notching were proposed in [25, 26]. The former antenna embeds only a narrow slit on the exciting stub, whereas both a C-shaped narrow slit on the feeding element and a microstrip resonator at the inner slot were employed in the latter antenna. It is clearly seen that the narrow slit with the length of $\lambda_g/2$ or $\lambda_g/4$, where λ_g is a guided wavelength, is designed by inserting it on either the patch or ground plane for band notching [8–15, 25]. The small coupling parasitic strips or resonators placed, either on the same side or opposite side of the patch, were employed in [16–23], whereas both the narrow slit on the patch and the resonator on the opposite side were used in [24, 26]. It is apparent that the extra element could be used to reject undesired frequency, but this leads to more complicated structure. Also, using the narrow slits to control the rejected frequency results in many parameters needs to be considered. Besides, utilizing these techniques will be more complicated when applying with real antennas.

In this paper, an embedded filter consisting of a rectangular slot with a quarter-wavelength strip, useful to be employed in a compact UWB antenna to realize a single-band notch at 5.5 GHz, is proposed. By integrating the proposed filter in a previous UWB antenna, proposed by the authors in [5], it is easy to reduce the energy emission in the undesired frequency band. The details concerning the antenna design, the parametric study, and the experimental validation will be presented in the following sections.

2. Antenna Design

2.1. A Compact UWB Antenna. A compact UWB antenna designed in [5] is used as baseline antenna for this research. All details of the UWB antenna design are briefly described. Figure 1 shows the antenna geometry, the realized prototype, and the simulated and measured return losses of the baseline antenna, respectively. According to the structure in Figure 1(a), the antenna was designed with the height of $0.56\lambda_g$ and the width of $0.3\lambda_g$, where λ_g is a guided wavelength of the lowest operating frequency. The slot stubs were inserted at the central line of CPW to enhance the impedance matching. As shown in Figure 1(b), the baseline antenna prototype was fabricated on a single metallic side of FR4 substrate with thickness of 1.6 mm, relative permittivity of 4.4, and loss tangent of 0.019. The SMA connector was used for measurement purpose. The measured result shows the extremely large impedance bandwidth ($S_{11} < -10$ dB) of over 123.23%, covering 2.85 GHz to exceed 12 GHz, as shown in Figure 1(c). Although the simulated and measured results show acceptable agreement with some discrepancies, the baseline antenna capably operates covering the entire UWB frequency range. The fabrication tolerances and the discontinuity introduced by the transition between the SMA and the CPW feeding line are responsible for the discrepancies observed in the experimental measurements.

The physical behavior of guided wave to radiated wave on gradual curvature transition was analyzed, resulting in the simulated surface current distribution results on the radiating patch of the baseline antenna at frequencies of 3.1, 5, 7, and 9 GHz, as shown in Figure 2. It is clearly seen that the surface current distributions are very strong nearby the edges of curvature parts at all frequencies, whereas low current distributions are found on other parts. It is revealed that the gradual curvatures are major parts to radiate wave responding for extremely wide frequency range. On the other hand, when the current distribution paths on gradual curvatures are changed or disturbed, more impact to electrical characteristics of the antenna occurrs. To design the antenna with frequency rejection, the extra element with band notched function is introduced placing nearby the curvature part of radiating patch. In this work, a filter based on a quarter-wavelength strip in rectangular-shaped slot is integrated in the baseline antenna presented in [5] to reduce the energy emission in the frequency band located around 5.5 GHz. As it will be shown later, the proposed filter does not significantly affect the impedance bandwidth of the baseline antenna. Therefore, the conductor on patch is etched out with appropriate dimensions to form the rectangular-shaped slot.

2.2. Design of the Filter Integrated into the UWB Antenna. The mitigation of the EMIs in the frequency band centered around 5.5 GHz can be achieved by using a suitable filter integrated in the antenna structure. As mentioned, the notched band function could be applied to the baseline UWB

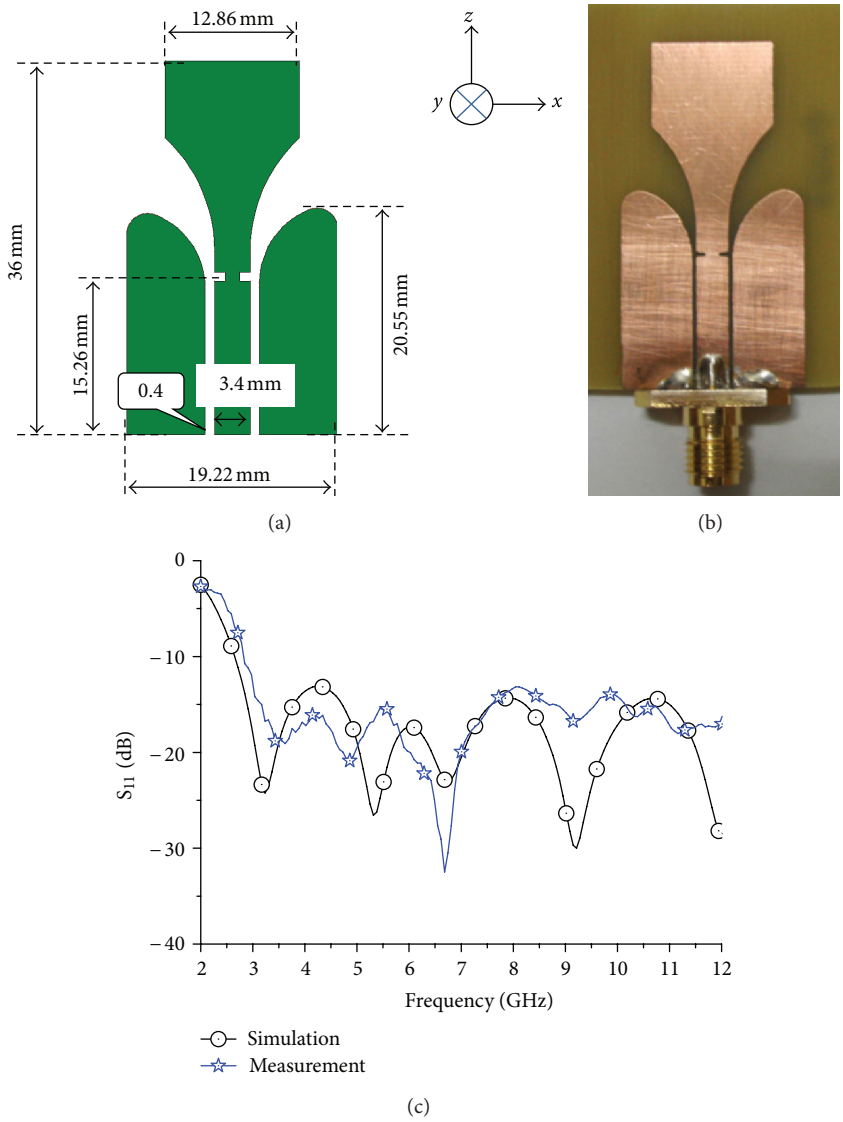

Figure 1: The baseline UWB antenna: (a) configuration, (b) the prototype, and (c) comparison return loss of simulated and measured results of the baseline antenna prototype.

antenna structure. In this work, two designed steps for the notched band are applied. Firstly, the proper rectangular-shaped slot, with w_s of 2.25 mm and h_s of 8.11 mm, is formed on the patch, as shown in Figure 3(a). Secondly, a small strip is placed at the lower inner edge of a rectangle slot (see Figure 3(a)). The length of this strip, which is about a quarter-wavelength at the rejected frequency of 5.5 GHz, is calculated as follows:

$$f_{\text{reject}} \cong \frac{3 \times 10^8}{4 l_s \times \sqrt{\varepsilon_{\text{eff}}}} \quad \text{Hz}, \tag{1}$$

where

$$\varepsilon_{\text{eff}} \approx \left(\frac{\varepsilon_r + 1}{2}\right). \tag{2}$$

From (1), the relative permittivity of dielectric and the length of small strip are denoted by ε_r and l_s, respectively. As seen in Figure 3(a), the small strip is inserted into the rectangular slot for band notching. A comparison of simulated return loss results, when varying the small strip length (l_s), is given in Figure 3(b). The other parameters are fixed when the l_s parameter is varied. Whereas the length of small strip is extended, the rejected frequency is moved to lower frequencies and vice versa. The proposed antenna capably rejects the frequency of 5.5 GHz by setting the optimal small strip length to be 7.27 mm. It is obvious that the length of small strip corresponds to an approximate quarter-wavelength at the rejected frequency. It can be concluded that the rejected frequency is controlled by the length of the small strip. Apparently, the rejection of the undesired frequency can be achieved as in the previous work in [9]. However, the structure proposed to reject the undesired frequency is more simple and easy to design since it requires the optimization of only one parameter.

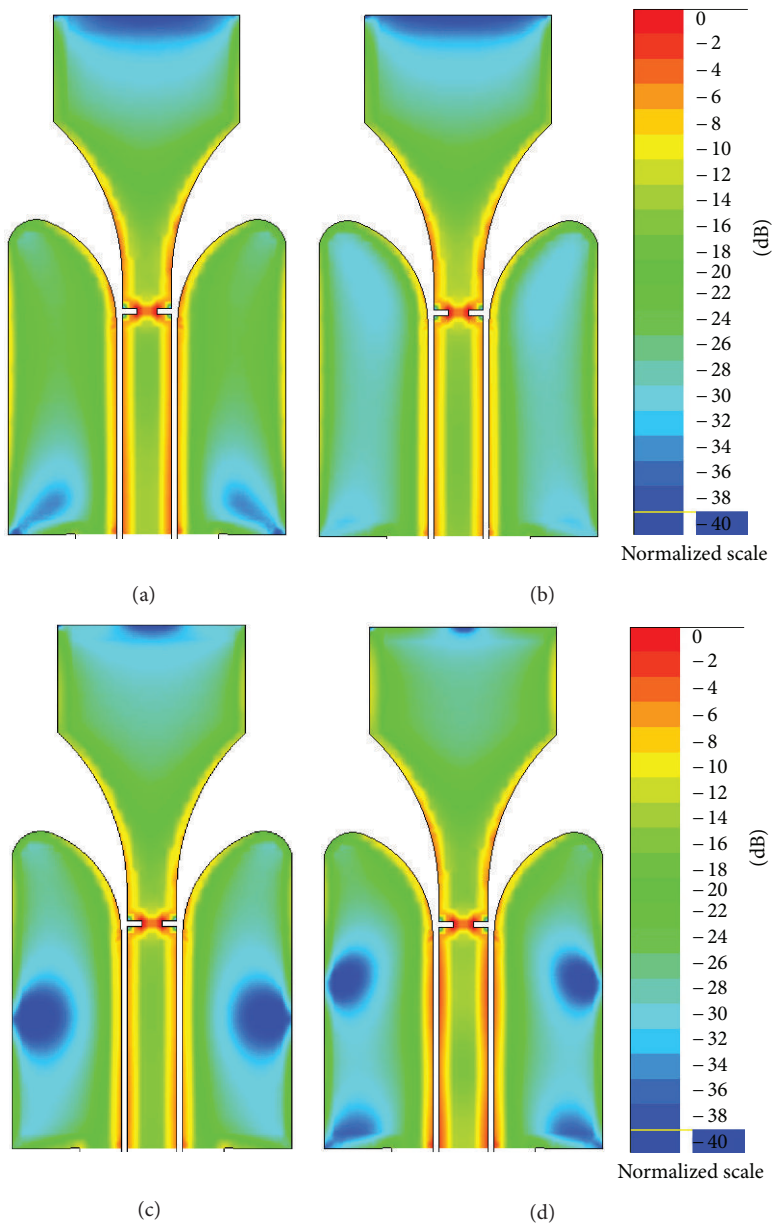

Figure 2: Simulated surface current distribution of the baseline antenna at frequencies of (a) 3.1 GHz, (b) 5 GHz, (c) 7 GHz, and (d) 9 GHz.

Figure 3(c) depicts the simulated return loss results when the h_r parameter, indicating the position of rectangular slot with the quarter-wavelength strip on the radiating patch, is varied. The other parameters are fixed when the h_r parameter is varied. It is seen that the notched bandwidth is slightly increased, whereas the h_r parameter is decreased and vice versa. While the h_r parameter is decreased, the rectangular slot with the quarter-wavelength strip is moved toward the gradual curvature parts. The electromagnetic coupling between the radiated parts and the quarter-wavelength strip is also increased. As a result, there is a significant change in input impedance of the antenna leading to mismatching and higher reflection coefficients. The characteristic impedance is significantly affected, resulting in a wider notched bandwidth. The optimal h_r parameter of 17.4 mm capably provides the notched bandwidth of 5.2–5.8 GHz. It is concluded that the notched bandwidth is controlled by the position of rectangular slot with the quarter-wavelength strip on radiating patch. In addition, the widths of quarter-wavelength strip and rectangular slot are fixed due to limited area on the patch.

The physical mechanism governing the behavior of the filter integrated into the antenna can be clarified using the surface current map excited in the vicinity of the filter's strip (see Figure 4). In particular, from Figure 4 it appears that at 5.5 GHz the surface current distribution is strongly concentrated in the lowerpart of the filter close the radiating part of the antenna. This feature is responsible for a strong reflection

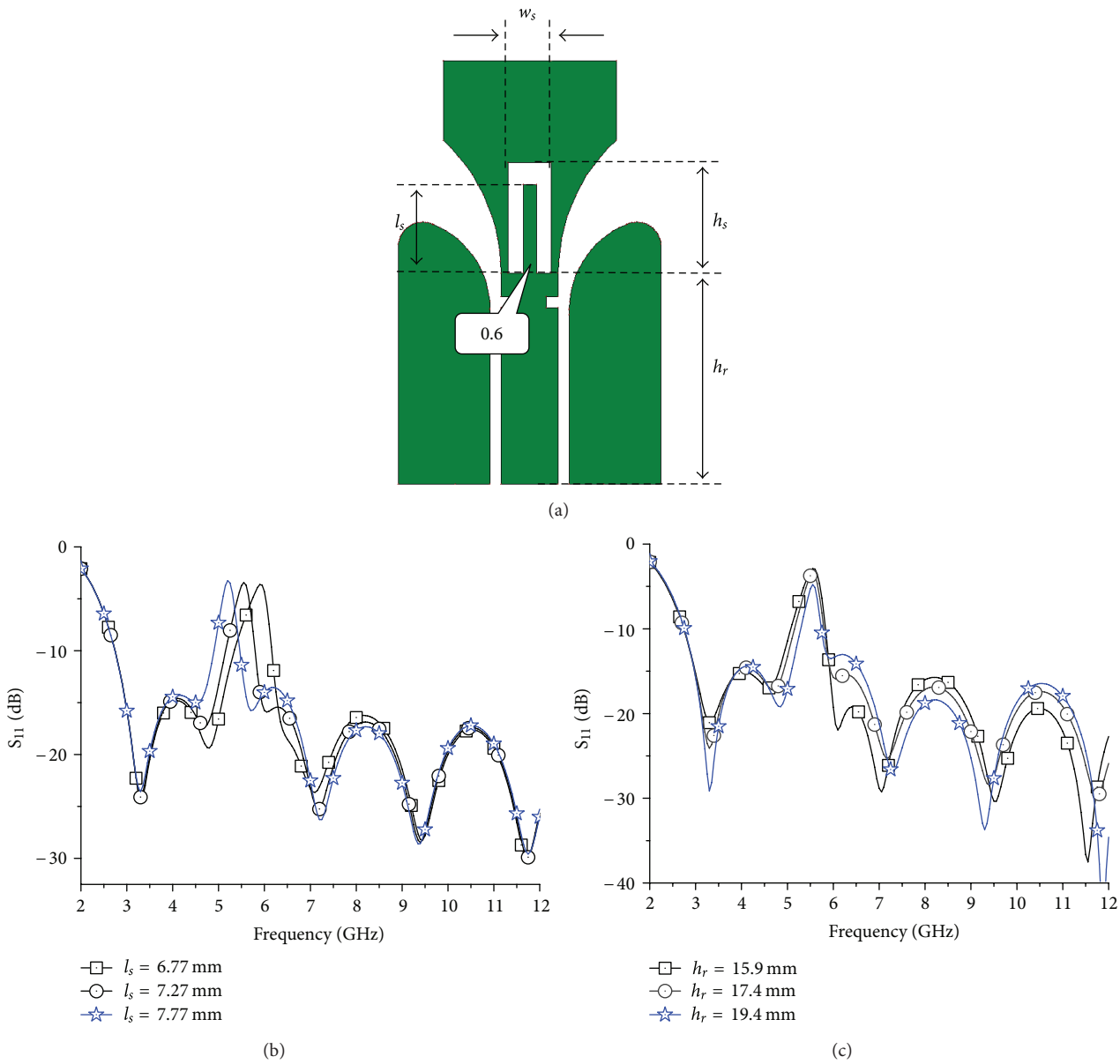

Figure 3: (a) Configuration of the proposed antenna, (b) S_{11} results when varying l_s, and (c) S_{11} results when varying h_r.

of the surface current, which determines an increment of the related return loss.

3. Implementation and Measurement Results

The proposed antenna has been realized using the optimized parameters obtained by means of the full-wave software Zeland IE3D. Photograph of the proposed antenna prototype is shown in Figure 5(a). The SMA connector is also employed to feed the signal for measurement purpose. A comparison of return losses between measured and simulated results is illustrated in Figure 5(b). From measured result, it is seen that the prototype antenna capably provides the operating frequency covering the entire UWB range and achieves the requirement of notched frequency range from 5.1 to 5.75 GHz. Besides, it is found that the center frequency of notched band slightly shifts to lower frequency. At lower band of 3.1–5 GHz, the lower edge frequency and the resonant frequency shift to higher; on the contrary, the resonant frequencies evidently shift to lower frequency at higher band of 6–10.6 GHz. The fabrication tolerances, the discontinuity introduced by transition between the SMA and CPW transmission line, and some inevitable nonuniformity of the substrate characteristics are the main causes of these unexpected behaviors.

The measured radiation pattern results of the proposed antenna at the frequencies of 3.1, 5, 7, and 9 GHz in xy and yz planes are illustrated in Figure 6. The measured copolarization is denoted by solid line with circle and star symbols, while the measured cross-polarization is denoted

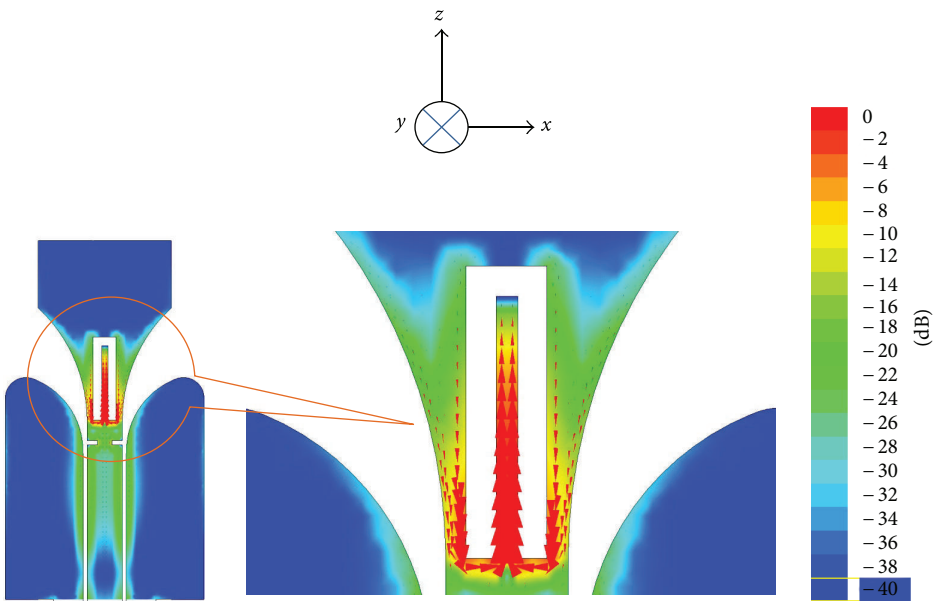

Figure 4: Surface current density excited near the filter's strip at the frequency of 5.5 GHz.

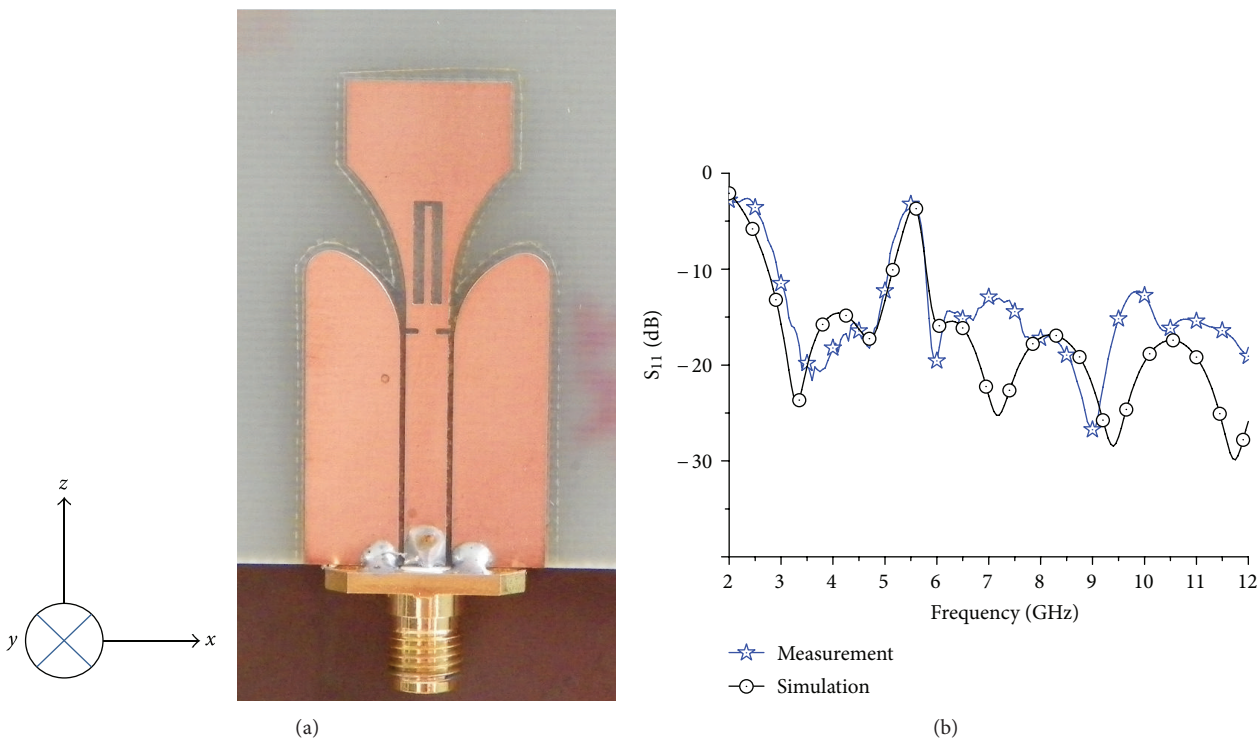

Figure 5: (a) The prototype antenna and (b) comparison of simulated and measured return losses.

by dash line with cross on triangle and rhombus symbols. In xy plane, radiation patterns of the proposed antenna show nearly to be omnidirectional at all frequencies, as shown in Figures 6(a) and 6(b). Additionally, the high level of cross-polarization occurring at the frequencies of 3.1 and 5 GHz is due to the strong deformation of the current paths caused by the presence of the quarter-wavelength strip and rectangular slot filter. The measured radiation patterns in yz plane are shown in Figures 6(c) and 6(d).The radiation patterns at all frequencies show likely bi-directional with some distortions due to some spurious emissions. The proposed antenna capably affords linear polarization.

The transfer function (S_{21}) and group delay time are measured by setting up two identical antennas face to face

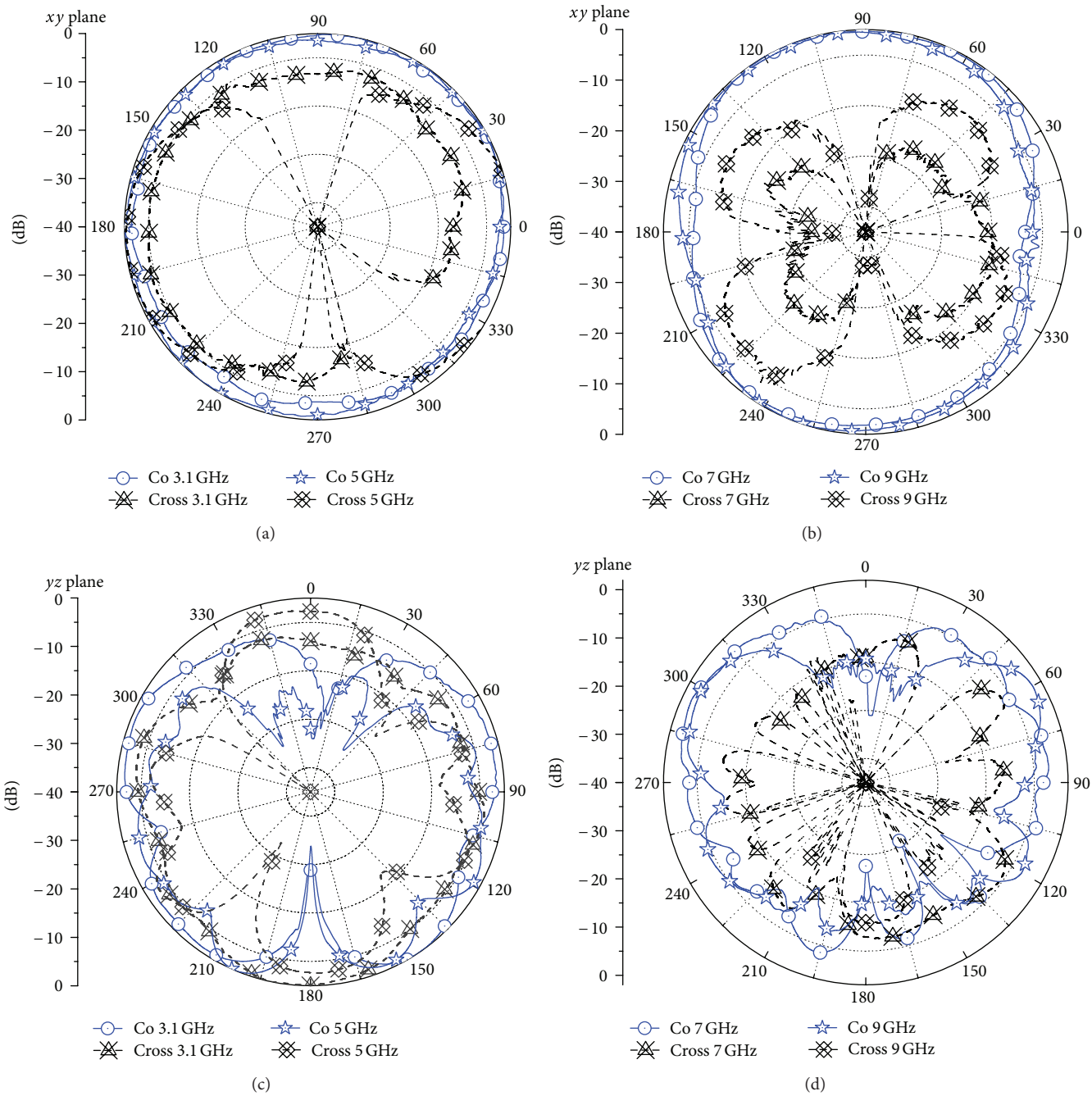

Figure 6: Measured radiation patterns at the frequencies of (a) 3.1, 5 GHz, (b) 7, 9 GHz in xy plane, and (c) 3.1, 5 GHz, (d) 7, 9 GHz in yz plane.

with distance of 0.35 m. Comparisons of measured transfer function and group delay time between the proposed antenna and the previous antenna (in [9]) are illustrated in Figures 7(a) and 7(b), respectively. It can be found that the transfer function of the proposed antenna prototype has been slightly improved with better frequency rejection. Both transfer function and group delay time obtained in this work are slightly more constant than the previous antenna due to the simple notched band structure.

Figure 8(a) depicts measured time domain characteristic results of the proposed antenna. It is seen that the transfer function is deeply sharp, which is −53.18 dB at the notched band center. The pass band across from 3.1 to 9 GHz affords the average S_{21} levels higher than −43.85 dB. When the frequency is over 9.2 GHz, the S_{21} gradually decreases and reaches minimum level of −50 dB at the frequency of 10.6 GHz. The constant group delay time of the proposed antenna presents an almost constant value within the working

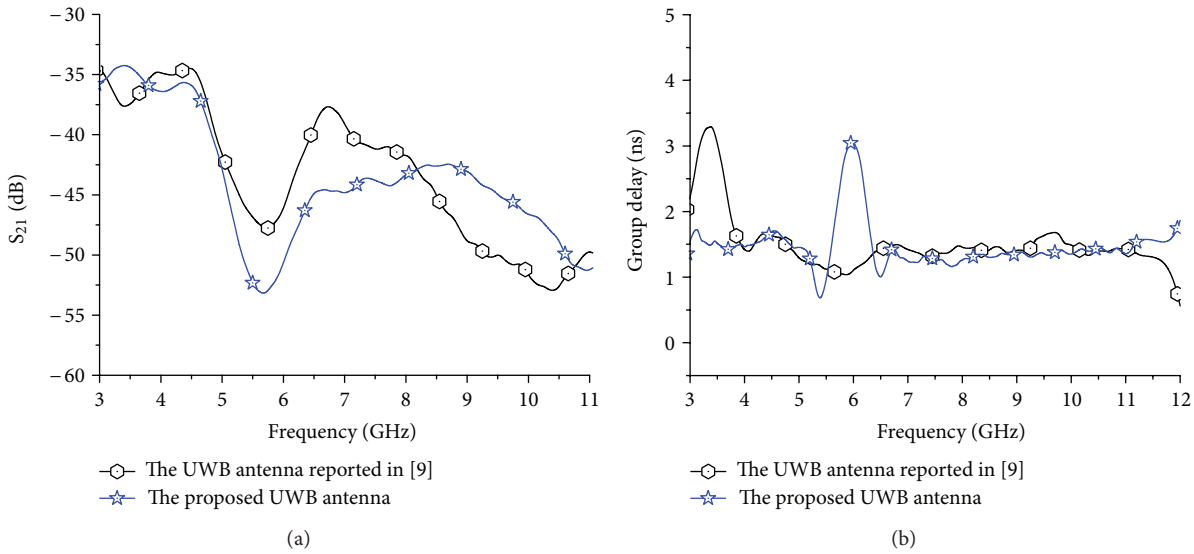

Figure 7: Comparison between the previous antenna and the proposed antenna (a) transfer function and (b) group delay time.

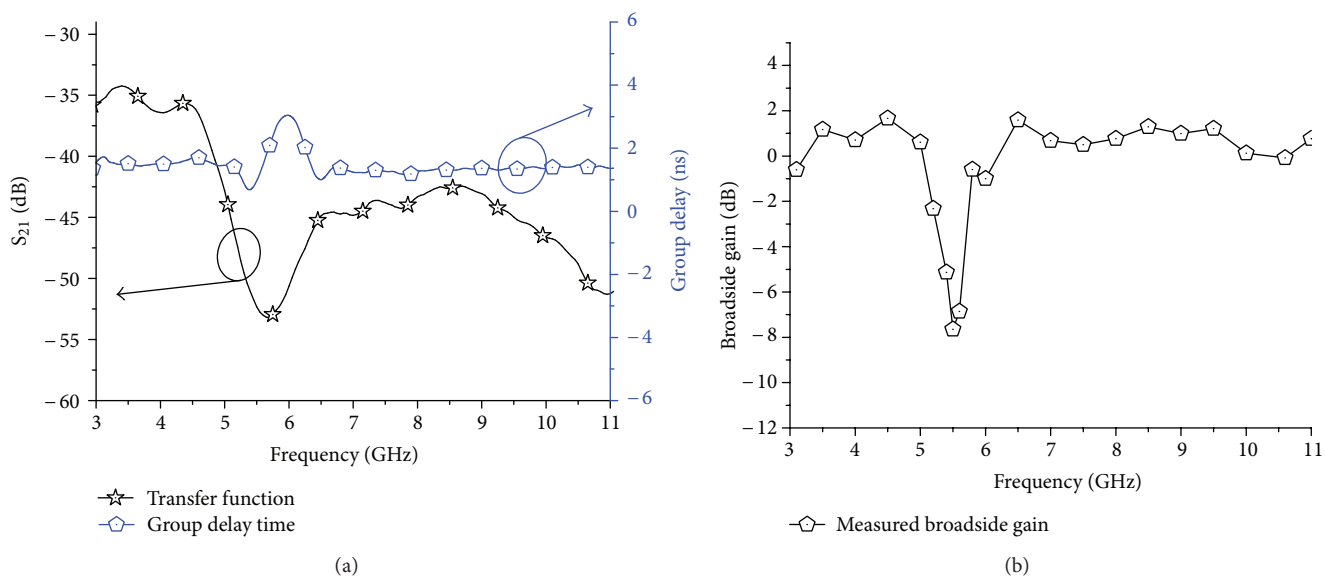

Figure 8: (a) Measured transfer function and group delay time and (b) measured broadside gain of the proposed antenna.

frequency bands, while in the notched band it exhibits a peak value of about 3 ns. It is indicated that the proposed antenna capably operates with good linear transmission performances and may be used for impulse radio applications with a little distortion. The measured broadside gain result of the proposed antenna is given, as shown in Figure 8(b). It is found that the antenna gain fluctuates within the range of −0.6 to 1.6 dB at the lower band of 3.1–5 GHz, and the maximum value is occurred at frequency of 4.5 GHz. The antenna gain is deeply sharp, which is −7.6 dB at the notched band center. At the higher band of 6–10.6 GHz, the measured broadside gain shows more constant than the lower band, and the maximum value of 1.6 dB is given at frequency of 6.5 GHz.

4. Conclusion

A compact UWB antenna with band notching at 5.5 GHz is proposed. All the details concerning the antenna design and the frequency behavior of the band notch filter have been presented. The rectangular slot is embedded into the radiating patch of the previous UWB antenna. The small strip with its length approximately a quarter-wavelength of 5.5 GHz is attached to the lower inner edge of the rectangular slot for band notching. The strong current distribution concentrates on the quarter-wavelength strip and lower part rectangular slot leading to a drastic change into the input impedance of the antenna. The high reflection coefficients and mismatching

of the input impedance occurred. Consequently, the amplitude of the radiated field decreases since the level of the surface current excited in the radiating part of the antenna has reduced. The center rejected frequency is controlled by adjusting the length of the quarter-wavelength strip. The notched frequency bandwidth is depended on the position of rectangular slot with the quarter-wavelength strip on radiating patch. The proposed antenna operates covering the entire UWB band except the notched band of 5.1–5.75 GHz. Having the minimized EMIs potential at frequency band of 5.5 GHz and radiation patterns nearly omnidirectional at all frequencies in xy plane, the proposed antenna is appropriate to use for various UWB applications.

Conflict of Interests

This paper has supported the framework of a Ph.D. thesis. The authors declare that there is no conflict of interests with IE3D software.

References

[1] N. Fortino, J. Y. Dauvignac, G. Kossiavas, and R. Staraj, "Design optimization of UWB printed antenna for omnidirectional pulse radiation," *IEEE Transactions on Antennas and Propagation*, vol. 56, no. 7, pp. 1875–1881, 2008.

[2] C. Deng, Y. J. Xie, and P. Li, "CPW-fed planar printed monopole antenna with impedance bandwidth enhanced," *IEEE Antennas and Wireless Propagation Letters*, vol. 8, pp. 1394–1397, 2009.

[3] R. Azim, M. T. Islam, and N. Misran, "Compact tapered-shape slot antenna for UWB applications," *IEEE Antennas and Wireless Propagation Letters*, vol. 10, pp. 1190–1193, 2011.

[4] H. Oraizi and S. Hedayati, "Miniaturized UWB monopole microstrip antenna design by the combination of Giusepe Peano and Sierpinski carpet fractals," *IEEE Antennas and Wireless Propagation Letters*, vol. 10, pp. 67–70, 2011.

[5] P. Moeikham and P. Akkaraekthalin, "A compact ultrawideband monopole antenna with tapered CPW Feed and slot stubs," in *Proceedings of the 8th International Conference on Electrical Engineering/ Electronics, Computer, Telecommunications and Information Technology (ECTI-CON '11)*, pp. 180–183, Khon Kaen, Thailand, May 2011.

[6] C.-H. Kang, S.-J. Wu, and J.-H. Tarng, "A novel folded UWB antenna for wireless body area network," *IEEE Transactions on Antennas and Propagation*, vol. 60, no. 2, pp. 1139–1142, 2012.

[7] G. Cappelletti, D. Caratelli, R. Cicchetti, and M. Simeoni, "A low-profile printed drop-shaped dipole antenna for wideband wireless applications," *IEEE Transactions on Antennas and Propagation*, vol. 59, pp. 3526–3535, 2011.

[8] L. Lizzi, G. Oliveri, P. Rocca, and A. Massa, "Planar monopole UWB antenna with UNII1/UNII2 WLAN-band notched characteristics," *Progress in Electromagnetics Research B*, no. 25, pp. 277–292, 2010.

[9] P. Moeikham, C. Mahatthanajatuphat, and P. Akkaraekthalin, "A compact ultrawideband monopole antenna with 5. 5 GHz notched band," *Progress in Electromagnetics Research C*, vol. 26, pp. 13–27, 2012.

[10] Q. X. Chu and Y. Y. Yang, "A compact ultrawideband antenna with 3.4/5.5 GHz dual band-notched characteristics," *IEEE Transactions on Antennas and Propagation*, vol. 56, no. 12, pp. 3637–3644, 2008.

[11] T. D. Nguyen, D. H. Lee, and H. C. Park, "Design and analysis of compact printed triple band-notched UWB antenna," *IEEE Antennas and Wireless Propagation Letters*, vol. 10, pp. 403–406, 2011.

[12] D. T. Nguyen, D. H. Lee, and H. C. Park, "Very compact printed triple band-notched UWB antenna with quarter-wavelength slots," *IEEE Antennas and Wireless Propagation Letters*, vol. 11, pp. 411–414, 2012.

[13] X.-J. Liao, H.-C. Yang, N. Han, and Y. Li, "UWB antenna with dual narrow band notches for lower and upper WLAN bands," *Electronics Letters*, vol. 46, pp. 1593–1594, 2010.

[14] Y.-B. Yang, F.-S. Zhang, F. Zhang, L. Zhang, and Y.-C. Jiao, "Design of novel wideband monopole antenna with a tunable notched-band for 2.4 GHZ WLAN and UWB applications," *Progress in Electromagnetics Research Letters*, vol. 13, pp. 93–102, 2010.

[15] S. K. Mishra and J. Mukherjee, "Compact printed dual band-notched U-shape UWB antenna," *Progress in Electromagnetics Research C*, vol. 27, pp. 169–181, 2012.

[16] A. M. Abbosh and M. E. Bialkowski, "Design of UWB planar band-notched antenna using parasitic elements," *IEEE Transactions on Antennas and Propagation*, vol. 57, no. 3, pp. 796–799, 2009.

[17] M. Zhang, Y. Z. Yin, J. Ma, Y. Wang, W. C. Xiao, and X. J. Liu, "A racket-shaped slot UWB antenna coupled with parasitic strips for band-notched application," *Progress in Electromagnetics Research Letters*, vol. 16, pp. 35–44, 2010.

[18] Y. Zhu, F. S. Zhang, C. Lin, Y. C. Jiao, and R. Zou, "Design of band-notched structure for UWB applications," *Electronics Letters*, vol. 47, no. 4, pp. 235–236, 2011.

[19] S. J. Wu and J. H. Tarng, "Planar band-notched ultra-wideband antenna with square-looped and end-coupled resonator," *IET Microwaves, Antennas and Propagation*, vol. 5, no. 10, pp. 1227–1233, 2011.

[20] S. J. Wu, C. H. Kang, K. H. Chen, and J. H. Tarng, "Study of an ultrawideband monopole antenna with a band-notched open-looped resonator," *IEEE Transactions on Antennas and Propagation*, vol. 58, no. 6, pp. 1890–1897, 2010.

[21] C. Y. Hong, C. W. Ling, I. Y. Tarn, and S. J. Chung, "Design of a planar ultrawideband antenna with a new band-notch structure," *IEEE Transactions on Antennas and Propagation*, vol. 55, no. 12, pp. 3391–3397, 2007.

[22] X. Li, H. L. Zheng, T. Quan, and Q. Chen, "A printed discone ultra-wideband antenna with dual-band notched characteristics," *Progress in Electromagnetics Research C*, vol. 27, pp. 41–53, 2012.

[23] C. Lin, P. Jin, and R. W. Ziolkowski, "Single, dual and tri-band-notched ultrawideband (UWB) antennas using capacitively loaded loop (CLL) resonators," *IEEE Transactions on Antennas and Propagation*, vol. 60, no. 1, pp. 102–109, 2012.

[24] W. T. Li, X. W. Shi, and O. Q. Hei, "Novel planar UWB monopole antenna with triple band-notched characteristics," *IEEE Antennas and Wireless Propagation Letters*, vol. 8, pp. 1094–1098, 2009.

[25] S. Mohammadi, J. Nourinia, C. Ghobadi, and M. Majidzadeh, "Compact CPW-fed rotated square-shaped patch slotantenna with band-notched function for UWBapplications," *Electronics Letters*, vol. 47, pp. 1307–1307, 2011.

[26] G. P. Gao, Z. L. Mei, and B. N. Li, "Novel circular slot UWB antenna with dual band-notched characteristic," *Progress in Electromagnetics Research C*, vol. 15, pp. 49–63, 2010.

Hindawi Publishing Corporation
International Journal of Antennas and Propagation
Volume 2012, Article ID 721412, 9 pages
doi:10.1155/2012/721412

Research Article

High Gain Compact Strip and Slot UWB Sinuous Antennas

Elson Agastra, Leonardo Lucci, Giuseppe Pelosi, and Stefano Selleri

Department of Electronics and Telecommunications, University of Florence, 3 Via Santa Marta, 50139 Florence, Italy

Correspondence should be addressed to Stefano Selleri, stefano.selleri@unifi.it

Received 5 October 2012; Accepted 17 October 2012

Academic Editor: Renato Cicchetti

Three ground-backed compact strip-and slot-sinuous antennas are analyzed. Proposed configuration allows for a single lobe, polarization-versatile, high efficiency, and ultrawide band antenna not needing a cumbersome lossy back cavity typical of conventional single-lobe sinuous antennas. Simulations show attained performances as well as tuning possibilities.

1. Introduction

In the last two decades, the advances in communication technology, in particular mobile communications, have drastically changed the lifestyles of people. Antenna engineers have contributed to this wireless revolution by designing high performance antennas for fixed base-stations and mobile portable terminals. The demands placed on mobile communication systems have increased remarkably, so antenna designers face many challenges: small or tiny sizes, low- or ultra-low-profiles, wide- or ultra-wide-operating bandwidths, multiple operative modes, polarization agility, and, of course, simple fabrication and low cost. As a result, antenna research and development have become a hot topic in both academia and industry.

Indeed ultra-wideband antennas are needed in many engineering applications not only in telecommunications, for example, in radar and direction-finding systems, through wall imaging, anti-collision radars, radio astronomy, and biomedical systems.

Hot topics in ultra-wideband antenna are printed structures [1] as the small size and light weight are mandatory to the antenna success. Many researches are concentrated on increasing the band width of the printed antenna [2, 3]. In any case, even if large bands are obtained, polarization purity and agility are not investigated [4–10]. Many of these researches have in common the development of a slot—rather than patch—structure.

Increasing the requirements for bandwidth, uniform antenna gain, and polarization agility, the antenna engineers need to consider the principles at the basis of frequency independent structures. Frequency-independent antennas exhibit some self-scaling property in their geometry where polarization, radiation pattern, and input impedance remain unchanged or vary with a limited, predictable, periodicity, over large bandwidths [11]. Spiral antennas are classified into different types: Archimedean spiral, logarithmic spiral, square spiral, star spiral, and so forth. Archimedean and logarithmic spirals are very popular configurations and among the most analyzed frequency independent antennas. Many research is concentrated on reducing spiral antenna size [12], but as the spiral antenna radiates two main lobes, one above and one below its plane, when a single radiation lobe is needed, an absorbing cavity is used to prevent radiation in one of the two half spaces [11].

To the spiral antenna, the sinuous antenna is a good alternative. It shares many of its features: it is planar, broadband and presents two lobes. On the other hand, while spirals have a circular polarization, sinuous antennas exhibit a linear polarization in their two-arm version, and dual linear polarization in their four arms version [11, 13]. Indeed the two available orthogonal linear polarizations can be used for polarization diversity in transmit/receive as well as to produce simultaneously a Left Hand Circular Polarization (LHCP) and a Right Hand Circular Polarization (RHCP) [11–15]. The antenna lower and higher frequency operation limits are determined, respectively, by the outer and inner diameters of the structure.

As the theoretical sinuous antenna radiates both above and below its plane, a broadband absorbing cavity is typically used to eliminate the radiation in one direction as any reflections from a metallic bottom would couple back

to the antenna feed and radiate with the opposite sense of polarization, spoiling polarization purity. Typically, the absorber-filled cavity for this antenna has a depth on the order of the antenna radius. Although the lossy cavity drastically reduces antenna efficiency below 50% and makes the complete structure quite bulky, most commercial sinuous antenna are realized this way [16, 17].

Better results might be reached via a stepped or conical cavity, so as to keep the back wall at a quarter wavelength from the active region. This can be done more compact by properly loading with a high permittivity material the cavity or by exploiting metamaterials; some interesting results for this two configurations are presented in the following. If, on the other hand, a flat ground is preferred, then a stepped permittivity can be used in the substrate to vary the electrical distance of the planar ground. Both these possibilities will be addressed in the following. In any case these configuration still needs a backing, possibly lossy, cavity of nonnegligible thickness.

A sinuous antenna in slot configuration is not burdened with most of these issue. Additionally, while the slot spiral also radiates bidirectionally, a deep, absorbing cavity is not necessary to force unidirectional radiation. In fact, a very shallow reflecting cavity is sufficient and leads to an appreciable increase in gain. The resulting complete antenna is very thin, making mounting much easier. Notwithstanding its better behavior, little research has been carried out for slot-sinuous antennas [18–20].

This paper is focused on the design of three four-arm sinuous antennas, enabling polarization agility if backed by an appropriate feeding network, and with increased efficiency (with respect to the lossy cavity backed one). Two of the proposed configurations exhibit a strip sinuous over a properly design backing cavity, while the last is a slot-sinuous configuration with a closer ground. In this latter configuration, by varying the distance from the ground, some control over the half power beam width (HPBW) can be obtained.

2. Sinuous Antenna Description

The standard sinuous antenna is composed of at least two arms, where each is composed by cells. The description of printed sinuous antenna can be founded in the DuHamel patent [13].

The slot-sinuous antenna is essentially the complementary structure of a conventional sinuous antenna. The fundamental analytical expression that permits to realize the sinuous antenna geometry is reported in (1)

$$\varphi = (-1)^p \alpha_p \sin\left[\frac{180\ln\left(r/R_p\right)}{\ln\left(\tau_p\right)}\right], \tag{1}$$

where r and φ are polar coordinates of the points on the curve relative to the pth cell, whose domain is $R_{p+1} \leq r \leq R_p$. Cell-1 corresponds to the outermost cell, with radius R_1, and, as a recursive rule, $R_p = \tau_{p-1}R_{p-1}$. α_p and τ_p are appropriate constants, describing the angular width and the scale factor of the antenna, much alike a printed log-periodic antenna.

The curve obtained by (1) is then rotated by $\pm\delta$ around the z axis to define the boundaries of one of the printed arms (Figure 1). As we are interested in the four arm structure, this arm is finally duplicated and rotated of 90°, 180°, and 270° about the origin creating the complete four arms antenna. For the slot antenna, the complementary structure is considered, where the above described surfaces are etched on a ground plane, rather than metalized over a substrate.

To validate the chosen layout, a FEM analysis of the proposed structure is performed via Ansoft HFSS, both in free space and with a backing cavity. The geometry parameters considered here for all configurations are: $R_1 = 14\,\text{mm}$, $\alpha_p = \alpha = 45°$, $\tau_p = \tau = 0.77$, $\delta_p = \delta = 22.5°$, $P = 11$ (total number of cells). The α and δ chosen lead to a self-complementary structure. The chosen values for R_1 and P lead to a theoretical band spanning from 6 GHz to 18 GHz (3 : 1 frequency band). It is worth noticing that the slot configuration needs an outer ground ring, so only for this case, while the radius of the antenna is still 14 mm the radius of the whole structure extends to 18 mm.

Both the strip-and slot-sinuous antennas inherently radiates bidirectionally.

3. Strip Sinuous with Compact Cavity

Classical sinuous antennas are strip ones; that is, gray area in Figure 1, representing one of the antenna arms, is a metal patch over a dielectric substrate, whereas in a slot-sinuous antenna, the gray area in Figure 1 represents a hole etched in on a metallic ground, possibly over a dielectric slab.

To attain unidirectional radiation, strip-sinuous antennas are usually backed with a cavity filled with an absorbing material [16, 21]. This causes an efficiency drop of at least 50% and a corresponding lowering in Gain.

Better results would be attained by backing the antenna with a conducting plane acting as a mirror. For the mirror to have its maximum effect the mutual distance between the antenna and the reflecting ground must be one quarter wavelength. If this is trivial in narrow-band applications it is a requirement impossible to meet in wide and ultra wide band applications.

In this particular case, being the antenna working in an active region mode, where just one or two of the bend in each arm of the sinuous strip do actually radiate, it is possible to devise some solution to obtain a reflecting mirror at a quarter wavelength from the active region.

Two solutions are presented here, in the first one several concentric cylindrical shells of dielectric materials are placed beneath the substrate on which the antenna is printed. All cylindrical shells share the same height h and the reflecting ground plane is placed at the bottom. Eight cylindrical shells are considered; their inner and outer radius r_p and r_{p+1} ratio is still τ as for the sinuous antenna. Each shell permittivity and permeability is tuned so that the height h is $\lambda/4$ at the frequency for which the bend of the sinuous strip immediately above the shell is actively radiating (Figure 2 and Table 1). High losses materials are exploited to attain a better frequency behavior. The corresponding gain diagrams are reported in Figure 3.

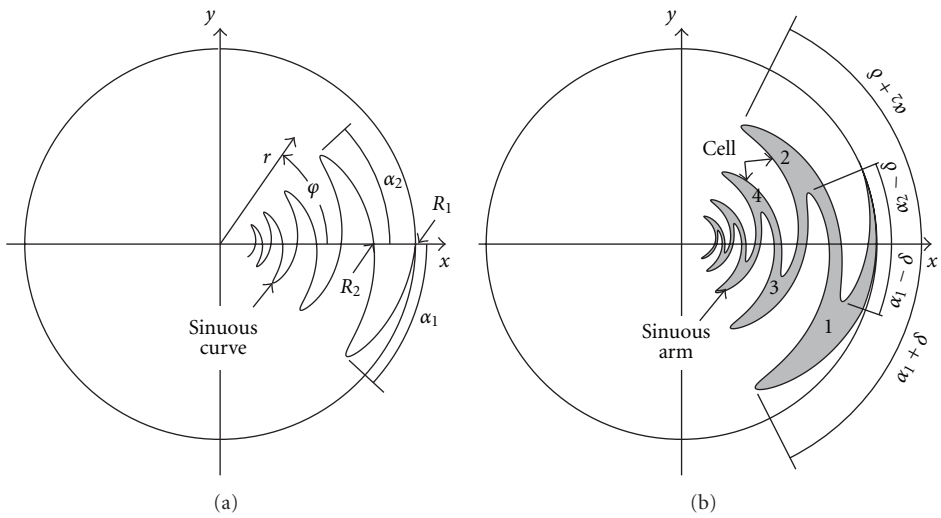

Figure 1: Sinuous curve design and relative parameters.

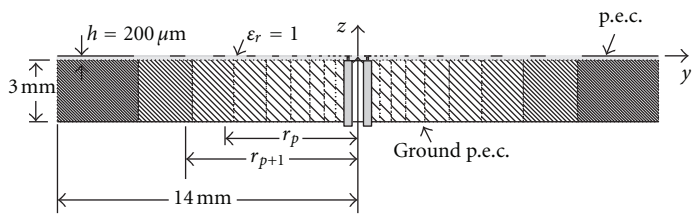

Figure 2: Sinuous antenna over a substrate comprising concentric dielectric cylinders of varying permittivity.

Table 1: Material parameters.

Shell	0 (inner)	1	2	3	4	5	6	7 (outer)
ε_r	1	1	1.3	2.3	3.8	6.5	10.9	18.36
$\tan\delta$	0.5	0.5	0.5	0.5	0.5	0.5	0.5	0.5

Figure 3 also reports the patterns for the corresponding—free space—sinuous antenna, whose gain is about 5.5 dB in circular polarization. This proposed design is generally better than the free space sinuous for what concerns polarization purity, being the cross-polar components lower, but losses introduced in the dielectric lower the gain, especially at lower frequencies, where fields fill a larger volume of dielectric. At best, at high frequencies, the gain is equal to that of the free space sinuous, since all the back lobe power is absorbed by the dielectric.

Finally, in Figure 4 the reflection coefficient of one of the four arms is presented. As it can be seen in Figure 2 the sinuous arms are fed via four via holes in the 200 μm substrate, the 3 mm thick cavity is crossed by four coaxial cables, whose inner conductor is connected to the sinuous arms, while the shields are mutually connected. A suitable modal expansion is hence enforced at the far end of the coaxial cables, beneath the ground plane, and S_{11} computed there.

The second solution presents a conical ground plane, tailored so as to be at one quarter wavelength from the active region for each frequency in the band (Figure 5), and without any losses.

To reduce the cone height a dielectric of high permittivity might be used, but for the sake of easiness of construction and low costs a Rogers RT/duroid 5880 ($\varepsilon_r = 2.2$) has been employed. Results are reported in Figure 6; curves show a gain comparable with that of the free space sinuous, but much wider 3 dB beams, thanks to the defocusing properties of the conical reflector. Cross-polar is better than that in the in free space sinuous at lower frequencies and comparable or slightly worse at higher frequencies.

Even more compact structures might be attained by resorting to a ground realized by a perfect magnetic conductor very close to the strip. This can be realized, in narrow band, by a periodic arrangement of metallic patches which realizes the metamaterials properties of a magnetic conductor. If patches' dimensions are varied akin to what is done in the first setup for permittivities then the ground can be tuned to work at the frequency at which the arm of the sinuous above is active.

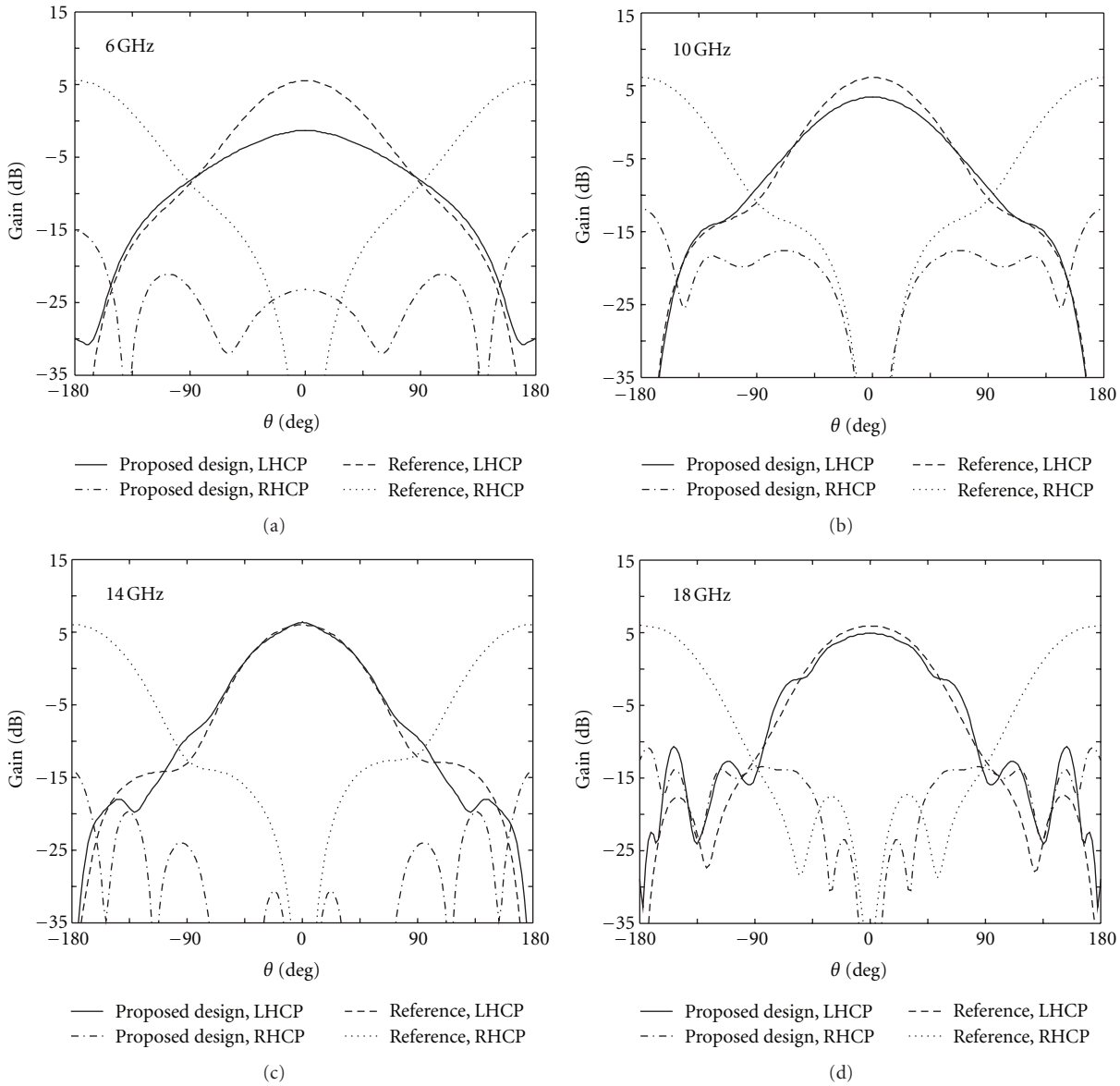

Figure 3: Simulated Gain diagrams of the structure backed with lossy concentric dielectric cylinders, at $\phi = 0$ compared to the free space sinuous.

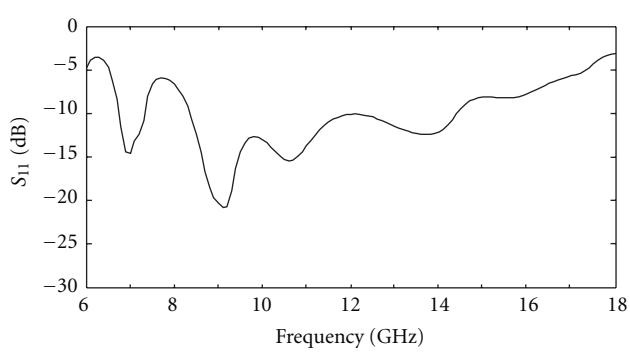

Figure 4: S_{11} at the feed port for any of the four sinuous arms.

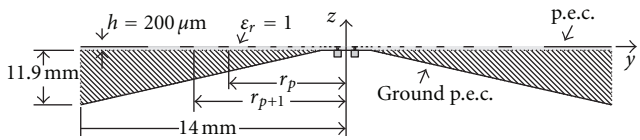

Figure 5: Sinuous antenna over a conical ground plane comprising a dielectric loading.

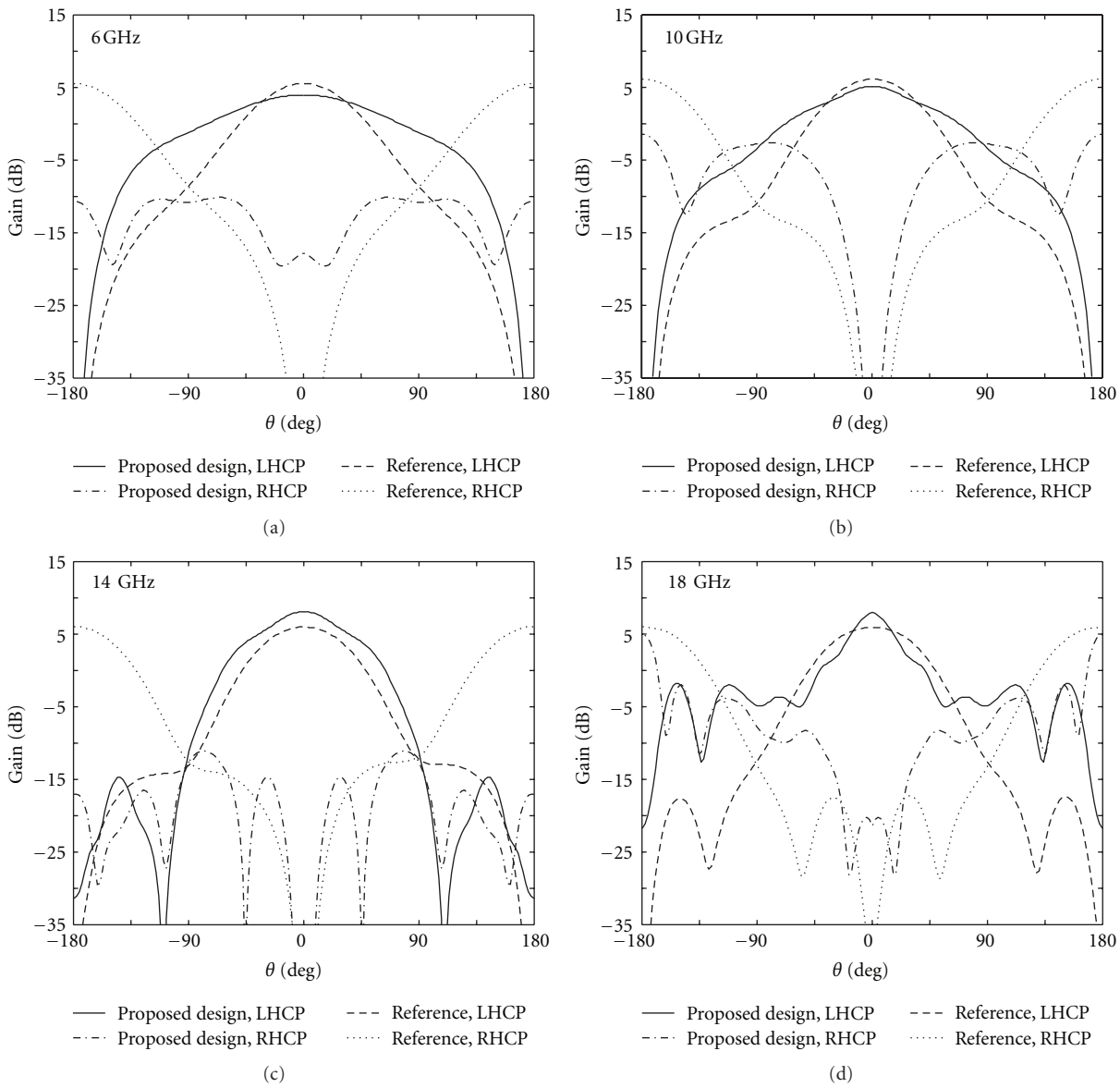

Figure 6: Simulated far-field patterns of the structure backed by a conical ground plane $\phi = 0$ compared to the free space sinuous antenna pattern.

4. Slim Slot Configuration

To overcome the aforementioned issues, nor a large lossy cavity nor an artificial metamaterials implementing a perfect magnetic conductor is necessary. Whereas radiating sources in a standard sinuous are electric currents, which does not radiate if placed in the vicinity of a ground plane, radiating sources in a slot-sinuous are the equivalent magnetic currents on the slots, hence a ground plane can be brought closer to the slots.

The presence of the ground plane close to the slots ideally will increase the current amplitude by a factor of two. Consequently the radiated electric field and maximum gain are expected to grow at most of 6 dB with respect

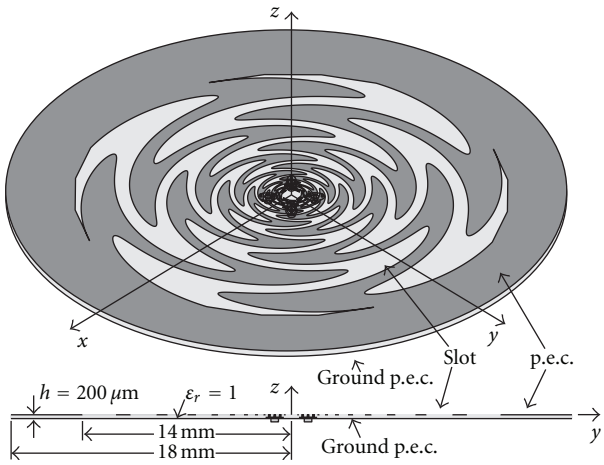

Figure 7: 3D model of the analysed slot-sinuous structure and dimensions.

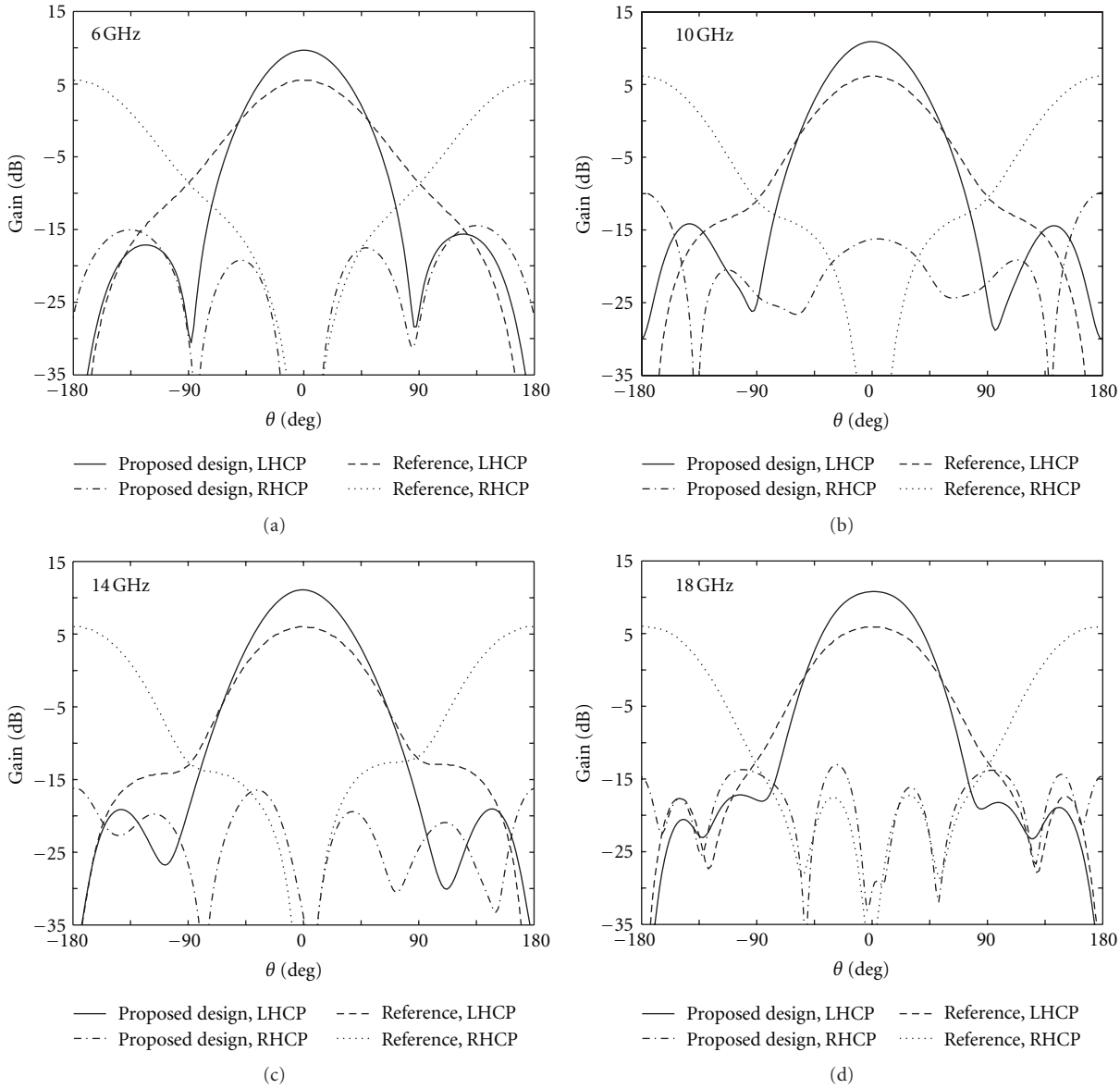

Figure 8: Simulated far-field patterns of the proposed slot structure at $\phi = 0$, compared to the free space sinuous antenna pattern.

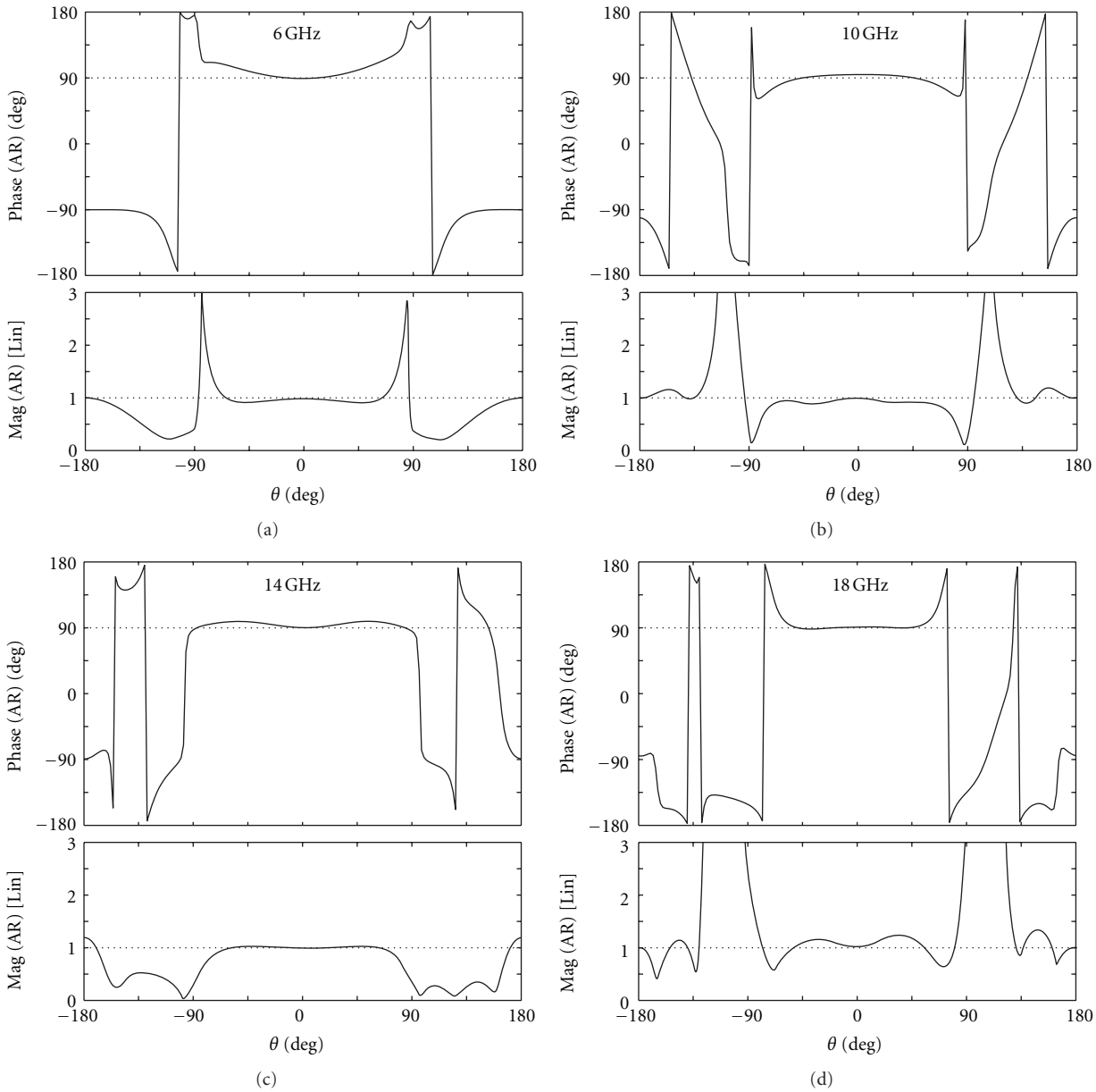

Figure 9: Axial ratio (AR) and phase between the two orthogonal components for the proposed slot structure.

to the standard sinuous antenna in free space, whose gain is about 5.5 dB in circular polarization. The slot-sinuous presented here, thanks to the ground plane, should hence present a maximum peak gain of about 11.5 dB.

In general, placing the ground plane at less than $\lambda/4$ at the highest frequency leads to a constructive sum of direct and reflected radiation in the upper space.

In this paper the ground plane to slot plane distance h is varied from 200 μm to 1 mm to show the effect of the ground on the antenna parameters. Such distances are about 83 to 16 times smaller than the smallest wavelength in free space ($\approx$16.7 mm @ 18 GHz). A dielectric of $\varepsilon_r = 1$ is chosen. Other relevant geometrical parameters are inserted in Figure 7.

In Figure 8 the gain of the proposed structure for the ground to slot distance $h = 200\,\mu$m is plotted for four representative frequencies in the range 6–18 GHz, both for LHCP (copolar) and RHCP (cross-polar). Cuts are presented on the $\phi = 0$ plane for the sake of brevity, as antenna symmetry leads to substantially equal results on the orthogonal ($\phi = 90^\circ$) and any other plane. Similar results are obtained for $h = 600\,\mu$m and $h = 1$ mm, again not presented here for brevity. To better compare the proposed structure to the standard one, Figure 8 presents also the gain for the free space, not ground backed, sinuous slot structure. This better gain and extreme thinness is in a trade-off with the antenna reflection coefficient, which is slightly worse than in the previous cases.

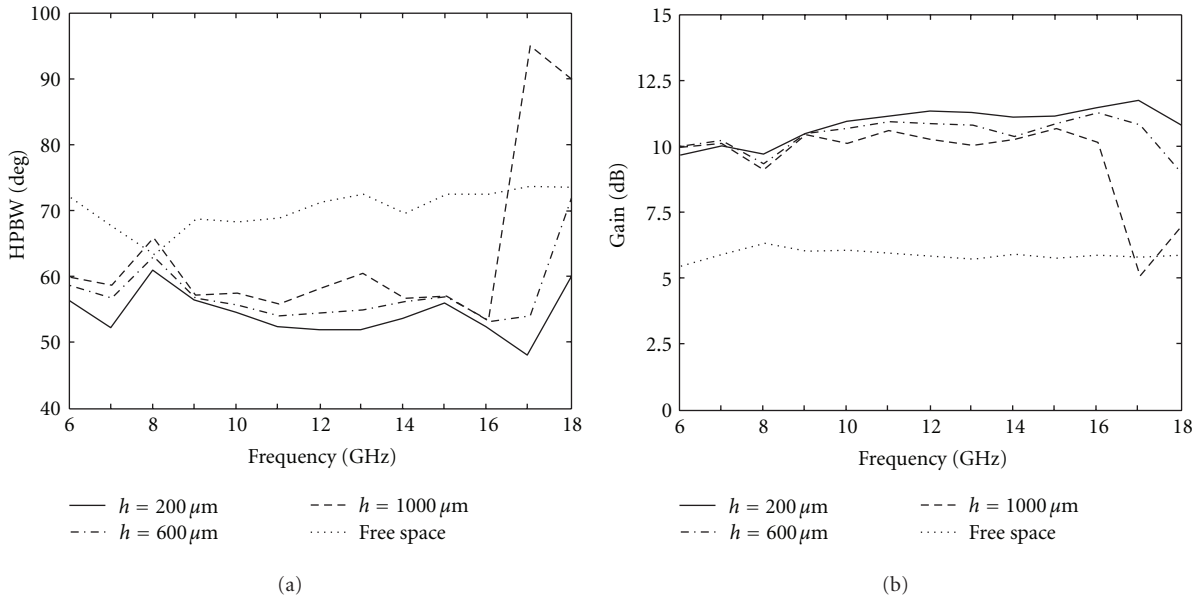

Figure 10: HPBW and maximum gain in the frequency band of the proposed slot structure for three different distances h, compared to the free space standard one.

To evaluate the circular polarization purity, the axial ratio (AR) and the phase between the two orthogonal electric field components E_θ and E_ϕ are shown, at the same four frequencies, in Figure 9. The phase of $-90°$ observed for back radiation indicates a reversal of polarization for back radiation. Anyway, the front to back ratio is less than -20 dB for this design. Both the axial ratio and the phase clearly indicate the transition from linear polarization (AR = 0, or AR = ∞ and phase = 0 or $\pm 180°$) to circular polarization (AR = 1 and phase = $\pm 90°$).

The presented structure shows a mean gain around 11 dB and a HPBW around 50–60 deg. Modifying the ground plane distance from the slot aperture, a limited control on the HPBW can be obtained as Figure 10 shows. The high variation visible around 17-18 GHz for the highest h value is due to some direct radiation from the feeding pins, which are designed similar to those in [18, 19].

Finally Figure 11 shows a comparison between the peak realized gain of the three structures. The best being the slot configuration, followed by the strip sinuous with conical ground, where no losses are present but the conical reflector causes a widening of the beam. The worse being of course the strip sinuous backed by the lossy dielectrics.

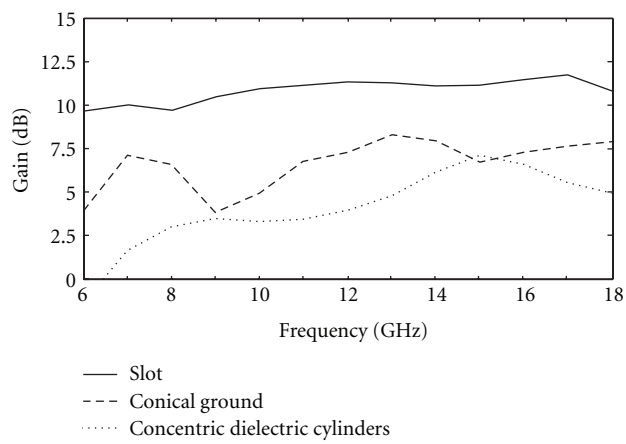

Figure 11: Maximum gain as a function of frequency for the slot-sinuous with 200 μm substrate compared with the maximum gains attained by the strip sinuous with conical ground, and the strip sinuous with concentric cylinders of varying permittivities in the backing cavity.

5. Conclusion

In this paper three broadband low-profile cavity-backed sinuous antennas have been presented. The two cavity backed configurations present an overall diameter of 28 mm and a thickness of 3 mm or 12 mm; the slot configuration has an overall diameter of 36 mm and a smaller thickness, all configurations working from 6 to 18 GHz. The attained nominal gain of the best configuration, the slot one, is greater than 10 dB and excellent circular polarization properties are shown. Full wave analysis was carried out exploiting FEM. Structures with greater radius can allow for lower operational frequencies and hence larger bandwidths. Furthermore, a limited control on some antenna parameters (HPBW) has been shown to be possible by varying the ground distance.

References

[1] Z. N. Chen and M. Y. W. Chia, *Broadband Planar Antennas—Design and Applications*, John Wiley & Sons, Hoboken, NJ, USA, 2006.

[2] M. N. Afsar, Y. Wang, and R. Cheung, "Analysis and measurement of a broadband spiral antenna," *IEEE Antennas and Propagation Magazine*, vol. 46, no. 1, pp. 59–64, 2004.

[3] X. M. Wang, L. Zhang, J. P. Xiong, and Y. C. Jiao, "Printed microstrip-line-fed elliptical slot antenna with very wide bandwidth," *Journal of Electromagnetic Waves and Applications*, vol. 22, no. 14-15, pp. 1865–1871, 2008.

[4] T. Hong, S. X. Gong, W. Jiang, Y. X. Xu, and X. Wang, "A novel ultra-wide band antenna with reduced radar cross section," *Progress in Electromagnetics Research*, vol. 96, pp. 299–308, 2009.

[5] D. Chen and C. H. Cheng, "A novel compact ultra-wideband (UWB) wide slot antenna with via holes," *Progress in Electromagnetics Research*, vol. 94, pp. 343–349, 2009.

[6] A. A. Lotfi Neyestanak, "Ultra wideband rose leaf microstrip patch antenna," *Progress in Electromagnetics Research*, vol. 86, pp. 155–168, 2008.

[7] A. Mehdipour, K. Mohammadpour-Aghdam, and R. Faraji-Dana, "Complete dispersion analysis of vivaldi antenna for ultra wideband applications," *Progress in Electromagnetics Research*, vol. 77, pp. 85–96, 2007.

[8] A. A. Eldek, A. Z. Elsherbeni, and C. E. Smith, "Rectangular slot antenna with patch stub for ultra wideband applications and phased array systems," *Progress In Electromagnetics Research*, vol. 53, pp. 227–237, 2005.

[9] G. Cappelletti, D. Caratelli, R. Cicchetti, and M. Simeoni, "A low-profile printed drop-shaped dipole antenna for wideband wireless applications," *IEEE Transactions on Antennas and Propagation*, vol. 59, no. 10, pp. 3526–3535, 2011.

[10] J. Y. Sze, T. H. Hu, and T. J. Chen, "Compact dual-band annular-ring slot antenna with meandered grounded strip," *Progress in Electromagnetics Research*, vol. 95, pp. 299–308, 2009.

[11] T. A. Milligan, "Frequency-independent antennas," in *Modern Antenna Design*, pp. 521–571, IEEE Press, John Wiley & Sons, Hoboken, NJ, USA, 2nd edition, 2005.

[12] Q. Liu, C. L. Ruan, L. Peng, and W. X. Wu, "A novel compact archimedean spiral antenna with gap-loading," *Progress in Electromagnetics Research Letters*, vol. 3, pp. 169–177, 2008.

[13] R. H. DuHamel, "Dual polarized sinuous antenna," US Patent 4658262, 1987.

[14] J. P. Scherer, "The dual polarized sinuous antenna," *Journal of Electronic Defense*, vol. 13, no. 8, pp. 73–75, 1990.

[15] T. Chu and H. G. Oltman Jr., "The sinuous antenna," *Microwave Systems News and Communications Technology*, vol. 18, pp. 40–48, 1988.

[16] Y. Yan and Q. Cao, "Microwave absorbing properties of sinuous antenna filled with absorbing material," in *Proceedings of the IEEE International Conference on Ultra-Wideband (ICUWB'10)*, vol. 1, pp. 1–4, September 2010.

[17] S. Palreddy, A. I. Zaghloul, and R. Cheung, "An optimized lossy back cavity loaded four arm sinuous antenna," in *Proceedings of the IEEE Antennas and Propagation Society International Symposium (APSURSI)*, pp. 1–4, Toronto, Canada, July 2010.

[18] M. C. Buck, J. Burford, and D. S. Filipović, "Multiband two arm slot sinuous antenna," in *Proceedings of the IEEE Antennas and Propagation Society Symposium*, pp. 165–168, June 2004.

[19] M. C. Buck and D. S. Filipović, "Split-beam mode four-arm slot sinuous antenna," *IEEE Antennas and Wireless Propagation Letters*, vol. 3, no. 1, pp. 83–86, 2004.

[20] E. Agastra, "A high gain slot Sinuous antenna," *Atti della Fondazione Giorgio Ronchi*, vol. 66, no. 5, pp. 635–639, 2011.

[21] L-3 Communications, Randtron Antenna Systems, http://www.l-3com.com/randtron/dcpantenna.htm.

Hindawi Publishing Corporation
International Journal of Antennas and Propagation
Volume 2012, Article ID 602780, 6 pages
doi:10.1155/2012/602780

Research Article

Compact, Frequency Reconfigurable, Printed Monopole Antenna

Ricardo Gonçalves,[1,2] Pedro Pinho,[1,2] and Nuno B. Carvalho[1,3]

[1] *Instituto de Telecomunicações – Aveiro, Campus Universitário de Santiago, 3810-193 Aveiro, Portugal*
[2] *Área Departamental de Engenharia Electrónica, Telecomunicações e Computadores, Instituto Superior de Engenharia de Lisboa, Rua Conselheiro Emídio Navarro 1, 1959-007 Lisboa, Portugal*
[3] *Departamento de Electrónica, Telecomunicações e Informática, Universidade de Aveiro, 3810-193 Aveiro, Portugal*

Correspondence should be addressed to Ricardo Gonçalves, rgoncalves@av.it.pt

Received 23 July 2012; Revised 29 September 2012; Accepted 19 October 2012

Academic Editor: Renato Cicchetti

This paper proposes a possible implementation of a compact printed monopole antenna, useful to operate in UMTS and WLAN bands. In order to accomplish that, a miniaturization technique based on the application of chip inductors is used in conjunction with frequency reconfiguration capability. The chip inductors change the impedance response of the monopole, allowing to reduce the resonant frequency. In order to be able to operate the antenna in these two different frequencies, an antenna reconfiguration technique based on PIN diodes is applied. This procedure allows the change of the active form of the antenna leading to a shift in the resonant frequency. The prototype measurements show good agreement with the simulation results.

1. Introduction

Antenna miniaturization is the result of the continuous search for smaller and compact electronic equipment that can present the same or even better performance.

There are many examples of techniques used for antenna miniaturization for different applications. For printed antennas, an approach is presented in [1], where a metamaterial is used between the radiating element and the ground plane of a printed circular patch, in order to reduce its resonant frequency. Another example is presented in [2], where a Koch fractal printed monopole is used to resonate at 2.5 GHz, granting a 21% reduction in size. In [3, 4], chip inductors are used in order to reduce the resonant frequency of printed C-monopoles, without changing the size and radiation characteristics and with minor losses to the radiating efficiency and gain. This is an interesting approach, since it is quite simple to fabricate, and it is not expensive. However it leads to narrower bandwidths.

Due to the growth of the wireless technologies and the appearance of new systems associated to communication devices, the development of interoperable devices is of great interest, and since the antennas are indispensable to wireless communication equipments, there is a great scientific interest for antennas capable of working in different frequency bands.

To achieve this goal, multiband and UWB antennas have been proposed in literature [5]. Besides these types, another possible class of radiant structures consists of the so-called reconfigurable antennas.

Reconfigurable antennas have the ability to change one or more of its radiation characteristics in real time, such as the resonant frequency, the bandwidth, the radiation pattern, or even the polarization [6]. There are different ways to achieve these changes, and different techniques have been presented, but all those techniques are based on suitable modifications of the size or shape of the antenna in order to obtain specific radiation performances.

Reference [7] shows a possibility of creating reconfigurability, using a set of printed antennas on a circular area, which is changed using a motor and thus allows the change of the resonant frequency of the structure. This solution is not very feasible because it requires the design of several printed antennas very close to each other that end up suffering from coupling and subsequently distort the radiation pattern. Besides requiring assembly and operation of an engine, this makes the structure larger and heavier.

Another solution, smaller and more adaptable, is presented in [8–10], where MEMS (Microelectromechanical Switches), which can be activated or deactivated with a low voltage source, are employed to connect and disconnect specific elements of the antenna, so changing the overall antenna size and shape resulting in an effective change in the resonant frequency. This is a very attractive solution, given the characteristics of the MEMS; however, these are hard to fabricate and so this can be quite an expensive solution.

PIN diodes are usually inexpensive and exist in abundance on the market in various packages and configurations, which make them a versatile alternative for the implementation of reconfigurability in antennas. Nevertheless, there are few applications of PIN diodes adopted to achieve frequency reconfigurable printed antennas intended for mobile devices [11–13].

An approach to printed antenna's polarization reconfigurability is presented in [14]. Other example is presented in [15], in which, an array of antennas for a MIMO system achieve frequency reconfigurability by using PIN diodes, allowing to change the operating frequency of the antenna. Some examples on the use of PIN diodes for frequency reconfigurability in WLAN applications are presented in [16, 17].

The aim of this paper is to present a compact reconfigurable monopole antenna suitable to operate in the WLAN (2.4 GHz) and UMTS (2.0 GHz) bands using chip inductors and PIN diodes. A particular emphasis is given to the miniaturization process whose details are reported in the next section. So far, to the authors' knowledge, there are no examples published in the scientific literature adopting the mentioned devices for the proposed wireless applications.

2. Simulation Models

The antenna proposed in this paper is designed with two lumped components inserted in a printed monopole, in order to make it small and to allow the change in resonant frequency. To miniaturize the antenna structure, a chip inductor from Coilcraft was used. According to [3, 18], this element can be modeled with a series equivalent circuit composed of a series resistance R and an inductor L, whose values depend on the frequency (see Figure 1).

Based on the expressions that describe the previous plot presented in [3] and the values presented in the inductor datasheet [18], the equivalent impedance and inductance can be calculated for the lower frequency which is where the inductor has more influence. At 2.0 GHz, this chip inductor can be modeled by an equivalent resistance (R) of 1.7 Ω and inductance (L) of 8.2 nH.

The PIN diode used to switch the elements of the antenna is a commercial device from Avago Technologies [19]. According to [20], in forward bias the PIN diode has an equivalent circuit corresponding to an inductor in series with a resistor, while in reverse bias it results equivalent to an inductor in series with a parallel resistor and a capacitor.

The equivalent resistance of the diode decreases as the bias current increases. According to [21], the resistance has a minimum value of about 3 Ω for bias currents above 10 mA, and it exceeds 1 kΩ for bias currents near zero (0.01 mA). The capacitance depends upon the reverse voltage and frequency; however, its value shows small variations from 0.2 pF, for frequencies above 1 GHz. These are the values considered in the numerical simulation.

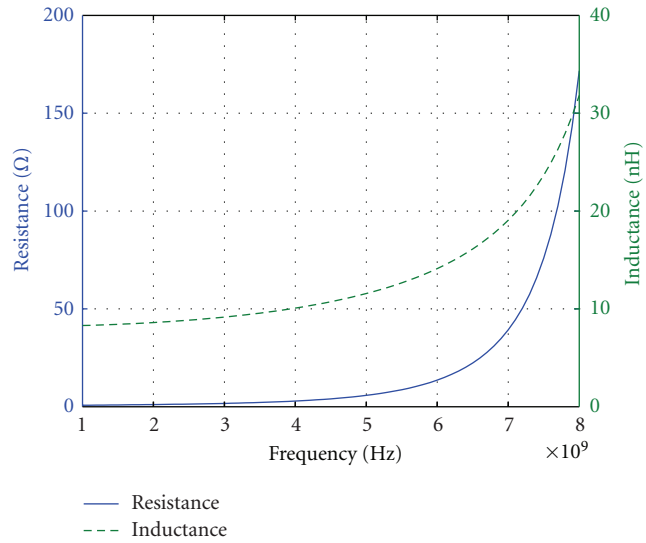

Figure 1: Chip inductor's equivalent circuit elements versus frequency.

Table 1: Proposed antenna dimensions.

Parameter	Dimension (mm)
L_1, L_2, L_3, L_4	24, 3.35, 6.0, 4.0
L_5, L_6, L_I, L_{gnd}, L_{sub}	13.6, 5.0, 1.0, 21, 28.5
W_0, W_1, W_2	3.3, 1.5, 1.5
W_{sub}, gap_I, gap_D	20, 0.5, 2.0

3. Antenna Design

The antenna proposed in this paper is a C-monopole antenna, printed upon an Arlon CuClad 217 substrate, with a relative permittivity (ε_r) of 2.17, a loss tangent ($\tan\delta$) of 0.0009 and 0.787 mm height. The antenna geometry is presented in Figure 2, while the corresponding dimensions are presented in Table 1.

The monopole and a feeding microstrip line, which also matches the input impedance of the antenna to 50 Ω, are printed in the top face of the substrate and the ground plane is at the bottom face. The inductor is placed in the central arm of the monopole, while the diode is placed in the top arm as shown in Figure 2.

The area of the antenna is $20 \times 7.5\,\text{mm}^2$, and the total area of the antenna plus the feeding line is $20 \times 28.5\,\text{mm}^2$. The total length of the monopole, considering the diode in forward bias, is 20.95 mm, which would correspond to a resonant frequency of 3.596 GHz, while the total length considering the diode in reverse bias is of 9.85 mm, which would correspond to a resonant frequency of about 7.61 GHz. However, due to the introduction of the chip inductor and

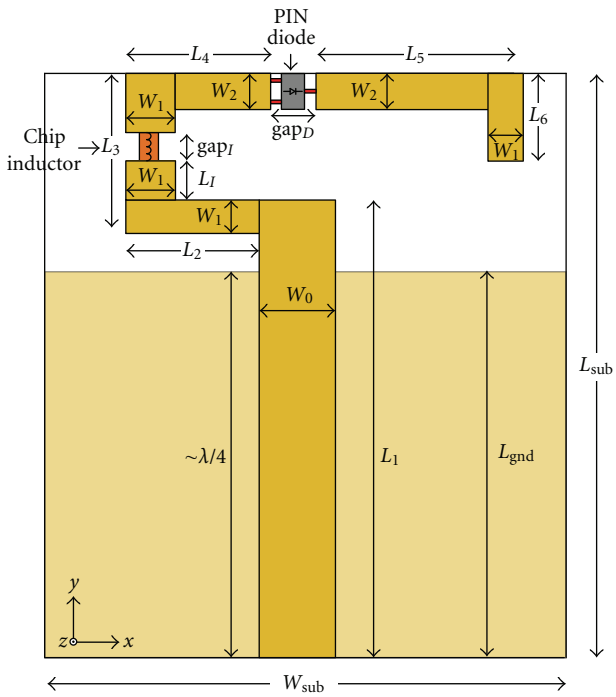

Figure 2: Proposed antenna geometry.

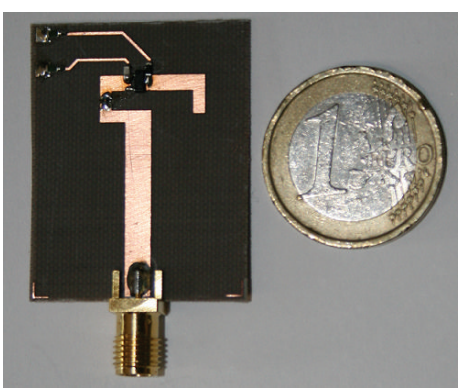

Figure 3: Prototype of the proposed antenna.

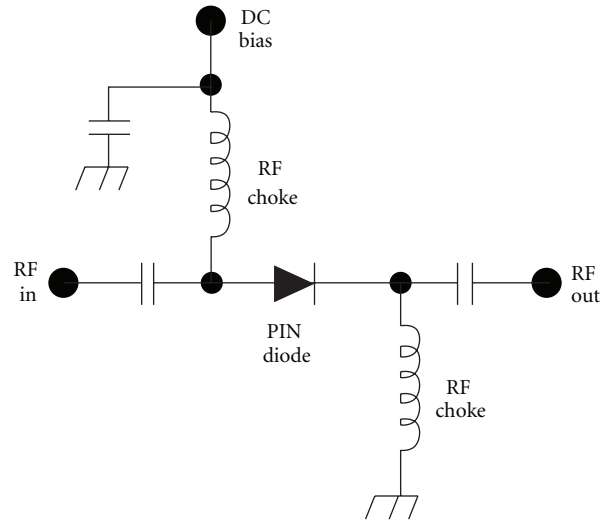

Figure 4: SPST circuit using a PIN diode.

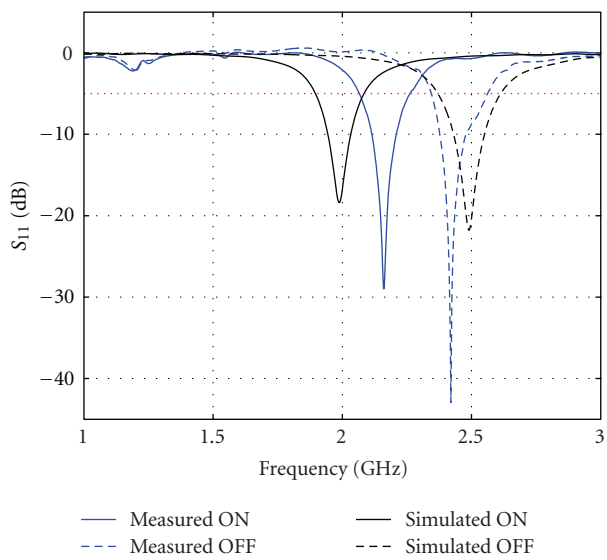

Figure 5: Simulated (black) and measured (blue) return loss for the PIN diode in "ON" (solid) and "OFF" (dashed) state.

the PIN diode, the resonant frequency in both antenna configurations turns to be smaller, resulting in a reduced volume occupation.

The prototyped antenna is slightly wider than the simulated model due to the introduction of the diode polarization circuit, as can be seen in Figure 3.

The polarization circuit of the PIN diode is a simple SPST (Single Pole Single Throw) switch configuration, as shown in Figure 4. The RF choke inductors are used to isolate the DC voltage source from the RF signal.

4. Simulation Results

For simulation purposes CST Microwave Studio 2011 [21] was used.

4.1. Return Loss. Figure 5 shows the simulated and measured return loss (S_{11}) for the proposed monopole antenna, considering the diode in both states of conduction.

The impedance matching is done with a $\lambda/4$ microstrip line, which is designed for the highest frequency of operation, resulting in a higher return loss for the lowest operation band. This line was adjusted based on the numerical simulation so that both frequencies could present satisfactory result.

The definition of a small antenna is presented in [22], according to which, an antenna is considered small if $ka < 0.5$, where k is the free-space wavenumber and a is the radius of the smallest sphere which encloses the antenna. The ka factor for the proposed antenna is 0.49 at the lowest working frequency, which means that this is a small antenna; in that

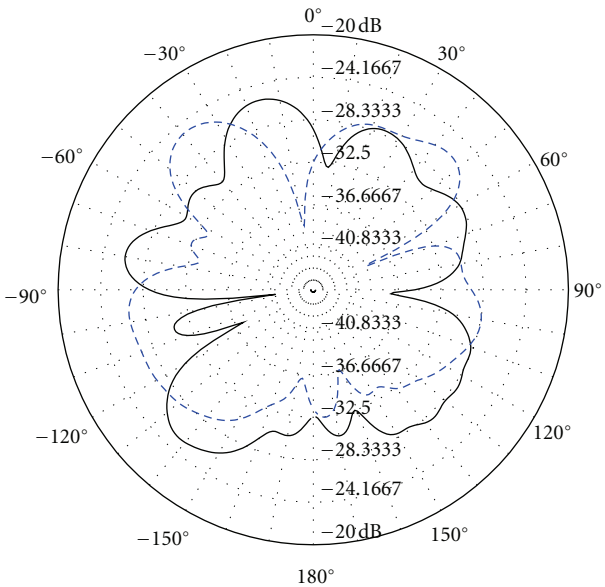

Figure 6: Measured radiation pattern at 2.2 GHz on XZ plane (blue) and YZ plane (black).

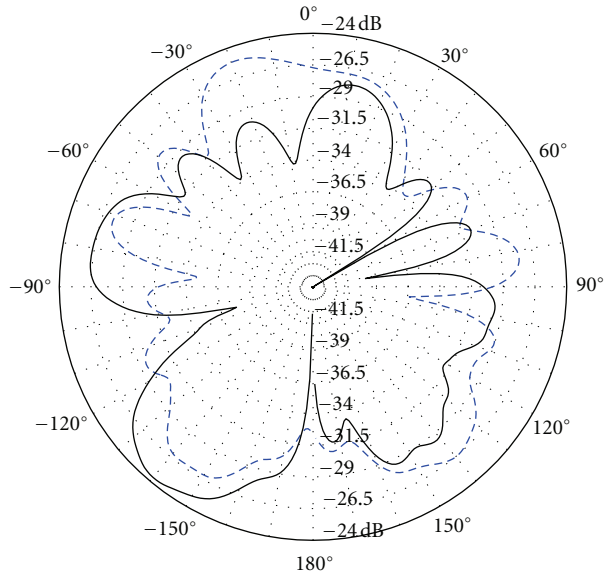

Figure 7: Measured radiation pattern at 2.4 GHz on XZ plane (blue) and YZ plane (black).

sense, the bandwidth of the antenna was considered for $S_{11} < -5$ dB.

The diode is controlled with a voltage source; the "OFF" state is the default with no power source, while the "ON" state is obtained with 3 V and 35 mA.

The simulated results present a bandwidth from 1.93 to 2.17 GHz when the diode is "ON", and from 2.4 to 2.6 GHz when the diode is "OFF". This means that it can nearly support UMTS bands, since these are located between 1.92 to 2.17 GHz. In addition, it can support WLAN service since this band is defined between 2.4 to 2.5 GHz. The measured results present a difference to the simulated numerical results. In particular, the "OFF" band is fairly good, from 2.39 to 2.55 GHz, while the "ON" band is shifted, falling above the UMTS band.

4.2. Radiation Pattern. The measured radiation pattern for the realized prototype is presented in Figures 6 and 7, for the XZ and YZ planes (see Figure 2). The connections to the polarization circuit were present inside the anechoic chamber during the measurements, which is one source of the large number of lobes in the obtained pattern.

The gain is rather small, presenting values around 0.65 dB at 2.4 GHz, and 0.05 dB for the lower frequency. These values are slightly lower when compared to a normal printed monopole; however they do not represent such a great loss. The radiation efficiency is around 77.5% at 2.0 GHz, and 80.3% at 2.4 GHz. These are fairly good values, taken into consideration the small dimensions of the antenna and the presence of the PIN diode and chip inductor.

The measured polarization was linear for the highest frequency, and elliptical for the lowest frequency.

4.3. Lumped Element Effects. The measurements performed on the realized antenna prototype shows some deviations

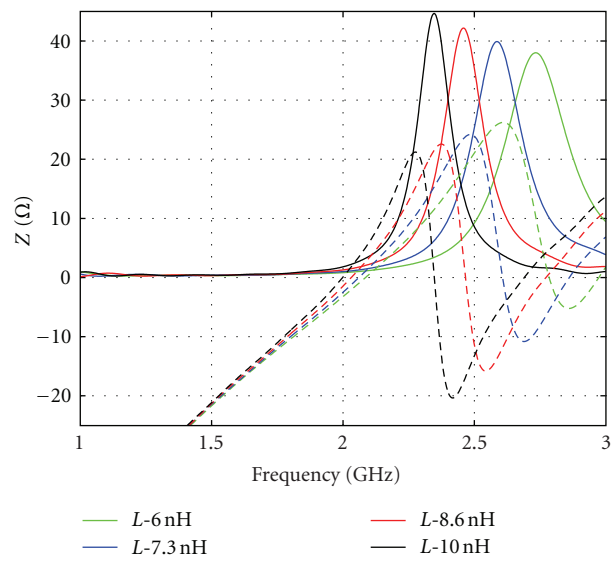

Figure 8: Frequency behavior of the real (solid lines) and imaginary (dashed lines) part of the antenna input impedance versus the inductance values of the chip inductor.

with respect to the performances predicted by the numerical simulation. However, this phenomenon is expected given the variations that can occur in the antenna behavior due to the PIN diode parasitic elements and to the dispersion of the inductor parameters.

Figure 8 shows the real and imaginary part of the antenna input impedance with respect to the chip inductor characteristics.

It is clear that for higher inductance values, the resonant frequency of the antenna is lower. Moreover, the bandwidth is also narrower.

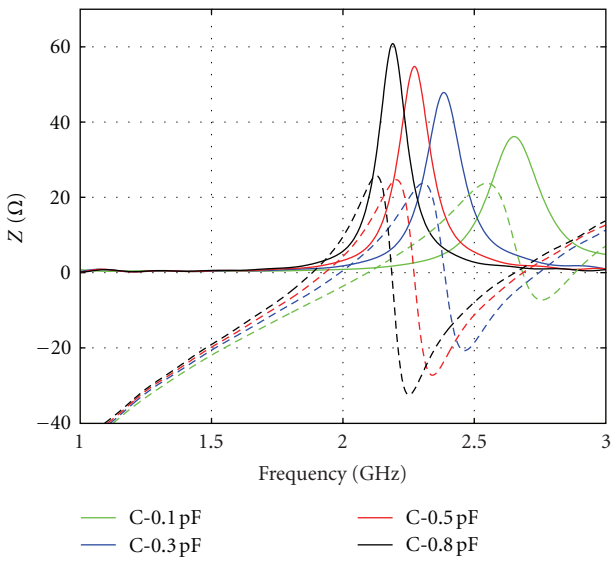

Figure 9: Frequency behavior of the real (solid lines) and imaginary (dashed lines) part of the antenna input impedance versus the PIN diode capacitance values.

Besides the inductor value, the diode capacitance also shows a large influence over the resonant frequency and bandwidth. Figure 9 shows the real and imaginary part of the antenna input impedance response as the capacitance value of the PIN diode increases.

The increased capacitance leads to a resonant frequency reduction and narrower bandwidth. Moreover, the effect of the capacitance on the impedance may lead to considerable mismatches, due to the increased value observed.

Besides the variations presented so far, the fact that the components are soldered to the radiating element of the antenna and also the diode polarization circuit, which may not present a perfect DC and RF signal isolation, might be possible causes for the antenna detuning.

5. Conclusion

In this paper a very small printed monopole antenna with frequency reconfiguration capability was presented, which uses PIN diodes as a key design strategy. It was shown that it is possible to use PIN diodes in conjunction with chip inductors, in order to obtain a very small antenna that can work in two different frequency bands. However, this results in a reduction of the gain and of the bandwidth of the considered antenna.

The design and sizing of this type of antenna are rather complex and all the parasitic characteristics of the different components must be known and taken into account, to make the best possible modeling of it. However this is not always possible. Little variations in the diode capacitance and inductance can change both of the resonant frequencies. Nevertheless, good agreements between the simulated and measured results were obtained, with a seemingly omnidirectional radiation pattern.

Acknowledgments

The authors acknowledge the Portuguese FCT/MCTES for financing the project PTDC/EEA-TEL/122681/2010—PROENERGY-WSN—Prototypes for Efficient Energy Self-Sustainable Wireless Sensor Networks.

References

[1] R. O. Ouedraogo, E. J. Rothwell, A. R. Diaz, K. Fuchi, and A. Temme, "Miniaturization of patch antennas using a metamaterial-inspired technique," *IEEE Transactions on Antennas and Propagation*, vol. 60, no. 5, pp. 2175–2182, 2012.

[2] S. S. Gaikwad, M. Singh, A. Ajey, and S. S. Karthikayen, "Size miniaturized fractal antenna for 2. 5 GHz application," in *Proceedings of the IEEE Students Conference on Electrical, Electronics and Computer Science*, Bhopal, India, 2012.

[3] Q. Luo, J. R. Pereira, and H. M. Salgado, "Compact printed monopole antenna with chip inductor for WLAN," *IEEE Antennas and Wireless Propagation Letters*, vol. 10, pp. 880–883, 2011.

[4] Q. Luo, H. M. Salgado, and J. R. Pereira, "Compact printed monopole antenna array for dualband WLAN application," in *Proceedings of the International Conference on Computer as a Tool (EUROCON '11)*, pp. 1–4, Lisbon, Portugal, April 2011.

[5] G. Cappelletti, D. Caratelli, R. Ciccetti, and M. Simeoni, "A low-profile printed drop-shaped dipole antenna for wideband wireless applications," *IEEE Transactions on Antennas and Propagation*, vol. 59, no. 10, pp. 3526–3535, 2011.

[6] J. L. Volakis, *Antenna Engineering Handbook*, McGraw-Hill, 4th edition, 2007.

[7] Y. Tawk, J. Costantine, and C. G. Christodoulou, "A rotatable reconfigurable antenna for cognitive radio applications," in *Proceedings of the IEEE Radio and Wireless Symposium (RWS '11)*, pp. 158–161, Phoenix, Ariz, USA, January 2011.

[8] M. Unlu, Y. Damgaci, H. S. Mopidevi, O. Kaynar, and B. A. Cetiner, "Reconfigurable, tri-band RF MEMS PIFA antenna," in *Proceedings of the IEEE International Symposium on Antennas and Propagation (APS '11)*, Spokane, Wash, USA, 2011.

[9] N. Haridas, A. T. Erdogan, T. Arslan et al., "Reconfigurable MEMS antennas," in *Proceedings of the NASA/ESA Conference on Adaptive Hardware and Systems (AHS '08)*, pp. 147–154, June 2008.

[10] R. Valkonen, C. Luxey, J. Holopainen, C. Icheln, and P. Vainikainen, "Frequency-reconfigurable mobile terminal antenna with MEMS switches," in *Proceedings of the 4th European Conference on Antennas and Propagation (EuCAP '10)*, Barcelona, Spain, April 2010.

[11] Y. K. Park and Y. Sung, "A reconfigurable antenna for quadband mobile handset applications," *IEEE Transactions on Antennas and Propagation*, vol. 60, no. 6, pp. 3003–3006, 2012.

[12] M. I. Lai, T. Y. Wu, J. C. Hsieh, C. H. Wang, and S. K. Jeng, "Design of reconfigurable antennas based on an L-shaped slot and PIN diodes for compact wireless devices," *IET Microwaves, Antennas and Propagation*, vol. 3, no. 1, pp. 47–54, 2009.

[13] M. Komulainen, M. Berg, V. K. Palukuru, H. Jantunen, and E. Salonen, "Frequency-reconfigurable dual-band monopole antenna for mobile handsets," in *Proceedings of the IEEE Antennas and Propagation Society International Symposium (AP-S '07)*, pp. 3289–3292, Honolulu, Hawaii, USA, June 2007.

[14] M. S. Nishamol, V. P. Sarin, D. Tony, C. K. Aanandan, P. Mohanan, and K. Vasudevan, "An electronically

reconfigurable microstrip antenna with switchable slots for polarization diversity," *IEEE Transactions on Antennas and Propagation*, vol. 59, no. 9, pp. 3424–3427, 2011.

[15] A. Ghasemi, N. Ghavehchian, A. Mallahzadeh, and S. Sheikholvaezin, "A reconfigurable printed monopole for MIMO application," in *Proceedings of the 6th European Conference on Antenas and Propagation (EUCAP '12)*, Prague, Czech Republic, 2012.

[16] D. E. Anagnostou and A. A. Gheethan, "A coplanar reconfigurable folded slot antenna without bias network for WLAN applications," *IEEE Antennas and Wireless Propagation Letters*, vol. 8, pp. 1057–1060, 2009.

[17] A. Ramadan, M. Al-Husseini, Y. Tawk, K. Y. Kabalan, and A. El-Hajj, "A novel frequency/pattern-reconfigurable microstrip antenna for WLAN applications," in *Proceedings of the 4th European Conference on Antennas and Propagation (EuCAP '10)*, Barcelona, Spain, April 2010.

[18] "Coilcraft," SPICE Model for Coilcraft 0402HP, http://www.coilcraft.com/pdf_viewer/showpdf.cfm?f=pdf_store:spice_0402hp.pdf.

[19] Avago Technologies, http://www.avagotech.com/pages/home/.

[20] W. E. Doherty Jr. and R. D. Joos, *The Pin Diode Circuit Designer's Handbook*, Microsemi Corporationc, 1st edition, 1998.

[21] "Avago Technologies," DATASHEET HSMP-386x, http://www.avagotech.com/docs/AV02-0293EN.

[22] R. C. Hansen, "Fundamental limitations in antennas," *Proceedings of the IEEE*, vol. 69, no. 2, pp. 170–182, 1981.

Hindawi Publishing Corporation
International Journal of Antennas and Propagation
Volume 2012, Article ID 427841, 6 pages
doi:10.1155/2012/427841

Research Article

Parasitic-Element-Loaded UWB Antenna with Band-Stop Function for Mobile Handset Wireless USB

Yohan Lim,[1] Young Joong Yoon,[1] and Byungwoon Jung[2]

[1] *Department of Electric and Electronic Engineering, Yonsei University, Seoul 120-749, Republic of Korea*
[2] *MC R&D Campus B, 60-39, LG Electronics, Seoul 153-801, Republic of Korea*

Correspondence should be addressed to Young Joong Yoon, yjyoon@yonsei.ac.kr

Received 7 August 2012; Revised 5 October 2012; Accepted 6 October 2012

Academic Editor: Renato Cicchetti

A UWB antenna loaded by parasitic elements for wireless USB of mobile handsets is proposed for UWB service in which a band-stop function of 5.725–5.825 GHz WLAN band is required. Two kinds of parasitic elements are incorporated into a rectangular radiator to obtain enhanced impedance bandwidth and band-stop function. The proposed antenna is very compact in size. Wide bandwidths of 3.15–4.75 GHz and 7.2–10.2 GHz are achieved while 5.725–5.825 GHz is notched. Three different shapes of conventional mobile terminals are also considered for measurement.

1. Introduction

Ultra-wideband (UWB) antenna technology has been one of the most fascinating design areas in indoor communications, and it has been used with a variety of antennas [1–10]. It has the merits of high-speed transmission rate, low power consumption, and simple hardware configuration over conventional wireless communication systems. The main challenge for UWB antennas is to maintain high performance over a large bandwidth while having small dimensions. Another design concern is that a UWB antenna can allow a potential interference with a wireless local area network (WLAN) [11–13]. Recently, there have been attempts to include UWB systems in USB dongles [14–17]. However, previous UWB antennas for wireless USB devices are too large to be inserted into the terminals of mobile handsets, and interference with the WLAN was not considered in these designs.

In this paper, a UWB antenna for wireless USB for mobile handsets is proposed that has both small size and a band-stop function at the upper WLAN band of 5.725–5.825 GHz. Two parasitic elements are used to achieve wideband characteristics and the band-stop function. A tapered and folded feed line is also used to obtain an enhanced impedance matching characteristic [18]. All simulations in this work were carried out using CST Microwave Studio. A design example of the proposed antenna is demonstrated.

2. Antenna Structure

The three dimensional configuration of the proposed antenna with its planar figure is shown in Figure 1. A rectangular radiator and parasitic elements are fabricated on the FR4 substrate with a dielectric constant of 4.5 and a height of 1 mm and mounted in the top left-hand corner of a mobile handset board. The optimum design parameters are: AW = 6.4 mm, AL = 6 mm, SL = 4.95 mm, GW = 8 mm, GL = 2.5 mm, BW = 2.6 mm, FL = 7 mm, and FW = 1.5 mm. The size of the radiator is 6.4 mm × 6 mm × 3 mm, and the antenna clearance is 14.4 mm × 16 mm. It has not only very compact size, but also low profile. The PCB size is 35 mm × 80 mm × 1 mm, which is typical for mobile handsets. The proposed antenna is composed of a rectangular radiator, a folded and tapered feed line, a parasitic element (1) on each side of the folded feed line, and a parasitic element (2) on each side of the rectangular radiator. The rectangular radiator has similar characteristics to general planar monopoles [4]. The parasitic elements (1) and (2) are connected to each other, and each

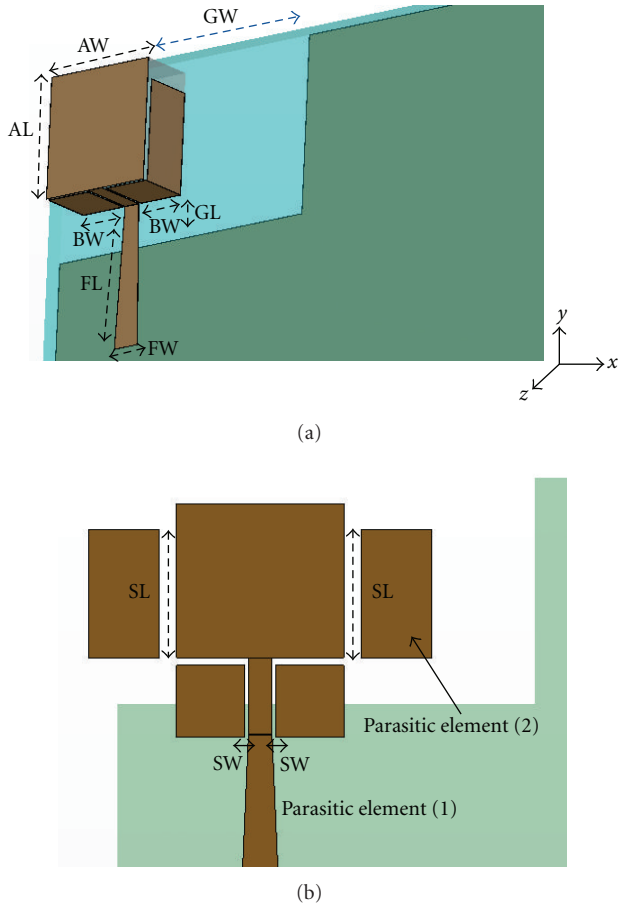

Figure 1: Configuration of the proposed antenna. (a) Designed structure, (b) planar figure.

element has a different role. The parasitic elements (1) can operate as additional radiators due to their coupling with the rectangular radiator, and these elements radiate at the higher end of the band. The gaps between the radiator and the parasitic elements (2) operate as lambda/4 short stubs, achieving a band-stop function at 5.725–5.825 GHz in the upper WLAN band by incorporating a parasitic element (2) into each side of the radiator [2, 3]. These also act as resonators that confine the energy formed by the fields around the 5.725–5.825 GHz bands, and the stop band can be made to correspond to the length (SL) of the parasitic element (2). A folded and tapered feed line is used for miniaturization of the proposed antenna and for enhanced impedance matching.

3. Simulated Results Analysis

Based on our simulations using CST Microwave Studio, the proposed antenna is designed and optimized to operate in all UWB bands of 3.15–4.75 GHz and 7.2–10.2 GHz for VSWR less than 2, including the band-stop function of 5.725–5.825 GHz in the upper WLAN. According to the return loss characteristics of the proposed antenna, the most strongly influencing factor is the gap (SW) between the folded feed

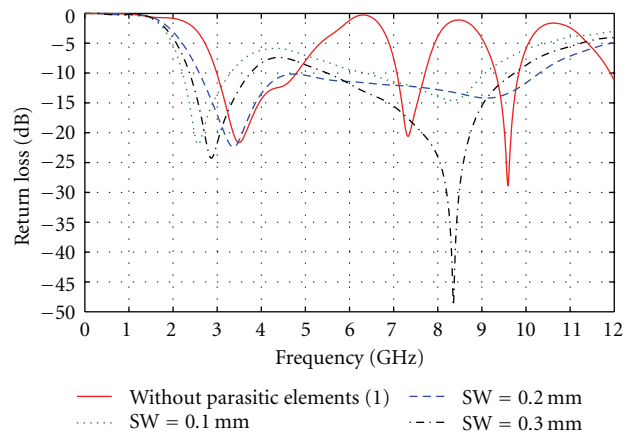

Figure 2: Simulated return losses due to width of gap (SW) between a folded feed line and a parasitic element (1).

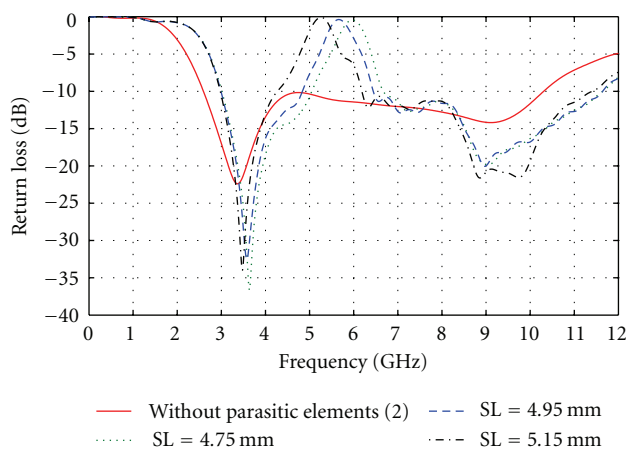

Figure 3: Simulated return losses due to height (SL) of a parasitic element (2).

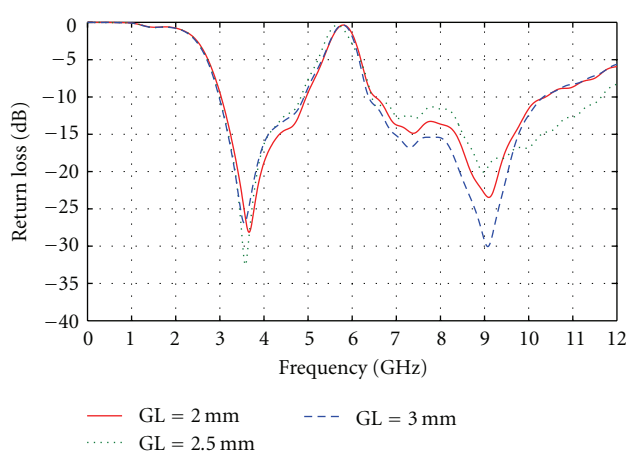

Figure 4: Simulated return losses due to parameter GL.

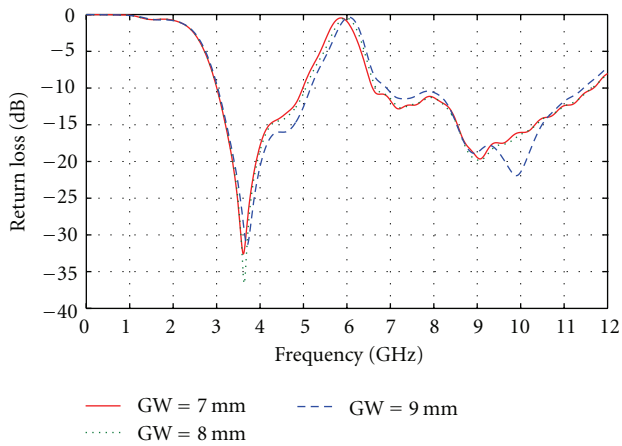

Figure 5: Simulated return losses due to parameter GW.

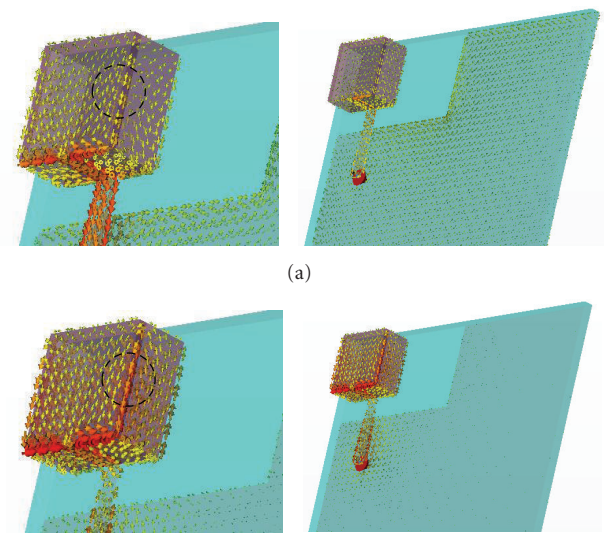

Figure 6: Current distribution of gaps between radiator and side parasitic elements for band-stop. (a) 3.15 GHz, (b) 5.8 GHz.

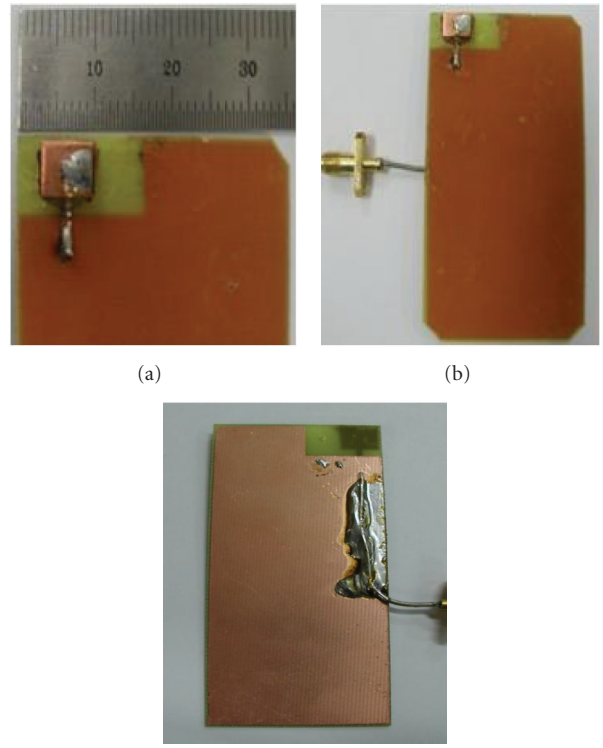

Figure 7: Photo of the proposed antenna.

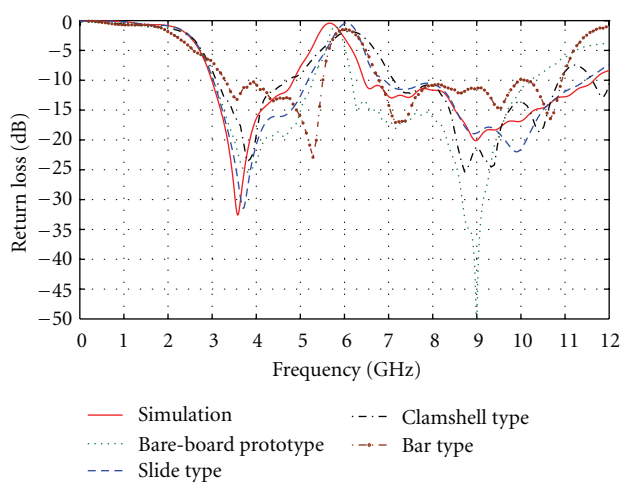

Figure 8: Measured return loss of the proposed antenna for the various mobile terminals.

line and each parasitic element (1). The results are shown in Figure 2 and compared with an antenna without parasitic elements (1). It can be seen that impedance matching can be enhanced by adding parasitic elements into the radiator and adjusting their widths. The width of 0.2 mm is determined after considering characteristic of return losses.

The variations of design parameters due to SL are shown in Figure 3. It can be observed that the desired band-stop characteristic can be obtained from the gap formed by adding a parasitic element (2), and the center frequency for the band-stop function can be varied by adjusting the height (SL) of a parasitic element (2). The length of SL is determined to be 4.95 mm which is the lambda/4 at about 5.725–5.825 GHz for considering dielectric constant of 4.5 in the dielectric block. The return losses of the proposed antenna due to parameter GL and GW are also shown in Figures 4 and 5. It can be observed that their patterns are not largely influenced by those parameters. The current distribution around lambda/4 short stubs for the band-stop function at 3.15 GHz, compared with 5.8 GHz, is shown in Figure 6. Currents around the radiator and gaps have the same direction, and currents are distributed to the entire ground plane at 3.15 GHz, while opposite currents are strongly generated at gaps, and most of the currents are not delivered to the ground plane at 5.8 GHz.

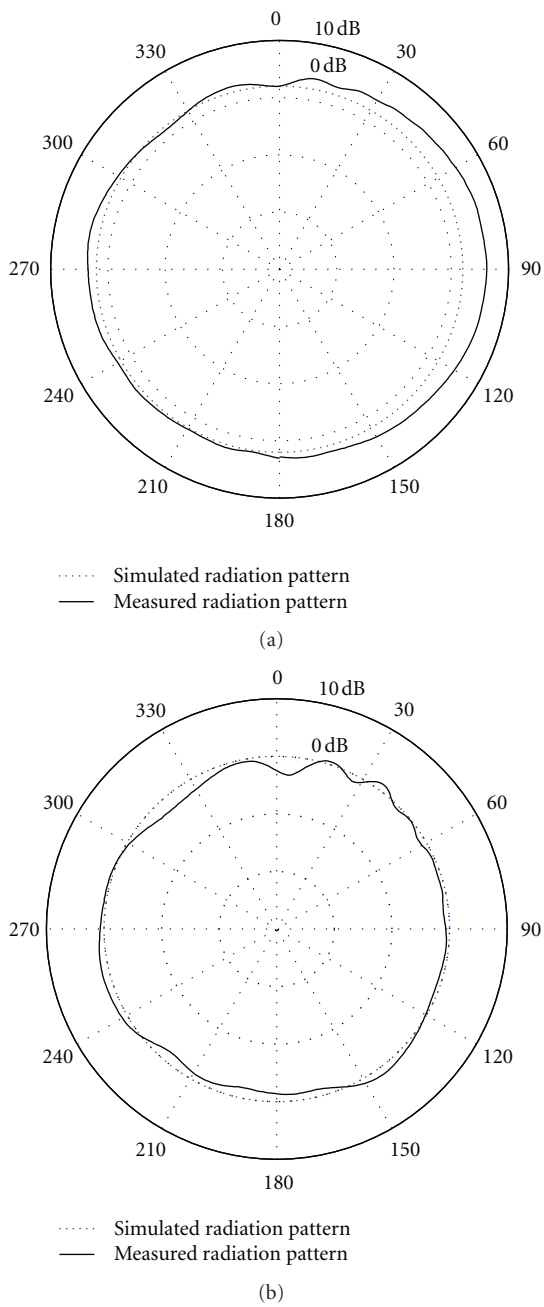

Figure 9: Simulated and measured XZ-plane patterns of the proposed antenna, 10 dB per division. (a) 3.15 GHz, (b) 7.2 GHz.

4. Experimental Results

Photos of the proposed antenna on the PCB are provided in Figure 7, showing that the proposed antenna has a very compact size. The proposed antenna is located in the top left corner of the PCB. It is directly fed by coaxial cable on the reverse side of the PCB, and the feeding point is connected through a via. The tapered feed line of the antenna is directly printed on the PCB and dielectric block. The main radiator and parasitic the elements (1) and (2) are also attached to the dielectric block after each etched pattern is fabricated.

Table 1: Absolute gain of the proposed antenna for the various mobile terminals.

Model	Maximum gain [dBi]		
	3.15 GHz	5.8 GHz	7.2 GHz
Bare-board prototype	5.75	−14.34	1.07
Slide type	1.71	−13.42	0.21
Clamshell type	2.79	−16.24	2.65
Bar type	1.42	−18.15	1.31

The proposed antenna was housed in three kinds of handset terminals of bar, slide, and clamshell type in order to conduct measurements, and those return losses are shown in Figure 8 compared with the return loss of a bare-board prototype type that does not consider handset terminals. That shows that the impedance bandwidths with VSWR less than 2 are 3.15–4.75 GHz and 7.2–10.2 GHz. These cover all UWB bands and reject the band at 5.725–5.825 GHz. The measured radiation patterns of the proposed antenna are compared with simulated results at 3.15 and 7.2 GHz, as shown in Figure 9. These radiation patterns are omni-directional, and it is observed that the measurement and simulation results are in good agreement.

The radiation patterns of the proposed antenna housed variously with handset terminals of bar, slide, and clamshell types were also measured at 3.15, 5.8, and 7.2 GHz, as shown in Figure 10. The antenna housed with handset terminals is influenced by the terminals, distorting those patterns. Table 1 shows the measured maximum gain of the proposed antenna, which is the absolute gain considering the reflections from the antenna [19]. It varies from 1.07 dBi to 5.75 dBi on the XZ-plane except in the stop band of the proposed antenna which has maximum gain from −0.21 to 2.79 when the antenna is housed with a mobile terminal.

5. Conclusion

We proposed a UWB antenna loaded by parasitic elements for mobile handsets to operate over all UWB bands with a band-stop function. This design can have wide impedance matching due to the parasitic elements (1) that are incorporated into both sides of a folded feed line. Moreover, the proposed antenna can have band-stop characteristic that are created by adjusting the lengths of a pair of parasitic elements (2). This proposed method can cover all UWB bands of 3.15–4.75 GHz and 7.2–10.2 GHz for VSWR less than 2, while 5.725–5.825 GHz is notched. The proposed antenna has very compact size and it is very easy to implement by bending a simple metal plate into a compact structure. Ultimately, this design has strong potential for the next generation of convergence between UWB system and mobile handsets.

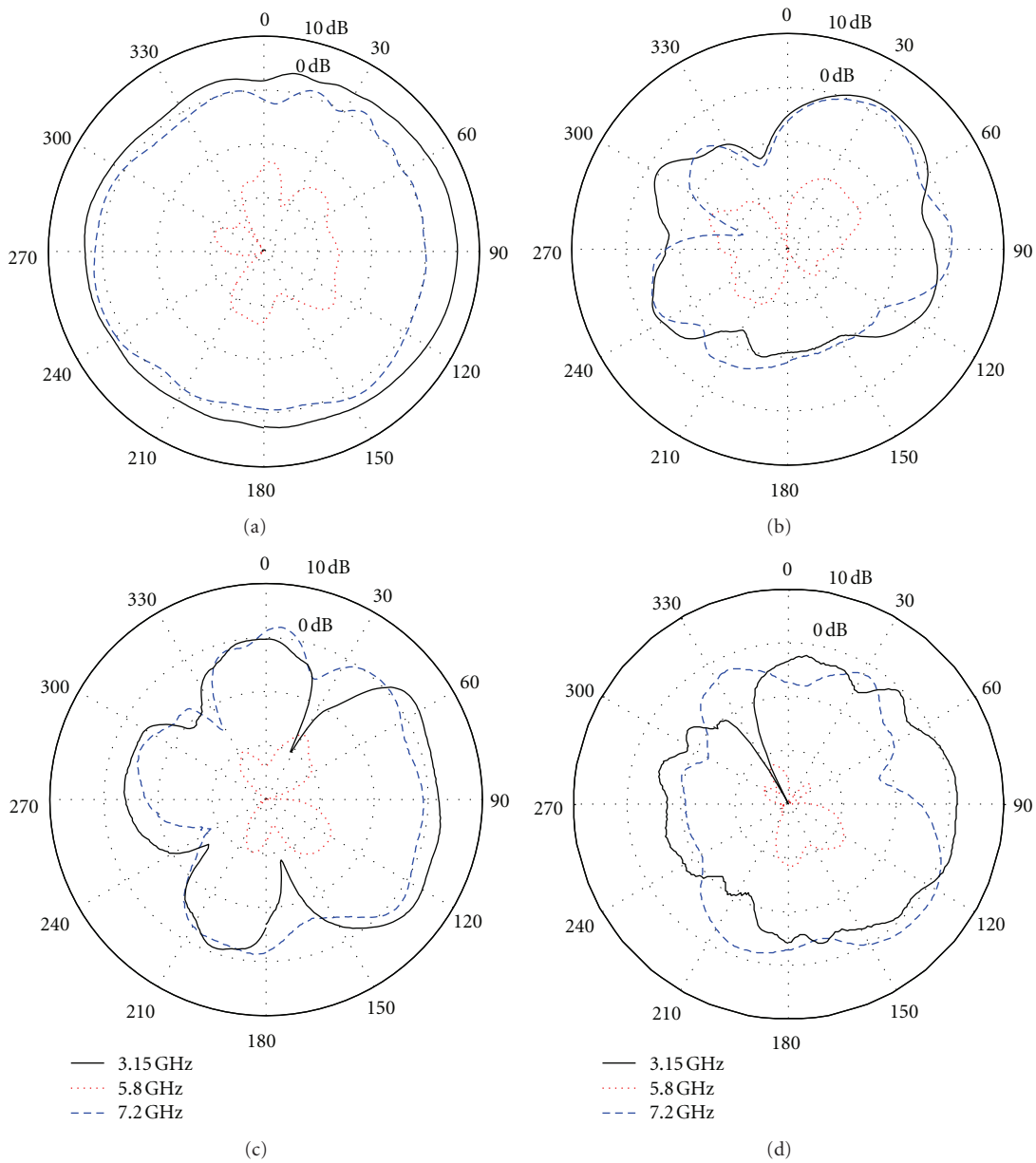

Figure 10: Measured XZ-plane pattern of the proposed antenna for the various mobile terminals, 10 dB per division. (a) Bare-board prototype, (b) slide type, (c) clamshell type, (d) bar type.

Acknowledgment

This research was supported by LG Electronics, Seoul, Korea.

References

[1] J. Timmermann, M. Porebska, C. Sturm, and W. Wiesbeck, "Investigating the influence of the antennas on UWB system impulse response in indoor environments," in *Proceedings of the 4th European Radar Conference (EURAD '07)*, pp. 283–286, October 2007.

[2] I. J. Yoon, H. Kim, Y. J. Yoon, Y. H. Kim, and H. K. Yoon, "Ultra-wideband tapered slot antenna with band cutoff characteristic," *Electronics Letters*, vol. 41, no. 11, pp. 629–630, 2005.

[3] H. K. Yoon, Y. J. Yoon, H. Kim, and C. H. Lee, "Flexible ultra-wideband polarization diversity antenna with band-notch function," *IET Microwaves, Antennas & Propagation*, vol. 5, no. 12, pp. 1463–1470, 2011.

[4] Y. Lim, H. K. Yoon, S. Kwak, B. S. Lee, Y. J. Yoon, and Y. H. Kim, "The design of three-dimensional folded fat-monopole antenna for UWB radio system," *International Journal of Microwave and Optical Technology*, vol. 1, no. 2, pp. 813–819, 2006.

[5] H. K. Yoon, W. S. Kang, Y. J. Yoon, and C. H. Lee, "A flexible UWB antenna attachable to various kinds of materials," in *Proceedings of the IEEE International Conference on Ultra-Wideband (ICUWB '07)*, pp. 204–209, September 2007.

[6] R. Fallahi, A. A. Kalteh, and M. G. Roozbahani, "A novel UWB elliptical slot antenna with band-notched characteristics,"

Progress in Electromagnetics Research, vol. 82, pp. 127–136, 2008.

[7] Z. A. Zheng and Q. X. Chu, "CPW-fed ultra-wideband antenna with compact size," *Electronics Letters*, vol. 45, no. 12, pp. 593–594, 2009.

[8] G. Cappelletti, D. Caratelli, R. Cicchetti, and M. Simeoni, "A low-profile printed drop-shaped dipole antenna for wideband wireless applications," *IEEE Transactions on Antennas and Propagation*, vol. 59, pp. 3526–3535, 2011.

[9] A. Godard, L. Desrumaux, V. Bertrand et al., "A transient UWB antenna array used with complex impedance surfaces," *International Journal of Antennas and Propagation*, vol. 2010, Article ID 243145, 8 pages, 2010.

[10] C.-H. Liao and D.-C. Chang, "A large aperture UWB antenna array for real beam radar imaging," *International Journal of Antennas and Propagation*, vol. 2012, Article ID 639603, 7 pages, 2012.

[11] K. S. Ryu and A. A. Kishk, "UWB antenna with single or dual band-notches for lower WLAN band and upper WLAN band," *IEEE Transactions on Antennas and Propagation*, vol. 57, no. 12, pp. 3942–3950, 2009.

[12] W. Li, X. Shi, T. Zhang, and Y. Song, "Novel UWB planar monopole antenna with dual band-notched characteristics," *Microwave and Optical Technology Letters*, vol. 52, no. 1, pp. 48–51, 2010.

[13] J. Xu, D. Y. Shen, G. T. Wang, X. H. Zhang, X. P. Zhang, and K. Wu, "A small UWB antenna with dual band-notched characteristics," *International Journal of Antennas and Propagation*, vol. 2012, Article ID 656858, 7 pages, 2012.

[14] S. W. Su, J. H. Chou, and K. L. Wong, "Internal ultrawideband monopole antenna for wireless USB dongle applications," *IEEE Transactions on Antennas and Propagation*, vol. 55, no. 4, pp. 1180–1183, 2007.

[15] D. D. Krishna, M. Gopikrishna, C. K. Aanandan, P. Mohanan, and K. Vasudevan, "Ultra-wideband slot antenna for wireless USB dongle applications," *Electronics Letters*, vol. 44, no. 18, pp. 1057–1058, 2008.

[16] Y. C. Chang, C. Y. Wu, and C. C. Chiu, "A ultra-wideband monopole antenna for wireless applications," in *Proceedings of the International Kharkov Symposium on Physics and Engineering of Microwaves, Millimeter and Submillimeter Waves (MSMW"10)*, June 2010.

[17] H.-C. Tang and K.-H. Lin, "Miniaturized asymmetrical triangle UWB antenna for WUSB dongle applications," in *Proceedings of the IEEE International Symposium on Antennas and Propagation*, pp. 1467–1469, 2011.

[18] A. Abdin, "Characteristics of a multi bandwith gear microstrip antenna using a taper for feeding," in *Proceedings of the Progress in Electromagnetic Research Symposium (PIERS '09)*, Beijing, China, March 2009.

[19] C. A. Balanis, *Modern Antenna Handbook*, John Wiley & Sons, Hoboken, NJ, USA, 2008.

Hindawi Publishing Corporation
International Journal of Antennas and Propagation
Volume 2012, Article ID 695190, 4 pages
doi:10.1155/2012/695190

Application Article

Optimized Ultrawideband and Uniplanar Minkowski Fractal Branch Line Coupler

Mohammad Jahanbakht[1] and Mohammad Tondro Aghmyoni[2]

[1] *Department of Electronic Engineering, Shahr-e-Qods Branch, Islamic Azad University, Tehran, Iran*
[2] *Institute of Postgraduate Studies, Multimedia University, Selangor, 63100 Cyberjaya, Malaysia*

Correspondence should be addressed to Mohammad Jahanbakht, mjahanbakht@yahoo.com

Received 17 May 2012; Accepted 27 July 2012

Academic Editor: Renato Cicchetti

The non-Euclidean Minkowski fractal geometry is used in design, optimization, and fabrication of an ultrawideband (UWB) branch line coupler. Self-similarities of the fractal geometries make them act like an infinite length in a finite area. This property creates a smaller design with broader bandwidth. The designed 3 dB microstrip coupler has a single layer and uniplanar platform with quite easy fabrication process. This optimized 180° coupler also shows a perfect isolation and insertion loss over the UWB frequency range of 3.1–10.6 GHz.

1. Introduction

Recently, ultrawideband technology has been used in many branches of science and wide range of applications such as radars, navigation, telemetry, mobile satellite communications, biomedical systems, the direct broadcast systems, and remote sensing utilities. The design of an appropriate microwave device for these systems is one of the major challenging tasks.

Microstrip power divider and coupler designs and topologies which achieved compact size and broadband operation of the component could be categorized in some major methods including

(a) wideband stub matching,

(b) multistaging of the ordinary components,

(c) multilayer and multiwafer packaging technologies,

(d) deforming the shapes and using alternative geometries.

As an instance of the first category, a 3 dB power divider on microstrip line is analyzed and designed in [1] using UWB stub matching technique. This divider is formed by installing a pair of stepped-impedance, open-circuited stubs, and parallel-coupled lines to two symmetrical output ports.

Also in this class, an UWB microstrip power divider with good isolation and sharp roll-off skirt is proposed in [2]. By introducing a pair of quarter-wavelength short-circuited stubs and parallel-coupled lines to 2 symmetrical output ports, good performance in terms of equal power splitting is achieved. By virtue of direct-current chocked and half-wavelength transmission zeros of short-circuited stubs, out-of-band roll-off skirt near the cutoff frequencies is sharpened.

Multistaging of the well-known Wilkinson power divider is used in [3] to achieve an UWB coplanar waveguide balun for operation over 800–5000 MHz. Another well-established example of the multistaging method is proposed in [4]. Thereby, an optimized microstrip 3-stage Wilkinson power divider based on lowpass filter is presented. The particle swarm optimization method and method of moment have been used to broaden the bandwidth to effectively cover 1–8 GHz which is equal to 155.6% fractional bandwidth.

Multistaging of the T-junctions in slot line topology has also been presented in [5]. This compact and out-of-phase uniplanar power divider operates over the ultra wideband frequency range.

The third alternative category is to use multilayer substrates. A multilayer in-phase power divider with ultrawideband behavior is presented in [6]. The proposed divider

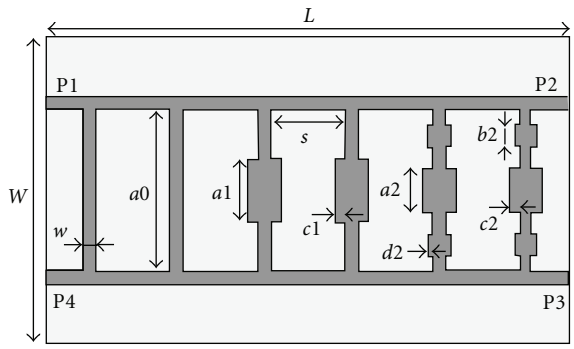

Figure 1: Profile of the UWB microstrip branch line coupler which consists of 2 × ordinary, 2 × first-order, and 2 × second-order Minkowski fractal branches.

Table 1: Topology and widebanding techniques comparison between 3 dB couplers and power dividers.

Reference number	Transmission line	UWB technique
[1]	Microstrip	Wideband stub matching
[2]	Microstrip	Wideband stub matching
[3]	CPW	Multistage Wilkinson
[4]	Microstrip	Multistage Wilkinson
[5]	Slot line	Multistage T-junctions
[6]	Microstrip	Multilayer substrate
[7]	Parallel strip lines	Multilayer substrate
[8]	Slot line	Multilayer substrate
This work	Microstrip	Fractal deformation

exploits broadside coupling via a multilayer microstrip slot configuration. The design method is based on conformal mapping techniques.

Two other UWB multilayer power dividers are presented in [7, 8]. In [7], a low-loss transition from a coaxial transmission line to a double-sided parallel-strip line is presented. On the other hand, a slot line topology with bandpass filtering is used in [8].

The UWB techniques in the references are compared together in Table 1. Most of these works are using microstrip lines and a few others use other alternatives. According to author's survey, usage of fractal geometries is not reported in branch line coupler designs, so far.

Fractal deformation in design and fabrication of an UWB branch line coupler will be demonstrated in the next sections. The Minkowski fractal will be used to redesign an ordinary 3 dB coupler and broaden its bandwidth. The coupler dimensions are optimized and the final tuned structure is fabricated. The measured and analyzed results will be presented and compared.

2. Coupler Design and Theory

Fractals are non-Euclidean geometries with some amazing behaviors and specifications. These geometries have been used in articles to achieve multiband radiation, band width broadening, and size reduction [9]. These benefits are actually resulting from curvature's self-similarity, which means these geometries represent a certainly finite area which is bounded in a theoretically infinite line.

Table 2: Proposed coupler dimensions [mm].

L	W	w	s	$a0$	$a1$	$c1,2$	$a2$	$b2$	$d2$
45	30	1.1	6.4	13.9	5.4	0.9	3.7	1.9	0.5

The Minkowski fractal is used in this paper to broaden the bandwidth and shrink the size of a branch line coupler. The UWB coupler profile is shown in Figure 1. This coupler possesses four ports where the input power at P1 splits equally between output ports P2 and P3. The 4th port is isolated and terminated using a matched load.

This coupler has 6 branches of parallel lines. Two of them are conventional straight lines and the remaining 4 branches have Minkowski fractals of 1st and 2nd orders. When fractal order approaches to infinity, the segment length approaches to zero and the circumference grows boundlessly. Meanwhile, the area still remains finite.

This coupler is mounted on TMM13 Rogers substrate with dielectric constant of 12.80, dielectric loss tangent of 0.002, and substrate thickness of 1.27 mm. Coupler dimensions are presented in Table 2. These dimensions are initially set to the values of a conventional branch line coupler and then tuned through a simple optimization procedure in ANSOFT HFSS 13.0.

The well-known quasi-Newton optimization method is selected with 500 iterations. Except for L, W, w, s, and a0; all other variables in Table 2 are defined as optimization variables. The goal is set to gain minimum inbound and maximum outbound return losses and also to achieve 3 dB insertion loss.

As can be seen in Figure 1, in two 2nd-order branch lines, each straight segment of the 1st order should be replaced with order one itself (to enforce self-similarity). This means that the central big square ought to have small squares protruding from each side, while it has not!

The reason is laid beneath optimization. After optimization process, the area and size of these outgrowths get smaller than realizable margins, and therefore omitted from the design.

According to the uniplanar and single-layer structure of the coupler, it has very easy fabrication process. Besides, based on the optimized fractal geometry of the coupler, it owns a compact size and broad bandwidth. These features of the coupler will be studied in the next section.

3. Results and Discussion

Hereby some terms have to be suggested for easier understanding of the text. Similar to Figure 1, a conventional branchline coupler consists of 4 ports and 6 branches of straight lines. If someone replaces the 6 ordinary branches with first-order Minkowski fractals, a 1st-order fractal couplerwill be achieved.

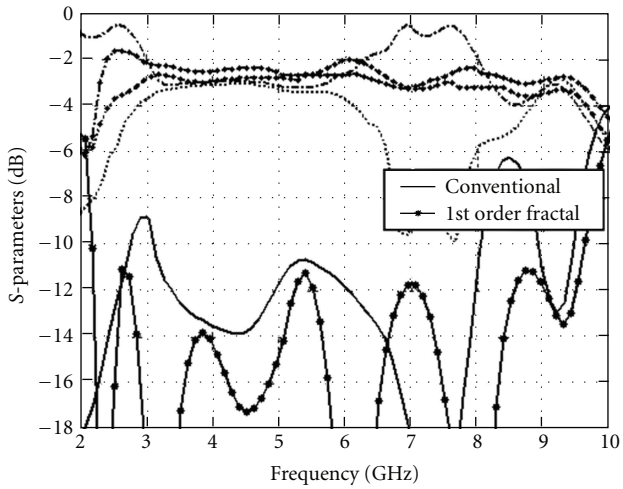

Figure 2: Scattering S11 (—), S21 (−·), and S31 (· · ·) parameters of the conventional branch line coupler and 1st-order Minkowski branch line coupler.

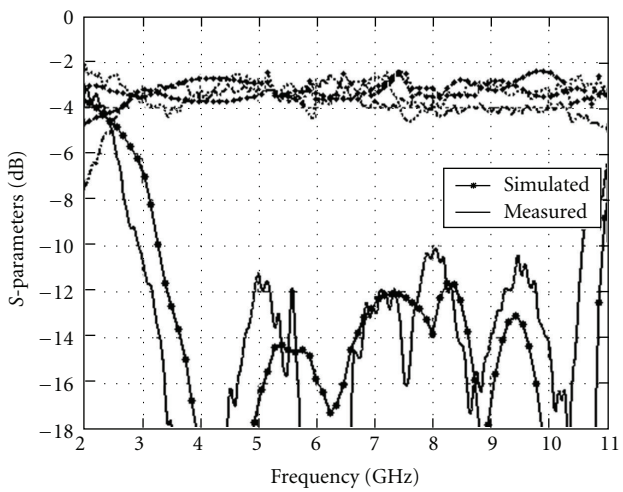

Figure 3: Simulated and measured Scattering S11 (—), S21 (−·), and S31 (· · ·) parameters of the UWB Minkowski branch line coupler.

In Figure 2, scattering parameters of the conventional branch line coupler has been compared with 1st-order fractal. The operating 3 dB frequency range of the conventional coupler is 3.2–6.2 GHz. This bandwidth extended to 2.6–9.5 GHz by using 1st-order fractal.

As a consequence of Figure 2, one may think of adding extra orders of the same fractal lines to extend the bandwidth. As shown exactly in Figure 1, by adding two 2nd-order lines to the conventional and 1st-order fractal branches, the operating frequency range of the coupler would expand enough to cover the UWB necessity. This property is investigated in Figure 3 where the simulation and measurement results are compared and shown a good agreement.

According to Figure 4, the phase difference at the output ports P2 and P3 remains 180 degree over the entire frequency range. Adding extra orders of the fractals has no major effect

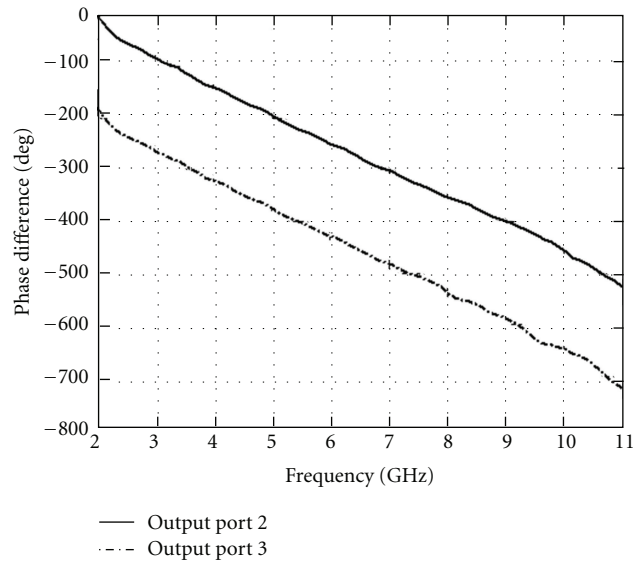

Figure 4: Measured output phase difference of the UWB Minkowski branch line coupler.

Table 3: Frequency and size comparison between 3 dB couplers and power dividers.

Reference Number	Frequency Range [GHz]	Size [mm × mm]	Size (Electrical)
[1]	3.1–10.6	40 × 50	$0.9\lambda \times 1.1\lambda$
[2]	3.1–10.6	35 × 50	$0.8\lambda \times 1.1\lambda$
[5]	3.1–10.6	40 × 50	$0.9\lambda \times 1.1\lambda$
[6]	3.1–10.6	Two × 20 × 30	Two × $0.45\lambda \times 0.7\lambda$
[7]	3.1–10.6	Two × 20 × 30	Two × $0.45\lambda \times 0.7\lambda$
This work	3.1–10.6	30 × 45	$0.7\lambda \times 1.0\lambda$

on the results and could make the fabrication process more risky and challenging.

Electrical and mechanical size of some 3 dB couplers and power dividers are compared in Table 3. All these references cover the UWB frequency range and this work has the smallest size and area.

The fabricated uniplanar coupler profile is shown in Figure 5. This optimized coupler has the overall size of 30 × 45 mm^2 with 110% fractional bandwidth. The 4th port of this coupler has to be terminated to a matched load. This coupler shows 180° phase difference between output ports P2 and P3 with more than 10 dB isolation between them.

4. Conclusion

A 3 dB and 180° fractal branch line coupler is designed, optimized, and fabricated. The Minkowski fractal geometry is used to make a small and single-layer microstrip pattern with overall size of 30 × 45 mm^2. This branch line coupler covers the ultrawideband frequency range with 110% fractional bandwidth. This optimized UWB coupler is fabricated and its insertion loss, return loss, and the output phase difference

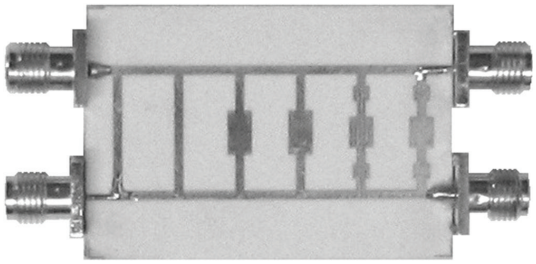

Figure 5: The fabricated profile of the UWB Minkowski branch line coupler.

have been measured, which showed a good agreement with the simulation results.

Acknowledgment

This work is published as a result of a research proposal named, "Design, Simulation, and Fabrication of a High Efficient LDMOS Power Amplifier". This proposal is approved and sponsored by the Shahre-Qods Branch, Islamic Azad University.

References

[1] S. W. Wong and L. Zhu, "Ultra-wideband power divider with good in-band splitting and isolation performances," *IEEE Microwave and Wireless Components Letters*, vol. 18, no. 8, pp. 518–520, 2008.

[2] S. W. Wong and L. Zhu, "Ultra-wideband power dividers with good isolation and improved sharp roll-off skirt," *IET Microwaves, Antennas and Propagation*, vol. 3, no. 8, pp. 1157–1163, 2009.

[3] J. S. Lim, U. H. Park, Y. C. Jeong et al., "800–5000 MHz ultra-wideband CPW balun," *Electronics Letters*, vol. 42, no. 18, p. 1037, 2006.

[4] A. H. Naghavi, M. Tondro-Aghmiyouni, M. Jahanbakht, and A. A. Lotfi Neyestanak, "Hybrid wideband microstrip Wilkinson power divider based on lowpass filter optimized using particle swarm method," *Journal of Electromagnetic Waves and Applications*, vol. 24, no. 14-15, pp. 1877–1886, 2010.

[5] M. E. Bialkowski and A. M. Abbosh, "Design of a compact UWB out-of-phase power divider," *IEEE Microwave and Wireless Components Letters*, vol. 17, no. 4, pp. 289–291, 2007.

[6] A. M. Abbosh, "Ultra wideband inphase power divider for multilayer technology," *IET Microwaves, Antennas and Propagation*, vol. 3, no. 1, pp. 148–153, 2009.

[7] T. W. Eubanks and K. Chang, "Low-loss ultra-wideband double-sided parallel-strip line transition and power divider," *Electronics Letters*, vol. 46, no. 1, pp. 93–94, 2010.

[8] K. Song and Q. Xue, "Novel ultra-wideband (UWB) multilayer slotline power divider with bandpass response," *IEEE Microwave and Wireless Components Letters*, vol. 20, no. 1, pp. 13–15, 2010.

[9] D. H. Werner and S. Ganguly, "An overview of fractal antenna engineering research," *IEEE Antennas and Propagation Magazine*, vol. 45, no. 1, pp. 38–57, 2003.